

## Department of Precision and Microsystems Engineering

### Actuator concept comparison for the next-gen Ampelmann hexapod platform

Thomas Frateur

Report no : 2021.012  
Coach : Dr.ir. H. Polinder  
Professor : Dr.ir. R.A.J. van Ostayen  
Specialisation : Mechatronic system design  
Type of report : Master Thesis  
Date : 24-02-2021



# Actuator concept comparison for the next-gen Ampelmann hexapod platform

by

Thomas Frateur

to obtain the degree of Master of Science  
in context of research at Ampelmann B.V.  
at the Delft University of Technology,  
to be defended publicly on Wednesday February 24, 2021 at 13:30.

Student number:	4303555	
Project duration:	February 15, 2020 – February 24, 2021	
Company supervisor:	Ir. A. Verweij	Ampelmann
Thesis committee:	Dr. ir. R.A.J. van Ostayen,	TU Delft, supervisor
	Dr. ir. H. Polinder,	TU Delft, supervisor
	Dr. ir. A. Jarquin Laguna,	TU Delft
	Ir. J.P.A. Nijssen,	TU Delft

*This thesis is confidential and cannot be made public until February 24, 2023.*

An electronic version of this thesis is available at <http://repository.tudelft.nl/>.



# Preface

This thesis report is the culmination of a little over a year worth of work for my master thesis project. I started this project at a desk of the Ampelmann headquarters in Delft to research possible mass and efficiency improvements in their hexapod systems. Although the project direction remained the same, Covid-19 changed the location and with that the kind of interaction during such a project somewhat drastically. Performing a graduation project largely from the confines of the four walls in my student room has had advantages but also posed its unique challenges.

With that in mind, I would like to thank everyone who supported me in the last year and enabled me to complete this project either by letting me pick their brain or providing a distraction in these strange times.

Most importantly I would like to thank my three supervisors, Ron van Ostayen, Henk Polinder and Alexander Verweij for the many hours of video conferencing to discuss progress and the next steps of my research. Both the practical engineering insights provided by Alexander and the academic smarts of Ron and Henk where of large importance to this work.

I would also like to thank my family, and in particular my parents for their continuous support through my somewhat tortuous study career and the different decision moments it brought with it. This work is the direct result of the many conversations about aspirations to follow and fears to overcome.

Prefaces should not add a lot of extra reading to a report, so without further ado, I would like to present to you, what should be, the report concluding my study career at the TU Delft.

Thomas Frateur

# Contents

<b>1</b>	<b>Introduction</b>	<b>6</b>
1.1	Ampelmann . . . . .	6
1.2	Next-gen A-type platforms . . . . .	7
1.3	Next-gen actuator . . . . .	7
1.4	Reading guide . . . . .	9
<b>2</b>	<b>Modelling strategy</b>	<b>10</b>
2.1	Model scope . . . . .	10
2.2	Actuator description . . . . .	11
2.2.1	EMA mechanical cylinder . . . . .	12
2.2.2	EHA hydrostatic pump . . . . .	13
2.3	General model strategy . . . . .	13
2.4	Actuator modelling . . . . .	15
2.4.1	Actuator power relations . . . . .	15
2.4.2	Actuator mass relations . . . . .	16
2.4.3	Constraints . . . . .	17
2.5	Actuator requirements . . . . .	17
<b>3</b>	<b>Electro mechanical actuator, sizing and loss model development</b>	<b>18</b>
3.1	Introduction . . . . .	18
3.2	System description and method . . . . .	19
3.2.1	Actuator description . . . . .	19
3.2.2	Component choices . . . . .	20
3.2.3	Modelling method . . . . .	20
3.3	Sizing model development . . . . .	22
3.3.1	List of symbols . . . . .	22
3.3.2	Sizing of the mechanical cylinder . . . . .	23
3.3.3	Sizing of the gearbox . . . . .	29
3.4	Loss model development . . . . .	32
3.4.1	List of symbols . . . . .	33
3.4.2	Mechanical cylinder losses . . . . .	34
3.4.3	Gearbox losses . . . . .	37
3.5	Constraints . . . . .	38
3.6	Conclusions . . . . .	38
3.6.1	Mass and power loss trends . . . . .	38
3.6.2	Model use . . . . .	39
3.6.3	Future work . . . . .	39
<b>4</b>	<b>Electro hydrostatic actuator, sizing and loss model development</b>	<b>41</b>
4.1	Introduction . . . . .	41
4.2	System description and method . . . . .	42
4.2.1	Actuator description . . . . .	42
4.2.2	Component choices . . . . .	43
4.2.3	Modelling method . . . . .	43
4.3	Sizing model development . . . . .	45
4.3.1	List of symbols . . . . .	45

4.3.2	Sizing of the hydraulic cylinder . . . . .	46
4.3.3	Piping and manifolds . . . . .	49
4.3.4	Sizing of the hydrostatic pump . . . . .	50
4.3.5	Hydraulic fluid . . . . .	52
4.4	Loss model development . . . . .	52
4.4.1	List of symbols . . . . .	53
4.4.2	Hydraulic cylinder losses . . . . .	53
4.4.3	Hydrostatic pump losses . . . . .	55
4.4.4	pipe and manifold losses . . . . .	58
4.5	Constraints . . . . .	59
4.6	Conclusions . . . . .	59
4.6.1	Mass and power loss trends . . . . .	59
4.6.2	Model use . . . . .	60
4.6.3	Future work . . . . .	61
<b>5</b>	<b>Servo motor modelling</b>	<b>62</b>
5.1	Sizing model development . . . . .	62
5.1.1	List of symbols . . . . .	63
5.1.2	Configuration modelling . . . . .	63
5.1.3	Static mass modelling . . . . .	64
5.1.4	Rotating mass modelling . . . . .	65
5.2	Loss model development . . . . .	68
5.2.1	List of symbols . . . . .	68
5.2.2	Power transmission . . . . .	68
5.2.3	Electric losses . . . . .	69
5.2.4	Mechanical losses . . . . .	70
5.2.5	PMSM loss trends . . . . .	71
<b>6</b>	<b>High power linear actuator properties in hexapod applications</b>	<b>72</b>
6.1	Introduction . . . . .	72
6.2	Method . . . . .	73
6.2.1	Actuator description . . . . .	73
6.2.2	General model strategy . . . . .	75
6.2.3	Actuator model . . . . .	76
6.3	General Actuator properties . . . . .	77
6.3.1	General sizing relations . . . . .	77
6.3.2	Component power loss relations . . . . .	78
6.4	Case study . . . . .	79
6.4.1	Actuator configurations . . . . .	79
6.4.2	Neutral configuration comparison . . . . .	83
6.4.3	Power loss properties . . . . .	84
6.4.4	Requirement variation . . . . .	86
6.5	Conclusions . . . . .	86
<b>7</b>	<b>Conclusion</b>	<b>88</b>
7.1	Future work . . . . .	90
	<b>Bibliography</b>	<b>90</b>
<b>A</b>	<b>Mechanical transmission equations</b>	<b>100</b>
A.1	Planetary roller screw sizing . . . . .	100
A.2	Cylinder housing sizing . . . . .	101
A.3	Gear sizing . . . . .	102
A.4	Planetary roller screw losses . . . . .	104
A.4.1	Geometry related losses . . . . .	104
A.4.2	Rolling friction coefficient . . . . .	104
A.5	Gearbox losses . . . . .	106
A.5.1	Forces and speed . . . . .	106
A.5.2	Gear losses . . . . .	106

A.5.3	Bearing losses . . . . .	108
A.6	Loss model properties . . . . .	108
A.6.1	Mechanical cylinder losses . . . . .	109
A.6.2	Helical gearbox losses . . . . .	112
<b>B</b>	<b>Hydrostatic transmission equations</b>	<b>118</b>
B.1	Hydraulic cylinder sizing . . . . .	118
B.1.1	Piston rod sizing . . . . .	118
B.1.2	Cylinder housing sizing . . . . .	119
B.2	Pipe loss model . . . . .	120
B.2.1	Pipe flow resistance loss . . . . .	120
B.2.2	Pipe restriction loss . . . . .	121
B.3	Seal friction model . . . . .	121
B.4	Loss model properties . . . . .	122
<b>C</b>	<b>Servo motor equations</b>	<b>124</b>
C.1	Sizing models . . . . .	124
C.1.1	Configuration sizing . . . . .	124
C.1.2	Load sizing . . . . .	127
C.1.3	Static mass fit . . . . .	127
C.2	PMSM parameters . . . . .	129
<b>D</b>	<b>General parameters and equations</b>	<b>130</b>
D.1	General parameters . . . . .	130
D.2	Cubic Mean Load . . . . .	130
D.3	Scaling coefficients . . . . .	131
<b>E</b>	<b>Sensitive information</b>	<b>132</b>
E.1	Ampelmann actuator Requirements . . . . .	132
E.2	Ampelmann actuator test timeseries . . . . .	132
E.3	Hydrostatic pump losses . . . . .	132
E.4	Preliminary design tool . . . . .	132
<b>F</b>	<b>Papers</b>	<b>133</b>
F.1	EMA sizing and loss model development . . . . .	133
F.2	EHA sizing and loss model development . . . . .	133
F.3	High power linear actuator properties in hexapod applications . . . . .	133
<b>G</b>	<b>Literature review</b>	<b>134</b>
G.1	Introduction . . . . .	134
G.2	Ampelmann specifications . . . . .	134
G.3	Linear actuator technologies . . . . .	140
G.4	Actuator comparison . . . . .	163
G.5	Project proposal . . . . .	172
G.6	Summary . . . . .	183
<b>H</b>	<b>Glossary</b>	<b>184</b>

# Chapter 1

## Introduction

### 1.1 Ampelmann

Ampelmann B.V. wants to make offshore crew access as easy as crossing the street. The Ampelmann A-type motion compensation platform is a hexapod type platform developed to transfer personnel and light cargo between a moving ship and a fixed offshore structure. Figure 1.1 shows such a system in action while transferring personnel to an offshore platform. The Ampelmann A-type is capable of operating in sea states up to 3m Hs while moving 20 personnel or 100kg of cargo in under 5 minutes.

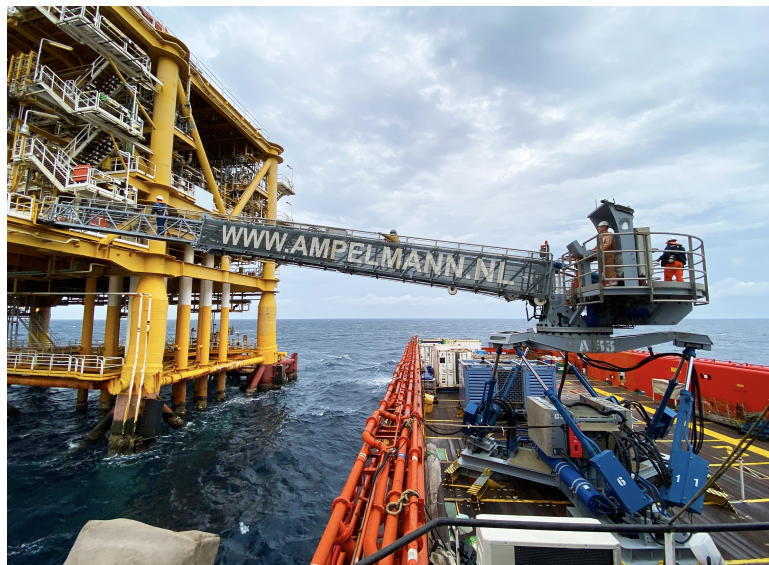


Figure 1.1: Ampelmann A-type crew transfer gangway (Ampelmann Operations B.V.)

**The hexapod platform** A hexapod or Stewart platform is a three dimensional motion platform with 6 actuated degrees of freedom. The platform has six linear actuators mounted in a slanted triangular configuration between a vessel fixed frame and a moving platform base. In the Ampelmann A-type, the hexapod is used to compensate vessel motion and create a still standing platform with respect to a fixed structure. To be able to operate in the conditions mentioned above, the hexapod linear actuators should each be capable of outputting 150kN at  $1\text{m s}^{-1}$  over a stroke of 2m. The current A-type actuators are conventional linear hydraulic actuators with a centralised hydraulic power unit (HPU) and cylinder mounted valve control. Hydraulic accumulators are used as a buffer to store potential energy in the system.

**Basic operation** To compensate the wave induced motion of the vessel, hexapod actuators move in a largely sinusoidal fashion. Upon start-up the hexapod actuators rest on their physical end stops. During operation, actuators move sinusoidally to compensate motion of the vessel and keep the mounted platform still in the air. At the end of the operation, the hexapod is moved back to its resting position in which all actuators rest on

their end stops. The position of the platform with respect to its moving reference frame is therefore exactly the same at the start and end of the operation as is shown in Figure 1.2. As such, the work performed by the platform or by each individual actuator is equal to zero for every given operational cycle. Using efficiency to describe the actuator performance is therefore unsuited as the mean output power of the actuators is zero while the mean input power determined by the system losses is larger than zero. A much better metric to describe the actuator performance is the use of actuator energy consumption or mean power draw for a specific task. The mean power draw of the actuator represent the losses in the actuator for this specific task.

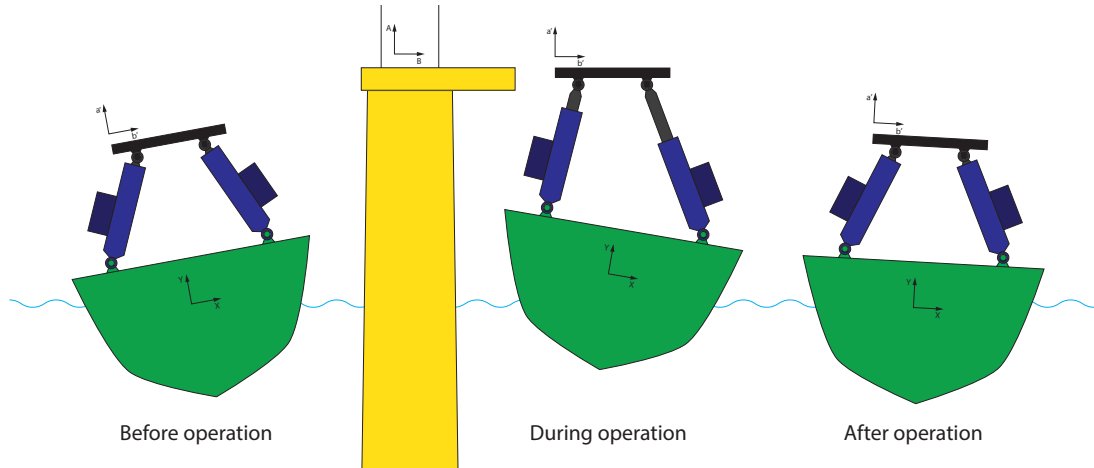


Figure 1.2: Basic 2D representation of the Ampelmann hexapod platform operation.

## 1.2 Next-gen A-type platforms

For future A-type models, Ampelmann is looking to decrease the system mass and increase the system efficiency of its platform. Increasing system efficiency is a general trend found in industry based on two main drives. An important aspect in increasing efficiency is defined by environmental considerations; achieving more with less environmental costly resources. Increased efficiency however also has a financial consequence as the lowered energy usage decreases operating costs. Similarly, reducing system mass can impact operational costs directly, especially in mobile applications such as the Ampelmann hexapod. The vessels carrying the Ampelmann platforms are often away from the shore for longer periods of time. The lower the system mass footprint of the Ampelmann hexapod, the more payload capacity of the vessel remains for cargo, hence increasing the economic value of the vessel trip. Furthermore, the Ampelmann system is often mounted on a pedestal on the vessel deck resulting in strict limits on the system mass for stability requirements.

Different strategies to minimize system mass and increase system efficiency can be thought of. Note that the focus is on the motion platform and not on the connected bridge structure shown in Figure 1.1. A first option would be to compare different kinematics for the motion platform on their mass and loss properties. The hexapod however is a proven system at Ampelmann and should not be changed. The hexapod kinematics are therefore used in the remainder of this report as a fixed setup. Another option would be to add gravity compensation to the motion platform as mentioned in [129]. A spring like device or separate hydraulic column could be installed along the actuators to compensate the gravitational force of the mounted platform. In theory this would only require the actuators to deliver the acceleration forces of the platform. However, the gravity loading of the hexapod actuators is far from constant due to the extending bridge mounted on the hexapod. As the bridge rotates in the horizontal plane during operation, gravity loading changes drastically. The changing gravity load makes balancing the motion platform difficult. The next step is looking at the actuator technology used to drive the hexapod platform.

## 1.3 Next-gen actuator

Linear actuators are devices capable of converting electrical to linear mechanical energy. Often a rotary motor is used to drive a rotary to linear hydraulic or mechanical transmission. Linear actuators in high power applications are often dominated by conventional hydraulic technology. Conventional hydraulics are known for their high loss factors with maximum system efficiencies ranging around 35% [100, 180]. In the aviation industry, a development

called the more electric aircraft (MEA) found that electro hydrostatic actuators (EHA) and electro mechanical actuators (EMA) both offer significant advantages on both system efficiency [22, 33, 128] and reduced actuator mass [22, 41, 128, 163]. Both MEA incorporate decentralised actuator components in contrast to the conventional hydraulic actuators which use centralised motors and pumps to deliver hydraulic power to different hydraulic cylinders.

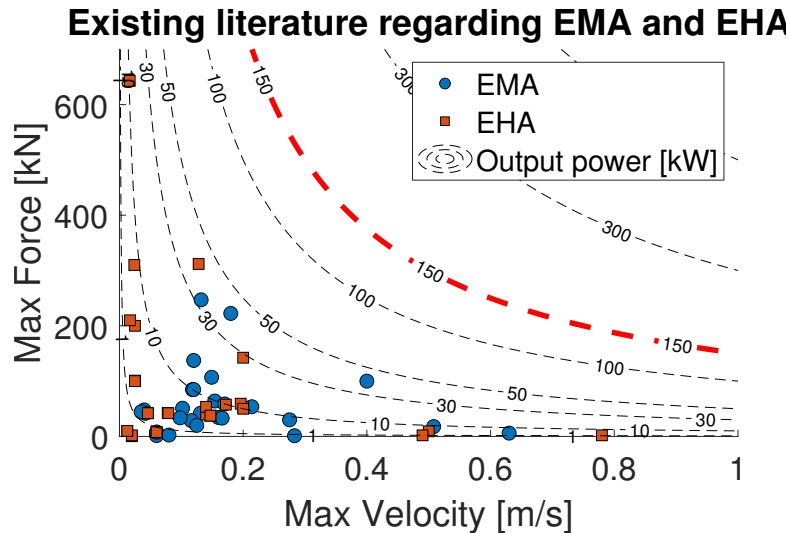


Figure 1.3: Existing actuator studies in literature ranked on maximum output force and velocity (Appendix G).

Both EHA and EMA are driven by an electric rotary machine to convert electrical energy in rotary mechanical energy. The EHA uses a hydrostatic transmission with a pump and hydraulic cylinder to obtain a linear force and velocity. Similarly, the EMA uses an (optional) gearbox and a screw mechanism to obtain the same linear force and velocity output. Both technologies have specific properties, however comparison between both options are lacking in literature for high power applications. Figure 1.3 shows various actuator studies found in literature ranked on their maximum output force and velocity. Existing literature is seen to exist on EMA and EHA for power levels up to approximately 45kW. For higher power levels, existing research is lacking and no clear benefits of one over the other technology are defined. To further the knowledge on the use of EHA and EMA linear actuators for high power applications fundamental actuator scaling properties need to be defined.

In this report actuator models describing the mass and power losses for a given task are developed and combined in a preliminary design tool for the EMA and EHA actuator. The use of a preliminary design tool ensures the most optimal configurations of both actuator technologies can be compared on their respective mass and power loss properties to find the optimal actuator technology for the Ampelmann A-type hexapod. While the focus of this report is on the sea motion compensating steward platform actuator, actuator properties and power loss models are applicable to a multitude of high power actuation applications. The focus on a specific actuator application in this report is necessary as operating regimes determine the power loss behaviour of the actuator.

**Actuator potential** Especially with respect to the system energy use, the use of different actuator technologies in the Ampelmann hexapod application has high potential of improving performance. As stated before, the typical operational cycle of the Ampelmann hexapod performs no net work. As such, the system is ideally suited for energy regeneration implementations. Electric machines are known for their motoring and generating capabilities or four quadrant operation. Four quadrant operation means the actuator can drive the load forward and backwards in which case the force and velocity vectors point in the same direction. The actuator can also be driven forward and backward by the load in which case the force and velocity vectors point in opposite directions. When using a closed system such as the EMA and EHA described above, this four quadrant operation is also feasible. Given the power loss in the actuator system is lower than the power applied to the actuator by the load, the actuator can regenerate power from the load to electric power which can be stored. The potential of a four quadrant capable actuator is illustrated with an example.

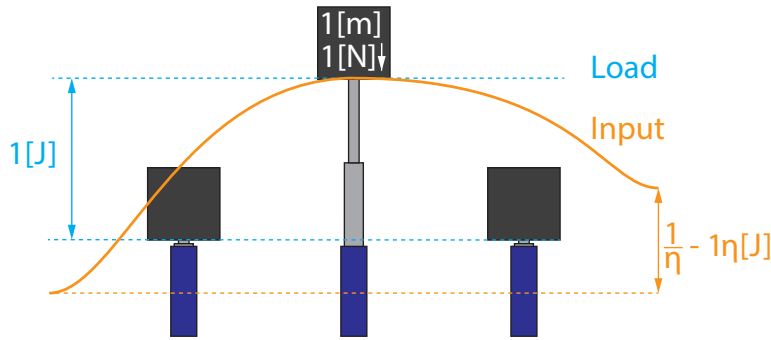


Figure 1.4: Actuator driving and back driving example

Consider the simple application of lifting a gravity based load up and back down with the start and end point at the exact same location as shown in Figure 1.4. The energy needed to lift the 1[N] load 1[m] up is equal to 1J while the energy needed to lower the load back is  $-1\text{J}$ . No net energy is therefore needed to lift and lower the load back down. When the load is driven by a 100% efficient four quadrant actuator, the energy to lift the load is taken from the grid and the negative energy to lower the load is delivered back to the grid due to back driving of the actuator. No net energy is therefore taken from the grid at the end of the operation. Unfortunately no actuator is 100% efficient. When using a fixed efficiency of 80%, the energy taken from the grid to lift the load is 1.25[J]. The connected load has the potential of delivering 1[J] back to the grid, however, only 80% of this energy is delivered back to the grid. Hence the net energy delivered by the grid is 0.45[J] instead of zero. The efficiency of the actuator is determined by power losses in the power path of the actuator due to for example friction. When back driving the actuator, a situation can occur in which the power losses in the system are higher than the instantaneous power delivered to the actuator by the load. In this case the actuator is self locking, and positive power is needed from the actuator to facilitate lowering of the load. Actuators which are always self locking are non back drivable actuators and can never work in generating mode. Self locking actuators therefore pose higher requirements on the electrical grid connection.

## 1.4 Reading guide

To direct the reader to the relevant chapters corresponding to their interests and to facilitate an easy read, this section described the structure of this report and highlights the relations between the different chapters.

The main content of this report is structured around three draft papers found in Chapters 3, 4 and 6. These first two draft papers describe the development of the actuator models and the resulting general mass scaling and power loss sensitivities for the EMA and EHA transmission respectively. The draft paper of Chapter 6 describes the modelling of a preliminary design tool for the EMA and EHA using the models described in Chapters 3 and 4. A case study is performed on the Ampelmann actuator to identify the advantages of one over the other actuator technology for this high power linear actuator application. All three draft papers can be read separately without further information. For the reader interested only in modelling of EMA and EHA actuator transmission mass and power losses or the preliminary design tool results, these chapters suffice.

For readers who are interested in the entire work, it is highly recommended to read the preceding literature review to this report which can be found in Appendix G. Next, Chapter 2 starts with the general modelling strategy required to determine the optimal actuator technology for the Ampelmann A-type. The need for the models described in Chapters 3 and 4 is explained here. Chapter 3 and 4 discuss the model development of the EMA and EHA transmission respectively and shows the sensitivities found in the mass and power loss properties of these transmissions. Chapter 5 is added to detail the modelling of the servo motor driving both the EMA and EHA transmissions. As models for the PMSM servo motor are readily available this chapter just describes the use of these models to develop the overarching motor model. The reader interested in further developing this work is also highly encouraged to read Appendix A and B for the equations behind the relations discussed in Chapter 3 and 4 respectively. Chapter 6 combines the models described in Chapter 3, 4 and 5 to develop a high power linear actuator preliminary design tool. The optimal actuator configurations found for a case study on the Ampelmann A-type actuator are discussed and general actuator properties are described to develop a general understanding of the differences between EMA and EHA actuators. Finally, Chapter 7 discusses the results found in Chapter 6 with the specific Ampelmann A-type in mind to determine which actuator solution is best suited for the next generation Ampelmann A-type hexapod platform.

# Chapter 2

## Modelling strategy

Linear actuators convert electrical energy to linear mechanical energy to drive a load with a linear force and velocity. Two critical properties of the linear actuator with respect to the Ampelmann hexapod application are the actuator mass and the mean actuator power losses. Both the mass and power loss properties of the linear actuator are highly dependant on design choices defining the actuator configuration. To be able to compare different actuation technologies, a preliminary design tool capable of determining the mass and power losses of optimized actuators is needed for the most promising actuator technologies.

In this report, the development of such a preliminary design tool is discussed for the technologies introduced in Chapter 1. In this chapter, the general modelling approach is discussed and the different aspects of this report are introduced. This chapter can therefore be seen as global explanation of the detailed content in the remainder of this report.

First, the model scope in this report is detailed in Section 2.1. Next, the actuator technologies introduced in Chapter 1 are explained in more detail in Section 2.2. Afterwards the global modelling approach to obtain a linear actuator preliminary design tool is explained in Section 2.3. Finally, the actuator requirements corresponding to the specific Ampelmann application, which is the focus of this report, are detailed in Section 2.5.

### 2.1 Model scope

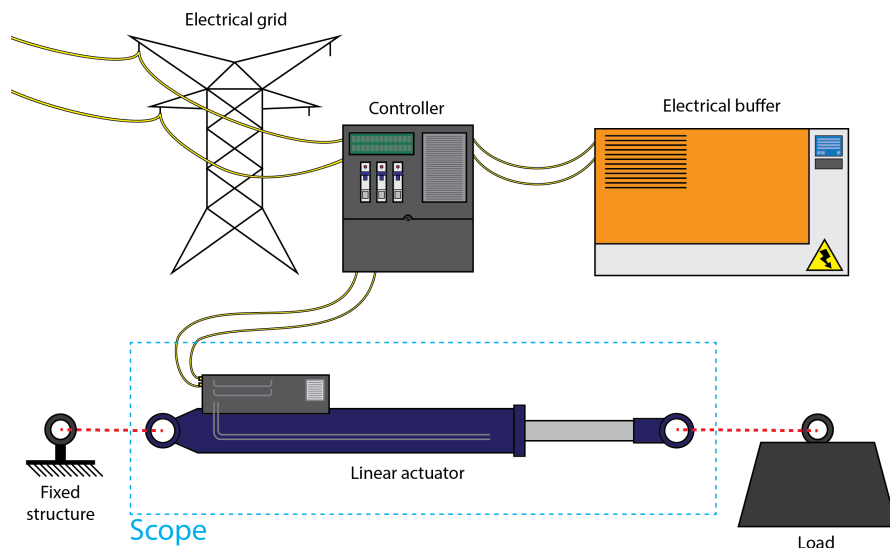


Figure 2.1: Linear actuator modelling scope

An actuation system consists of numerous components with each their own functions and properties. In modelling the actuator system, some clear boundaries are necessary to define the components under consideration

and the peripheral components which are ignored. Figure 2.1 shows a schematic representation of a typical electrical actuator system. The typical system consists of a load connected to the actual actuator. The actuator is connected to a controller which controls the electrical power to and from the actuator. The controller is connected to an electrical grid and to an electrical buffer. This buffer is used to dampen the peak power requirements of the actuator on the electrical grid by storing the electrical potential energy coming from the actuator in generating operation and releasing this energy to the actuator in motoring operation. The use of an electrical buffer means the power requirements on the grid are equal to the mean power losses in the system for a 0 net work task which is common for the Ampelmann platform.

In this report, only the actual actuator is considered, neglecting the load, controller, electric buffer and electric grid. The effects of the load on the actuator are described by a task specific time series including the force, velocity, acceleration and position of the actuator. The electric grid, buffer and controller of the system are assumed 100% efficient. This means the mean power use of the actuator is defined as the sum of all power going in and coming out of the actuator at the electrical actuator connections divided by the number of discretised working points in the task time series. Also mass properties of all components outside the model scope are neglected. Possible inertial forces on the actuator due to accelerations of its frame are not taken into account either. The actual linear actuator is further discussed in Section 2.2.

## 2.2 Actuator description

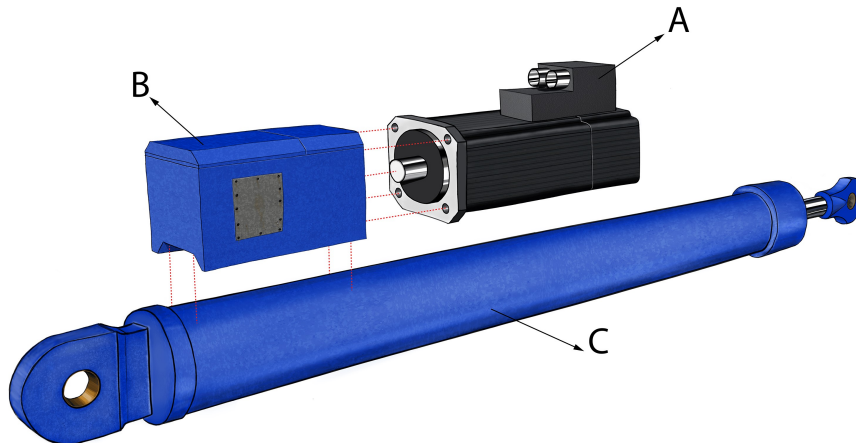


Figure 2.2: General components of the MEA

**General architecture** To understand actuator properties, the working of the linear actuator should be discussed first. For brevity the electro hydrostatic actuator (EHA) and electro mechanical actuator (EMA) can be described as a single type of linear actuator called the more electric actuator (MEA) in line with the existing naming convention in the aviation industry. The MEA has three major components which are visualized in Figure 2.2. The electric servo motor (A) is a universal component which can be considered equal in both the EHA and EMA. The servo motor is often implemented by a permanent magnet synchronous machine (PMSM) capable of four quadrant operation [44, 96, 174]. Connected to the motor is a power converter (B). This actuator component is needed to convert the rotary mechanical power from the motor to a form which can be used by the end effector (C) of the actuator. In the EMA, this converter is found in the form of an (optional) reduction gearbox reducing the motor speed and increasing the motor torque towards the end effector side. The EHA uses a hydraulic pump to convert the rotary mechanical power to fluid power. The end effector (C) is the actuator part which transfers the actuator power to the load. In the EMA the end effector is implemented as a mechanical cylinder with a screw mechanism inside. The EHA makes use of a hydraulic cylinder to drive the load. The simplified general operational principle of both actuators is given below.

**EHA operation** In the EHA, the servo motor drives the hydrostatic pump with a torque and speed. The hydrostatic pump in its turn pumps fluid around in a closed loop system resulting in a volumetric flow and pressure. This closed loop system consists of the A and B chamber of the hydraulic cylinder and the hydraulic pipes connecting the pump to the hydraulic cylinder. Pumping hydraulic fluid from one cylinder chamber to

the other creates a net force on the cylinder piston resulting in a linear force on the load. The volume flow in the cylinder results in linear motion of the piston which is also transferred to the connected load.

**EMA operation** Similarly in the EMA, the servo motor drives a gearbox with a torque and speed. The gearbox has helical gears inside to reduce the outgoing speed by a gear ratio factor. Ideally the outgoing torque is increased by this same gear ratio. The gearbox drives a mechanical cylinder screw with the outgoing torque and speed. The screw mechanism in the mechanical cylinder transfers the delivered torque and speed to a linear force and velocity by a screw transmission ratio.

**Actuator variations** Both the EMA and EHA are general actuator technologies. Within the general actuator technology, a multitude of variations are possible with respect to implementation of individual actuator parts. Both EMA and EHA variations are often described by the implementation of a single actuator component. In case of the EMA this component is the rotary to linear screw type transmission in the mechanical cylinder while for the EHA, the implementation of the pump technology is often used. In this report, only a single variation of both actuator technologies is detailed. These implementations are the planetary roller screw (PRS) and the fixed pump variable motor (FPVM) for the EMA and EHA respectively. Both component implementations are discussed below.

### 2.2.1 EMA mechanical cylinder

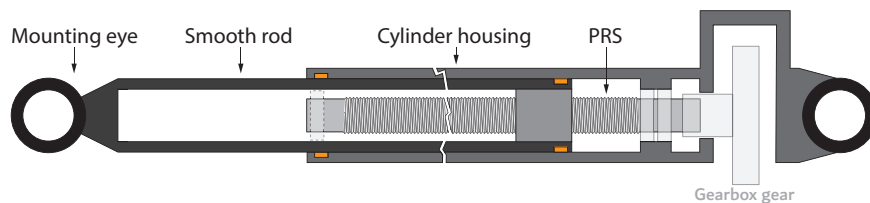


Figure 2.3: Mechanical cylinder architecture

The EMA mechanical cylinder substitutes the hydraulic cylinder of the EHA. The cylinder is a combination of a screw mechanism and a protective housing. The general architecture of the mechanical cylinder is shown in Figure 2.3. The cylinder housing ensures the screw mechanism is protected against lateral forces and the outside environment. The actual power transmission is performed by the screw mechanism. This screw mechanism transfers rotary mechanical power to linear mechanical power. The screw mechanism in this report is implemented by a planetary roller screw (PRS). Planetary roller screws are optimally suited for high load high velocity applications [98, 162] and are known for their high efficiency [167]. Figure 2.4 shows the main parts of the PRS. The screw is driven with a given speed and torque. The rotation of the screw results in rotation and translation of the contacting rollers. The rollers in turn contact the rotationally fixed nut causing a translation of the nut along the screw axis. The rollers effectively form a virtual thread between the screw and nut. The numerous contact points between the screw, rollers and nut result in a high load rating. The virtual thread created by the rollers decrease frictional losses significantly compared to the power screw and ball screw [167]. Additional gears and a gear-ring are added on the rollers and nut respectively to eliminate slip between both components [167].

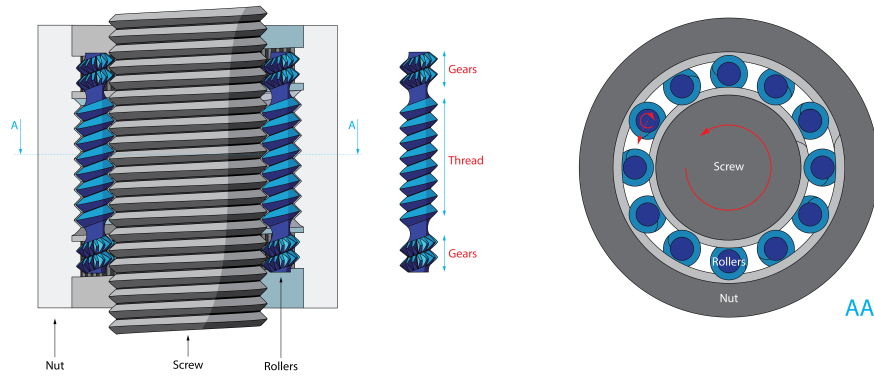


Figure 2.4: Planetary roller screw components and interaction.

## 2.2.2 EHA hydrostatic pump

The EHA uses a hydrostatic or positive displacement pump to pump fluid between the cylinder chambers of the hydraulic cylinder. Various implementations of the hydrostatic pump exist in literature. The axial and radial piston pump are the most common implementations with only small differences in general properties. In general the piston pump is widely accepted to be the most promising solution for high pressure systems such as the EHA [92, 158]. Figure 2.5 [130] shows a cross section of a typical axial piston pump. The pump has a rotating cylinder body and a stationary swash plate. The slippers on the swash plate force the pistons to move in and out the cylinder body during rotation. As such, hydraulic fluid is pumped from the low to high pressure side of the pump. Different control strategies exist for the hydrostatic piston pump, either the motor speed changes or the swash plate angle is changed to control the flow of the pump. In this report the fixed displacement pump option is used, meaning the swash plate angle is constant and the motor speed determines the volumetric output. The alternative is called a variable displacement pump in which motor speed is constant and the variable swash plate angle changes the volumetric output.

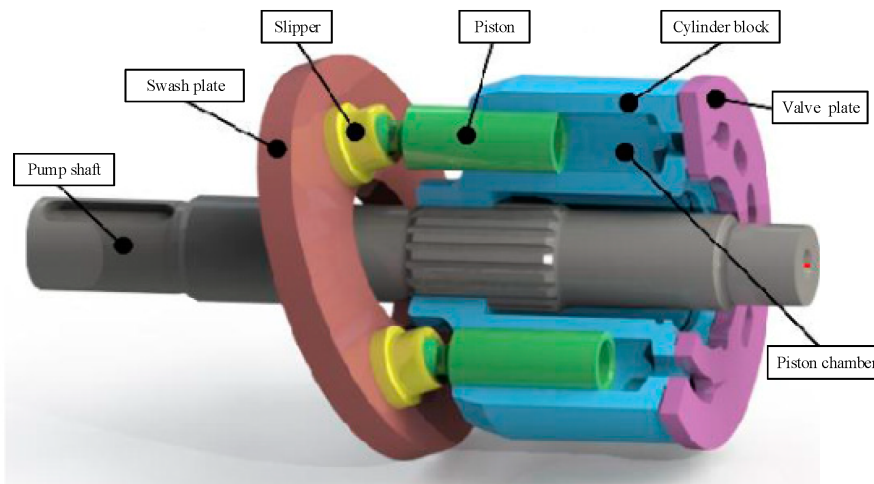


Figure 2.5: Axial piston pump main components [130].

## 2.3 General model strategy

Comparing the EMA and EHA for a specific application requires both the mass properties and the application specific mean power use for each proposed actuator. Both properties can be modelled using analytical models describing the sizing and power losses of the individual components of each actuator. Sizing models can determine component masses based on the required material to withstand the loading on the component and to house other components. Meanwhile, power loss models can determine working point efficiencies of each actuator component by describing the fundamental force and velocity related loss terms in this component. Sizing

of the different actuator components influences the component power losses, as such the mass and power loss properties of the actuator influence one another. Finding the optimal actuator configuration with the lowest mass and highest efficiency is therefore an optimization problem. As the mass and power loss optimization objectives don't necessarily result in the same actuator configurations, multiple optimized actuator configurations for the same actuator requirements can be found. A good way to portray multiple optimized actuator solutions is the use of a Pareto optimal front. Such a front portrays the most optimal actuator solution for different objective weight factors. By creating these Pareto optimal fronts for both the EHA and EMA, the optimal actuator configurations of both technologies can be determined and compared.

In this report, a preliminary design tool is developed to combine existing and newly developed actuator component mass and power loss models with an optimization step. The preliminary design tool determines the optimal actuator configurations with respect to a minimal actuator mass and minimal losses in a given task. The optimized configurations of both the EMA and EHA can then be compared on these properties. Figure 2.6 shows the general modelling approach for this preliminary design tool.

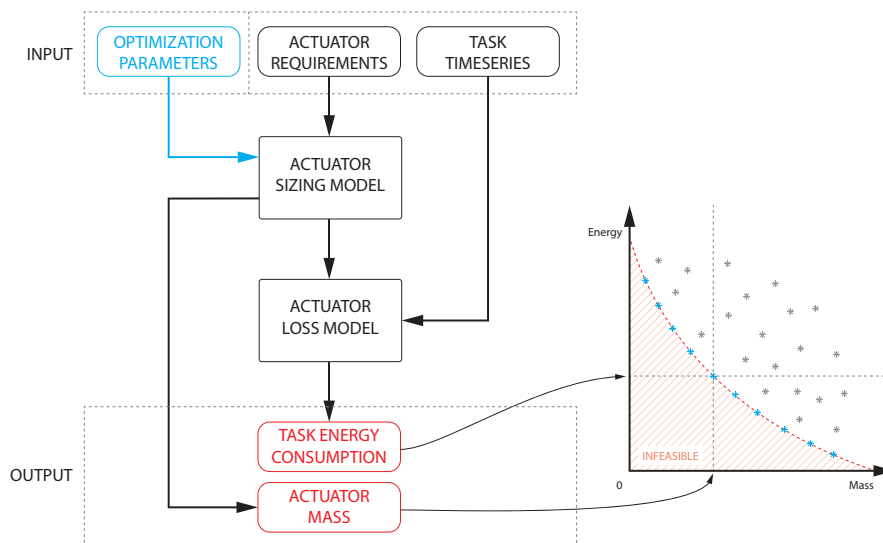


Figure 2.6: Actuator model approach.

To generate optimal actuator configurations for a specific application, actuator requirements describing the maximum loading, velocity and lifetime are used as input together with a representative task time series of the forces, velocities, accelerations and positions of the actuator. These inputs can be regarded as fixed input parameters during the optimization process. The optimization parameters are the free variables in the actuator design which describe the different actuator configurations. A list of used optimization parameters per actuator type is found in table 2.1.

For each set of optimization parameters and the fixed actuator requirements, the different actuator components are sized by a sizing model. The resulting sizing parameters and the discretized working points of the actuator found in the task time series are then used to determine the losses in the system. Each run with different optimization parameters therefore results in an actuator configuration with its own specific mass and task specific energy use. Constraints on machine limits such as maximum motor speed and eigenfrequencies ensure only feasible configurations are generated.

The actuator configurations where one objective can no longer decrease without increasing the other objective form a Pareto optimal front as shown with the blue dots in Figure 2.6. Actuator configurations on this front of the EMA and EHA can be compared to determine the optimal actuator technology for a specific application. The models portrayed by the boxes 'Actuator sizing model' and 'Actuator loss model' are described in Section 2.4.

Running the actuator model of Figure 2.6 for all possible optimization parameter combinations is very inefficient. The optimization process is therefore performed by an optimization algorithm. The optimization algorithm used in this study is the multi-objective feasibility enhanced particle swarm optimization (MOFEPSO) method [147]. The use of a particle swarm optimization method ensures non-continuous models can be used. Furthermore, by first calculating constraints to evaluate feasibility, the number of function evaluations is decreased significantly. The drawback of a non-gradient based optimization strategy is the optimized results are never guaranteed to

Table 2.1: Optimization parameters of the EMA and EHA

EMA		EHA	
Symbol	Description	Symbol	Description
$l_s$	Lead of the screw	$A_p$	Area of the cylinder piston
$r_r$	Radius of the rollers	$V_g$	Geometric volume of the pump
$N_s$	Number of screw thread starts	$N_p$	Number of pumps
$R_g$	Gear ratio of the reduction gears		

portray the absolute optimum. Results on the Pareto front are expected to show some variation depending on the starting conditions of the simulation. As the results of this optimization are preliminary design configurations, this is a reasonable trade of for a robust optimization algorithm.

## 2.4 Actuator modelling

The high power linear actuator preliminary design tool discussed in the previous section portrays the actuator sizing model and actuator loss model as black box input output models. Here the modelling of these parts is explained in more detail. To understand both sizing and loss calculations on the MEA, first the power relations between various actuator parts should be known. The power relations are needed to understand losses in the actuator and to define the sizing requirements of each actuator part, they are shown in Subsection 2.4.1. Mass relations of the MEA are discussed in Subsection 2.4.2. The development of the sizing and power loss models of the EMA and EHA are discussed in detail in Chapters 3 and 4 respectively.

### 2.4.1 Actuator power relations

The power relations of the actuator show how power is transferred through the different actuator components. Power is the product of a speed and force related term, as such ideally a transmission part can transfer power to different speed to force ratio's while keeping the power constant. In practice losses occur in the transfer of power through the actuator parts, effectively lowering the transferred power. The power relations between the three actuator parts of the MEA are visualized in Figure 2.7 and 2.8 for the EMA and EHA respectively. Actuators are sized according to requirements posed on the actuator load side. Similarly, input power is determined as a function of load side power requirements. Information on the load side can be regarded as known and  $F$ ,  $v$  and  $\dot{v}$  can be deemed the input parameters of the actuator model.

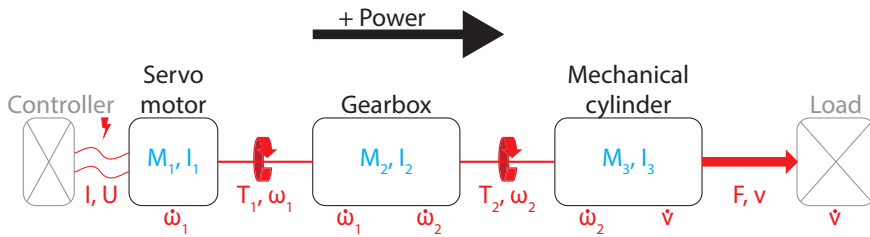


Figure 2.7: Power relations between EMA actuator parts.

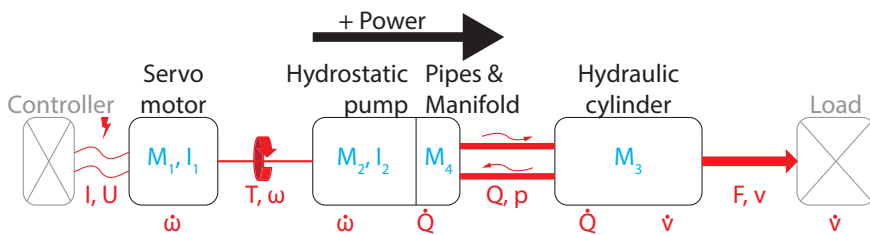


Figure 2.8: Power relations between EHA actuator parts.

Above power relations can be described by equations. Linearised mathematical power relations for the EMA are given as:

$$\begin{bmatrix} \omega_2 \\ T_2 \end{bmatrix} = \begin{bmatrix} C_\omega & 0 \\ 0 & C_T \end{bmatrix} \left( \begin{bmatrix} v \\ F \end{bmatrix} + \begin{bmatrix} 0 \\ M_{3,m} \end{bmatrix} \dot{v} + \begin{bmatrix} 0 \\ F_{cyl,loss} \end{bmatrix} \right) + \begin{bmatrix} 0 \\ I_3 \end{bmatrix} \dot{\omega}_2 + \begin{bmatrix} 0 \\ T_{screw,loss} \end{bmatrix} \quad (2.1)$$

$$\begin{bmatrix} \omega_1 \\ T_1 \end{bmatrix} = \begin{bmatrix} C_{t\omega} & 0 \\ 0 & C_{tT} \end{bmatrix} \begin{bmatrix} \omega_2 \\ T_2 \end{bmatrix} + \begin{bmatrix} 0 \\ I_2 \end{bmatrix} \dot{\omega}_2 + \begin{bmatrix} 0 \\ T_{gear,loss} \end{bmatrix} \quad (2.2)$$

$$\begin{bmatrix} U \\ I \end{bmatrix} = \begin{bmatrix} C_U & 0 \\ 0 & C_I \end{bmatrix} \left( \begin{bmatrix} \omega_1 \\ T_1 \end{bmatrix} + \begin{bmatrix} 0 \\ I_1 \end{bmatrix} \dot{\omega}_1 + \begin{bmatrix} 0 \\ T_{motor,loss} \end{bmatrix} \right) + \begin{bmatrix} 0 \\ I_{motor,loss} \end{bmatrix} \quad (2.3)$$

Similarly, the linearised mathematical power relations for the EHA are given as:

$$\begin{bmatrix} Q \\ p \end{bmatrix} = \begin{bmatrix} C_Q & 0 \\ 0 & C_p \end{bmatrix} \left( \begin{bmatrix} v \\ F \end{bmatrix} + \begin{bmatrix} 0 \\ M_{3,m} \end{bmatrix} \dot{v} + \begin{bmatrix} 0 \\ F_{cyl,loss} \end{bmatrix} \right) + \begin{bmatrix} 0 \\ p_{pipe,loss} \end{bmatrix} \quad (2.4)$$

$$\begin{bmatrix} \omega \\ T \end{bmatrix} = \begin{bmatrix} C_\omega & 0 \\ 0 & C_T \end{bmatrix} \begin{bmatrix} Q \\ p \end{bmatrix} + \begin{bmatrix} 0 \\ I_2 \end{bmatrix} \dot{\omega} + \begin{bmatrix} Q_{pump,loss} \\ T_{pump,loss} \end{bmatrix} \quad (2.5)$$

$$\begin{bmatrix} U \\ I \end{bmatrix} = \begin{bmatrix} C_U & 0 \\ 0 & C_I \end{bmatrix} \left( \begin{bmatrix} \omega \\ T \end{bmatrix} + \begin{bmatrix} 0 \\ I_1 \end{bmatrix} \dot{\omega} + \begin{bmatrix} 0 \\ T_{motor,loss} \end{bmatrix} \right) + \begin{bmatrix} 0 \\ I_{motor,loss} \end{bmatrix} \quad (2.6)$$

All coefficients  $C_{xx}$  related to the actuator velocity terms represent some type of transmission ratio linking velocities of different actuator components. All force related coefficients represent the inverse of this transmission ratio. Ideally, force and velocity transmission through an actuator part is only influenced by the transmission ratio which would result in a 100% efficient power transmission. In practice, the instantaneous power through the actuator part is influenced by inertia effects and by power losses in the system.

Power losses in the MEA are largely dominated by friction losses influencing the force related terms in the transmission as is typical in a form closed system. Only in the hydrostatic pump of the EHA, volumetric losses also impact the velocity related terms. Losses of the actuator are dependent on the working point of the actuator part. Hence both force and velocity related parameters influence instantaneous loss magnitude of the actuator part. As losses influence the working point of the upstream connected actuator part, losses at the end of the power path have a large influence on the total instantaneous power needed by the actuator. The power path is directed from the servo motor to the load in motoring operation and from the load to the servo motor in generating operation.

The transmission ratio coefficients  $C_{xx}$  of the EMA and EHA transmission components can be found in Subsections 3.2.3 and 4.2.3 respectively. The different loss factors found in the power relations of the MEA actuator are determined in Sections 3.4 and 4.4 for the EMA and EHA respectively. The same information is provided for the electric servo motor in Section 5.2. Equations defining the parameters needed in the equations above are boxed in for reference.

## 2.4.2 Actuator mass relations

Sizing of an actuator part influences losses of this actuator part but is also influenced by the losses of the actuator parts upstream of the power path. Losses in downstream actuator parts increase the force requirements on actuator parts upstream the positive power path. Sizing of actuator parts is mainly determined by the maximum force requirements on the actuator. For axial loaded parts dimensions are determined by buckling and yield requirements. Rotating parts have an additional requirement on shear strength while hydraulic parts are also sized for pressure requirements. Total actuator mass is the sum of all actuator components masses. A detailed description of general sizing rules for the actuator components is given in Sections 3.3 and 4.3 for the EMA and EHA respectively. The same information is provided for the electric servo motor in Section 5.1. Equations defining the parameters needed for the actuator mass are boxed in for reference.

### 2.4.3 Constraints

Actuator configurations are often limited by more than the optimal mass and efficiency. An example of such limit is the eigenfrequency of an actuator component. Driving the actuator close to or above the first eigenfrequency of a component might result in a lower mass or higher actuator efficiency. In practice this will result in undesired actuator behaviour which should be avoided. To ensure actuator configurations are bound within attainable working conditions, several constraints are imposed on the possible actuator configurations. Constraints are formulated in Sections 3.5 and 4.5 for the EMA and EHA respectively.

## 2.5 Actuator requirements

This report focusses on linear actuator technology for the Ampelmann A-type motion platform. This motion platform is actuated by six high power linear actuators each capable of delivering a certain output force and velocity. The requirements on the actuators of the Ampelmann A-type are shown in Table 2.2 for reference. Determining the correct actuator requirements is an entire research question on its own, as such, actuator requirements are taken as a given.

Table 2.2: Actuator requirements for the Ampelmann A-type motion platform

<b>Requirement</b>	<b>Value</b>	<b>Explanation</b>
$F_{max}$	150[kN]	Maximum linear output force of the actuator.
$v_{max}$	1[m s <sup>-1</sup> ]	Maximum linear output velocity of the actuator.
$P_{max}$	150[kW]	Maximum output power of the actuator.
$L_s$	2[m]	Linear stroke length of the actuator.
$L_{1m}$	100000[m]	Minimal actuator design lifetime.
$U_{phase}$	270[V]	Maximum phase voltage from the power grid.

## Chapter 3

# Electro mechanical actuator, sizing and loss model development <sup>1</sup>

### Abstract

*Electro mechanical and electro hydrostatic linear actuators are often used for different actuation applications up to 45 kW maximum output power. For applications requiring higher power output, the advantages of one over the other technology become unclear. Existing research clearly shows benefits of both technologies over conventional hydraulic actuation. This chapter describes the mathematical model development of the electro mechanical actuator to enable comparison of this actuator technology for different actuator requirements and applications.*

### 3.1 Introduction



Figure 3.1: Ampelmann A-type crew transfer gangway (Ampelmann Operations B.V.)

Linear actuators are devices capable of converting electrical energy to linear mechanical energy. Often a rotary motor is used to drive a rotary to linear hydraulic or mechanical transmission. Current developments in various technical fields concerning actuation are focused in a large part on efficiency. Efficiency is often important with respect to environmental considerations; achieving more with less environmental costly

resources. Increased efficiency however also has a financial consequence by lowering operating costs. Similarly, reducing actuator mass can impact operational costs directly. Especially in mobile actuator applications, system mass footprint becomes an important factor in the total payload capacity of the carrying vessel and therefore on the productivity of the vessel trip.

This chapter focusses on linear actuation of hexapod steward platforms which are capable of power output with an order of magnitude of  $10^5$  Watt. An example of such system is the Ampelmann A-type crew transfer gangway shown in Figure 3.1. These systems use six linear actuators to compensate vessel motion and create a still standing platform from which offshore crew can be transferred between the vessel and a fixed structure.

Linear actuators in high power applications are often dominated by conventional hydraulic technology. Conventional hydraulics are known for their high loss factors with maximum system efficiencies ranging around 35% [100, 180]. In the aviation industry, a development called the more electric aircraft (MEA) found that electro hydrostatic actuators (EHA) and electro mechanical actuators (EMA) both offer significant advantages on both system efficiency [22, 33, 128] and reduced actuator mass [22, 41, 128, 163].

Both EHA and EMA are driven by an electric rotary

<sup>1</sup>This chapter is based on the draft paper provided in Appendix F.1

machine to convert electrical energy in rotary mechanical energy. The EHA uses a hydrostatic transmission with a pump and hydraulic cylinder to obtain a linear force and velocity. Similarly, the EMA uses an (optional) gearbox and a screw mechanism to obtain the same linear force and velocity output. Both technologies have specific properties, however comparison between both options are lacking for high power applications. Figure 3.2 (Appendix G) shows various actuator studies found in literature ranked on their maximum output force and velocity. Literature is seen to exist on EMA and EHA for power levels up to approximately 45kW. For higher power levels, existing research is lacking and no clear benefits of one over the other technology are defined. To further the knowledge in the use of EHA and EMA linear actuators for high power applications mathematical models describing scaling and loss behaviour of these actuators are needed.

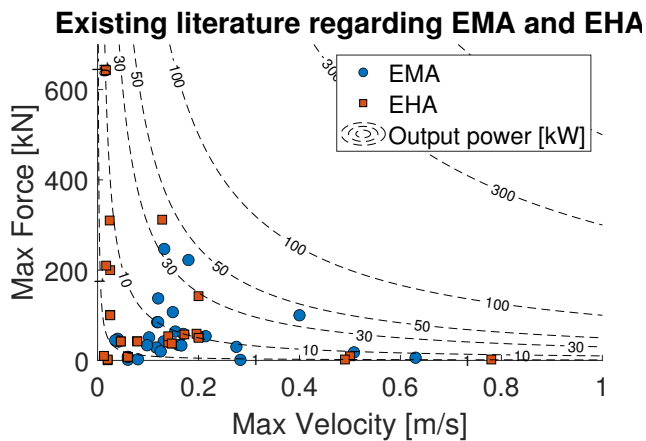


Figure 3.2: Existing actuator studies in literature ranked on maximum output force and velocity (Appendix G).

This chapter describes mathematical model development of sizing and loss models of the EMA. The focus of this chapter is on actuators for use in a sea motion compensating steward platform, however actuator properties and efficiency models are applicable to a multitude of high power actuation applications. The focus on a specific actuator application is necessary as operating regimes determine the power loss behaviour of the actuator. The developed actuator models have free variables which can later be used in an optimization algorithm to find the best possible actuator for the given requirements.

**Reading guide** To aid the reader in finding the contents of their interest in this chapter, this reading guide provides the general structure of the chapter. First, to better understand the requirements on the model developed in this chapter, Section 3.2 describes the general electro mechanical actuator operation and the overall model definitions. Next, Section 3.3 details the model development of the major actuator components

with the resulting scaling relations and comparison of modelled mass properties with catalogue data. Section 3.4 describes the development of the actuator power loss models. The sensitivities of the component power losses are determined with respect to the working point of the actuator. The resulting sizing and power loss trends are summarised in Section 3.6 along with implementation options of this model in further research.

Several dimensionless figures are shown in this chapter on a loglog scale to portray the different mass and power loss sensitivities. Note that all shown logarithmic scales have base 10. The reader interested in the detailed equations behind the relations discussed in this chapter for possible model iterations are referred to appendix A.

## 3.2 System description and method

### 3.2.1 Actuator description

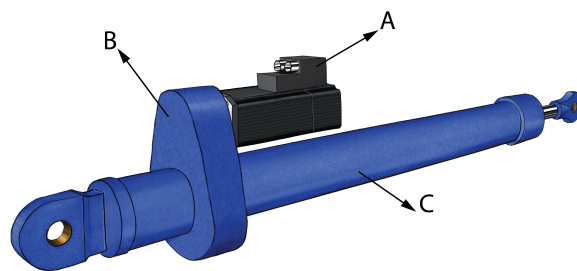


Figure 3.3: General components of the EMA

**EMA parts** To determine actuator properties, the basic parts and operation of the electro mechanical linear actuator should be discussed first. The EMA has three major components which are visualized in Figure 3.3. The electric servo motor (A) is often implemented with a permanent magnet synchronous machine (PMSM) capable of four quadrant operation. Connected to the motor is an (optional) reduction gearbox (B) reducing the speed and increasing the torque of the motor towards the end effector side. The end effector (C) is the actuator part which transfers the actuator power to the load. The end effector consists of a mechanical screw mechanism and a protective cylinder housing. The actuator is capable of four quadrant operation, meaning the actuator can be operated in the motoring regime and can be back driven to operate in generating mode. The simplified operational principle of the EMA in motoring operation is described below.

**EMA operation** The EMA converts electrical energy to linear mechanical energy. The servo motor of the EMA is connected through a controller to an elec-

trical grid. The voltage and the supplied current on the motor poles are converted to a rotational velocity and torque of the outgoing motor axle. The motor axle in its turn is connected to a reduction gearbox. The reduction gearbox reduces the rotational velocity while increasing the torque of the motor on the outgoing gearbox axle. Next, the gearbox output axle is connected to the screw of a screw mechanism. The rotational velocity and torque of the gearbox output shaft is translated to a linear force and velocity of the screw mechanism nut. Finally, the nut of the screw mechanism is fixed to the load by a smooth rod. Figure 3.5 shows the various component various movements in the actuator.

### 3.2.2 Component choices

The components of the EMA can be implemented in different ways. The servo motor is often implemented by a permanent magnet synchronous machine [44, 96, 174]. This component has well known properties and is not further discussed in this chapter. The mechanical cylinder has more implementation options. The most common implementations are the conventional power screw and the ball screw as active component. In this study, the planetary roller screw (PRS) is used as it is ideally suited for high velocities and heavy load applications [98, 162]. The PRS is also very resistant to shock loading [128] and has lower frictional losses compared to the ball screw [167]. Finally, the reduction gearbox is implemented as a single stage helical gearbox. Helical gearboxes are well known in industry and are often used to reduce the speed output of an electric motor. Later model iterations could look at implementing multiple gear stages to optimize the gearbox properties.

### 3.2.3 Modelling method

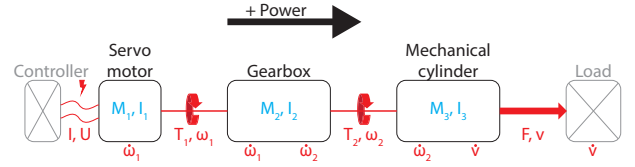


Figure 3.4: Power relations between EMA actuator parts.

To compare different actuator technologies, the mass and loss properties of the actuator should be well defined. To understand the models developed in this chapter, first the power relations between various actuator parts should be explained. The basic power relations between the three main actuator parts of the EMA are visualized in Figure 3.4. Each component acts as a transmission in the actuator power path with its associated losses and its own mass properties. Actuator parts are sized according to requirements posed on the actuator load side. Similarly, input power is determined as a function of load side power requirements. Therefore information on the load side can be regarded as known and  $F$ ,  $v$  and  $\dot{v}$  can be deemed the input parameters of the actuator model.

#### Power relations

For each transmission part shown in Figure 3.4, the power relations can be modelled with an equation. In general, power transmission is defined by a transmission ratio linking the velocity terms of the transmission in- and output. The ideal force terms are related by the inverse of this transmission ratio. In practical transmission parts, the power relations are also influenced by inertia effects and power losses. The linearised relations of each EMA component are mathematically described below:

$$\begin{bmatrix} \omega_2 \\ T_2 \end{bmatrix} = \begin{bmatrix} C_\omega & 0 \\ 0 & C_T \end{bmatrix} \left( \begin{bmatrix} v \\ F \end{bmatrix} + \begin{bmatrix} 0 \\ M_{3,m} \end{bmatrix} \dot{v} + \begin{bmatrix} 0 \\ F_{cyl,loss} \end{bmatrix} \right) + \begin{bmatrix} 0 \\ I_3 \end{bmatrix} \dot{\omega}_2 + \begin{bmatrix} 0 \\ T_{screw,loss} \end{bmatrix} \quad (3.1)$$

$$\begin{bmatrix} \omega_1 \\ T_1 \end{bmatrix} = \begin{bmatrix} C_{t\omega} & 0 \\ 0 & C_{tT} \end{bmatrix} \begin{bmatrix} \omega_2 \\ T_2 \end{bmatrix} + \begin{bmatrix} 0 \\ I_2 \end{bmatrix} \dot{\omega}_2 + \begin{bmatrix} 0 \\ T_{gear,loss} \end{bmatrix} \quad (3.2)$$

$$\begin{bmatrix} U \\ I \end{bmatrix} = \begin{bmatrix} C_U & 0 \\ 0 & C_I \end{bmatrix} \left( \begin{bmatrix} \omega_1 \\ T_1 \end{bmatrix} + \begin{bmatrix} 0 \\ I_1 \end{bmatrix} \dot{\omega}_1 + \begin{bmatrix} 0 \\ T_{motor,loss} \end{bmatrix} \right) + \begin{bmatrix} 0 \\ I_{motor,loss} \end{bmatrix} \quad (3.3)$$

**Mechanical cylinder** The mechanical cylinder converts rotary to linear force and motion with a screw type mechanism and is described by (3.1). The transmission ratio  $C_\omega$  of the cylinder is defined by the lead  $l_t$  of the screw type mechanism inside as:

$$C_\omega = \frac{2\pi}{l_t} [\text{rad m}^{-1}] \quad (3.4)$$

The force transmission  $C_T$  is then defined as:

$$C_T = \frac{l_t}{2\pi} [\text{m rad}^{-1}] \quad (3.5)$$

The total lead  $l_t$  of the screw is determined as [107]:

$$l_t = l_s + p \frac{r_s}{r_r} [\text{m}] \quad (3.6)$$

The parameters defining the total screw lead  $l_t$  are detailed in Subsection 3.3.2.

The various moving parts in the mechanical cylinder cause mechanical friction and the corresponding power losses. Figure 3.5 shows the moving interfaces in the mechanical cylinder. Linear bearings in the cylinder result in a friction force which is described by  $F_{cyl,loss}$  in (3.1). Similarly, the rotating components have an associated friction torque due to rolling and sliding friction which is captured by  $T_{screw,loss}$  in (3.1). These friction loss factors affect the required torque of the screw but don't influence the velocity terms of the transmission directly. The power loss components of the mechanical cylinder are detailed in Subsection 3.4.2.

Finally, the mechanical cylinder power loss relations are affected by inertia effects of the rotating screw mechanism and the linear acceleration of the moving cylinder parts. Moving masses and the moment of inertia of the mechanical cylinder are detailed in Subsection 3.3.2.

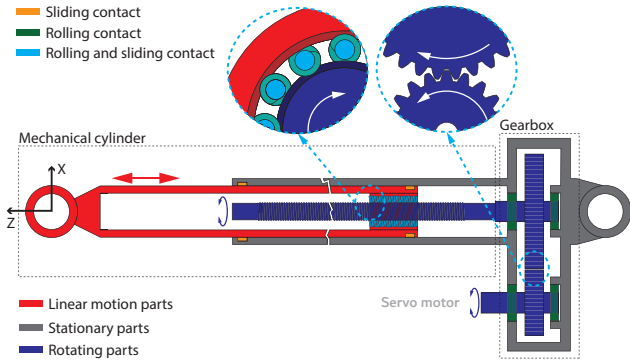


Figure 3.5: Moving interfaces in the EMA transmission

**Gearbox** The gearbox has a rotating in and output side and is described by (3.2). The transmission of the gearbox is defined by the gear ratio  $R_{gear}$  for the velocity and force related terms as:

$$C_{t\omega} = R_{gear} [-] \quad (3.7)$$

$$C_{tT} = \frac{1}{R_{gear}} [-] \quad (3.8)$$

The gear ratio in the gearbox is defined by the ratio of the gearwheel diameters:

$$R_{gear} = \frac{d_{g,1}}{d_{g,2}} [-] \quad (3.9)$$

Losses in the gearbox are all related to the rotating parts in the gearbox. Figure 3.5 shows the rotating interfaces of the gearbox. The major loss components are found in the friction of the gear teeth faces and the frictional moment of the bearings. The gearbox losses are captured by  $T_{gear,loss}$  in (3.2). Again, the friction forces affect the required torque on the gearbox input side. The power loss components of the gearbox are detailed in Subsection 3.4.3. The inertia effects in the gearbox are defined by the combined moment of inertia of the rotating gear pair. The moment of inertia of the gear pair is determined in Subsection 3.3.3.

**Servo motor** The servo motor forms the transmission between the electrical and mechanical power domain. Servo motor transmission ratio's and power losses are well defined in literature [117, 127, 142] and are not discussed further in this chapter. The power relations of the servo motor are discussed in Chapter 5.

**Losses in the EMA** Losses of the actuator parts are dependent on the working point of the actuator part. Hence both force and velocity related parameters influence the loss magnitude of the actuator. The working point information on the load side of the actuator is taken as a given in this chapter. As losses influence the working point of the upstream connected actuator part, losses at the end of the power path have a large influence on the total instantaneous power needed by the actuator. The power path is directed from the servo motor to the load in motoring operation and from the load to the servo motor in generating operation (see Figure 3.4). Next to the working point information of the actuator, the loss magnitude in the different actuator parts is also dependant on geometry related parameters which are defined in Section 3.3.

In general, the high power actuator applications under consideration often operate at frequencies below 1[Hz]. As such, the system is dominated by high masses and inertia's while dynamic effects only start occurring at much higher frequencies. In modelling the losses of the system a quasi static approach is therefore a reasonable simplification to reduce model complexity and calculation time. Losses in the EMA are modelled in Section 3.4 and 5.2. Equations defining the parameters needed in Equations 3.1, 3.2 and 3.3 are boxed in for reference.

### Sizing of the EMA

Sizing of an actuator part influences losses of this actuator part but is also influenced by the losses of the connected actuator parts. Losses in the mechanical

cylinder and gearbox for example should be compensated by the servo motor, hence increasing the load requirements on that actuator component. Sizing of actuator components is mainly determined by the maximum load requirements on the component. For axial loaded parts dimensions are determined by buckling and yield requirements. Rotating parts have an additional requirement on shear strength. The maximum load on the actuator is assumed a known parameter in this chapter. Together with the transmission ratio's described above and the component efficiency, the maximum loading on each component can be determined and sizing can be performed.

The main objective of sizing the different actuator components is finding the mass of an arbitrary actuator configuration. The mass of the EMA is simplified in this report to consist of the masses of its main components. Mounting hardware and additional peripherals are ignored with this approach. The total EMA mass with respect to the components shown in Figure 3.4 is then determined as:

$$M_{EMA} = M_1 + M_2 + M_3 \quad (3.10)$$

A detailed breakdown of the component sizing and the different component masses is given in Section 3.3 and 5.1. Equations defining the parameters needed in Equation 3.10 are boxed in for reference.

### 3.3 Sizing model development

Development of a mathematical sizing model of the EMA is necessary for two main reasons; the sizing model determines the total mass of the actuator and defines the geometrical parameters needed in the actuator loss models. Sizing is often based on the maximum load requirements of the actuator. Next to the load requirements, sizing is also influenced by free design variables which can later be used in an optimization step. Sizing of the EMA transmission is split up in sizing of the mechanical cylinder and sizing of the gearbox. Sizing model development of these components is discussed separately for these components in Subsections 3.3.2 and 3.3.3. The symbols used in the component sizing models are defined in Subsection 3.3.1. Material properties are shown in Appendix D.

#### 3.3.1 List of symbols

Symbol	Explanation	Unit
$\alpha_s$	Helix angle of the PRS screw	[rad]
$\beta$	Contact angle of the PRS screw	[rad]
$\rho_{st}$	Density of steel	kg m <sup>-3</sup>
$a_s$	Axial shift between the screw and motor axle	[m]
$C_{req}$	Required dynamic load rating of the PRS	[N]
$d_{g,i}$	Reference diameter of the pinion (i=1) and driven gear (i=2)	[m]
$F_{eq}$	Cubic mean loading of the actuator	[N]
$f_{spacing}$	Spacing factor of the PRS rollers	[-]
$h_g$	Width of the helical gears	[m]
$h_{ge}$	Inside height of the gearbox enclosure	[m]
$I_{gears}$	Total moment of inertia of the gear pair with respect to the screw acceleration	[kg m <sup>2</sup> ]
$I_{r,screw}$	Total moment of inertia of the PRS rollers with respect to the screw acceleration	[kg m <sup>2</sup> ]
$I_s$	Moment of inertia of the PRS screw around its own axis	[kg m <sup>2</sup> ]
$L_{ce}$	Length of the cylinder enclosure (housing)	[m]
$L_{cr}$	Length of the smooth extending cylinder rod	[m]
$L_n$	Length of the PRS nut	[m]
$L_r$	Length of the PRS roller thread	[m]
$L_s$	Length of the PRS screw/ stroke length	[m]
$L_{10}$	$L_{10}$ lifetime with 95% reliability	[m]
$l_r$	Lead of the PRS roller	[m]
$l_s$	Lead of the PRS screw	[m]
$l_t$	Total (effective) lead of the PRS	[m]
$M_{gear}$	Total mass of the gearbox	[kg]
$m_{ce}$	Mass of the cylinder enclosure (housing)	[kg]
$m_{cr}$	Mass of the smooth extending rod	[kg]
$m_{g,i}$	Mass of the pinion (i=1) and driven gear (i=2)	[kg]
$m_{gears}$	Mass of the gear pair	[kg]
$m_{ge}$	Mass of the gearbox enclosure	[kg]

$m_{oil}$	Mass of the gearbox oil	[kg]
$m_n$	Mass of the PRS nut	[kg]
$m_r$	Combined mass of the PRS rollers	[kg]
$m_s$	Mass of the PRS screw	[kg]
$N_{rollers}$	Number of rollers in the PRS mechanism	[-]
$O_{ge}$	Circumference of the gearbox enclosure	[m]
$p_s$	Pitch of the PRS screw	[m]
$R_{el}$	Effective length ratio of the PRS roller	[-]
$R_{gear}$	Gear ratio	[-]
$r_{ce,in}$	Inside radius of the cylinder enclosure (housing)	[m]
$r_{ce,out}$	Outside radius of the cylinder enclosure (housing)	[m]
$r_{cr,in}$	Inside radius of the smooth extending rod	[m]
$r_{cr,out}$	Outside radius of the smooth extending rod	[m]
$r_{ge,i}$	Outside radius of the gearbox around pinion (i=1) and driven gear (i=2)	[m]
$r_n$	Pitch radius of the PRS nut	[m]
$r_{n,out}$	Outside radius of the PRS nut	[m]
$r_r$	Pitch radius of the PRS roller	[m]
$r_s$	Pitch radius of the PRS	[m]
$S_{ge}$	Spacing between gears and gearbox wall	[m]
$t_{ce}$	Material thickness of the cylinder enclosure (housing)	[m]
$t_{ge}$	Material thickness of the gearbox enclosure	[m]
$t_n$	Simplified material thickness of the PRS nut	[m]
$V_{ce}$	Volume of the cylinder enclosure	[m <sup>3</sup> ]
$V_{cr}$	Volume of the cylinder rod	[m <sup>3</sup> ]
$V_{g,i}$	Volume of the pinion (i=1) and driven gear (i=2)	[m <sup>3</sup> ]
$V_{ge}$	Volume of the gearbox enclosure	[m <sup>3</sup> ]
$V_{ge,oil}$	Volume of the oil inside the gearbox	[m <sup>3</sup> ]
$V_n$	Volume of the PRS nut	[m <sup>3</sup> ]
$V_r$	Volume of the PRS rollers combined	[m <sup>3</sup> ]
$V_s$	Volume of the PRS screw	[m <sup>3</sup> ]
$Z$	Total number of contact points in the PRS mechanism	[-]
$Z_r$	Number of contact points per PRS roller	[-]

### 3.3.2 Sizing of the mechanical cylinder

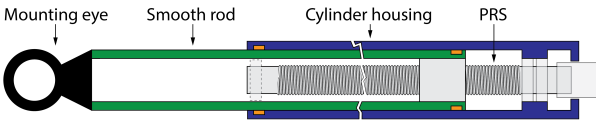


Figure 3.6: Mechanical cylinder architecture.

The mechanical cylinder is the end effector of the EMA. From the outside the mechanical cylinder resembles the hydraulic cylinder as it has a smooth extending cylinder rod and a cylinder housing as shown in Figure 3.6. The active part of the mechanical cylinder is however a mechanical planetary roller screw mechanism as discussed in Section 3.2. As stated above, sizing is mainly determined by the load requirements on the actuator. The mechanical cylinder is mainly loaded by axial forces when a swivelled connection to a frame and the load are assumed. The load bearing components are the smooth extending rod and the planetary roller

screw components. The cylinder housing is only loaded by the bearing contact forces found in the linear guide bearings of the smooth rod. Maximum load requirements on the mechanical cylinder are defined by the maximum design force of the actuator in the fully extended position. Geometrical sizing according to this load requirement to determine the masses of the mechanical cylinder components is discussed below. First the active screw mechanism is dimensioned after which the enclosure components are sized around the active components.

#### Screw sizing

The screw of the PRS determines in part the transmission ratio of the mechanism and the load rating of the mechanical cylinder. Figure 3.7 shows the screw with its main dimensions and the relevant peripherals. Note that the bearings and coupling block are drawn for reference only. Mass properties of these components are neglected in this model. The lead of the screw and the number of thread starts are free optimization parameters, other properties are determined below. Note that

the lead of the screw  $l_s$  and number of thread starts  $N_s$  are related to the screw pitch  $p_s$  shown in Figure 3.7 by:

$$l_s = p_s N_s \quad (3.11)$$

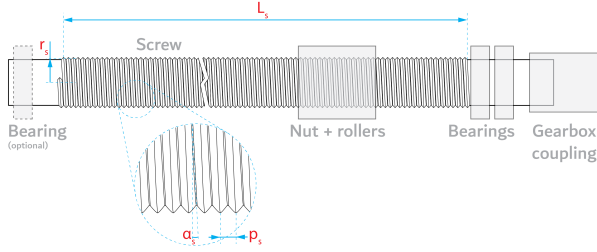


Figure 3.7: Planetary roller screw - screw sizing parameters.

**Load sizing** The screw shaft is the main load bearing active component in the mechanical cylinder. The axial load described above could result in buckling or yield failure. Meanwhile, as the screw translates rotational torque and velocity to linear force and motion, also shear is an important failure mode. The screw shaft radius can be dimensioned according to these requirements with the following assumptions:

- The screw is made from a solid shaft.
- The screw can be approximated by a solid smooth shaft with outer radius  $r$  equal to the minor radius of the screw for strength calculations (see Figure 3.8).
- The pitch radius is assumed to be 10% larger than the minor radius of the screw (see Figure 3.8).

The equations describing the minimum buckling, yield and shear radii of the screw are given in Appendix A.1. A fixed minimal fabrication radius is added to the sizing requirement to cap the screw radius lower bound in low load applications. The relations for the different radius requirements are found as  $r_{yield} = 2.71e-5F^{1/2}$ ,  $r_{shear} = 8.1e-4F^{1/3}l_s^{1/3}$ ,  $r_{buckling} = 8.27e-4F^{1/4}L_s^{1/2}$  and  $r_{fabrication} = 3.5e-3$ . The final minor radius of the screw can then be determined by taking the maximum value from all the different requirements as:

$$r_{min} = \max([r_{buckling}, r_{yield}, r_{shear}, r_{fabrication}])[m] \quad (3.12)$$

In accordance with the assumptions stated above, the actual pitch radius is then defined as:

$$r_s = 1.1r_{min} \quad (3.13)$$

Following above sizing criteria, the radius of the screw should be independent of the load rating (fabrication requirement) for low load ratings and proportional to either  $r_s \propto F^{1/2}$  (yield),  $r_s \propto F^{1/3}$  (shear) or  $r_s \propto F^{1/4}$  (Buckling).

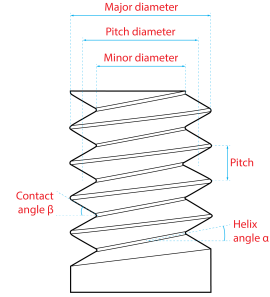


Figure 3.8: Schematic representation of an arbitrary screw with a single thread start.

The volume and mass of the screw is then determined in line with the assumptions stated above as:

$$V_s = r_s^2 \pi L_s [m^3] \quad (3.14)$$

$$m_s = V_s \rho_{st} [kg] \quad (3.15)$$

With  $\rho_{st}$  equal to the density of steel. Similarly, the screw moment of inertia is determined as:

$$I_s = 0.5m_s r_s^2 [kg m^2] \quad (3.16)$$

Using the radius proportionality defined above and assuming yield strength as the critical sizing criterium, the mass of the screw should scale as:

$$m_s \propto F \quad (3.17)$$

similarly, the moment of inertia of the screw should scale with the load rating as:

$$I_s \propto F^2 \quad (3.18)$$

The modelled mass properties of the PRS screw can be compared to catalogue data of existing screws. Both the screw mass and moment of inertia for different screw load ratings is shown in Figure 3.9 and 3.10 respectively. The screw mass model underestimates the screw mass on average by 8% with a standard deviation of  $\pm 12.8\%$ . The moment of inertia is underestimated on average by 13.4% with a standard deviation of  $\pm 25.3\%$ . The larger deviations and spread are explained by the higher order scaling of the moment of inertia.

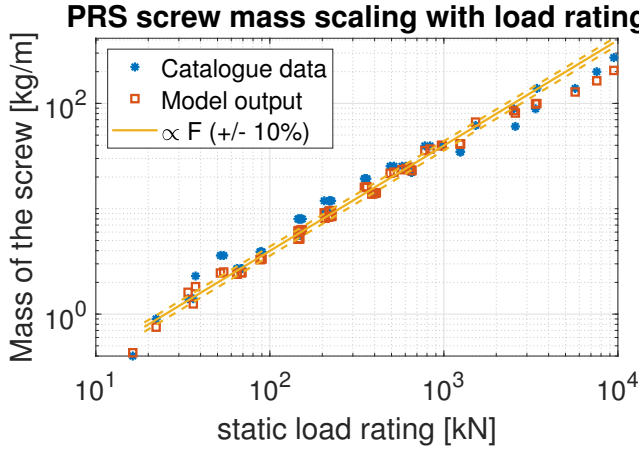


Figure 3.9: Mass per unit length of the PRS screw (loglog)

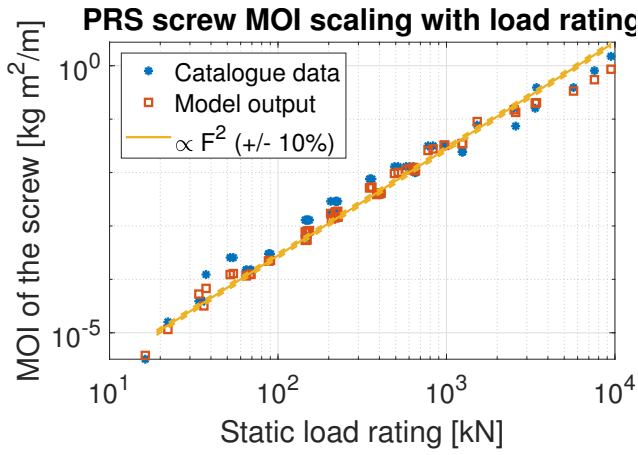


Figure 3.10: Moment of inertia per unit length of the PRS screw (loglog)

The yield criteria on the screw radius is clearly dominant in sizing the screw. Only at load ratings past 2000kN the trend line changes to the buckling criteria relations due to the longer stroke length of these screws in the catalogue data. Deviations from the trend line are due to changes in different parameters to match the catalogue specifications.

**Screw properties** Except for the mass properties of the screw, some geometrical parameters are needed for later power loss calculations. First, the helix angle of the screw  $\alpha_s$  describing the angle of the screw thread is calculated according to Equation 3.19[167]:

$$\alpha_s = \tan^{-1} \left( \frac{l_s}{2\pi r_s} \right) \quad (3.19)$$

The final parameter describing the screw thread is the contact angle of the thread. The contact angle depends on the exact geometry of the threads, however most commonly screws are designed to have a contact

angle of  $\beta = 45$  deg. Figure 3.8 shows both angles in a schematic representation.

### Roller sizing

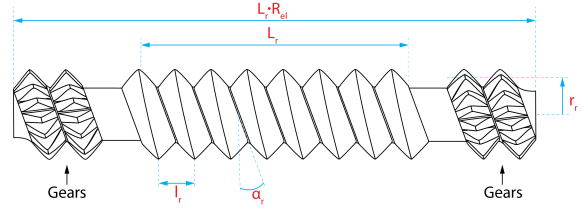


Figure 3.11: Planetary roller screw - roller sizing parameters.

The rollers in the PRS determine the dynamic load rating and transmission ratio of the mechanism. As such, sizing the rollers is an important step in designing a roller screw. Figure 3.11 shows a single roller with its main sizing parameters. The radius of the roller  $r_r$  is a free design variable, other properties are determined below.

**Roller properties** First, the basic properties of the thread on the rollers is determined. The thread of the rollers is characterised by a pitch radius  $r_r$  and a lead  $l_r$ . The radius is a free variable, however the lead of the roller is imposed by the lead and radius of the screw. The imposed lead of the roller is given in [167] by:

$$l_r = \frac{l_s}{\frac{r_s}{r_r} + 2} [\text{m}] \quad (3.20)$$

To properly size the rollers, the necessary dynamic load rating of the screw should be determined. The dynamic load rating  $C$  of the screw is dependent on the lifetime requirements as is evident when looking at the  $L_{10}$  lifetime model for ball bearings [109]. Using a factor to scale the  $L_{10}$  lifetime to a reliability of 99% found in [98, 153] and rewriting the lifetime equation for the dynamic load rating, the required load rating  $C_{req}$  is determined as:

$$C_{req} = \sqrt[3]{\frac{0.21L_{10}10^{-6}}{0.21l_t} F_{eq} [\text{N}]} \quad (3.21)$$

The dynamic load rating  $C$  of the PRS is determined by the amount of contact points between the screw, rollers and nut. [98] developed a model describing the PRS dynamic load rating based on a model for the ball screw. Rewriting this equation for the total number of contact points yield:

$$Z = \left( \frac{C_{req}}{f_c \cos^{0.86} \beta D_r^{1.8} \tan \beta \cos^{1/3} \alpha_s} \right)^{3/2} \quad (3.22)$$

Here  $f_c$  is a geometry coefficient set equal to  $74.87[\text{kg s}^{-2}]$  in [185],  $D_r$  is the pitch diameter of the roller in [mm].

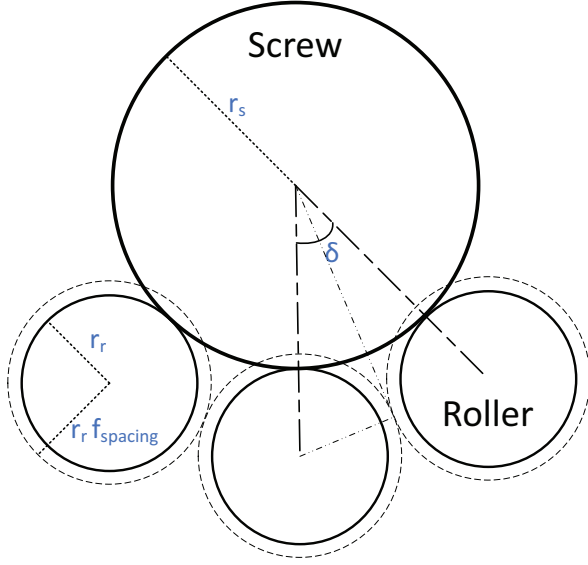


Figure 3.12: Schematic representation of the geometrical relation between the screw and rollers of the PRS.

The number of contact points is dependant on the number of rollers. The number of rollers is limited by the PRS geometry. Figure 3.12 shows a schematic representation of the screw and rollers. The minimum angle between two subsequent rollers  $\delta$  is mathematically described by:

$$\delta = 2 \sin^{-1} \left( \frac{r_r f_{spacing}}{r_s + r_r} \right) \quad (3.23)$$

Here  $f_{spacing}$  is a spacing factor between two subsequent rollers. The factor is expressed as a percentage of the roller diameter. The spacing factor is fixed to 105% as to give a spacing of 5% of the roller radius between the pitch radii of two subsequent rollers. The maximum amount of rollers in the PRS mechanism is then determined by:

$$N_{rollers} = \text{floor} \left( \frac{2\pi}{\delta} \right) \quad (3.24)$$

The floor function ensures the number of rollers is rounded down to an integer number. The amount of contact points per roller are then determined as:

$$Z_r = \text{ceil} \left( \frac{Z}{N_{rollers}} \right) \quad (3.25)$$

For each full helix turn of the roller, a single contact point/line with the screw exists. The required effective length of the rollers is therefore defined as:

$$L_r = l_r Z_r [\text{m}] \quad (3.26)$$

**Roller mass properties** The mass and moment of inertia of the rollers is dependant on the roller properties. The volume of the combined rollers is determined as:

$$V_r = N_{rollers} L_r R_{el} r_r^2 \pi [\text{m}^3] \quad (3.27)$$

Here  $R_{el}$  is the effective length ratio which is used to account for extra length of the roller for non modelled roller features. The effective length ratio is chosen as  $R_{el} = 1.1$ . The mass of the combined rollers is then defined as:

$$m_r = V_r \rho_{st} [\text{kg}] \quad (3.28)$$

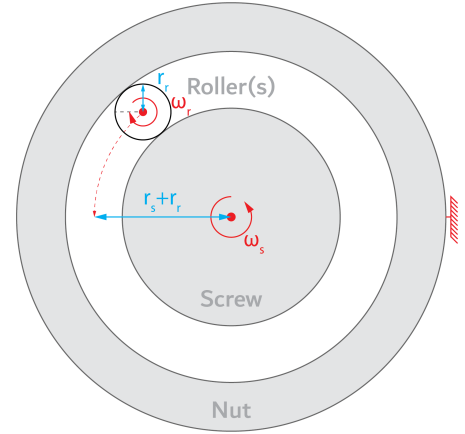


Figure 3.13: Roller motion around the screw and roller axis.

The moment of inertia definition of the rollers is slightly more complicated. The rollers have two axis of rotation, the roller individual centreline and the centreline of the screw as is seen in Figure 3.13. The moment of inertia of the rollers around their own axis is determined similarly to the moment of inertia of the screw as:

$$I_{r,own} = 0.5 m_r r_r^2 [\text{kg m}^2] \quad (3.29)$$

The moment of inertia of the rollers around the remote centre of rotation can be determined by representing the rollers as a point mass with a distance  $r_{r,remote}$  to the rotation axis equal to  $r_{r,remote} = r_s + r_r$ . The moment of inertia of the rollers around the screw axis is then given by:

$$I_{r,remote} = m_r r_{r,remote}^2 [\text{kg m}^2] \quad (3.30)$$

The total moment of inertia of the rollers with respect to the rotational acceleration of the screw can be determined by using the reduction ratios of a planetary

roller gear. The total moment of inertia of the rollers is then given as:

$$I_{r,screw} = I_{r,own} \frac{r_s/r_r}{2(1+r_s/r_r)} + I_{r,remote} \frac{r_s(r_n-r_r)}{2(r_r^2+r_r r_s)} [\text{kg m}^2] \quad (3.31)$$

The modelled roller inertia can be checked with catalogue data from [149]. Figure 3.14 shows the catalogue data next to the modelled output and the roller scaling law developed by [106]. The model data underestimates the roller inertia on average by 10% but with a standard deviation of  $\pm 55.7\%$ . Apart from the high order scaling of the moment of inertia this data could also indicate the assumption of the number of rollers and the resulting roller length is a crude approximation.

### Nut sizing

The final major component of the PRS is the nut. The nut is the translating part of the linear EMA. As the nut only translates, only the mass of the part should be determined. As the thread properties of the nut are completely defined by the screw and roller properties, nut properties are not needed in later loss calculations. A schematic representation of the nut is given in Figure 3.15.

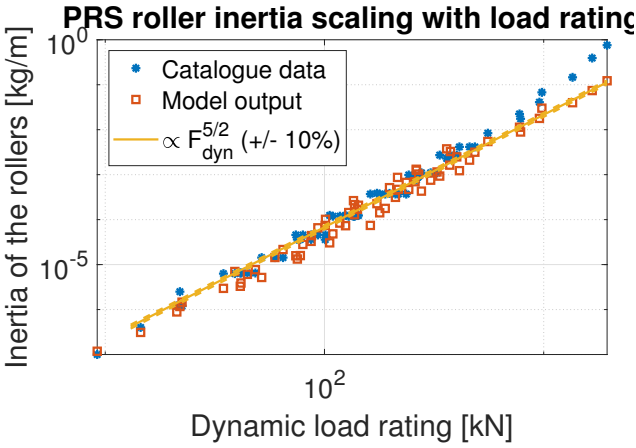


Figure 3.14: Moment of inertia of the PRS rollers (loglog)

**Nut mass properties** Dimensions of the nut follow from the geometry of the screw and rollers. The inside diameter should be capable of housing the screw and roller diameters. Similarly, the length of the nut should cover the length of the rollers. The length and internal pitch radius of the nut are defined as:

$$L_n = L_r R_{el} [\text{m}] \quad (3.32)$$

$$r_n = r_s + (2r_r) [\text{m}] \quad (3.33)$$

The outside radius of the nut is determined by the nut pitch radius and the material thickness. Material thickness of the nut is assumed to equal  $\frac{2}{3}th$  the screw radius:

$$r_{n,out} = r_n + t_n [\text{m}] \quad (3.34)$$

The volume of the nut and its respective mass are determined according to:

$$V_n = (r_{n,out}^2 - r_n^2) \pi L_n [\text{m}^3] \quad (3.35)$$

$$m_n = V_n \rho_{st} [\text{kg}] \quad (3.36)$$

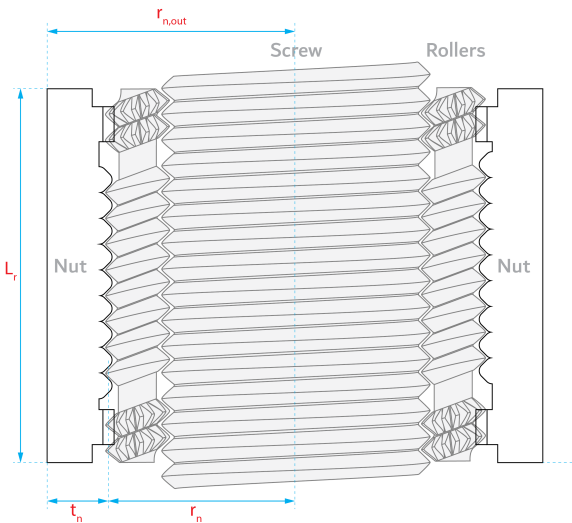


Figure 3.15: Planetary roller screw - nut sizing

Figure 3.16 shows the modelled mass of the nut roller combination next to catalogue data from [149] and a scaling law from [106]. The model data overestimates the mass on average by 5%, however a standard deviation of  $\pm 76\%$  is found.

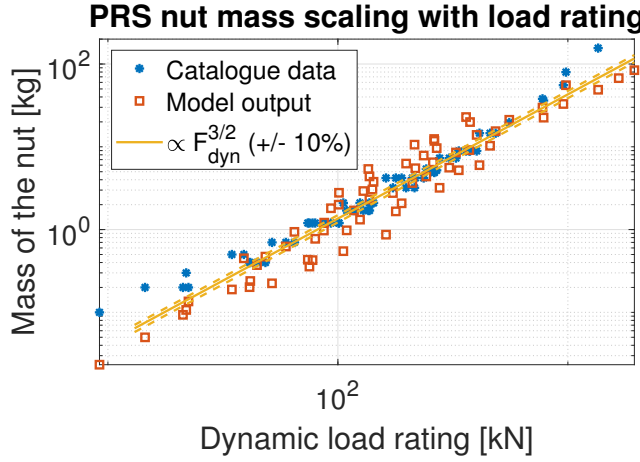


Figure 3.16: Mass of the PRS nut and rollers (loglog)

The spread of the modelled nut mass is significantly higher compared to the modelled mass of the screw. The large spread is partly due to the sizing of the rollers, however the nut material thickness assumption is a more important factor. Development of a physics based sizing model of the PRS nut could improve these results in future work.

### Extending rod sizing

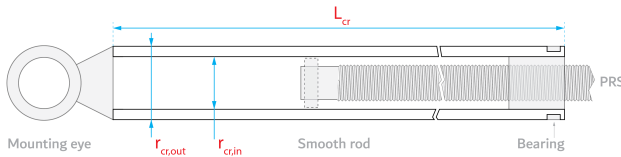


Figure 3.17: Mechanical cylinder - Smooth rod sizing

The smooth extending rod is fixed to the nut of the PRS and is able to move up and down with the motion of the actuator. It provides a smooth bearing and sealing surface for the linear bearings in the cylinder housing. Figure 3.17 shows the smooth extending rod with its peripherals and main sizing parameters.

**Rod load sizing** The cylinder rod is loaded with the same axial load as the PRS screw. Load sizing hence depends on the same buckling, yield and fabrication requirements as those used with the PRS screw. As the cylinder rod is a hollow tube, both inside and outside radii should be determined. The inside radius of the rod is equal to the outside radius of the nut  $r_{cr,in} = r_{n,out}$ . The outside radius is thus free to scale with above requirements. Buckling and yield calculations are shown in Appendix A.2 and can be approximated as:

$$r_{cr,out,buckling} = (2.5e-13FL_{cr} + r_{cr,in}^4)^{1/4} \quad (3.37)$$

$$r_{cr,out,yield} = (7.3e-10F + r_{cr,in}^2)^{1/2} \quad (3.38)$$

The length of the rod is assumed to equal the length of the screw  $L_{cr} = L_s$ . The minimum outside radius of the smooth extending rod  $r_{cr,out}$  is given by the maximum value of the buckling, yield and a fabrication requirement of 4[mm] thickness. The volume and mass of the smooth extending rod are then given as:

$$V_{cr} = (r_{cr,out}^2 - r_{cr,in}^2) \pi L_{cr} [\text{m}^3] \quad (3.39)$$

$$m_{cr} = V_{cr} \rho_{st} [\text{kg}] \quad (3.40)$$

By assuming the yield requirement on the cylinder rod outside diameter is leading as is the case for the PRS screw, the mass of the rod should behave according to:

$$m_{cr} \propto F \quad (3.41)$$

Figure 3.18 shows the modelled mass of the cylinder rod together with the expected scaling trend. At high load ratings, the yield sizing trend is followed exactly. However, at lower load ratings, the trend line is dominated by the fixed minimal material thickness defined by the fabrication requirement discussed above. A rod length of 2[m] is assumed in this figure.

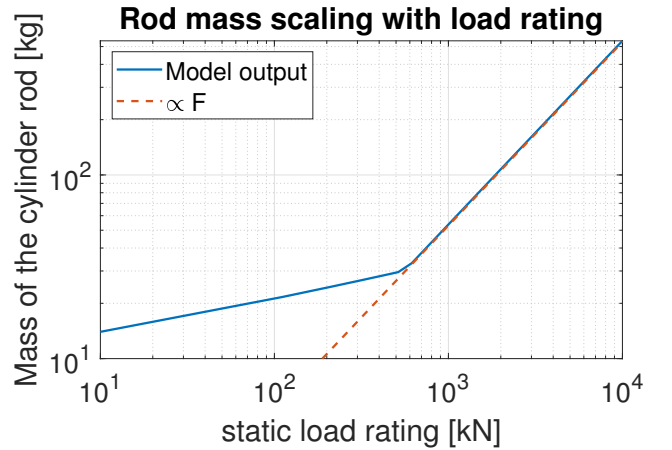


Figure 3.18: Mass of the cylinder rod (loglog)

### Cylinder housing

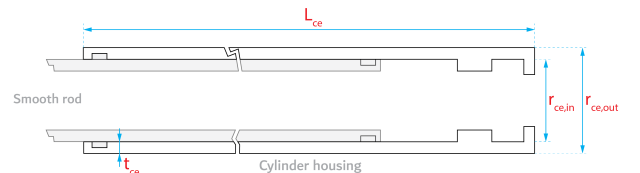


Figure 3.19: Mechanical cylinder - Cylinder housing sizing

The actual cylinder housing is largely a stationary part forming the interface between the fixed world and the PRS components, gearbox and motor. The cylinder

housing in its most basic form is a hollow cylinder as seen in figure 3.19. Its main dimensions are determined below. Note that the cylinder housing is only modelled to find the approximate additional mass to the actuator.

**Housing mass properties** Similar to the cylinder rod, the inside radius of the cylinder is defined by the outside radius of the smooth extending rod as  $r_{ce,in} = r_{cr,out}$ . Also the thickness of the cylinder housing is simplified to equal the thickness of the smooth extending cylinder as  $t_{ce} = t_{cr}$ . The outside radius of the cylinder housing is then determined according to  $r_{ce,out} = r_{ce,in} + t_{ce}$ . Finally the length of the cylinder enclosure is assumed to be 5% longer than the length of the smooth cylinder rod as  $L_{ce} = 1.05L_{cr}$  to account for bearing length. By assuming a single side closed cylinder, the volume and mass of the cylinder housing are defined as:

$$V_{ce} = ((r_{ce,out}^2 - r_{ce,in}^2) \pi L_{ce}) + (r_{ce,out}^2 \pi t_{ce}) \text{ [m}^3\text{]} \quad (3.42)$$

$$m_{ce} = V_{ce} \rho_{st} \text{ [kg]} \quad (3.43)$$

The wall thickness dependency on the cylinder rod properties results in similar mass properties of the cylinder housing compared to those of the cylinder rod.

### Mechanical cylinder mass properties

The total mass properties of the mechanical cylinder are the sum of the individual component mass properties. The total mechanical cylinder mass  $M_3$  used in (3.10) is therefore given as:

$$\boxed{M_3 = m_s + m_r + m_n + m_{cr} + m_{ce}} \quad (3.44)$$

Similarly, the moving mass of the mechanical cylinder  $M_{3,m}$  as used in (3.1) is defined as:

$$\boxed{M_{3,m} = m_r + m_n + m_{cr}} \quad (3.45)$$

The moment inertia of the mechanical cylinder  $I_3$  as used in (3.1) is defined only by the rolling components and therefore equal to the sum of (3.16) and (3.31) as:

$$\boxed{I_3 = I_s + I_{r,screw}} \quad (3.46)$$

### 3.3.3 Sizing of the gearbox

The gearbox is used between the mechanical cylinder and the electric motor to reduce the torque on the motor side and decrease the rotational velocity to the system. The gearbox is implemented as a single stage helical reduction gearbox with parallel input and output shafts. The gearbox has two main components: the

actual gear pair with their corresponding axles and the gear housing. The gear pair is the load bearing component of the gearbox. This components sizes based on the gear ratio optimization parameter and the rated torque of the actuator. The gearbox enclosure scales to fit the load sized gear pair. Sizing models of both components are discussed separately below.

### Gear pair sizing

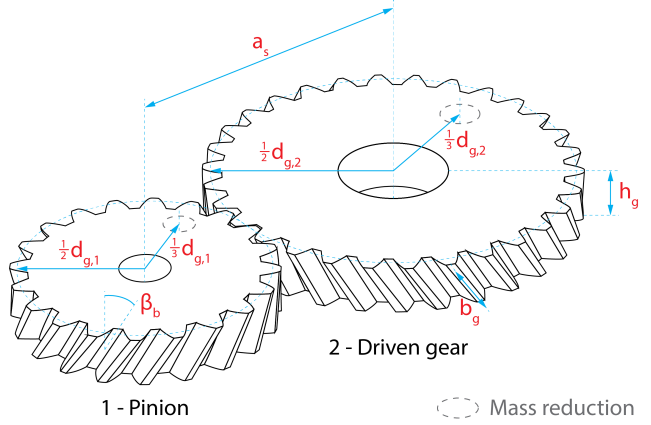


Figure 3.20: Helical gear pair dimensions and names.

The gear pair consists of two meshing helical gears parallel to each other. The gears in the gearbox are called the pinion (1) and driven gear (2) as seen in Figure 3.20. The gear ratio is the main property of the gearbox and is defined by:

$$R_{gear} = \frac{d_{g,1}}{d_{g,2}} \quad (3.47)$$

The gear ratio therefore is defined as the ratio between the pitch diameters of both gears. The actual gear diameters are defined by the axial spacing of both gear axles. As the gearbox only uses a single stage, the distance between the centres of both gears should remain constant for a similarly sized actuator. To simplify the sizing model, this distance is fixed to  $a_s = 0.2[m]$ . As the diameter of the gears is defined by non load dependant properties, load sizing of the gears only influences the height of the gears.

**Gear load sizing** Load sizing of a component always is determined by stress in the component material. Gears transmit mechanical power in the form of a torque and rotational motion. Torque on the pinion and driven gear is different, however the tangential force on the gear teeth faces as a result of the transmitted torque is equal in both gears. The stress in the gear teeth material is defined by the division of this tangential force by the cross sectional area of the gear teeth. As the cross sectional area of the gear teeth is

linearly related to the height of the gear and the tangential force is linearly related to the torque, the gear height is expected to scale according to:

$$h_g \propto T_{max} \quad (3.48)$$

[162] details the load sizing equation for helical gears in detail. The necessary equations are repeated in Appendix A.3 and can be approximated with:

$$h_g = 2.31e-6 T_{max} \left( 1 + \frac{3}{R_{gear}} + \frac{3}{R_{gear}^2} + \frac{1}{R_{gear}^3} \right) \quad (3.49)$$

**Gear mass properties** To determine the mass of the gears, the gears are assumed to be solid disks with outside diameter equal to the pitch diameter of the gears. A hole in the centre is left out where the axle of the gears is placed. The axle size for both gears is set equal to the radius of the PRS screw. To account for mass savings in the gear design, the final mass will be taken as 50% of the mass of the solid disks. The solid disk volumes of both the pinion and driven gear are determined according to:

$$V_{g,i} = \pi h_g \left( \left( \frac{d_{g,i}}{2} \right)^2 - \pi r_s^2 \right) [\text{m}^3] \quad (3.50)$$

Here  $i$  refers to the number of the gear as shown in Figure 3.20. The corresponding masses of both gears are determined from:

$$m_{gi} = V_{g,i} \rho_{st} [\text{kg}] \quad (3.51)$$

The total mass of both gears combined compensated for weight savings is defined by:

$$m_{gears} = 0.5 (m_{g,1} + m_{g,2}) [\text{kg}] \quad (3.52)$$

The moment of inertia of the gears is determined next. The moment of inertia of both gears is first determined around their individual axis. The mass reduction of the gears is implemented as negative point masses on  $2/3$ th of the gear radius as can be seen in Figure 3.20. The moment of inertia of each individual gear is determined from:

$$I_{g,i} = \frac{1}{2} \left( \left( \frac{d_{g,i}}{2} \right)^2 + r_s^2 \right) - 0.5 m_{g,i} \left( \frac{d_{g,i}}{3} \right)^2 [\text{kg m}^2] \quad (3.53)$$

As only the gear height sizes with the load, the mass of the gear pair is expected to scale with:

$$m_{gears} \propto T_{max} \quad (3.54)$$

Similarly, as the radius of the gears is not load dependant, the mass moment of inertia of the gears is expected to scale according to:

$$I_g \propto T_{max} \quad (3.55)$$

The modelled moment of inertia of the gear pair is compared to catalogue data in Figure 3.23.

### Gearbox enclosure

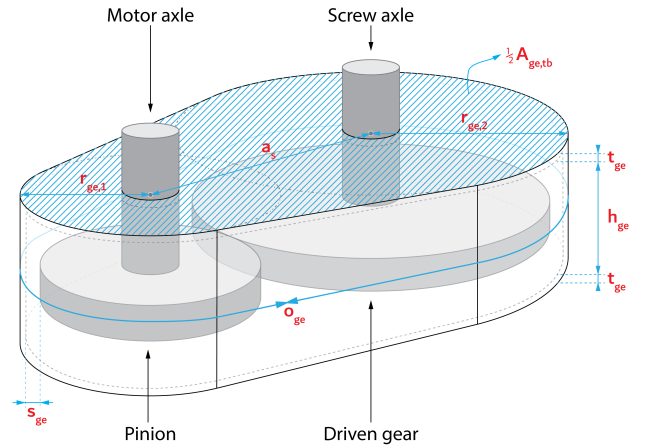


Figure 3.21: Gearbox housing with its main dimensions

The gear housing encloses the helical gears and contains the lubrication agent of the gears and bearings. The housing also forms the interface with the motor housing and the mechanical cylinder. The gearbox is only sized to find the approximate mass of the actuator, as such the geometry is heavily simplified. The overall architecture and dimensions of the gear housing are shown in figure 3.21.

**Sizing assumptions** To determine the mass of the gearbox, some assumptions are made to simplify the gear housing design. First, the gear housing internal dimensions are assumed to be determined by a fixed spacing distance  $s_{ge} = 2[\text{cm}]$  and the dimensions of the actual gear pair. Second, the thickness of the gear housing should be proportional to a maximum loading parameter. Here we assume the gear housing material thickness is proportional to the maximum tangential force on the gear teeth. Loading induces a stress in the enclosure material, the enclosure thickness should scale to keep the maximum stress in the enclosure constant with different load ratings. The proportionality is therefore given as:

$$t_{ge} \propto \sqrt{F_{max}} \quad (3.56)$$

This relation is valid assuming the second dimension determining the cross sectional area of the enclosure is proportional to the loading factor is the same way. The scaling parameter is determined as  $2.8e-4[m/N^{1/2}]$  based on a fit to existing gearbox data. The resulting outside radius of the gearbox around both gears is determined according to:

$$r_{ge,i} = \frac{d_{g,i}}{2} + s_{ge} + t_{ge} [m] \quad (3.57)$$

**Enclosure mass properties** The area of the top and bottom of the gearbox enclosure as seen in Figure 3.21 is calculated according to:

$$A_{ge,tb} = \frac{(r_{ge,1}^2 + r_{ge,2}^2) \pi}{2} + 2a_s \min([r_{ge,1}, r_{ge,2}]) + a_s |r_{ge,1} - r_{ge,2}| [m^2] \quad (3.58)$$

The resulting combined volume of the top and bottom slabs is defined by:

$$V_{ge,tb} = 2A_{ge,tb}t_{ge} [m^3] \quad (3.59)$$

The volume of the gear housing side walls is determined by assuming a thin walled structure. As such, the mean circumference is approximately equal to the outside circumference. The outside circumference of the gear housing is determined by:

$$o_{ge} = \pi (r_{ge,1} + r_{ge,2}) + 2\sqrt{a_s^2 + |r_{ge,1} - r_{ge,2}|^2} [m] \quad (3.60)$$

Finally, the height of the gearbox is determined. The inside height of the gearbox is determined by the height of the gears and the spacing factor  $S_{ge}$  as:

$$h_{ge} = h_g + 2s_{ge} [m] \quad (3.61)$$

The volume of the gear housing side walls is then determined by:

$$V_{ge,s} = h_{ge}o_{ge}t_{ge} [m^3] \quad (3.62)$$

Adding the top, bottom and side volumes, the total gearbox enclosure material volume can be determined as:

$$V_{ge} = V_{ge,tb} + V_{ge,s} [m^3] \quad (3.63)$$

Holes in the housing are not taken into account as the removed material mass in these holes would be gained back in the bearing supports and other features. The resulting mass of the gearbox is calculated as:

$$m_{ge} = V_{ge}\rho_{st} [kg] \quad (3.64)$$

According to above relation, mass of the enclosure is expected to scale proportional to the rated torque with:

$$m_{ge} \propto T_{max}^{1/2} \quad (3.65)$$

### Gearbox mass properties

The major component mass properties of the gearbox are determined above. Here the component mass properties are added to obtain the total gearbox mass properties. A final component influencing the gearbox mass not discussed before is the oil held in the gearbox enclosure for lubrication of the gears and bearings.

The mass of the gearbox oil is determined based on the free volume inside the gearbox enclosure. The internal free volume is approximated by subtracting the volume of the gears from the internal volume of the enclosure. The total oil volume is taken as  $1/3$ th the free volume:

$$V_{ge,oil} = \frac{1}{3} \left( o_{ge}h_{ge} - \sum_{i=1}^2 V_{g,i} \right) [m^3] \quad (3.66)$$

The resulting oil mass is determined from:

$$m_{oil} = V_{ge,oil}\rho_{goil} [kg] \quad (3.67)$$

With the three major component masses determined, the total mass of the gearbox  $M_2$  as used in (3.10) can be defined as:

$$M_2 = m_{gears} + m_{ge} + m_{oil} [kg] \quad (3.68)$$

The total moment of inertia is only affected by the gear pair moment of inertia as the effect of bearings is assumed to be negligible. Therefore the total moment of inertia of the gearbox  $I_2$  as used in (3.2) with respect to the screw side acceleration is given as:

$$I_2 = I_{g,1}R_{gear} + I_{g,2} [kg m^2] \quad (3.69)$$

The mass of the gearbox is expected to scale according to the enclosure trends defined above for low torque ratings. For higher torque ratings the mass of the gear pair is expected to become dominant.

The modelled mass of the gearbox can be compared to catalogue data from [124]. Figure 3.22 and 3.23 show the mass and moment of inertia for different load rated gearboxes and different gear ratio's.

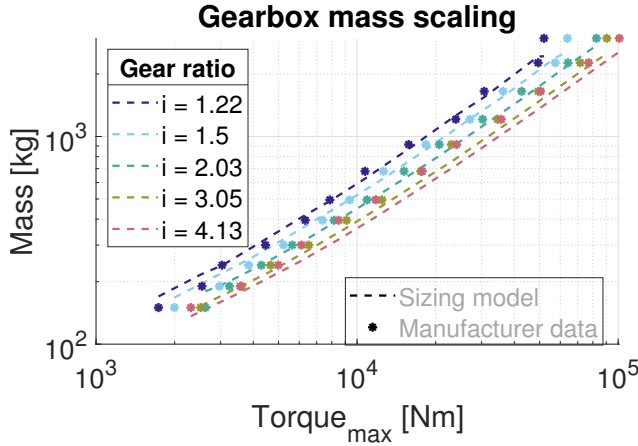


Figure 3.22: Mass of the the gearbox (loglog)

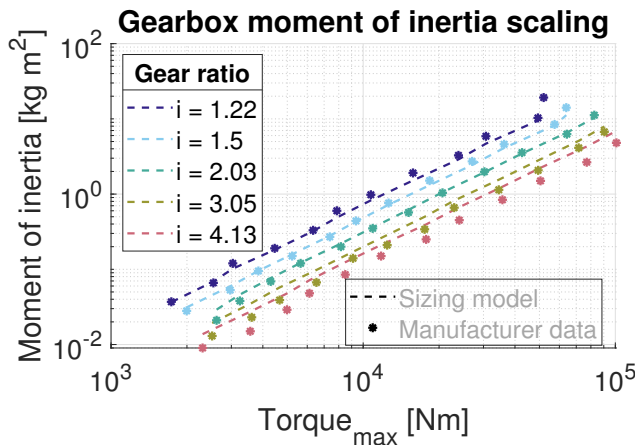


Figure 3.23: Moment of inertia of the gearpair on the motor side (loglog)

Both mass and moment of inertia properties of the gearbox match catalogue data reasonably well for lower gear ratio's. For gear ratio's above 2 both the mass and moment of inertia of the gearbox is overestimated by the model. Gear ratio's above 5 are not studied as those are not realistic in a single stage for application in the EMA. On average the model underestimates the gearbox mass by 7% with a standard deviation of  $\pm 10.8\%$ . In contrast the moment of inertia of the gearbox is over estimates on average by 23% with a standard deviation of  $\pm 26\%$ .

### 3.4 Loss model development

Development of a mathematical loss model of the EMA is needed to determine the energy requirements for a given actuator on a specific task. The EMA is a linear actuator which converts electrical energy in linear mechanical energy. Conversely, the linear actuator can also generate electrical energy due to a linear mechanical force and velocity input. The EMA is effectively

capable of four quadrant operation which means the actuator can be operated in forward and reverse motoring mode and in forward and reverse generating mode. The basics of the motoring regime of an actuator are widely known. However, the generating regime of an actuator is a less common concept. In rotary actuators (eg. electric motors), the capability of the motor to be used as a generator is known. Just as for the rotary actuators, linear actuators can be back driven to operate as a generator. By enforcing a force and velocity on the conventional output side of the EMA, the nut of the PRS forces the screw to rotate. The rotation of the screw is then led trough the gearbox, effectively increasing the rotational velocity towards the rotary motor. The rotary motor then delivers electric power back to the controller.

**Back drive ability** Back driving is an important concept in mobile linear actuator applications. In applications where the load can drive the actuator, back driving can regenerate the energy of the load to electrical energy which can be stored. When considering a full cycle of a back drivable actuator, power in the system is affected twice by the efficiency of the actuator. The efficiency of the actuator is determined by power losses in the power path of the actuator due to for example friction. When back driving the actuator, a situation can occur in which the power losses in the system are higher than the power delivered to the actuator by the load. In this case the actuator is self locking, and positive power is needed from the actuator to facilitate movement of the load. Actuators which are always self locking are non back drivable actuators and can never work in generating mode. Self locking actuators therefore pose higher requirements on the electrical grid connection. In applications where grid power is limited, back drive ability is very important.

**Model approach** Modelling the power loss behaviour with equations provides a way to compare the EMA to different actuator solutions for a specific application. Using a loss model to determine the losses for different discretised working points of the actuator in a task enables the calculation of the required energy to perform this task. In the subsections below, loss factors of each EMA component are determined and modelled based on the working point and component sizing variables. Different loss models for EMA components exist in literature, however these models are often not ready for use in a simulation based application. The used mathematical models and changes to these models are discussed and the overall loss trends with respect to the working point are shown. The list of symbols used in the component loss models is found in Subsection 3.4.1. Used constants are defined in Appendix D.

### 3.4.1 List of symbols

Symbol	Explanation	Unit
$\alpha_{EMA}$	Slanted angle of the actuator	[rad]
$\alpha_s$	Helix angle of the PRS screw	[rad]
$\beta$	Contact angle of the PRS screw	[rad]
$\eta_s$	Working point efficiency of the PRS mechanism	[-]
$\mu_f$	Coulomb kinetic friction coefficient of the cylinder bearings	[-]
$\mu_k$	Coulomb kinetic friction coefficient in the PRS	[-]
$\mu_r$	Rolling friction coefficient in the PRS	[-]
$\nu_s$	Kinematic viscosity of PRS lubricating oil	[mm <sup>2</sup> s <sup>-1</sup> ]
$\nu_l$	Kinematic viscosity of bearing lubricating oil	[m <sup>2</sup> s <sup>-1</sup> ]
$\omega_{out}$	Output speed of the gearbox	[rad s <sup>-1</sup> ]
$\phi_{ish}$	Inlet shear heating factor	[-]
$\phi_{rs}$	kinematic replenishment factor	[-]
$G_{rr}$	Geometry and load dependant factor	[-]
$\rho$	Friction angle of the PRS screw	[rad]
$\rho_l$	Mass density of lubricating oil	[kg m <sup>-3</sup> ]
$A_b$	Contact area of the cylinder bearings	[m <sup>2</sup> ]
$d_{g,2}$	Pitch diameter of the driven gear	[m]
$d_m$	Mean equivalent bearing diameter of the PRS	[m]
$F$	Axial force on the actuator	[N]
$F_b$	Cylinder bearing total friction force	[N]
$F_c$	Coulomb friction force	[N]
$F_n$	Normal force on the cylinder bearings	[N]
$F_{pl}$	Preload force on the PRS mechanism	[N]
$F_s$	Stiction friction force	[N]
$h_g$	Height of the gear	[m]
$k_v$	Coefficient of viscous friction	[kg s <sup>-1</sup> ]
$L_{ext}$	Extension length of the actuator	[m]
$L_M$	Moment arm between the cylinder bearings	[m]
$L_s$	Length of the PRS screw/ stroke length	[m]
$l_t$	Total (effective) lead of the PRS	[m]
$M_{EMA}$	Total mass of the actuator	[kg]
$m$	Gear teeth module	[m]
$N$	Normal force on the PRS mechanism	[N]
$P_b$	Bearing gearbox losses	[W]
$P_{g,loss}$	Power loss in the gearbox	[W]
$P_{load}$	Load dependant gearbox losses	[W]
$P_{no-load}$	No load gearbox losses	[W]
$P_{screw,loss}$	Power loss in the PRS screw	[W]
$r_{RP}$	Radius of curvature of the PRS roller helix	[m]
$r_s$	Pitch radius of the PRS screw	[m]
$T_{bending}$	Bending moment in the cylinder	[N m]
$T_{out}$	Output torque of the gearbox	[N m]
$T_r$	Rolling frictional moment	[N m]
$v$	Linear velocity of the actuator	[m s <sup>-1</sup> ]
$v_{stri}$	Stribeck velocity	[m s <sup>-1</sup> ]
$y_b$	Gap between cylinder and bearings at high velocity	[m]
$Z_r$	Number of contact points per PRS roller	[-]

### 3.4.2 Mechanical cylinder losses

The mechanical cylinder has loss components in both the PRS and the sliding interfaces of the smooth extending rod seen in Figure 3.6. In the ideal actuator mounting configuration, the losses of the PRS mechanism are expected to be much larger than the friction losses in the cylinder bearings. However, due to the slanted orientation of the cylinder, bending due to its own weight will result in higher bearing friction forces. Losses in the PRS and bearing friction losses are discussed separately below.

#### Planetary roller screw losses

Losses in the planetary roller screw occur due to rolling contact friction between screw, rollers and nut and due to slip between the screw and the rollers [128]. Further-

more the PRS has losses associated to the friction of the nut, seal friction, lubrication and hysteresis effects [128]. The friction of the seal on the PRS is expected to be much lower compared to roll and slip losses. Seal friction could even be eliminated by using a non-sealed PRS nut. Hysteresis effect losses are studied in ball bearing technology and are also found to be much smaller compared to other rolling losses [71]. Seal and bearing losses of the PRS are therefore neglected in this model.

**Existing models** The rolling contact friction and slip losses of the PRS are studied by [167]. The efficiency model of [167] shown in equation 3.70 captures the steady state behaviour of the PRS transmission based on the geometrical properties of the mechanism.

$$\eta_s = \frac{r_s \tan \alpha_s (\cos \alpha_s \cos \rho \sin \beta - \sin \alpha_s \sin \rho - \mu_k (\sin \alpha_s \cos \rho + \cos \alpha_s \sin \rho \sin \beta))}{r_s (\cos \rho \sin \alpha_s \sin \beta + \sin \rho \cos \alpha_s) + r_{RP} (1 - \cos \rho) (\sin \rho + \cos \rho) \cos \alpha_s \cos \beta} \quad (3.70)$$

Here  $\rho$  is the friction angle of the screw defined as:

$$\rho = \tan^{-1} \left( \frac{\mu_r}{r_{RP} \sin \beta} \right) \quad (3.71)$$

The PRS is mostly operates in steady state behaviour as is stated by [88]. As such, the use of a quasi steady state approach is warranted to find the global loss behaviour of the PRS. The model of [167] has some major simplifications which should be discussed:

- The coulomb kinetic coefficient of friction  $\mu_k$  is a fixed value.
- The rolling coefficient of friction  $\mu_r$  is a fixed value.
- The contact angle of the screw is fixed to  $\beta = 45\text{deg}$ .
- Lubrication effects are ignored.

The use of a fixed kinetic coefficient of friction is a widely accepted simplification in friction modelling. A coefficient  $\mu_k = 0.055$  is used in [167] which falls in the expected range for lubricated steel-steel contacts. This simplification is adopted just as the fixed contact angle of the screw.  $\beta = 45\text{deg}$  is the most common angle on commercial available screws and is proven to be the most practical angle in PRS applications [167].

**Model adaptations** In contrast to the kinetic coefficient of friction, the fixed value for the rolling coefficient of friction limits the usability of the model for use in a simulation based approach. The use of a fixed rolling coefficient of friction effectively removes load and speed dependencies from the loss model. In literature, the mean of experimental coefficient results is

often used. For general comparison of different transmissions on global efficiency this choice is warranted. However, to find the energy loss in the system for a given operation, force and speed dependencies should be included. Effects on the rolling coefficient of friction in the PRS are not readily found in literature. However, research on the rolling coefficient of friction in bearing technology is available. PRS contact mechanics are often modelled using equivalent balls, hence ball bearing rolling coefficients of friction should be representative for the PRS mechanism. Lubrication effects on the rolling friction can also be added to the rolling coefficient of friction.

The rolling frictional moment of ball bearings is semi-empirically modelled in [150] based on the working point and mean bearing diameter. The mean bearing diameter  $d_m$  is substituted as a function of the screw and roller radii:

$$d_m = \frac{r_s + r_r}{2} [\text{m}] \quad (3.72)$$

As the rolling frictional force is usually given by  $F_r = \mu_r N$  where  $N$  is the normal force, the rolling coefficient of friction can be obtained from the rolling frictional moment  $T_r$  as:

$$\mu_r = \frac{T_r}{r_s N} \quad (3.73)$$

The rolling frictional moment model from [150] is given as:

$$T_r = \phi_{ish} \phi_{rs} G_{rr} (\nu_s n)^{3/5} [\text{N m}] \quad (3.74)$$

Where  $n$  is the speed of the screw in [rpm]. The different loss factors are detailed in Appendix A.4. The inclusion of an inlet shear heating factor  $\phi_{ish}$  and a kinematic replenishment reduction factor  $\phi_{rs}$  ensure lubrication loss effects are taken into account.  $G_{rr}$  is a geometry and load dependant factor which can be approximated by:

$$G_{rr} = 0.3d_m^{1.97} \left( 3.55d_m^4 n^2 + 3.64 \frac{F}{Z_r} \right)^{0.54} \quad (3.75)$$

Ignoring the lubrication effects, the rolling friction losses at low speeds are therefore expected to scale according to:

$$P_{screw,loss} \propto F^{0.54} \quad (3.76)$$

$$P_{screw,loss} \propto v^{8/5} \quad (3.77)$$

At higher speeds fluid effects become apparent and the losses in the PRS are expected to drop due to a decreased fluid film thickness between contact points. As the adapted efficiency model results in working point efficiencies, the driving and back-driving torque of the PRS are given as:

$$T_{PRS,drive} = \frac{Fl_t}{2\pi} \frac{1}{\eta_s} [\text{N m}] \quad (3.78)$$

$$T_{PRS,backdrive} = \frac{Fl_t}{2\pi} \eta_s [\text{N m}] \quad (3.79)$$

The ideal PRS torque in a 100% efficient transmission is defined as:

$$T_{PRS,ideal} = \frac{Fl_t}{2\pi} [\text{N m}] \quad (3.80)$$

The modelled power losses in the PRS are shown in Figure 3.24 and 3.25 with respect to the required force and velocity respectively.

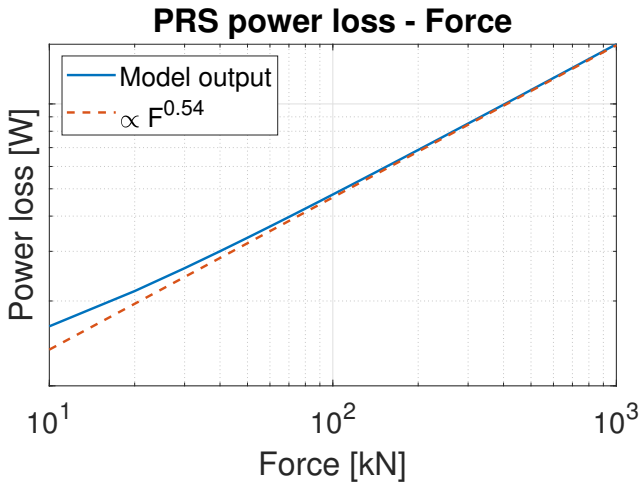


Figure 3.24: Power loss in the PRS - force (loglog)

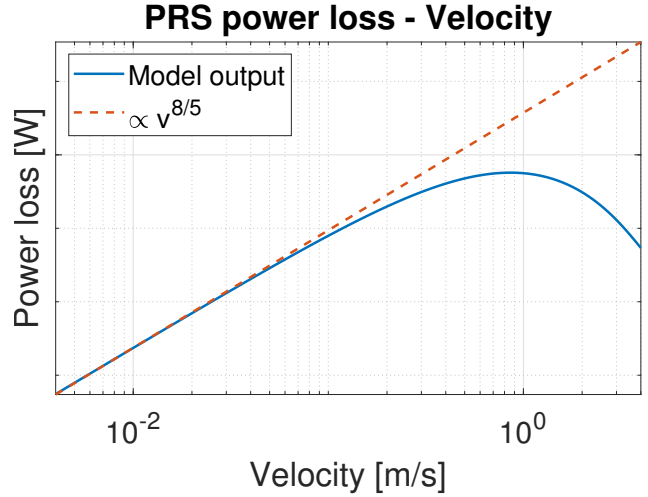


Figure 3.25: Power loss in the PRS - velocity (loglog)

The power loss is seen to decrease significantly with high velocities due to the decreased fluid film thickness. Note that the effects of the decreasing fluid film thickness is dependant on the rotational velocity of the screw. Depending on the lead of the screw the transition towards the reduced rolling friction shifts.

The screw friction torque used in (3.1) is defined as the difference between the required PRS torque for a given working points as defined in (3.78) and (3.79) and the ideal PRS torque (3.80):

$$T_{screw,loss} = T_{PRS} - T_{PRS,ideal} \quad (3.81)$$

### Cylinder bearing losses

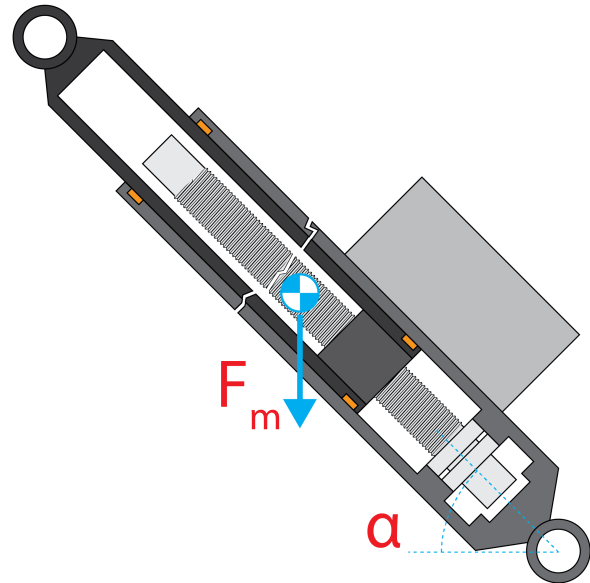


Figure 3.26: EMA cylinder in slanted orientation causing a bending moment on the cylinder due to actuator weight.

The cylinder housing and cylinder rod of the EMA interface through two linear bearings. These bearings guide the linear movement of the cylinder rod and ensure no lateral forces are transmitted to the PRS mechanism. The sliding friction between the bearing material and the smooth surfaces of the housing and rod cause power losses during operation. In an ideal cylinder the sliding friction forces are minimal, however due to the slanted orientation of the cylinder the own weight of the cylinder causes a bending moment resulting in high normal forces on the bearing material. Figure 3.26 shows a cross section of the cylinder with the respective bearings in orange. As the moment arm between both bearings changes with the position of the actuator, bearing friction is highly dependent on the position or extension of the actuator. The bearing friction forces in both cylinder types are linearly inversely proportional to the moment arm between both bearings and linearly proportional to the mass of the actuator.

**Friction modelling** The frictional forces on the bearings are expected to behave as a fluid lubricated contact. Therefore the Stribeck curve is ideally suited to model the cylinder friction [159, 80, 182]. [18] describes a Stribeck function specifically for determining losses in sliding contacts. The cylinder bearing friction force  $F_{cyl,loss}$  as used in (3.1) can therefore be defined as [18]:

$$F_{cyl,loss} = \left( F_c + (F_s - F_c) e^{(|v|/v_s)^i} \text{sign}(v) \right) + k_v v [\text{N}] \quad (3.82)$$

Here  $F_c$  is the coulomb friction force which is defined as:

$$F_c = F_n \mu_f [\text{N}] \quad (3.83)$$

The normal force  $F_n$  on the bearings is dependant on the moment arm of the bearings and mass and angle of the EMA. The moment arm can be calculated as a function of the actuator extension by:

$$L_M = L_{ext,max} + L_{M,min} - L_{ext} [\text{m}] \quad (3.84)$$

Here  $L_{ext,max}$  is the maximum cylinder extension,  $L_{M,min}$  is the minimum construction moment arm and  $L_{ext}$  is the extension of the actuator. The centre of mass of the EMA is assumed to be stationary at  $2/3$ th the cylinder housing length. The resulting bending moment on the cylinder due to its own weight is defined as:

$$T_{bending} = M_{EMAg} \frac{2}{3} L_s \cos(\alpha_{EMA}) [\text{N m}] \quad (3.85)$$

The normal force on the bearing surfaces is now given as:

$$F_n = \frac{T_{bending}}{L_m} + F_{pl} [\text{N}] \quad (3.86)$$

Where  $F_{pl}$  is a constant preload force. The stiction force  $F_s$  is assumed to be 30% larger than the coulomb friction force. Finally, the viscous coefficient of friction  $k_v$  is modelled by [93] as a function of the bearing contact area  $A_b$ , lubrication properties and the clearance between the bearing and contact surface at higher speeds  $y_b$ :

$$k_v = \frac{A_b \nu_l \rho_l}{y_b} [\text{kg s}^{-1}] \quad (3.87)$$

**Cylinder loss behaviour** The cylinder losses are only influenced by the frictional forces between the linear bearings and their contact surfaces. The bearing friction force is independent of the loading of the actuator as the bearing normal forces are oriented perpendicular to the load direction.

The cylinder losses are expected to increase with the extension of the cylinder rod as this decreases the moment arm between both bearing locations. As the moment arm is determined by a summation, the trend relation to the actuator extension is not exponential. The losses are expected to scale linearly with the velocity in the normal speed range. At higher velocities the viscous forces are expected to dominate with  $P_{visc} \propto v^2$  and at lower velocities the Stribeck effect is expected to flatten the loss trend with respect to the velocity.

Figure 3.27 and 3.28 show the loss trends of the cylinder bearings with respect to the actuator position and velocity respectively.

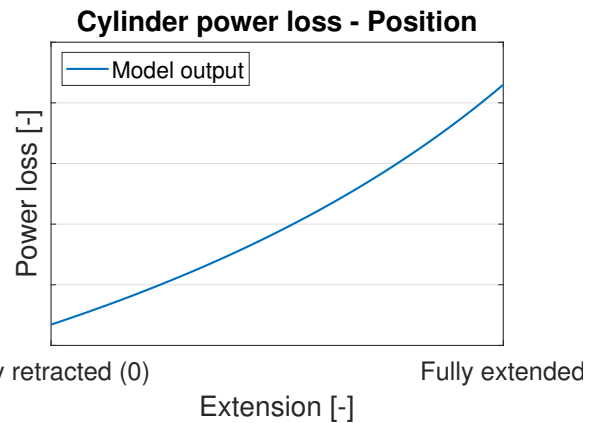


Figure 3.27: Power loss of the bearings - position

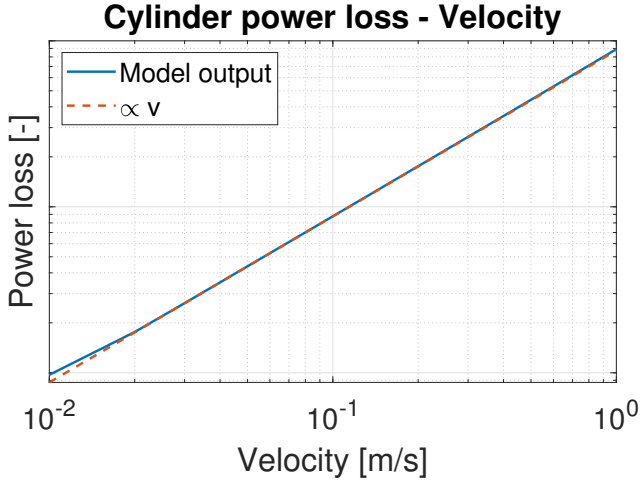


Figure 3.28: Power loss of the bearings - velocity (loglog)

### 3.4.3 Gearbox losses

The gearbox transmits torque and rotation between the motor and PRS screw. Depending on the ratio of the gear diameters, the speed and torque ratio are changed between the input and output axis. Torque and speed transmission occur by meshing of gear teeth on both gear wheels. In the meshing of the teeth, sliding between metal surfaces occurs, resulting in frictional losses. Next to losses due to sliding friction, the gearbox also has losses associated to the bearings supporting both gearbox axles.

#### Gear meshing losses

The planetary gearbox is a well researched transmission in literature. As such, different efficiency models for the gear mesh losses are available. Losses in the gears can be split into 'No-load gear losses' and 'Load dependant gear losses'. The no-load gear losses describe losses due to windage, oil churning and oil squeezing during meshing of the gears [119]. The load dependant gear losses describe friction between the gear flanks [94].

[94] describes a load dependent gear loss model based on the geometry related Ohlendorf's power loss factor [120] and a load and speed dependant average coefficient of friction [119]. The load dependant loss model of [94] is described in Appendix A.5.2 and can be approximated by ignoring lubrication effects as:

$$P_{load} = 0.64 \frac{(1 + R_{gear})^{4/5} \pi m}{R_{gear}^{8/3} d_{g,2}^{4/5} h_g^{1/5}} T_{out}^{6/5} \omega_{out}^{4/5} \quad (3.88)$$

The no-load power losses are modelled in [94] by a semi-empirical equation developed by [119]. It is important to note this equation is developed for a vertical gear

orientation where the gears in the mechanical transmission are oriented close to horizontal. Losses related to frictional forces in the lubricant will therefore differ. The no-load loss model of [94] is repeated in Appendix A.5.2 and can be approximated by:

$$P_{no-load} = 230 h_g \left( \omega_{out} \frac{d_{g,2} + 2m}{2} \right)^{3/2} \quad (3.89)$$

Gear meshing power losses are found to be proportional to the torque with  $P_{load} \propto T^{6/5}$ , an experimental lubrication correction factor reduces this relationship to  $P_{load} \propto T^{6/5-0.0651}$  [119]. The relation of gear losses with the speed is different for load dependant and no-load losses. Load dependant losses scale with the speed by  $P_{load} \propto \omega^{4/5}$  [119]. No-load losses scale by  $P_{no-load} \propto \omega^{3/2}$  [119]

#### Bearing losses

Bearing losses are the result of the frictional moment in the bearings. Bearing losses are often empirically modelled. Here a model by [10] is used. As axial and radial loads on the bearing are well constraint in this application only load independent bearing losses are taken into account. As such, no load dependency is expected in the bearing losses. The model of [10] is detailed in appendix A.5 and can be approximated by:

$$P_b = 3.85e - 7\omega_{out}^{5/3} d_{ma}^3 \quad (3.90)$$

Here  $d_{ma}$  is the mean bearing diameter which is assumed to be 15% larger than the screw axle diameter  $d_{ma} = 1.15(2r_s)$ . It is important to note that possible seal friction losses in the gearbox are ignored. This is a valid assumption as both shaft openings are facing upwards and are connected to either the motor housing or the mechanical cylinder.

#### Total losses

The total gearbox power losses are determined by summing all loss components defined above:

$$P_{gear,loss} = P_{load} + P_{no-load} + P_b [W] \quad (3.91)$$

Alternatively the gearbox losses can be expressed as a friction torque  $T_{gear,loss}$  experienced on the motor side as used in (3.2):

$$T_{gear,loss} = \frac{P_{gear,loss}}{\omega_1} \quad (3.92)$$

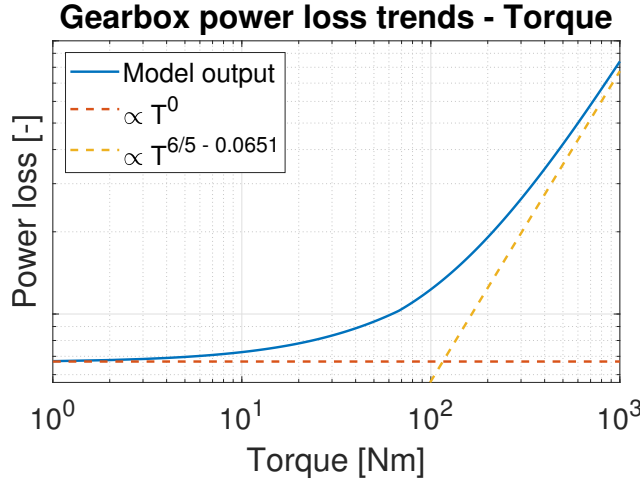


Figure 3.29: Gearbox power loss trend - torque (loglog)

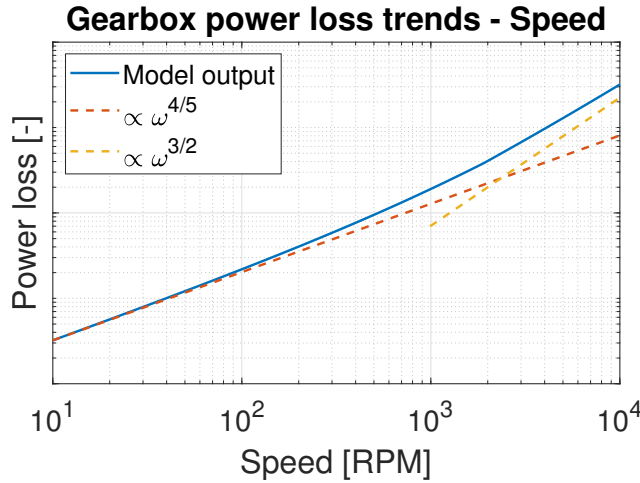


Figure 3.30: Gearbox power loss trend - velocity (loglog)

The total losses in the gearbox are expected to be dominated by the gear meshing losses. At low loads the no-load losses should dominate while at higher loads the load dependant losses take over. Figure 3.29 shows the load dependant gearbox losses and corresponding trend lines.

The loss trends with respect to the speed of the gearbox are expected to scale according to the load dependant losses. At higher speeds the no-load losses should take over. Depending on the loading of the gears, the transition point between both trends changes. Figure 3.30 shows the modelled speed dependant gearbox losses and corresponding trend lines. Note that speeds above 3000[RPM] are not used in practice. Losses in the bearings only become dominant at speeds not reached during normal operation.

## 3.5 Constraints

Actuator constraints limit the possible actuator configurations with physical limits which are not necessarily imposed by the mass and power loss models. The EMA transmission is constrained by two constraint which are detailed below.

**PRS screw speed** The speed of the PRS screw is limited by the eigenfrequency of the PRS. The critical speed of the PRS is determined empirically by [144] as a function of the screw diameter  $d_s$  and the screw length  $l_s$ :

$$n_{crit} = \frac{86.4e3d_s k}{l_s^2} [\text{rpm}] \quad (3.93)$$

Here  $k$  is the support bearing factor which is equal to  $k = 1.55$  for the PRS [50]. An additional safety factor to remain under the critical speed of 80% is enforced in the PRS speed constraint.

**Motor speed** The speed of the motor can not increase indefinitely. Next to the electrical limitations, motor speed is often limited by the balancing of the rotor and the resulting high centrifugal forces on the rotor and bearings. Maximum motor speed of the servo motors used in high power actuators is assumed to be constant at:

$$n_{max} = 3300[\text{rpm}] \quad (3.94)$$

The majority of the servo motors found in the industry are rated around this speed.

## 3.6 Conclusions

This chapter discussed the model development of the components used in the electro mechanical actuator with exception of the rotary motor driving the actuator transmission. Model development is performed to obtain mass and power loss models which can facilitate fast sizing and comparison of different actuator configurations against other actuator technologies. New and adapted existing models to describe the required EMA parameters are discussed. Furthermore several trends are found describing the component masses with respect to the load rating and the power loss properties with respect to the working point of the actuator.

### 3.6.1 Mass and power loss trends

Mass and power loss trends follow from the various models discussed in this chapter for every transmission component. Mass and power loss trends aid in understanding general behaviour of the EMA. The dominating trends found in Sections 3.3 and 3.4 for actuators

capable of delivering 100[kN] and more are repeated below. For the absolute masses and losses the equations described in these sections should be used as these can not simply be described by a single proportionality coefficient.

**Mass scaling** The mechanical cylinder is found to scale approximately linear with the load rating as most parts scale according to yield strength requirements:

$$M_{cylinder} \propto F \quad (3.95)$$

The mass of the gearbox is found to scale with the square root of the torque rating at low torque rating. At higher torque rating the trend changes to a linear relation as the mass of the gear pair starts to dominate the enclosure mass:

$$M_{gearbox} \propto T^{1/2} + T \quad (3.96)$$

As such the mass of the gearbox is expected to dominate at low load ratings while the mass of the mechanical cylinder dominates at high load ratings. The moment of inertia of the mechanical cylinder and the gearbox are found to scale respectively with:

$$I_{cylinder} \propto F^2 \quad (3.97)$$

$$I_{gearbox} \propto T \quad (3.98)$$

Again, the mechanical cylinder moment of inertia is expected to dominate high load rated actuators.

**Power loss behaviour** Loss behaviour is determined based on the working point of the actuator. The power loss scaling law of the mechanical cylinder with respect to the force on the actuator is found to be:

$$P_{cylinder} \propto F^{1/2} \quad (3.99)$$

The gearbox gear mesh losses scale with respect to the torque on the gears. The power loss relation of the gearbox with respect to the torque is given as:

$$P_{gearbox} \propto T^{6/5-0.0651} \quad (3.100)$$

The losses with respect to the velocity are dominated by the friction losses in the cylinder bearings at lower speeds. At high velocities, the rolling friction losses in the RPS mechanism become dominant:

$$P_{cylinder} \propto v + v^{8/5} \quad (3.101)$$

Losses of the gearbox with respect to the velocity include bearing losses, lubrication related losses on the

gear mesh and gear meshing friction. In the normal operation window, losses are expected to scale with:

$$P_{gearbox} \propto \omega^{4/5} \quad (3.102)$$

The cylinder losses are also influenced by the extension of the actuator due to an own weight induced bending moment. The further the actuator is extended the higher the bearing losses in the cylinder become.

### 3.6.2 Model use

The developed mass and power loss models describe the electro mechanical actuator assuming quasi static operation. The actuator model is capable of determining the approximate actuator mass and mean power use for an arbitrary actuator configuration. These configurations are determined by free design variables of the actuator which are the lead of the planetary roller screw  $l_s$ , the radius of the planetary roller screw rollers  $r_r$ , the number of thread starts of the planetary roller screw  $N_s$  and the gear reduction ration  $R_{gear}$ . Further input parameters needed in the model are the maximum load and speed requirements on the actuator, the desired lifetime of the actuator and a representative time series describing the normal operation of the actuator in force, velocity, acceleration and position data.

The main purpose of the developed actuator model is providing a tool which can be used in a preliminary design tool to find the optimal electro mechanical actuator configurations for a specified application. Development of a similar actuator model for the electro hydrostatic actuator as shown in Chapter 4 enables comparison of both actuator technologies for a specific application. As comparison of different high power actuators is the focus of the developed model, scaling and power loss trends are more important than the absolute values of the actuator properties. Masses and losses of smaller peripherals are therefore neglected. For low power actuators actuator properties are expected to deviate significantly due to for example the neglected masses of mounting hardware, cabling and lubrication systems.

### 3.6.3 Future work

In developing and testing the actuator model, some model parts are shown to need further improvement in future model iterations. For the reader interested in possible follow up research, future work suggestions are stated here.

A major simplification in the electro mechanical actuator model is the use of a single stage gearbox design. Use of the single stage gearbox limits the practical achievable gear ratio. As the axial shift of the gearbox is used to bridge the mechanical cylinder screw axle and

the motor axle, the diameters of the gears inside the gearbox are relatively large which affects both the mass and power loss properties of the gearbox. Development of a gearbox model using a variable number of stages would benefit the accuracy of this model part. Development of a variable number of gear stages would also require the gear teeth module to be modelled as a function of the gear sizes.

Another aspect for future research is the validation of the actuator power loss models. Mass models are validated using manufacturer data of existing components. Power loss data is generally not available to validate the power loss models in a similar fashion. The use of existing sub models found in literature and the physics

based explanation of the loss trends provides a reasonable prediction of model accuracy. However, experimental validation of the complete power loss model would greatly benefit the certainty of the loss model results. Especially with respect to the no load power losses in the gearbox, the effect of using a horizontal gearbox orientation instead of a vertical orientation on the modelled losses should be determined.

Finally, future research could focus on the model development of similar electro mechanical actuator implementations within the development framework explained in this chapter. Other actuator implementations can then be compared to the electro mechanical actuator based on the planetary roller screw.

## Chapter 4

# Electro hydrostatic actuator, sizing and loss model development <sup>1</sup>

### Abstract

*Electro mechanical and electro hydrostatic linear actuators are often used for different actuation applications up to 45 kW maximum output power. For applications requiring higher power output, the advantages of one over the other technology become unclear. Existing research clearly shows benefits of both technologies over conventional hydraulic actuation. This chapter describes the mathematical model development of the electro hydrostatic actuator to enable comparison of this actuator technology for different actuator requirements and applications.*

### 4.1 Introduction



Figure 4.1: Ampelmann A-type crew transfer gangway (Ampelmann Operations B.V.)

Linear actuators are devices capable of converting electrical energy to linear mechanical energy. Often a rotary motor is used to drive a rotary to linear hydraulic or mechanical transmission. Current developments in various technical fields concerning actuation are focused in a large part on efficiency. Efficiency is often important with respect to environmental considerations; achieving more with less environmental costly

resources. Increased efficiency however also has a financial consequence by lowering operating costs. Similarly, reducing actuator mass can impact operational costs directly. Especially in mobile actuator applications, system mass footprint becomes an important factor in the total payload capacity of the carrying vessel and therefore on the productivity of the vessel trip.

This chapter focusses on linear actuators of hexapod steward platforms which are capable of power output with an order of magnitude of  $10^5$  Watt. An example of such system is the Ampelmann A-type crew transfer gangway shown in Figure 4.1. These systems use six linear actuators to compensate vessel motion and create a still standing platform from which offshore crew can be transferred between the vessel and a fixed structure.

Linear actuators in high power applications are often dominated by conventional hydraulic technology. Conventional hydraulics are known for their high loss factors with maximum system efficiencies ranging around 35% [100, 180]. In the aviation industry, a development called the more electric aircraft (MEA) found that electro hydrostatic actuators (EHA) and electro mechanical actuators (EMA) both offer significant advantages on both system efficiency [22, 33, 128] and reduced actuator mass [22, 41, 128, 163].

Both EHA and EMA are driven by an electric rotary

<sup>1</sup>This chapter is based on the draft paper provided in Appendix F.2

machine to convert electrical energy in rotary mechanical energy. The EHA uses a hydrostatic transmission with a pump and hydraulic cylinder to obtain a linear force and velocity. Similarly, the EMA uses an (optional) gearbox and a screw mechanism to obtain the same linear force and velocity output. Both technologies have specific properties, however comparison between both options are lacking for high power applications. Figure 4.2 (Appendix G) shows various actuator studies found in literature ranked on their maximum output force and velocity. Existing literature is seen to exist on EMA and EHA for power levels up to approximately 45kW. For higher power levels, existing research is lacking and no clear benefits of one over the other technology are defined. To further the knowledge in the use of EHA and EMA linear actuators for high power applications mathematical models describing scaling and loss behaviour of these actuators are needed.

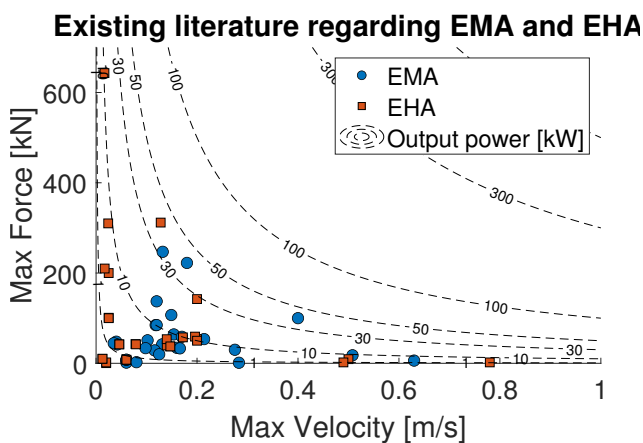


Figure 4.2: Existing actuator studies in literature ranked on maximum output force and velocity (Appendix G).

This chapter describes mathematical model development of sizing and loss models of the EHA. The focus of this chapter is on actuators for use in a sea motion compensating steward platform, however actuator properties and efficiency models are applicable to a multitude of high power actuation applications. The focus on a specific actuator application is necessary as operating regimes determine the power loss behaviour of the actuator. The developed actuator models have free design variables which can later be used in an optimization algorithm to find the best possible actuator for the given requirements.

**Reading guide** To aid the reader in finding the contents of their interest in this chapter, this reading guide provides the general structure of the chapter. First, to better understand the requirements on the model developed in this chapter, Section 4.2 describes the general electro hydrostatic actuator operation and the overall model definitions. Next, Section 4.3 details the

model development of the major actuator components with resulting scaling relations and comparison of modelled mass properties with catalogue data. Section 4.4 describes the development of the actuator power loss models. The main sensitivities of the component power losses are determined with respect to the working point of the actuator. The resulting sizing and power loss trends are summarised in Section 4.6 along with implementation options of this model in further research.

Several dimensionless figures are shown in this chapter on a loglog scale to portray the different mass and power loss sensitivities. Note that all shown logarithmic scales have base 10. The reader interested in the detailed equations behind the relations discussed in this chapter for possible model iterations are referred to appendix B.

## 4.2 System description and method

### 4.2.1 Actuator description

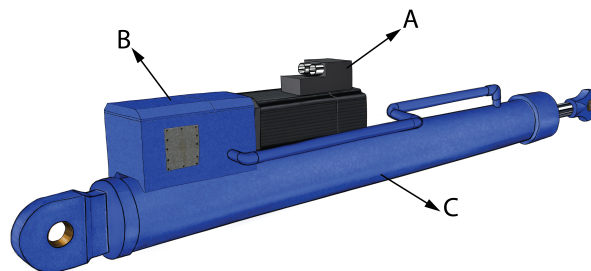


Figure 4.3: General components of the EHA

**EHA parts** To determine actuator properties, the basic parts and operation of the electro hydrostatic linear actuator (EHA) should be discussed first. The EHA has three major components which are visualized in Figure 4.3. The electric servo motor (A) is often implemented by a permanent magnet synchronous machine (PMSM) capable of four quadrant operation. Connected to the motor is a hydrostatic pump with manifold (B), the pump converts the rotary mechanical power of the motor to hydraulic power for use in the end effector (C). The end effector (C) is the actuator part which transfers the actuator power to the load. The end effector is a hydraulic double acting cylinder with symmetric cylinder chambers. The pump is connected through a manifold and pipes to both cylinder chambers. The actuator is capable of four quadrant operation, meaning the actuator can be operated in the motoring regime and can be back driven to operate in generating mode. The simplified operational principle of the EHA in motoring operation is given below.

**EHA operation** The EHA converts electrical energy to linear mechanical energy with an intermediate conversion to hydraulic fluid energy. The general architecture of the EHA transmission is shown in Figure 4.4. The servo motor of the EHA is connected through a controller to an electrical grid. The voltage and the supplied current on the motor poles are converted to a rotational velocity and torque of the outgoing motor axle. The motor axle in its turn is connected to the hydrostatic pump. Turning the hydrostatic pump axle at a certain speed results in a proportional volume flow through the pump. The torque on the pump axle translates to a relative fluid pressure. Hydraulic fluid is effectively pumped from one cylinder chamber to the other cylinder chamber. The resulting pressure differential between both cylinder chambers induces a net force on the piston and connected piston rod. The flow velocity results in a proportional velocity of the piston and piston rod. The hydraulic system also has an additional charge pump connected by one way valves to compensate fluid leakage and keep the low pressure side of the pump at a minimum pressure to avoid cavitation and increase actuator stiffness. The end of the piston rod is connected to the load and transfers the actuator power to the load.

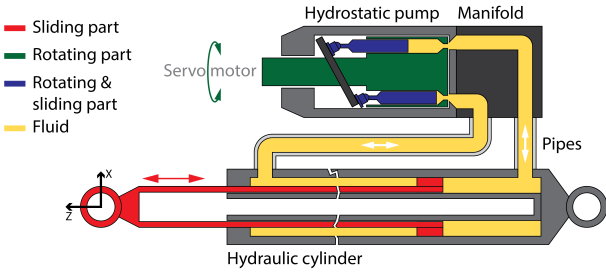


Figure 4.4: Moving parts in the EHA transmission

## 4.2.2 Component choices

The components of the EHA can be implemented in different ways. The servo motor is often implemented by a permanent magnet synchronous machine [44, 96, 174]. This component has well known properties and is not further discussed in this chapter. The hydrostatic pump knows many different variations. Here the pump is implemented with an straight axle piston pump.

These pumps are known for their high volumetric efficiency, especially at higher pressures [92]. No difference is made between the radial and axial straight axle piston pump in this chapter. The hydraulic cylinder of the EHA is largely similar to the hydraulic cylinders used in conventional hydraulic actuators. As the hydraulic system is a closed loop system in the EHA, the use of symmetric cylinder chambers is necessary.

## 4.2.3 Modelling method

To compare actuator technologies, the mass and loss properties of the actuator should be well defined. To understand the models developed in this chapter, first the power relations between various actuator parts should be explained. The basic power relations between the three main actuator parts of the EHA are visualized in Figure 4.5. Actuator parts are sized according to requirements posed on the actuator load side. Similarly, input power is determined as a function of load side power requirements. Therefore information on the load side can be regarded as known and  $F$ ,  $v$  and  $\dot{v}$  can be deemed the input parameters of the actuator model.

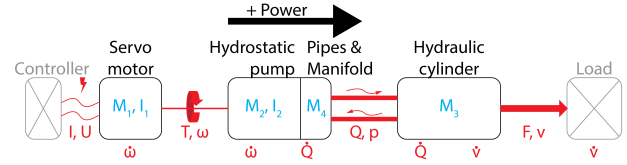


Figure 4.5: Power relations between EHA actuator parts.

## Power relations

For each transmission part shown in Figure 4.5, the power relations can be modelled with equations. In general, power transmission is defined by a transmission ratio linking the ideal velocity terms of the transmission in- and output. The ideal force terms are related by the inverse of this transmission ratio. In practical transmission parts, the power relations are also influenced by inertia effects and power losses. The linearised relations of each EHA component are mathematically described below:

$$\begin{bmatrix} Q \\ p \end{bmatrix} = \begin{bmatrix} C_Q & 0 \\ 0 & C_p \end{bmatrix} \left( \begin{bmatrix} v \\ F \end{bmatrix} + \begin{bmatrix} 0 \\ M_{3,m} \end{bmatrix} \dot{v} + \begin{bmatrix} 0 \\ F_{cyl,loss} \end{bmatrix} \right) + \begin{bmatrix} 0 \\ p_{pipe,loss} \end{bmatrix} \quad (4.1)$$

$$\begin{bmatrix} \omega \\ T \end{bmatrix} = \begin{bmatrix} C_\omega & 0 \\ 0 & C_T \end{bmatrix} \begin{bmatrix} Q \\ p \end{bmatrix} + \begin{bmatrix} 0 \\ I_2 \end{bmatrix} \dot{\omega} + \begin{bmatrix} Q_{pump,loss} \\ T_{pump,loss} \end{bmatrix} \quad (4.2)$$

$$\begin{bmatrix} U \\ I \end{bmatrix} = \begin{bmatrix} C_U & 0 \\ 0 & C_I \end{bmatrix} \left( \begin{bmatrix} \omega \\ T \end{bmatrix} + \begin{bmatrix} 0 \\ I_1 \end{bmatrix} \dot{\omega} + \begin{bmatrix} 0 \\ T_{motor,loss} \end{bmatrix} \right) + \begin{bmatrix} 0 \\ I_{motor,loss} \end{bmatrix} \quad (4.3)$$

**Hydraulic cylinder** The hydraulic cylinder converts fluid power to linear force and motion and is modelled in (4.1). The transmission ratio of the cylinder for the force and velocity related terms is defined by the area of the piston  $A_p$  as:

$$C_Q = A_p [\text{m}^2] \quad (4.4)$$

$$C_p = \frac{1}{A_p} [\text{m}^{-2}] \quad (4.5)$$

Losses in the hydraulic cylinder occur due to friction in the sliding contact interfaces of the piston and piston rod with bearings and seals. Figure 4.6 shows the different sliding interfaces in the hydraulic cylinder. Note that possible sealing surfaces between the piston rod and guide rod are neglected. Mechanical friction in the hydraulic cylinder is captured by the friction force  $F_{cyl,loss}$  in (4.1). While the same sliding contact interfaces also form a barrier to hydraulic fluid leakage, leakage in the cylinder can safely be neglected as explained in Subsection 4.4.2. An additional loss component related to the hydraulic cylinder is found in the pipes connecting the cylinder with the hydrostatic pump. Flow friction in these pipes result in a pressure drop which is described by  $p_{pipe,loss}$  in (4.1). The hydraulic cylinder and pipe loss components are modelled in Subsections 4.4.2 and 4.4.4.

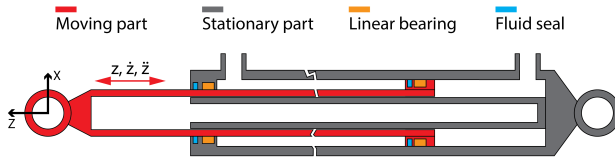


Figure 4.6: Hydraulic cylinder sliding contact interfaces

The moving mass of the hydraulic cylinder  $M_{3,m}$  also influences the power relations due to inertia effects. The moving mass of the cylinder is described in Subsection 4.3.2.

**Hydrostatic piston pump** The hydrostatic piston pump forms the transmission between the mechanical and fluid power domain and is described by (4.2). The transmission ratio for the force and velocity related terms are defined by the volumetric displacement  $V_g$  of the pump:

$$C_\omega = \frac{2\pi}{V_g} [\text{rad m}^{-3}] \quad (4.6)$$

$$C_T = \frac{V_g}{2\pi} [\text{m}^3 \text{rad}^{-1}] \quad (4.7)$$

The hydrostatic piston pump has a lot of moving parts and sliding contact interfaces. Figure 4.21[130] shows the various components interfacing in the pump. As the hydrostatic pump contains hydraulic fluid and is lubricated by this same fluid, two types of losses occur in these interfaces. First, friction occurs on the sliding surfaces resulting in a frictional torque on the pump axis. The friction losses are described by  $T_{pump,loss}$  in (4.2). Next to friction, the moving interfaces in the pump also cause hydraulic fluid leakage. The pump leakage losses are captured by the leakage flow  $Q_{pump,loss}$  in (4.2). Both the pump friction and leakage losses are detailed in Subsection 4.4.3.

As the pump contains a variety of rotating parts, the power relations are affected by inertia effects. The moment of inertia of the hydrostatic piston pump is determined in Subsection 4.3.4.

**Servo motor** The servo motor forms the transmission between the electrical and mechanical power domain. Servo motor transmission ratio's and power losses are well defined in literature [117, 127, 142] and are not discussed further in this chapter. The power relations of the servo motor are discussed in Chapter 5.

**Losses in the EHA** Losses of the actuator parts are dependent on the working point of the actuator part. Hence both load and velocity related parameters influence instantaneous loss magnitude of the actuator part. The working point information on the load side of the actuator is taken as a given in this chapter. As losses influence the working point of the upstream connected actuator part, losses at the end of the power path have a large influence on the total instantaneous power needed by the actuator. The power path is directed from the servo motor to the load in motoring operation and from the load to the servo motor in generating operation (see Figure 4.5). Next to the working point information of the actuator, the loss magnitude in the different actuator parts is also dependant on geometry related parameters which are defined in Section 4.3.

In general, the high power actuator applications under consideration often operate at frequencies below 1[Hz]. As such, the system is dominated by high masses and inertia's while dynamic effects only start occurring at much higher frequencies. In modelling the losses of the system a quasi static approach is therefore a reasonable simplification to reduce model complexity and calculation time. Losses in the EHA are modelled in Section 4.4 and 5.2. Equations defining the parameters needed in Equations 4.1, 4.2 and 4.3 are boxed in for reference.

## Sizing of the EHA

Sizing of an actuator part influences losses of this actuator part but is also influenced by the losses of the connected actuator parts. Losses in the hydraulic cylinder and pump for example should be compensated by the servo motor, hence increasing the load requirements on that actuator component. Sizing of actuator components is mainly determined by the maximum load requirements on the component. For axial loaded parts dimensions are determined by buckling and yield requirements. Rotating parts have an additional requirement on shear strength and hydraulic parts also require pressure resistance. The maximum load on the actuator is assumed a known parameter in this chapter. Together with the transmission ratio's described above and the component efficiency, the maximum loading on each component can be determined and sizing can be performed.

The main objective of sizing the different actuator components is finding the mass of an arbitrary actuator configuration. The mass of the EHA is simplified in this report to consist of the masses of its main components. Mounting hardware and additional peripherals are ignored with this approach. The total EHA mass with respect to the components shown in Figure 4.5 is then determined as:

$$M_{EHA} = M_1 + M_2 + M_3 + M_4 + M_{fluid} \quad (4.8)$$

A detailed breakdown of the component sizing and the different component masses is given in Section 4.3 and 5.1. Equations defining the parameters needed in Equation 4.8 are boxed in for reference.

## 4.3 Sizing model development

Development of a mathematical sizing model of the EHA is necessary for two main reasons; the sizing model determines the total mass of the actuator and defines the geometrical parameters needed in the actuator loss models. Sizing is often based on the maximum power requirements of the actuator. Next to the power requirements, sizing is also influenced by free design variables which can later be used in an optimization step. Sizing of the EHA is split up in sizing of the hydraulic cylinder and sizing of the hydrostatic pump. Sizing model development of these components is discussed separately in Subsections 4.3.2 and 4.3.4. Sizing relations of the permanent magnet synchronous machine are well known in literature, the PMSM is not further discussed in this chapter. The list of symbols used in the component sizing models is found in Subsection 4.3.1. Material properties are shown in Appendix D.

### 4.3.1 List of symbols

Symbol	Explanation	Unit
$\rho_{hf}$	Mass density of hydraulic fluid	[kg m <sup>-3</sup> ]
$\rho_{st}$	Mass density of steel	[kg m <sup>-3</sup> ]
$\rho_{cst}$	Mass density of cast steel	[kg m <sup>-3</sup> ]
$\sigma_t$	Allowable pipe material stress	[N mm <sup>-2</sup> ]
$A_p$	Cross sectional area of the piston	[m <sup>2</sup> ]
$d_{flow}$	Hydraulic pipe flow diameter	[m]
$I_{pump}$	Moment of inertia of the pump	[kg m <sup>2</sup> ]
$L_{ch}$	Length of the cylinder housing	[m]
$L_p$	Length of the piston	[m]
$L_{pipe}$	Total length of the hydraulic pipes	[m]
$L_{r,a}$	Length of the piston rod	[m]
$L_s$	Stroke length of the actuator	[m]
$m_{ch}$	Mass of the cylinder housing	[kg]
$m_{cyl}$	Mass of the hydraulic cylinder	[kg]
$m_{fluid}$	Mass of the hydraulic fluid	[kg]
$m_{manifold}$	Mass of the hydraulic manifold	[kg]
$m_p$	Mass of the piston	[kg]
$m_{pipe}$	Mass of the hydraulic pipes	[kg]
$m_{pump}$	Mass of the hydrostatic pump	[kg]
$m_r$	Mass of the piston rod	[kg]
$m_{rg}$	Mass of the rod guide	[kg]
$p_{low}$	Minimum allowed pressure in the system	[Pa]
$p_{max}$	Maximum system pressure	[Pa]

$Q_{max}$	Maximum volume flow	$[\text{m}^3 \text{s}^{-1}]$
$r_{ch,i}$	Inside radius of the hydraulic cylinder	$[\text{m}]$
$r_{ch,o}$	Outside radius of the hydraulic cylinder	$[\text{m}]$
$r_p$	Radius of the piston	$[\text{m}]$
$r_{r,i}$	Inside radius of the piston rod	$[\text{m}]$
$r_{r,o}$	Outside radius of the piston rod	$[\text{m}]$
$t_{ch}$	Hydraulic cylinder material thickness	$[\text{m}]$
$t_p$	Pressure thickness of the hydraulic pipes	$[\text{m}]$
$t_r$	Piston rod material thickness	$[\text{m}]$
$t_{r,g}$	Rod guide material thickness	$[\text{m}]$
$t_{rod,ratio}$	Thickness ratio of the piston rod	$[-]$
$V_{fluid}$	Volume of the hydraulic fluid	$[\text{m}^3]$
$V_g$	Volumetric pump displacement	$[\text{cm}^3/\text{rev}]$
$v_{flow}$	Maximum design flow velocity	$[\text{m s}^{-1}]$
$v_{max}$	Maximum design actuator velocity	$[\text{m s}^{-1}]$

### 4.3.2 Sizing of the hydraulic cylinder

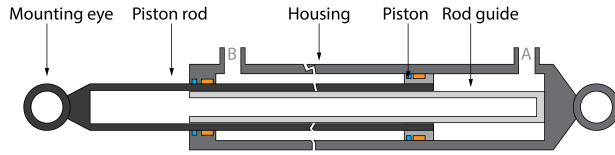


Figure 4.7: Hydraulic cylinder architecture.

The hydraulic cylinder is the end effector of the EHA. The hydraulic cylinder has a smooth piston rod connected to the piston inside the cylinder housing. The piston rod is hollow to accommodate the guide rod. The guide rod ensures the piston area of the A and B chamber have approximately the same area. The simplified geometry of the hydraulic cylinder is shown in Figure 4.7. As stated above, sizing is mainly determined by the load requirements on the actuator. The cylinder rod is mainly loaded by axial forces when a swivelled connection to a frame and the load are assumed. The cylinder housing is loaded by the fluid pressure inside. However, in case the cylinder rod gets stuck in the guide bearings, the housing is also loaded by axial forces. Maximum load requirements on the hydraulic cylinder are defined by the maximum design force of the actuator in the fully extended position. Geometrical sizing according to these load requirements to determine the masses of the hydraulic cylinder components is discussed below.

#### Piston rod sizing

First, the piston rod or smooth rod shown in Figure 4.8 is dimensioned. The piston rod is assumed to be hollow for weight saving purpose and to accommodate the guide rod. The guide rod is necessary to obtain a symmetric piston area in both cylinder chambers.

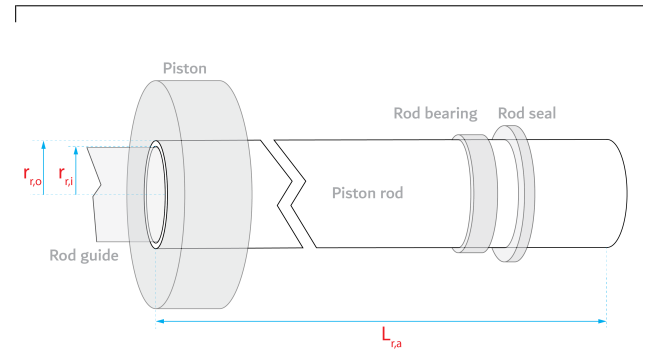


Figure 4.8: Simplified piston rod geometry with main sizing dimensions.

**Load sizing** The rod radius is dimensioned based on its axial loading. The axial loading poses requirements on the yield strength and critical buckling load of the piston rod. Additionally the rod is also loaded by the pressure in the cylinder. To facilitate load-sizing, a fixed thickness ratio of the hollow piston rod is assumed:

$$t_{rod,ratio} = \frac{r_{r,o}}{r_{r,i}} = 1.2 \quad (4.9)$$

The outside radius can first be determined according to the buckling and yield requirements. The minimal piston rod radius calculations according to these criteria are shown in Appendix B.1 and can be approximated by:

$$r_{r,o-buckling} = 1.52e-3F^{1/4}L_s^{1/2} \quad (4.10)$$

$$r_{r,o-yield} = 1.2e-4F^{1/2} \quad (4.11)$$

The outside and inside radius of the piston rod are then determined according to:

$$r_{r,o} = \max([r_{r,o-buckling}, r_{r,o-yield}]) \quad [\text{m}] \quad (4.12)$$

$$r_{r,i} = \frac{r_{r,o}}{t_{ratio}} [\text{m}] \quad (4.13)$$

To ensure the rod can withstand the hydraulic fluid pressure, the required material thickness to withstand the pressure is defined according to DNVGL class guidelines [46] as:

$$t_{pressure} = \frac{p_{max} r_{r,o-mm}}{10\sigma_t - 0.5p_{max}} \quad (4.14)$$

With  $p_{max}$  the maximum design pressure in [bar] and  $r_{r,o-mm}$  the outside radius of (4.12) in [mm]. This equation is further detailed in Appendix B.1. The inside radius of the rod is adapted if the pressure thickness is critical.

**Mass properties** The mass of the rod is determined by the radii and the length of the rod. The length of the rod is dependant on the stroke length of the actuator and some sizing parameters of the cylinder housing (see subsection 4.3.2):

$$L_{r,a} = L_s + L_p + d_{flow} + 2t_{ch} [\text{m}] \quad (4.15)$$

The mass of the rod is subsequently given by:

$$m_r = \pi (r_{r,o}^2 - r_{r,i}^2) L_{r,a} \rho_{st} [\text{kg}] \quad (4.16)$$

As only the radius of the piston rod sizes with the load, assuming yield is the critical requirement, the piston rod mass is expected to scale according to:

$$m_r \propto F \quad (4.17)$$

### Rod guide sizing

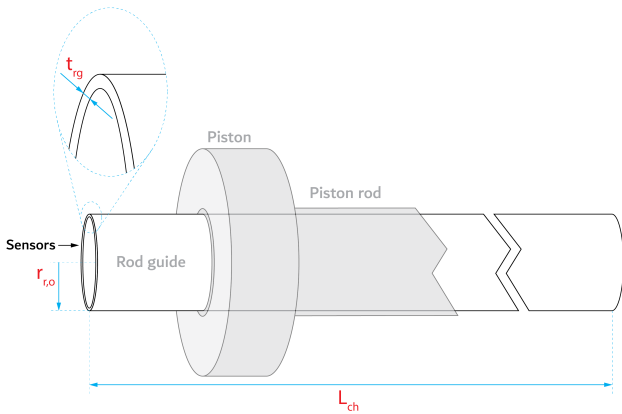


Figure 4.9: Simplified rod guide geometry with main sizing dimensions.

The hollow piston rod has a guide on the opposite side of the cylinder called the rod guide. Figure 4.9 shows the rod guide and its main dimensions. This guide is there to ensure and approximately symmetric piston area and to house the position sensors of the cylinder. The rod guide is a stationary hollow tube with the outside radius equal to the inside radius of the piston rod. The thickness of the rod guide is assumed to be half the thickness of the piston rod as this is a non-load bearing component  $t_{rg} = \frac{t_r}{2}$ . The mass of the rod guide is therefore given by:

$$m_{rg} = \pi (r_{r,i}^2 - (r_{r,i} - t_{rg})^2) L_{ch} \rho_{st} [\text{kg}] \quad (4.18)$$

As the radius of the rod guide is proportional to the radius of the piston rod, the same mass trend is expected for this component.

### Piston sizing

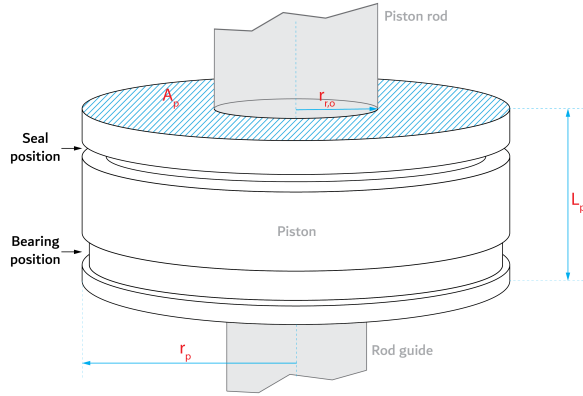


Figure 4.10: Hydraulic cylinder simplified piston with main sizing dimensions.

The piston of the hydraulic cylinder is the actual interface of the hydraulic to mechanical energy transmission. The piston is a cast steel part and is modelled as a hollow thick walled cylinder as seen in Figure 4.10. The cut-outs for the seals and bearing material are neglected in the mass calculations. The main sizing parameter of the piston is the free design piston area  $A_p$  parameter. The piston area determines the transmission ratio of the hydraulic cylinder. The required outside piston radius is dependent on the outside radius of the piston rod. The piston radius is determined according to:

$$r_p = \sqrt{\frac{A_p + r_{r,o}^2 \pi}{\pi}} [\text{m}] \quad (4.19)$$

The length of the piston should be capable of withstanding the pressure differential between both cylinder chambers. However, the piston side wall should also be wide enough to accommodate a linear bearing. The length of the piston is assumed to be equal to the radius of the piston with  $L_p = r_p$ . The simplified mass of the piston can then be determined from:

$$m_p = \pi (r_p^2 - r_{r,o}^2) L_p \rho_{cst} [\text{kg}] \quad (4.20)$$

### Cylinder housing sizing

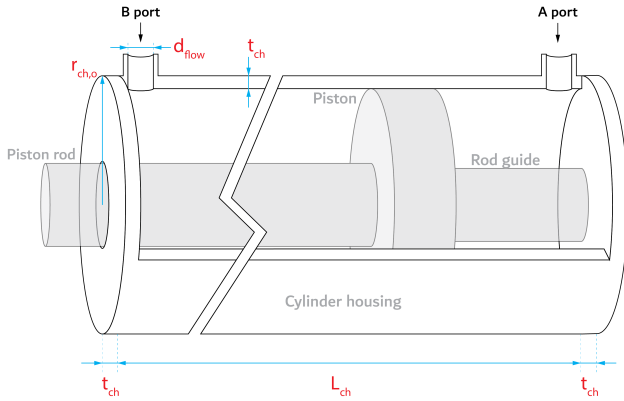


Figure 4.11: Simplified housing geometry with main sizing dimensions.

The final component of the hydraulic cylinder is the cylinder housing. The cylinder housing forms the effective outside walls of the cylinder chambers and provides a bearing and sealing surface for the piston and piston rod bearings and seal. The cylinder housing also provides an interface with the hydraulic tubing to and from the hydrostatic pump. Figure 4.11 shows the main geometry of the hydraulic cylinder housing and the main sizing parameters.

**Main dimensions** The cylinder housing and the piston form both cylinder chambers of the hydraulic cylinder. As the piston should slide on the inside walls of the housing, the inside radius of the housing can be simplified to equal to piston radius:

$$r_{ch,i} = r_p \quad (4.21)$$

The internal housing length of the cylinder is also sized around the other cylinder components. The housing should be able to accommodate the free length of the rod, the length of the piston and the diameters of both the A and B port as can be seen in Figure 4.11. The free length of the rod is equal to the maximal stroke length of the actuator. The total internal length is mathematically given as:

$$L_{ch,i} = L_s + L_p + 2d_{flow} [\text{m}] \quad (4.22)$$

The hydraulic fluid diameter of the A and B port is determined separately below. The last free geometric parameter is the outside radius of the housing. The outside radius is sized to withstand both axial loading and loading due to the fluid pressure. Both requirements are defined in the DNVGL class guidelines for hydraulic cylinders [46]. With the previously defined parameters, the equations found in the DNVGL document can be rewritten to obtain the required outside housing radius. The derived equations can be found in Appendix B.1 and are approximated as:

$$r_{ch,o-yield} = \left( 4.4e-9F + \frac{r_{ch,i}}{\pi} \right)^{1/2} \quad (4.23)$$

$$r_{ch,o-buckling} = \left( F + \frac{2.47e12r_{ch,i}^4}{L_s^2} \right)^{1/4} L_s^{1/2} \quad (4.24)$$

$$r_{ch,o-pressure} = r_{ch,i} + 6.9e-5 \frac{p_{max} r_{ch,i}}{4355 - 5e-6 p_{max}} \quad (4.25)$$

Here  $p_{max}$  is the absolute pressure in the cylinder given by:

$$p_{max} = \frac{F}{A_p} + p_{low} \quad (4.26)$$

The required minimal outside housing radius is then determined from:

$$r_{ch,o} = \max([r_{ch,o-yield}, r_{ch,o-buckling}, r_{ch,o-pressure}]) [\text{m}] \quad (4.27)$$

**Hydraulic flow diameter** To properly size the length of the hydraulic cylinder housing, the flow diameters of the A and B port should be known. The required diameters of the hydraulic ports are determined to limit the maximum fluid velocity and the resulting

fluid friction losses. Hydraulic cylinder manufacturers recommend a maximum flow velocity for high pressure lines of  $v_{flow} = 25 \text{ft/s} \approx 7.5 \text{m/s}^{-1}$  [155]. The required flow diameter to achieve this velocity limit is given as:

$$d_{flow} = \sqrt{\frac{4}{\pi}} \sqrt{\frac{Q_{max}}{v_{flow}}} [\text{m}] \quad (4.28)$$

With  $Q_{max}$  the maximum required fluid flow rate in  $[\text{m}^3 \text{s}^{-1}]$ .

**Mass properties** The mass of the cylinder housing can be determined by simplifying the housing geometry to three basic parts. Figure 4.12 shows these basic parts. The volumes of each part are calculated according to:

$$V_{ch,1} = \pi (r_{ch,o}^2 - r_{r,o}^2) (2t_{ch}) [\text{m}^3] \quad (4.29)$$

$$V_{ch,2} = \pi (r_{ch,o}^2 - r_{ch,i}^2) L_{ch} [\text{m}^3] \quad (4.30)$$

$$V_{ch,3} = \pi r_{ch,o}^2 (2t_{ch}) [\text{m}^3] \quad (4.31)$$

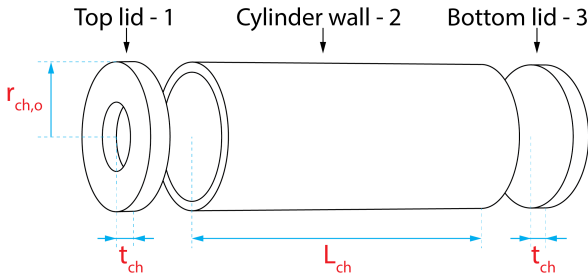


Figure 4.12: Simplified cylinder housing parts

Here the thickness of the top and bottom part is defined as:

$$t_{ch} = r_{ch,o} - r_{ch,i} [\text{m}] \quad (4.32)$$

The total mass of the simplified housing is proportional to the sum of these individual volumes:

$$m_{ch} = (V_{ch,1} + V_{ch,2} + V_{ch,3}) \rho_{st} [\text{kg}] \quad (4.33)$$

### Hydraulic cylinder mass

The hydraulic cylinder mass  $M_3$  as used in (4.8) is determined by summing the different cylinder component masses determined before as:

$$M_3 = M_{cyl} = m_r + m_{rg} + m_p + m_{ch} \quad (4.34)$$

Similarly, the moving mass of the hydraulic cylinder  $M_{3,m}$  as used in (4.1) is defined as:

$$M_{3,m} = m_r + m_p \quad (4.35)$$

The cylinder mass is dominated by the mass of the cylinder housing and the piston rod. As some dimensions are not directly related to the load but to the dimensions of other components, the total cylinder mass is not expected to follow the individual trends of the cylinder components. The mass trends of the complete cylinder are plotted in Figure 4.13.

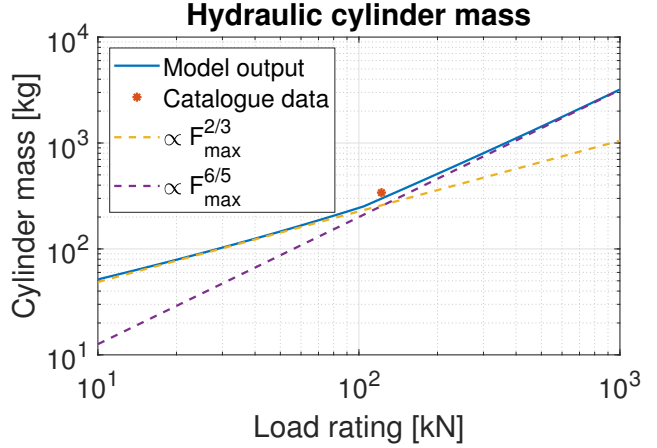


Figure 4.13: Hydraulic cylinder mass trends (loglog)

At lower load ratings the cylinder mass is seen to scale approximately with:

$$M_{cyl} \propto F_{max}^{2/3} \quad (4.36)$$

At higher load ratings the cylinder mass is approximately described by:

$$M_{cyl} \propto F_{max}^{6/5} \quad (4.37)$$

Very few catalogue data on symmetric hydraulic cylinder mass is available. A single data point is used to check model results. Trend line validation with more data points should be performed in further research.

### 4.3.3 Piping and manifolds

The manifold and piping between the hydrostatic pump and the hydraulic cylinder transport hydraulic fluid through the EHA system. The manifold is a combination of inlet and outlet connections and valves necessary in the hydraulic circuit. Both pump sides are connected to the manifold. From the manifold two pipes extend to both the hydraulic cylinder ports. The manifold and pipes enable the pump to pump hydraulic fluid from one to the other cylinder chamber.

## Pipe sizing

The hydraulic pipes in the EHA should be sized to minimize fluid friction losses. The sizing of the hydraulic flow diameter is already discussed in the sizing of the hydraulic cylinder housing. To determine the mass of the pipes, the length and outside radius should be determined.

The length of the piping is proportional to the length of the actuator. The distance between the hydrostatic pump and the A port is negligible while the distance between the pump and the B port is at least as long as the total actuator stroke. The total length of the piping is approximated as:

$$L_{pipe} = 2 \cdot 0.3 + L_s [\text{m}] \quad (4.38)$$

Two additional pipes of in total 60[cm] are added to the stroke length of the actuator. These pipes represent the additional pipe lengths needed to connect the main pipe to the cylinder and pump. The required pipe thickness can be calculated according to the pressure thickness requirements found in the DNVGL standard [46]:

$$t_p = \frac{p_{max} r_{flow}}{10\sigma_t - 0.5p_{max}} [\text{m}] \quad (4.39)$$

The mass of the pipes is then given as:

$$m_{pipe} = L_{pipe} \pi \left( (r_{flow} + t_p)^2 - (r_{flow})^2 \right) \rho_{st} [\text{kg}] \quad (4.40)$$

The relative mass of the pipes is expected to be very small with respect to the total EHA system mass.

## Manifold sizing

The EHA manifold houses the connections to and from the pump and hydraulic cylinder. Inside different valves are used to connect an external charge pump needed to compensate leakages and keep the low pressure side on a fixed pressure. Hydraulic manifolds are custom made components and not much mass and sizing data is available in literature.

The mass of the manifold is difficult to calculate analytically due to the many variations in its configuration. The mass of the manifold will be approximated by fitting a curve through two known manifold masses based on their matched cylinder properties.

It is reasonable to assume the manifold mass is related to the maximum fluid flow velocity. As maximum pressure in the EHA system is almost always a fixed value between 280 and 330 bar, a possible dependency on the pressure can be neglected. The pipes and valves in the manifold should have a cross sectional area which

scales linearly with the maximum fluid volume flow to keep the fluid velocity constant. Therefore the characteristic length value should size with:

$$l^* \propto \sqrt{Q_{max}} \quad (4.41)$$

Here  $Q_{max}$  is given by the product of the cylinder piston area and the maximum occurring velocity:  $Q_{max} = A_p v_{max}$ . Assuming the manifold scales in three dimensions proportional to the characteristic length, the mass relation is found as:

$$m_{manifold} \propto Q_{max}^{3/2} \quad (4.42)$$

Fitting above relation through two known manifold masses and allowing a constant offset parameter, the following equation is obtained:

$$m_{manifold} = 422 + 1.53e5 (A_p v_{max})^{3/2} [\text{kg}] \quad (4.43)$$

The scaling law fit is shown in Figure 4.14. Further validation of this scaling law with more data should be performed in later research.

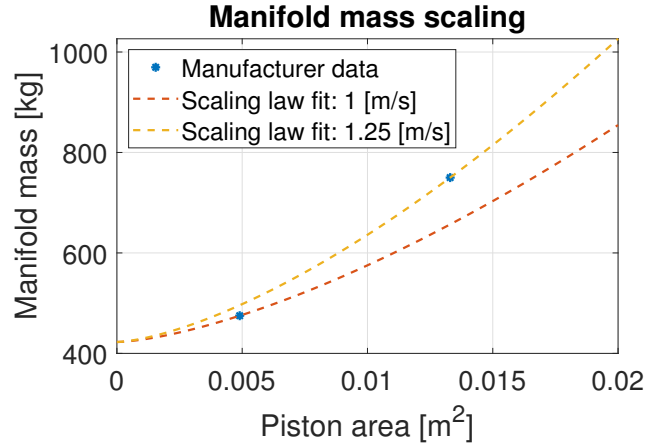


Figure 4.14: Manifold mass scaling with the hydraulic cylinder volume.

## Pipe and manifold mass

The total pipe and manifold mass  $M_4$  as used in (4.8) is defined as the sum of both component masses:

$$M_4 = m_{pipe} + m_{manifold} \quad (4.44)$$

### 4.3.4 Sizing of the hydrostatic pump

The hydrostatic pump pumps hydraulic fluid between both cylinder chambers. The pump effectively transforms rotary mechanical energy from the motor to hydraulic energy. The main sizing parameter of the pump

is the volumetric displacement  $V_g$ . The volumetric displacement is the geometric internal volume of the pump chambers and represents the ideal volume of fluid per revolution which the pump can deliver. The proposed pump is the fixed pump variable motor (FPVM) piston pump which uses radial or axial pistons on a fixed angle swash plate to pump fluid. The volume flow of the pump is determined by the speed of the pump axle. The piston pump is a very complex part, properly modelling this pump requires a lot of specific knowledge and is outside the scope of this research. As catalogue data of these type of pumps exist, a simple physics based scaling law can be derived to fit to existing data.

**Mass scaling law** The main sizing parameter of the hydrostatic piston pump is the volumetric displacement as stated above. Assuming a constant global pump density, the mass of the pump is expected to scale linearly with the pump volume. Another scaling factor could be the pressure inside the pump, however, as almost all piston pumps are rated to a pressure of 280[bar], the pressure dependency can be neglected. The pump mass relation could thus be given by:

$$m_{pump} \propto V_g \quad (4.45)$$

Above stated scaling law can be fitted to manufacturer data of radial piston pumps. Figure 4.15 shows the pump masses of various existing radial piston pumps and the fitted scaling law. The mass of the pump  $M_2$  as used in (4.8) is then defined by the data fit as:

$$M_2 = 0.73V_g[\text{kg}] \quad (4.46)$$

It is important to note that the volumetric displacement  $V_g$  is given in  $[\text{cm}^3/\text{rev}]$ .

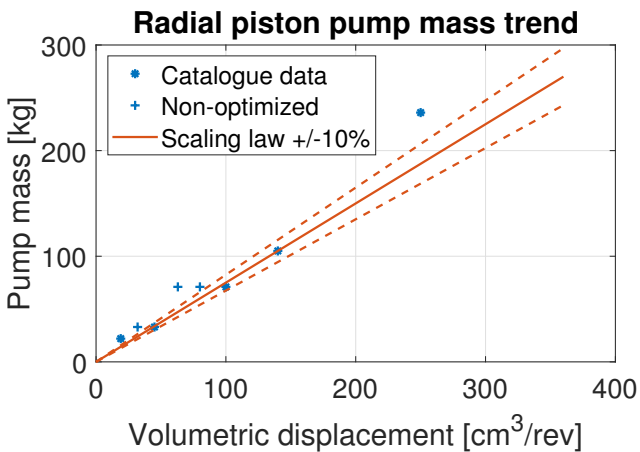


Figure 4.15: Radial pump mass, manufacturer data and scaling law fit.

The catalogue data in Figure 4.15 is divided in two categories. The main pump dimensions are labelled

as catalogue data. The manufacturer also offers pump units with decreased volumetric displacement in pump casings of higher displacement units. These pumps are labelled 'non-optimized' as their mass is proportional to the maximum volumetric displacement possible with its case size. The mass scaling law (4.45) is fitted to the middle three main pump sizes. Those three sizes align very well with the proposed scaling law. Especially the largest available pump size is seen to be much heavier compared to the scaling law with the model underestimating the mass by 20%. A few explanations are possible. Either this pump size is not optimized for mass, the same casing would be able to provide a larger volumetric displacement. Alternatively the effective density of the pump has also a displacement dependency. Finally, the middle three pump sizes could be under designed, giving unrealistically low masses effectively pulling down the fitted scaling law from the physical expected result. More pump data is needed to check this. The first explanation is deemed the most reasonable and the scaling law fit seen in (4.46) is used to model pump mass. The smallest pump size mass is also underestimated by 34.5%, here it is reasonable to assume non modelled fabrication requirements become more important in small pumps.

**Moment of inertia scaling law** The radial piston pump has a substantial part of its mass rotating with the motor speed of the actuator. As such, the moment of inertia of the pump is an important parameter in simulating the actuator. To obtain a scaling law for the pump inertia, we can build from the mass scaling law (4.45). The moment of inertia is related to the mass by:

$$I_{pump} \propto M_{pump}l^2 \quad (4.47)$$

Here  $l$  is a characteristic length factor. Rewriting the characteristic length factor in terms of the characteristic volume, a moment of inertia scaling law can be given as:

$$I_{pump} \propto V_g^{5/3} \quad (4.48)$$

The moment of inertia scaling law can be fitted to manufacturer data of existing radial piston pumps. Figure 4.16 shows the moment of inertia of various radial piston pumps and the fitted scaling law. The moment of inertia of the pump  $I_2$  as used in (4.8) is then given by the data fit as:

$$I_2 = 0.1V_g^{5/3}[\text{kg m}^2] \quad (4.49)$$

Again the volumetric displacement  $V_g$  is given in  $[\text{cm}^3/\text{rev}]$ .

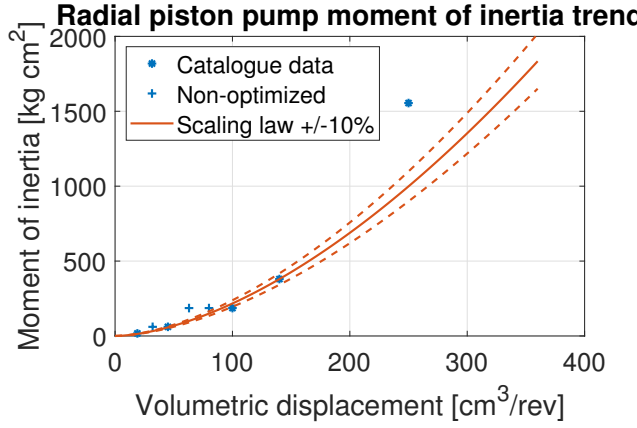


Figure 4.16: Radial pump moment of inertia, manufacturer data and scaling law fit.

Figure 4.16 maintains the same categorization of catalogue data as explained with Figure 4.15. The moment of inertia scaling law is again fitted to the middle three main pump dimensions. The lower main pump sizes all follow the fitted scaling law within approximately 10%. The highest available displacement model is again seen to deviate from the scaling law. The larger deviation is due to the higher order relation with the volumetric displacement of the moment of inertia compared to the mass relation. More pump data is necessary to explain the reason of this deviation at higher volumetric displacements.

#### 4.3.5 Hydraulic fluid

Next to the hardware in the hydrostatic transmission, also the hydraulic fluid has a mass. The mass of the hydraulic fluid can be calculated by calculating the internal volume of all hydrostatic transmission components. Additional hydraulic fluid to compensate for fluid leakage is ignored in this calculation.

First, the hydraulic fluid volume of the hydraulic cylinder is calculated. The hydraulic fluid volume of the cylinder is approximately equal to the internal volume of the cylinder housing minus the piston, piston and piston rod volume contained by the cylinder housing. The fluid volume in the cylinder is given by:

$$V_{fluid,cylinder} = A_p (L_{ch} - L_p) [\text{m}^3] \quad (4.50)$$

Next, the fluid volume in the pipes is determined. The internal volume of the simplified pipes is given as:

$$V_{fluid,pipes} = \pi L_{pipe} \left( \frac{d_{flow}}{2} \right)^2 [\text{m}^3] \quad (4.51)$$

Finally, the volume in the hydrostatic pump can be determined. The fluid volume inside the hydrostatic pump can be simplified to equal the volumet-

ric displacement volume of the pump. Therefore  $V_{fluid,pump} = V_g$ .

The resulting mass of the hydraulic fluid in the system  $M_{fluid}$  as used in (4.8) is then defined as:

$$M_{fluid} = (V_{fluid,cylinder} + V_{fluid,pipes} + V_{fluid,pump}) \rho_{hf} [\text{kg}] \quad (4.52)$$

Here  $\rho_{hf}$  is the density of hydraulic fluid.

## 4.4 Loss model development

Development of a mathematical loss model of the EHA is needed to determine the energy requirements for a given actuator on a specific task. The EHA is a linear actuator which converts electrical power in linear mechanical power with an intermediate conversion to hydraulic fluid power. Conversely, the linear actuator can also generate electrical energy due to a linear mechanical force and velocity input. The EHA is effectively capable of four quadrant operation which means the actuator can be operated in forward and reverse motoring mode and in forward and reverse generating mode. The basics of the motoring regime of an actuator are widely known. However, the generating regime of an actuator is a less common concept. In rotary actuators (eg. electric motors), the capability of the motor to be used as a generator is known. Just as for the rotary actuators, linear actuators can be back driven to operate as a generator. By enforcing a force and velocity on the conventional output side of the EHA, the hydraulic cylinder converts this to a fluid pressure and volume flow. In the pump the pressure is converted to a torque and the volume flow is transferred to a rotary velocity of the pump axis. The rotary motor then delivers electric energy back to the grid.

**Back drive ability** Back driving is an important concept in mobile linear actuator applications. In applications where the load can drive the actuator, back driving can regenerate the energy of the load to electrical energy which can be stored. When considering a full cycle of a back drivable actuator, power in the system is affected twice by the instantaneous efficiency of the actuator. The instantaneous efficiency of the actuator is determined by power losses in the power path of the actuator due to for example friction. When back driving the actuator, a situation can occur in which the power losses in the system are higher than the instantaneous power delivered to the actuator by the load. In this case the actuator is self locking, and positive power is needed from the actuator to facilitate movement of the load. Actuators which are always self locking are non back drivable actuators and can never work in generating mode. Self locking actuators therefore pose higher requirements on the electrical grid connection.

In applications where grid power is limited, back drive ability is very important.

**Model approach** Modelling the power loss behaviour with equations provides a way to compare the EHA to different actuator solutions for a specific application. Using a loss model to determine the losses for different discretised working points of the actuator in a task enables the calculation of the required energy to perform this task. In the subsections below, loss

factors of each EHA component are determined and modelled based on the working point and component sizing variables. Different loss models for EHA components exist in literature, however these models are often not ready for use in a simulation based application. The used mathematical models and changes to these models are discussed and the overall loss sensitivities with respect to the working point are shown. The list of symbols used in the component loss models is found in Subsection 4.4.1. Used constants are defined in Appendix D.

#### 4.4.1 List of symbols

Symbol	Explanation	Unit
$\epsilon$	Maximum radial deformation of the seal	[%]
$\mu_{hf}$	Kinematic viscosity of hydraulic fluid	[m <sup>2</sup> s <sup>-1</sup> ]
$\omega$	Pump rotational speed	[rad s <sup>-1</sup> ]
$\rho_{hf}$	Mass density of hydraulic fluid	[kg m <sup>-3</sup> ]
$E_{seal}$	Young modulus of the pressure seal material	[Pa]
$g$	Gravitational acceleration constant	[m s <sup>-2</sup> ]
$L_{pipe}$	Total length of the hydraulic pipes	[m]
$P_{cyl}$	Power loss in the cylinder	[W]
$P_{pipe}$	Power loss in the hydraulic pipes	[W]
$P_{pump}$	Power loss in the pump	[W]
$P_{visc}$	Bearing viscous power loss	[W]
$P_{volumetric}$	Volumetric power loss in the pump	[W]
$p_{\delta}$	System pressure	[Pa]
$\delta p_p$	Pipe pressure drop	[Pa]
$Q_c$	Compressibility leakage flow in the pump	[m <sup>3</sup> s <sup>-1</sup> ]
$Q_t$	Laminar flow leakage	[m <sup>3</sup> s <sup>-1</sup> ]
$Q_{leakage}$	Leakage flow of the pump	[m <sup>3</sup> s <sup>-1</sup> ]
$Q_t$	Turbulent flow leakage	[m <sup>3</sup> s <sup>-1</sup> ]
$r_{seal}$	Radius of the pressure seal interface	[m]
$s_p$	contact width of the seal	[m]
$T_c$	Coulomb friction torque in the pump	[N m]
$T_{ch}$	Churning friction torque in the pump	[N m]
$T_{friction}$	Total frictional torque in the pump	[N m]
$T_{turb}$	Flow friction torque in the pump	[N m]
$T_v$	Viscous friction torque in the pump	[N m]
$t_{seal}$	Thickness of the pressure seal material	[m]
$V_{fluid,pipe}$	Fluid volume in the hydraulic pipes	[m <sup>3</sup> ]
$V_g$	Volumetric pump displacement	[cm <sup>3</sup> /rev]

#### 4.4.2 Hydraulic cylinder losses

The hydraulic cylinder is the end effector of the EHA. From the simplified cylinder architecture in Figure 4.7, several sliding interfaces between the moving cylinder parts can be identified. These are the linear bearing and pressure seal on the piston rod and the linear bearing on the piston. Other interfaces exist between the guide rod and the piston rod, but losses in these inter-

faces are assumed to be negligible.

The bearing and seal interfaces have two types of losses associated with them. First, friction losses occur due to the contact of two moving objects. Secondly, as all interfaces are contacting hydraulic fluid at one or two sides, hydraulic fluid leakage across these interfaces would result in volumetric losses. From practical experience in industry, detectable leakage in a hydraulic

cylinder indicates a broken cylinder and results in the replacement of this cylinder. Leakage losses in the hydraulic cylinder can therefore be neglected.

Frictional losses in the hydraulic cylinder can be split in frictional losses of the linear bearings and frictional losses of the pressure seal. Both loss factors are discussed and modelled separately below.

### Bearing frictional losses

Bearing friction in the hydraulic cylinder occurs in two locations: on the piston rod bearing and on the piston bearing. Both bearings are shown in orange in Figure 4.17. In reality multiple bearing rings of different stiffness are used in these types of hydraulic cylinder, here only the stiffest bearing ring is assumed to affect frictional forces.

Ideally, bearing friction is only dependant on the preload on the bearings from assembly. However, due to the slanted orientation of the cylinder, normal force on the bearings is affected by the actuator mass induced bending moment in the cylinder. As the moment arm between both bearings is dependant on the position of the actuator, bearing friction is highly dependent on the position or extension of the actuator. The bearing friction force is independent of the loading of the actuator as the bearing normal forces are oriented perpendicular to the load direction.

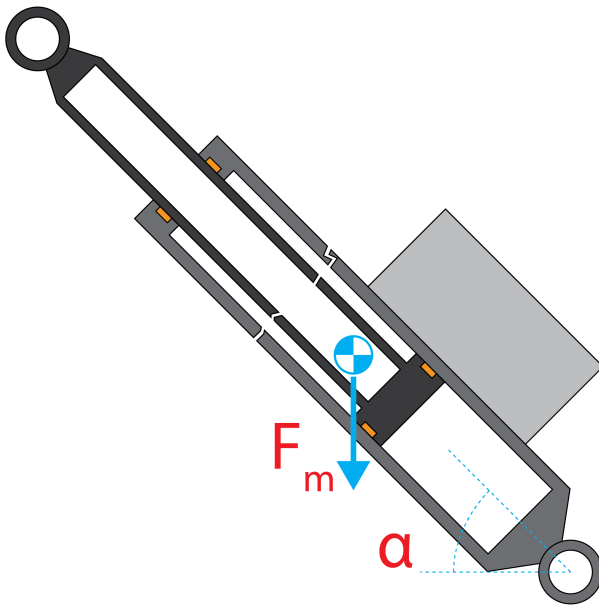


Figure 4.17: Hydraulic cylinder in slanted orientation

**Friction model** The bearings of the hydraulic cylinder are lubricated by the hydraulic fluid in the cylinder chambers. As such the friction forces between the bearings and the bearing surfaces follow the properties of fluid lubricated contacts. The Stribeck curve is ideally suited to model this type of friction forces [65]. [18] de-

scribes a Stribeck function specifically for determining losses in sliding contacts.

The use of this model in combination with the position dependant normal force on the bearings to obtain the bearing friction force  $F_{bearing,loss}$  is discussed in detail in Chapter 3.4.1.

The bearing losses are expected to increase with the extension of the cylinder rod as this decreases the moment arm between both bearing locations. As the moment arm is determined by a summation, the trend relation to the actuator extension is not exponential. The losses are expected to scale linearly with the velocity in the normal speed range. At higher velocities the viscous forces are expected to dominate with  $P_{visc} \propto v^2$  and at lower velocities the Stribeck effect shows a small peak corresponding to the stiction force of the bearings.

Figure 4.18 and 4.19 show the frictional forces of the cylinder bearings with respect to the actuator position and velocity respectively.

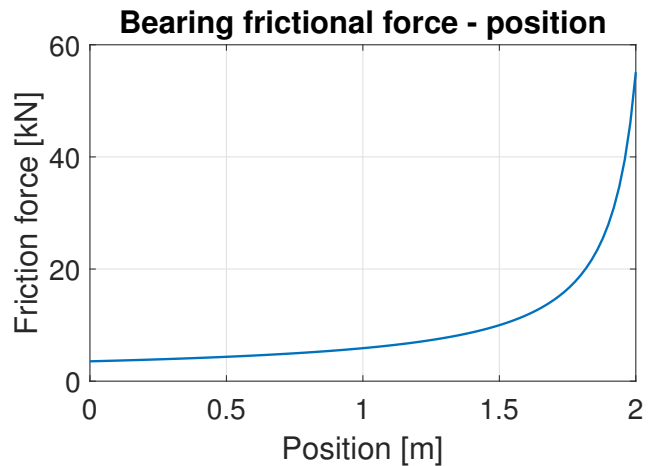


Figure 4.18: Cylinder bearing friction - position

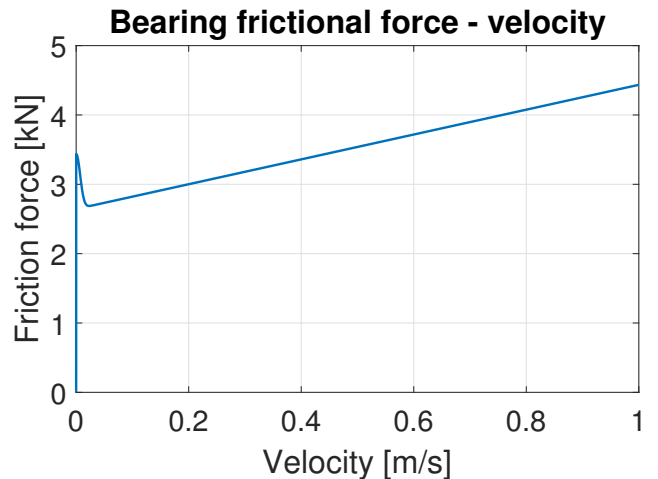


Figure 4.19: Cylinder bearing friction - velocity

## Seal frictional losses

Seal friction in the hydraulic cylinder is very similar to the bearing friction. Seals are also lubricated by a thin fluid film from the hydraulic fluid in the cylinder chamber. As the bearings can be assumed to be much stiffer compared to the cylinder bearings, the normal force on the seals can be assumed independent of the actuator extension. Due to the nature of high pressure step oil seals, seal friction is also largely independent of the working pressure in the cylinder.

As the friction of the seals is described by boundary lubrication effects, the Stribeck function used for the bearing friction and described by [18] is still valid [159, 80, 182]. As such the seal friction force is expected to scale linearly with the actuator velocity for the entire viscous region of the velocity range. As the normal force on the seals is not influenced by the bending moment in the cylinder, seal friction forces can be up to two orders of magnitude smaller compared to bearing friction forces. The implementation of the Stribeck friction model to determine the seal friction force  $F_{seal,loss}$  is explained in Chapter 3.4.1 and Appendix B.3. Note that the mass dependant normal force on the bearings of the equations in Chapter 3.4.1 is replaced by the constant normal force on the seal defined by [18]:

$$F_n = \pi (2(r_{seal} - t_{seal}) + t_{seal}) s_p \sigma_{av} \quad (4.53)$$

with  $\sigma_{av}$  the average contact pressure of the seal which is modelled in [91] as:

$$\sigma_{av} = (2\epsilon + 0.13) \frac{\pi E_{seal}}{6} \quad (4.54)$$

Figure 4.20 shows the modelled seal friction force.

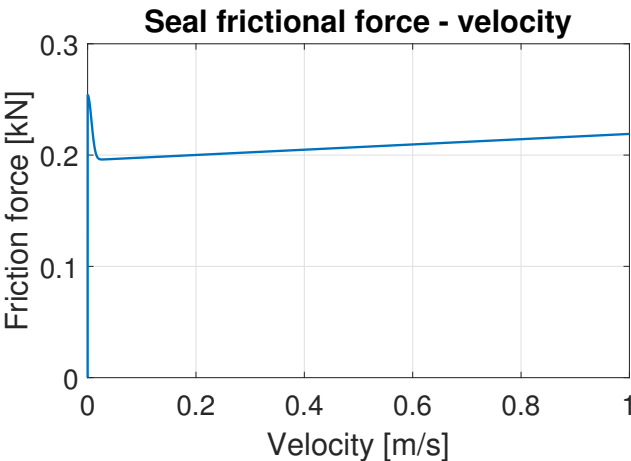


Figure 4.20: Cylinder seal friction force - velocity

The velocity dependant friction force clearly shows the stick slip behaviour at low velocities and the viscous friction trend at higher velocities.

## Total cylinder losses

The total friction losses in the hydraulic cylinder is the sum of the seal friction losses  $P_{seal}$  and the bearing friction losses  $P_{bearing}$ . The cylinder friction power losses can be expressed as a friction force  $F_{cyl,loss}$  as used in (4.1) as:

$$F_{cyl,loss} = F_{seal,loss} + F_{bearing,loss} \quad (4.55)$$

### 4.4.3 Hydrostatic pump losses

The hydrostatic pump converts rotary mechanical power to hydraulic fluid power and vice versa. Just as any actuator component the hydrostatic pump has losses associated to its operation. Unlike the hydraulic cylinder however, the hydrostatic pump has losses both in the mechanical and in the fluid domain. Figure 4.21 [130] shows the architecture of a typical axial piston pump. Frictional losses occur in the mechanical interfaces between the swash plate and slipper, the slipper and piston and the piston and cylinder block. Volumetric losses occur due to fluid leakage between the slipper and piston, piston and cylinder block and between the cylinder block and the valve plate.

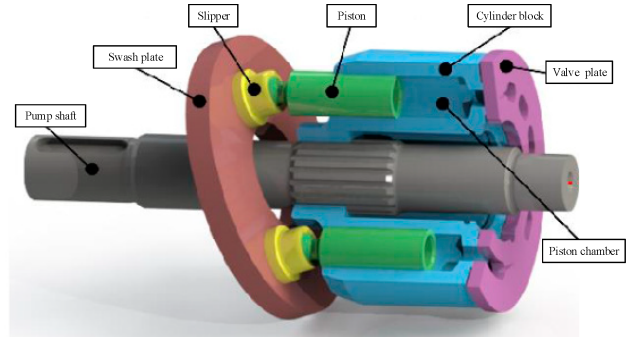


Figure 4.21: Axial piston pump architecture [130].

Losses in the hydrostatic piston pump are less well researched in literature compared to other component losses. Due to the complex anatomy of the piston pump, analytical modelling of the pump losses is difficult without extensive component size models and implemented design choices. [84] describes an extensive parametric model of the axial piston pump using detailed sizing parameters. By relating detailed design parameters to the volumetric displacement of the pump, loss scaling with pump mass can be determined. Using known experimental pump efficiency surfaces, the simplified pump efficiency model coefficients can be determined. Modelling of the mechanical and volumetric losses is discussed separately below.

## Mechanical loss modelling

Friction losses are best described by the frictional moment in the pump. Various speed dependant friction losses can be found in the piston pump. Viscous friction is caused by the resistance of hydraulic fluid to shear, the resulting friction torque is just as seen in the hydraulic cylinder linearly related to de pump speed  $T_v \propto \omega$ . Churning friction torque is proportional to the speed by  $T_{ch} \propto \omega^2$  according to [84]. Finally, flow friction torque can be related to the speed by  $T_{turb} \propto \omega^{-1}$  [84]. This inverse linear relation can be found by using an inverse linear relation between the friction factor and the Reynolds number as is found in laminar flow. The linear relationship between the Reynolds number and the fluid velocity translates in the proportionality above.

Friction losses are also dependant on the pressure differential over the pump. Pressure dependant friction torque is determined by coulomb friction and the flow friction losses. Coulomb friction is linearly proportional to the normal force and therefore proportional to the pressure as  $T_c \propto p$ . The flow friction losses are

proportional to the pressure by  $T_{turb} \propto p^{3/2}$  according to [84].

Using the model of [84] and replacing detailed sizing parameters with volumetric displacement relations, the following geometry related factors for respectively the viscous friction loss coefficient, coulomb friction loss coefficient, churning friction loss coefficient and flow friction loss coefficient are found:

$$K_v \propto V_g^{2/3} \quad (4.56)$$

$$K_c \propto V_g \quad (4.57)$$

$$K_{ch} \propto V_g \quad (4.58)$$

$$K_f \propto V_g^{2/3} \quad (4.59)$$

With the model of [84], the frictional torque in the pump  $T_{pump,loss}$  used in (4.2) is then found as:

$$T_{pump,loss} = K_v|\omega| + K_c p \delta + K_{ch} \omega^2 + K_f \left( \frac{p \delta^{3/2}}{|\omega|} \right) + T_{l0} [\text{N m}] \quad (4.60)$$

Here  $T_{l0}$  is a constant friction term. The fitting coefficients of the geometry related friction coefficients are shown in Appendix E.3.

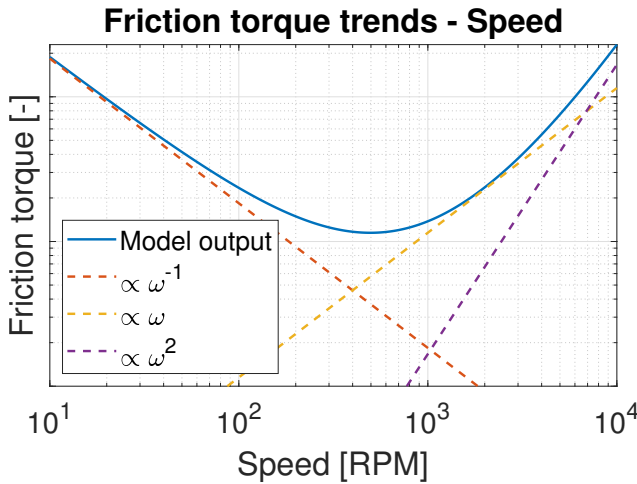


Figure 4.22: Pump friction torque - Speed (loglog)

The resulting speed related trends in the pump torque losses are shown in Figure 4.22. Slow speed losses are clearly dominated by the fluid flow friction while viscous friction and churning friction become dominant at higher speeds.

Similarly, the pressure dependant pump friction torque trends are shown in Figure 4.23. Friction torque is almost independent of the pressure at low pressures. At higher pressures first coulomb friction becomes dominant after which flow friction losses define the friction trend.

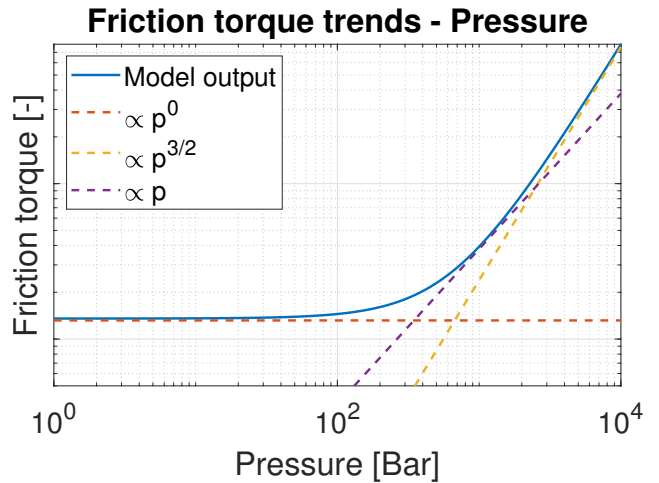


Figure 4.23: Pump friction torque - Pressure (loglog)

## Volumetric loss modelling

Volumetric losses in the piston pump are determined by fluid leakage between different interfaces of the hydrostatic pump. As fluid power is determined by the product of the volume flow  $Q$  and the fluid pressure  $p_\delta$ , volumetric losses are defined as:

$$P_{volumetric} = \frac{Q_{leakage}}{p_\delta} \quad (4.61)$$

Multiple factors influence volumetric losses in the pump. The compressibility of the hydraulic fluid causes a decrease in the volume of the hydraulic fluid [84] proportional with the pressure  $V_{decrease} \propto p$ . The equivalent leakage is therefore proportional to the pump speed by  $Q_c \propto \omega$  [84]. The laminar flow leakage through the different moving interfaces is proportional to the pressure by  $Q_l \propto p$  [84]. According to [84], the leakage

through the valve transition notches is turbulent flow and proportional to  $Q_t \propto p^{1/2}$ .

Using the model of [84] and replacing detailed sizing parameters with volumetric displacement relations, the following geometry related factors for respectively the laminar flow loss coefficient, turbulent flow loss coefficient and compressibility flow loss coefficient are found:

$$C_l \propto V_g^{-1/3} \quad (4.62)$$

$$C_t \propto V_g^{2/3} \quad (4.63)$$

$$C_c \propto V_g \quad (4.64)$$

With the model of [84], the fluid leakage flow in the pump  $Q_{pump,loss}$  used in (4.2) is then found as:

$$Q_{pump,loss} = C_l \frac{p_\delta}{\mu_{hf}} + C_t \sqrt{\frac{p_\delta}{\rho_{hf}}} + C_c \omega p_\delta + Q_{l0} [\text{L min}^{-1}] \quad (4.65)$$

Here  $Q_{l0}$  is a constant leakage term. The fitting coefficients of the geometry related leakage flow coefficients are shown in Appendix E.3.

The resulting speed and pressure dependant volumetric loss trends are shown in Figure 4.24 and 4.25 respectively. At low speeds the leakage flow is almost independent on the speed, only at higher speeds the compressibility effects become noticeable. The leakage proportionality to the pressure can be largely explained by the compressibility and laminar leakage losses with the compressibility related leakage dominating in the operational pressure range.

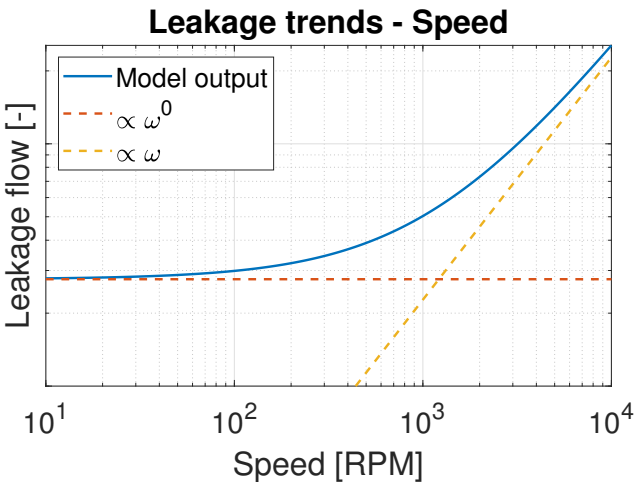


Figure 4.24: Pump leakage flow - Speed (loglog)

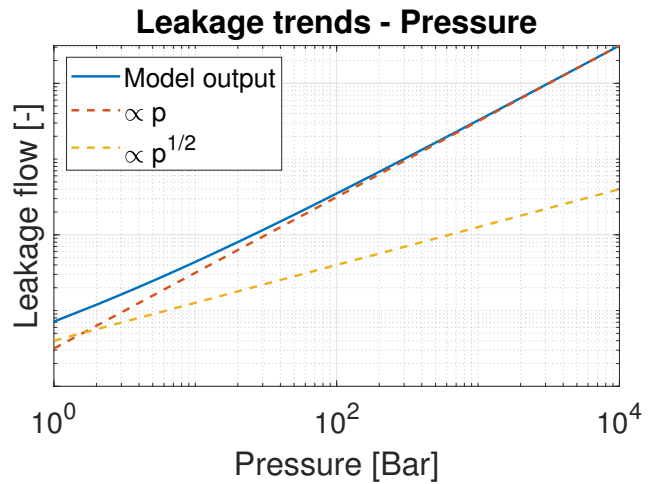


Figure 4.25: Pump leakage flow - Pressure (loglog)

## Combined pump losses

The combination of mechanical and volumetric losses result in the total hydrostatic pump losses. The trends of both types of losses can be combined to obtain the total pump loss trend. Figure 4.26 and 4.27 show these combined losses and the main trend lines with respect to the speed and pressure respectively.

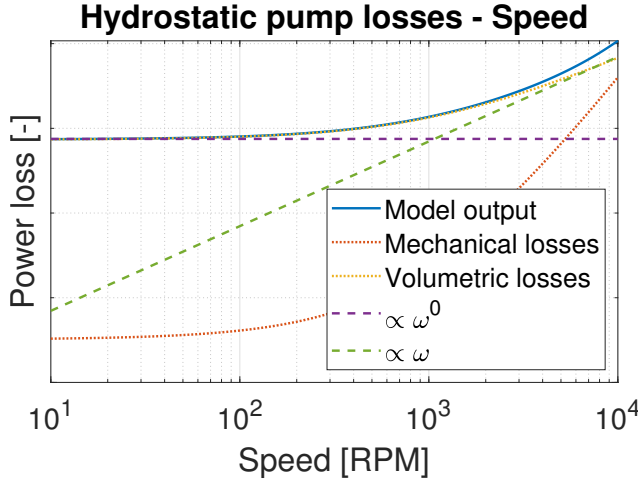


Figure 4.26: Total pump power loss - Speed (loglog)

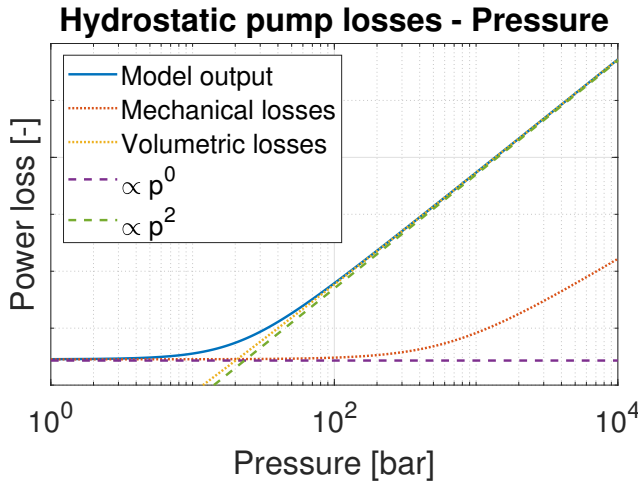


Figure 4.27: figure  
Total pump power loss - Pressure (loglog)

The speed dependant losses are dominated by the volumetric losses across the feasible speed region of the pump. As such the power loss trend is independent of the speed at low pump speeds and proportional to the pump speed for higher speeds:

$$P_{pump} \propto \omega \quad (4.66)$$

The pressure dependant losses are dominated by the mechanical losses at very low operating pressures. At high pressures the volumetric losses become dominant giving the power loss relation as:

$$P_{pump} \propto p^2 \quad (4.67)$$

#### 4.4.4 pipe and manifold losses

The power path between the hydrostatic pump and hydraulic cylinder leads through the manifold and hydraulic pipes. Friction between the hydraulic fluid and

the pipe walls, together with gravity effects result in a pressure drop across these components. The pressure drop translates in a power loss.

Pressure drops in the pipes are determined by velocity dependant pipe friction and by friction due to restrictions in the pipes such as the 90 deg bends in the pipe. Furthermore, the head loss due to gravity should be taken into account. Pressure drop in the manifold is assumed to be only affected by the flow resistance in valves.

Pipe flow resistance is often modelled using the Darcy Weisbach equations [176]. The implemented equations are found in Appendix B.2 and can be approximated with:

$$\delta p_{p,laminar} = 9.4e-3 L_{pipe} v \quad (4.68)$$

and

$$\delta p_{p,turbulent} = 1.29e-1 L_{pipe} v^2 \quad (4.69)$$

Transition of the laminar and turbulent loss models is modelled as a fraction of the Reynolds number between 2300 and 4000. The transition is explained in detail in Appendix B.2.

Losses in the pipe restrictions such as corners and valves are also derived from Darcy Weisbach. The implemented equations are found in Appendix B.2 and can be approximated with:

$$\delta p_r = 1.32e-2 v^2 \quad (4.70)$$

The head loss due to gravity is independent of the velocity and can be given as:

$$\delta p_g = V_{fluid,pipe} \rho_{hf} g L_{pipe} [\text{Pa}] \quad (4.71)$$

The total pressure drop in the pipes and manifold  $p_{pipe,loss}$  used in (4.1) is defined as the sum of the individual pressure drops:

$$p_{pipe,loss} = \delta p_p + \delta p_r + \delta p_g \quad (4.72)$$

Figure 4.28 shows the fluid velocity dependant pressure drop trends. At low velocities the gravity induced head loss dominates. At higher velocities the transition between laminar and turbulent flow losses can be seen.

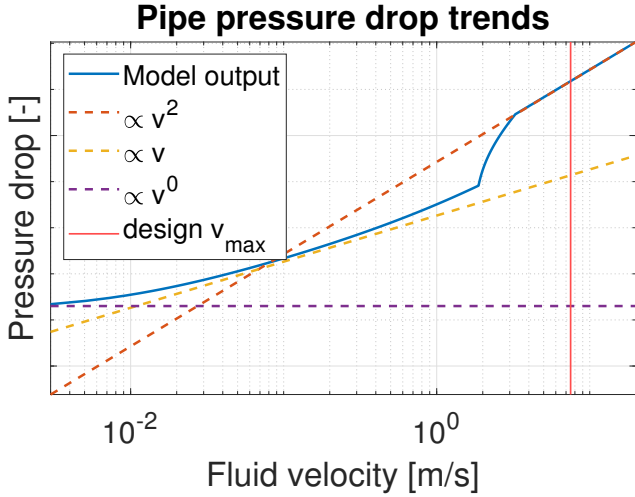


Figure 4.28: Pipe pressure drop trends - fluid velocity (loglog)

The maximum design velocity of the fluid flow  $v_{max}$  is explained in Subsection 4.3.2.

## 4.5 Constraints

Actuator constraints limit the possible actuator configurations with physical limits which are not necessarily imposed by the mass and power loss models. The EHA is constrained by 4 different constraints which are discussed below.

**Hydraulic cylinder eigenfrequency** The hydraulic cylinder operates at relatively low frequencies. However, to ensure the eigenfrequency of the cylinder is not triggered during operation, actuator configurations with low eigenfrequencies should be constrained.

The eigenfrequency of the hydraulic cylinder is modelled by [56] as a function of the piston area  $A_p$ :

$$\omega_n = 2A_p \sqrt{\frac{\beta_{hf}}{m_{load}V_{cf}}} [\text{rad s}^{-1}] \quad (4.73)$$

Where  $\beta_{hf}$  is the bulk modulus of the hydraulic fluid,  $m_{load}$  is the mass of the load and cylinder combined and  $V_{cf}$  is the hydraulic fluid volume in the system. To keep the actuator frequencies far from the cylinder eigenfrequency, the constraint is active when the acceleration profile frequencies are larger than  $1/4\omega_n$ .

**Pump flow** Pump flow is determined by the volumetric displacement of the pump and the speed of the pump shaft. The maximum flow in a given pump is therefore determined by the maximum speed of the pump. The maximum speed of the pump is limited by lubrication effects and eigenfrequency of the pump.

[118] models the maximum pump flow with an empirical relation to the volumetric displacement  $V_g [\text{cm}^3/\text{rev}]$  as:

$$Q_{max} = 10.67V_g^{2/3} [1 \text{ min}^{-1}] \quad (4.74)$$

**Pressure** Pressure in the system is a function of the load on the actuator and the piston area of the cylinder. Most components of the EHA in practice are rated to similar pressures, as such the maximum working pressure in the EHA configurations is limited by a fixed value equal to:

$$p_{max} = 330 \text{e}5 [\text{Pa}] \quad (4.75)$$

**Motor speed** The speed of the motor can not increase indefinitely. Next to the electrical limitations, motor speed is often limited by the balancing of the rotor and the resulting high centrifugal forces on the rotor and bearings. Maximum motor speed of the servo motors used in high power actuators is assumed to be constant at:

$$n_{max} = 3300 [\text{rpm}] \quad (4.76)$$

The majority of the servo motors found in the industry are rated around this speed.

## 4.6 Conclusions

This chapter discussed the model development of the components used in the electro hydrostatic actuator with exception of the rotary motor driving the actuator transmission. Model development is performed to obtain mass and power loss models which can facilitate fast sizing and comparison of different actuator configurations against other actuator technologies. New and adapted existing models to describe the required EHA parameters are discussed. Furthermore several trends are found describing the component masses with respect to the load rating and the power loss properties with respect to the working points of the actuator.

### 4.6.1 Mass and power loss trends

Mass and power loss trends follow from the various models discussed in this chapter for every transmission component. Mass and power loss trends aid in understanding general behaviour of the EHA. The dominating trends found in Sections 4.3 and 4.4 for actuators capable of delivering 100[kN] and more are repeated below. For the absolute masses and losses the equations described in these sections should be used as these can not simply be described by a single proportionality coefficient.

**Mass scaling** The mass of the hydrostatic transmission used in the EHA can be approximated by summing the masses of the hydraulic cylinder, the manifold and the hydrostatic pump. For load ratings above 100[kN] the hydraulic cylinder is found to scale approximately to the load rating according to:

$$m_{cyl} \propto F_{max}^{6/5} \quad (4.77)$$

According to the self developed scaling law, the manifold mass scales with the maximum volumetric flow through the actuator according to:

$$m_{manifold} \propto Q_{max}^{3/2} \quad (4.78)$$

More extensive validation of this scaling law should be performed in later research. Finally, the mass of the pump is found to scale linearly with the pump volumetric displacement as:

$$m_{pump} \propto V_g \quad (4.79)$$

As the pump also has a rotating part, the moment of inertia is of importance. The moment of inertia of the pump is found to scale according to:

$$I_{pump} \propto V_g^{5/3} \quad (4.80)$$

As shown, only the hydraulic cylinder scales directly with the load rating of the actuator. Manifold and pump masses are very dependant on design choices with respect to the cylinder area and the pump displacement.

**Power loss behaviour** Loss behaviour is determined based on the working point of the actuator. Power losses of the EHA transmission are found in the hydraulic cylinder, the hydraulic pipes and manifold and in the hydrostatic pump.

The power loss scaling law of hydraulic cylinder with respect to the velocity of the actuator in the major part of the operating velocity window is found to be:

$$P_{cyl} \propto v^2 \quad (4.81)$$

The power losses in the hydraulic cylinder were found to be independent of the instantaneous loading of the cylinder. However, losses in the cylinder are dependant on the position of the actuator.

The losses in the hydrostatic pump are dependant on mechanical and volumetric losses. The pressure dependant losses are shown to be dominated by the mechanical losses at low pressures. At higher pressures the volumetric losses take over giving the loss relation of:

$$P_{pump} \propto p^2 \quad (4.82)$$

With respect to the speed, the pump losses are dominated by the volumetric losses. Only at very high speeds, the mechanical losses start to dominate. These speeds are in practice never reached due to eigenfrequency and balancing constraints. The speed dependant pump losses are independent of the speed at low velocities as seen in the volumetric loss trends. At higher velocities this relation is approximately given by:

$$P_{pump} \propto \omega \quad (4.83)$$

Finally, the losses in the hydraulic pipes and manifold are considered. The main loss relations are found with respect to the speed and dependant on laminar or turbulent fluid flow. During the main operating speed window, the pipe losses are given as:

$$P_{pipe} \propto \omega^2 \quad (4.84)$$

## 4.6.2 Model use

The developed mass and power loss models describe the electro hydrostatic actuator assuming quasi static operation. The actuator model is capable of determining the approximate actuator mass and mean power use for an arbitrary actuator configuration. These configurations are determined by free design variables of the actuator which are the area of the cylinder piston  $A_p$ , the volumetric displacement of the pump  $V_g$  and the number of pump-motor combinations  $N_p$ . This last variable is added to enable redundancy options in the hydraulic circuit. Further input parameters needed in the model are the maximum load and speed requirements on the actuator, the desired lifetime of the actuator and a representative time series describing the normal operation of the actuator in force, velocity, acceleration and position data.

The main purpose of the developed actuator model is providing a tool which can be used in a preliminary design tool to find the optimal electro hydrostatic actuator configurations for a specified application. Development of a similar actuator model for the electro mechanical actuator as shown in Chapter 3 enables comparison of both actuator technologies for a specific application. As comparison of different high power actuators is the focus of the developed model, scaling and power loss trends are more important than the absolute values of the actuator properties. Masses and losses of smaller peripherals are therefore neglected. For low power actuators actuator properties are expected to deviate significantly due to for example the neglected masses of mounting hardware, cabling and an additional charge pump in the actuator system.

### 4.6.3 Future work

In developing and testing the actuator model, some model parts are shown to need further improvement in future model iterations. For the reader interested in possible follow up research, future work suggestions are stated here.

The model part with the largest uncertainty is the model describing the mass of the hydraulic manifold connecting the hydrostatic pump to the hydraulic cylinder pipes. The hydraulic manifold contains the various valves and connections to control the additional flow caused by leakage replenishment and pressure compensation. The mass of this actuator part is modelled using a physics based scaling assumption and fit to a single example manifold. Data on existing manifolds is not readily available in literature and is therefore very difficult to validate. Development of a more detailed manifold model describing the different

components in the manifold and their mass properties is a valuable addition to the developed actuator model.

In general, mass model validation is performed using manufacturer data of existing components. Power loss data is generally not available to validate the power loss models in a similar fashion. The use of existing sub models found in literature and the physics based explanation of the loss trends provides a reasonable prediction of model accuracy. However, experimental validation of the complete power loss model would greatly benefit the certainty of the loss model results.

Finally, future research could focus on the model development of similar electro hydrostatic actuator implementations within the development framework explained in this chapter. Other actuator implementations can then be compared to the electro hydrostatic actuator based on the fixed pump variable motor strategy.

# Chapter 5

## Servo motor modelling

The servo motor of the MEA converts electrical power to mechanical power. In motoring operation the servo motor drives the actuator transmission by delivering a torque and rotation speed to the axle of the hydrostatic pump or reduction gearbox of the EHA and EMA respectively. In generating operation, the servo motor is driven by torque and rotation speed to deliver electrical power back to the grid or an electrical buffer.

Industrial servo motors are often implemented by a permanent magnet synchronous machines (PMSM). The PMSM technology is known for its high torque to inertia ratio and due to its high efficiency compared to the most common induction motor technology [96]. Also power density of these type of machines is higher compared to the induction machine, resulting in a lower mass motor [96]. In literature, also fault tolerant PMSM architectures are proposed [133, 133] which can operate with only 2 out of 9 phases. The use of fault tolerant architectures severely reduces the risk of using a single motor to drive the actuator transmission.

Mass and power loss properties of the servo motor in EHA and EMA applications scale according to the same scaling laws. However, as both actuator transmission types may pose different requirements on the motor for maximum torque and maximum velocity, modelling the servo motor mass and power losses is a necessary part to determine the overall properties of the EHA and EMA. The PMSM servo motor is a well known technology, and different sizing and efficiency models are available in literature. This chapter details how existing models are combined to model the PMSM behaviour for use in a simulation based actuator analysis.

Model development of the PMSM servo motor is split in two main parts. First the development of a sizing model is discussed in Section 5.1 with the goal of determining the motor mass for a given application. Afterwards, the used power loss model of the PMSM is discussed in Section 5.2 and the loss behaviour with respect to the working point is shown. Note that figures portraying sensitivities in the mass and power loss scaling are shown on a loglog scale with base 10 for easy identification of the different trends.

### 5.1 Sizing model development

Development of a mathematical sizing model of the servo motor is necessary for two main reasons; the sizing model determines the total mass of the motor, and it defines the geometric configuration parameters needed in the motor loss model. Sizing of the electric motor is based on the rated torque and the thermal requirements on the motor. The thermal requirements on the motor are governed by the load cycle and influence mainly the cooling capacity and therefore the static mass of the PMSM. In general, the mass of the PMSM can be split in the static mass and the rotating mass determining the moment of inertia of the PMSM. The static mass is mainly determined by the size of the housing, the amount of copper in the windings and the rotating mass. The rotating mass is determined by the size of the rotor steel and the dimensions of the rotor axle. Sizing model development is split up in configuration modelling, static mass modelling and rotating mass modelling. These models are discussed in the sections below. The list of symbols used in the PMSM sizing models is found in Subsection 5.1.1.

### 5.1.1 List of symbols

Symbol	Explanation	Unit
$\rho_{force}$	Force density of the rotor	$[\text{N m}^{-2}]$
$\rho_{es}$	Mass density of electrical steel	$[\text{kg m}^{-3}]$
$f_e$	Maximum electrical frequency	$[\text{Hz}]$
$I_{ax}$	Moment of inertia of the rotor axle	$[\text{kg m}^2]$
$I_{PMSM}$	Total moment of inertia of the PMSM	$[\text{kg m}^2]$
$I_{rotor}$	Moment of inertia of the rotor	$[\text{kg m}^2]$
$L_{ax}$	Length of the rotor axle	$[\text{m}]$
$L_b$	width of the motor bearings	$[\text{m}]$
$L_m$	Core length of the PMSM	$[\text{m}]$
$L_{rotor}$	Length of the rotor	$[\text{m}]$
$m_{ax}$	Mass of the rotor axle	$[\text{kg}]$
$m_{PMSM}$	Total mass of the PMSM	$[\text{kg}]$
$m_{rotor}$	Mass of the rotor	$[\text{kg}]$
$n_{max}$	Maximum design speed of the motor	$[RPM]$
$p$	Number of magnetic poles	$[-]$
$p_p$	Number of magnetic pole pairs	$[-]$
$phase$	Number of phases used	$[-]$
$q$	Number of stator slots per pole	$[-]$
$Q$	Total number of stator slots	$[-]$
$r_{ax}$	Radius of the rotor axle	$[\text{m}]$
$r_{rotor}$	Radius of the rotor	$[\text{m}]$
$t_g$	Air gap width	$[\text{m}]$
$T_{rated}$	Rated torque of the PMSM	$[\text{N m}]$
$V_{ax}$	Volume of the rotor axle	$[\text{m}^3]$
$V_{rotor}$	Volume of the rotor	$[\text{m}^3]$

### 5.1.2 Configuration modelling

In designing the PMSM, different configurations are possible depending on the load and speed requirements. These configurations determine the loss behaviour of the servo motor. The different configuration parameters necessary for loss modelling in Section 5.2 are determined using existing models from literature. The most important parameters are discussed here. Models used from literature are discussed in Appendix C.1.1

**Number of pole pairs** The pole pairs of the PMSM are the electrical poles of the same polarity on opposite sides of the stator housing. The number of pole pairs are dependant on the maximum electrical frequency and the maximum rated speed of the machine. The total number of single poles necessary in the machine are calculated as:

$$p = \frac{120f_e}{n_{max}} \quad (5.1)$$

The number of pole pairs is exactly half of the number of poles. The number of pole pairs should be an even number, as such the number of pole pairs is defined as:

$$p_p = \text{ceil}\left(\frac{p}{2}\right) \quad (5.2)$$

The possible change in number of poles due to the ceiling function should be compensated with the electrical frequency. The number of stator slots per pole per phase are then determined according to:

$$q = \frac{Q}{\frac{p_p}{2} \text{phase}} \quad (5.3)$$

The total number of slots in the PMSM are determined with a slots per pole relation. For fast turning servo applications, a common slots per pole relation is  $3/2$  [123]:

$$Q = \frac{3 p_p}{2} \quad (5.4)$$

### 5.1.3 Static mass modelling

The static mass of the PMSM is the total mass of the machine including the machine housing mass, the mass of all the windings and the rotating mass. The static mass is not only influenced by load requirements, but also by thermal requirements. A machine capable of outputting a high torque for a long time should have a high cooling capacity and the associated high mass of the machine housing. Thermal modelling of the motor is outside the scope of this research. In literature mass properties of the PMSM are well defined and scaling laws are developed. To give an accurate estimate of the motor mass of servo type motors, a scaling law can be fitted to known mass data of PMSM servo's. [30] describes the PMSM mass relation according to:

$$m_{PMSM} \propto T_{rated}^{6/7} \quad (5.5)$$

Fitting this scaling law to known mass data of servo type permanent magnet synchronous machines gives the fitting coefficient to determine the servo motor mass. The total servo motor mass  $M_1$  as used in (2.3) and (2.6) is then given as:

$$M_1 = 1.45 T_{rated}^{6/7} \quad (5.6)$$

The raw servo motor mass data from catalogue data is detailed in Appendix C.1.3. The mass fit is shown in Figure 5.1. The fitted scaling law overestimates the motor mass on average by 3.4% with a standard deviation of  $\pm 14.6\%$ .

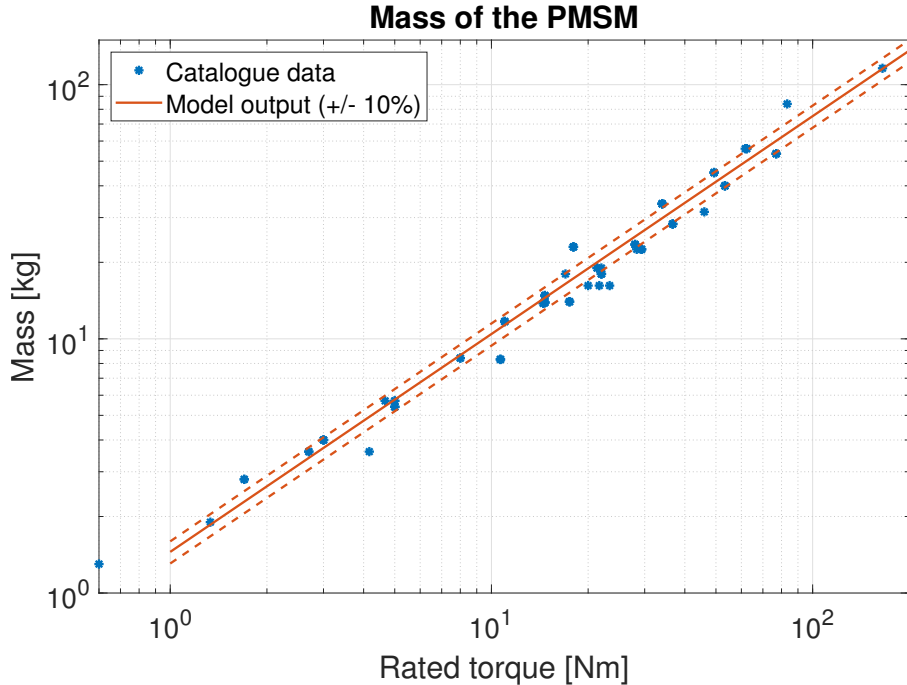


Figure 5.1: PMSM mass scaling law fit (loglog)

The rated torque of the machine is assumed to be equal to the maximum occurring torque on the actuator during normal operation. Short torque requirements above the rated torque are permissible with permanent magnet synchronous machines. These higher torque requirements can occur in load peaks on the motor.

### 5.1.4 Rotating mass modelling

The rotating mass of the PMSM consists of the mass of the rotor and the mass of the rotor axle. The rotor of the PMSM is made from electrical steel and permanent magnet material to form the magnetic poles. The rotating mass of the rotor is important as it determines the moment of inertia of the PMSM.

#### Rotor sizing

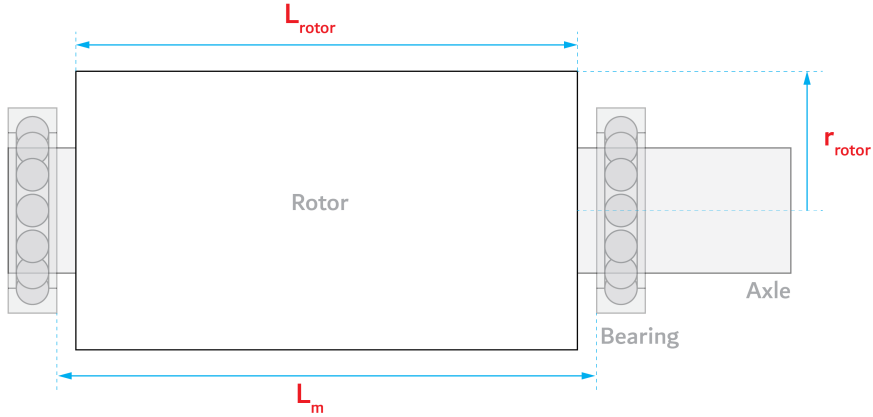


Figure 5.2: PMSM simplified rotor geometry and sizing parameters.

Rotor sizing is governed by the shear forces acting on the metal due to the electro magnetic forces in the motor. Figure 5.2 shows the simplified geometry of the rotor body and its main sizing parameters. The approximate volume of the PMSM rotor is often determined based on the rated torque and a typical force density factor  $\rho_{force} = 20e3[\text{N m}^{-2}]$  [142]:

$$V_{rotor} = \frac{T_{rated}}{2\rho_{force}} [\text{m}^3] \quad (5.7)$$

By assuming the length ratio of the PMSM is defined by  $L = 2r$ , the rotor radius can be calculated as:

$$r_{rotor} = \sqrt[3]{\frac{V_{rotor}}{2\pi}} [\text{m}] \quad (5.8)$$

Similarly, the effective length of the rotor is defined as:

$$L_{rotor} = 2r_{rotor} [\text{m}] \quad (5.9)$$

The core length of the machine takes the effective rotor length in account and allows for an air gap between the rotor and the motor housing:

$$L_m = L_{rotor} + 2t_g [\text{m}] \quad (5.10)$$

## Axle sizing

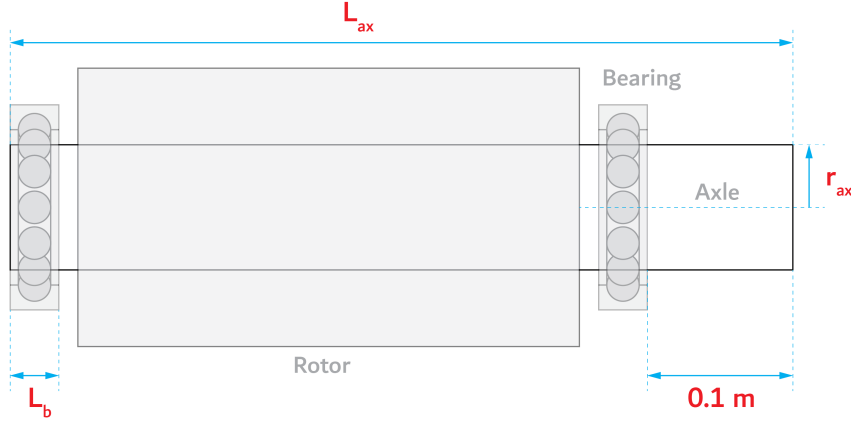


Figure 5.3: PMSM simplified axle geometry and sizing parameters.

The rotor is fixed to the rotating motor axle. The motor axle is connected outside the motor housing to either the hydrostatic pump of the EHA or the gearbox of the EMA. The axle transfers the torque and speed of the motor to these components. The motor axle is sized based on the rated torque of the PMSM. Figure 5.3 shows the simplified geometry of the motor axle and its main sizing parameters.

As the axle should be capable of withstanding the torque induced shear forces, the minimum radius of the axle  $r_{ax}$  is determined by shear force requirements. The shear force calculations are shown in Appendix C.1.2 and are approximated by:

$$r_{ax} = 1.6e-3T_{rated} \quad (5.11)$$

The axle length can be determined next by assuming a 10cm stick out of the motor axle from the motor housing and a fixed bearing width  $L_b$ :

$$L_{ax} = L_m + 2L_b + 0.1[\text{m}] \quad (5.12)$$

The total volume of the axle is then given as:

$$V_{ax} = \pi r_{ax}^2 L_{ax} [\text{m}^3] \quad (5.13)$$

### mass properties

The moving mass of the PMSM is the sum of the rotor and axles mass. Both masses can be determined by assuming a uniform density of both parts. For the rotor mass, this means the density of the electrical steel and the density of the permanent magnet material are assumed to be equal. The mass of the axle and rotor are respectively given by:

$$m_{ax} = V_{ax} \rho_{st} [\text{kg}] \quad (5.14)$$

$$m_{rotor} = (V_{rotor} - (\pi r_{ax}^2 L_{rotor})) \rho_{es} [\text{kg}] \quad (5.15)$$

The volume of the rotor is here corrected for the axle material going through the rotor. More important than moving mass of the PMSM is the resulting moment of inertia. The moment inertia of both the axle and rotor can be simply determined from their respective masses as:

$$I_{ax} = \frac{1}{2} m_{ax} r_{ax}^2 [\text{kg m}^2] \quad (5.16)$$

$$I_{rotor} = \frac{1}{2}m_{rotor} (r_{rotor}^2 + r_{ax}^2) [\text{kg m}^2] \quad (5.17)$$

As the moment of inertia for both components is determined around the same axis of rotation, they can simply be summed to obtain the total moment of inertia of the PMSM:

$$I_{PMSM} = I_{ax} + I_{rotor} [\text{kg m}^2] \quad (5.18)$$

Both the radius of the rotor and the radius of the axle scale with the rated torque due to shear force requirements as:

$$r^* \propto T^{1/3} \quad (5.19)$$

Using this relation and substituting values in the equations above, the following scaling law for the servo motor moment of inertia  $I_1$  as used in (2.3) and (2.6) is found:

$$I_1 = I_{PMSM} = 2.4e-5T^{5/3} [\text{kg m}^2] \quad (5.20)$$

In Figure 5.4 the modelled moment of inertia of the PMSM is plotted against the moment of inertia of several existing PMSM servo motors in catalogue data.

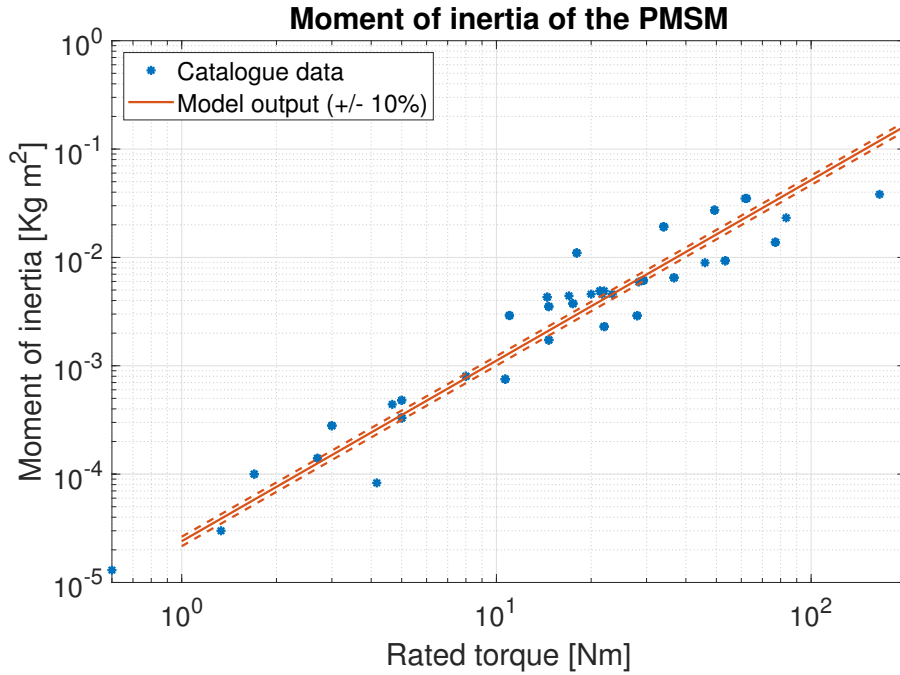


Figure 5.4: Moment of inertia of the PMSM, scaling trends (loglog)

The overall moment of inertia scaling trend is seen to match the catalogue data. However the deviation of the model results with respect to the catalogue data can reach up to 400%. On average the model overestimates the moment of inertia by 9.4% with a standard deviation of  $\pm 66\%$ . The large spread of the moment of inertia is largely explained by different possible length ratio's in the design of a servo motor. The moment of inertia can be optimized for different applications by changing the length ratio of the machine. The differences in moment of inertia of the PMSM is explained in a white paper by Schneider Electric [4]. In this report the moment of inertia is determined according to the fixed length ratio described above.

## 5.2 Loss model development

Development of a mathematical loss model of the PMSM servo motor is needed to determine the energy requirements for a given actuator on a specific task. Together with the actuator transmission losses determined in Chapter 3 and 4 for the EMA and EHA respectively, the total power requirements of both actuators can be determined for each discretized working point in the task time series. Back drivability, as discussed in previous chapters enables negative power in the system, meaning power can be regenerated by the actuator and delivered back to the electric grid. Multiplying the discretized power requirements with the time step and summing the discretized energy requirements of the entire task time series, the total energy usage for a given task can be determined.

While the motor losses should scale similarly in both actuator applications, the requirements on the motor and with that the instantaneous losses will differ. As such, the motor losses should be taken into account to compare both EHA and EMA energy requirements.

The PMSM converts electrical power in mechanical power and vice versa. Subsection 5.2.2 details the transmission of electrical voltage and current to mechanical torque and rotation speed. In the power conversion, losses occur in both the electrical domain and in the mechanical domain. Both loss types are modelled below based on the size of the motor and the working point of the actuator.

### 5.2.1 List of symbols

Symbol	Explanation	Unit
$\omega$	Rotational speed	$[\text{rad s}^{-1}]$
$\phi_{av}$	Maximum magnetic flux per pole	[J]
$EMF$	Electromotive force	[V]
$f_c$	Instantaneous electrical frequency	[Hz]
$I$	Electrical current	[A]
$I_s$	Instantaneous phase current	[A]
$k_{ws}$	Harmonic winding factor	[-]
$N_s$	Number of stator turns	[-]
$P_{cu}$	Copper losses of the PMSM	[W]
$P_{Fe}$	Iron losses of the PMSM	[W]
$P_{mech}$	Mechanical losses of the PMSM	[W]
$P_{PWM}$	Additional losses of the PMSM	[W]
$P_{PMSM}$	Total losses of the PMSM	[W]
$p_p$	Number of magnetic pole pairs	[-]
$r_{rotor}$	Radius of the rotor	[m]
$R_s$	Phase winding resistance	$[\Omega]$
$T$	Mechanical torque	[N m]
$u$	Electrical potential	[V]
$v_r$	Surface speed of the rotor	$[\text{m s}^{-1}]$

### 5.2.2 Power transmission

Power transmission in the ideal actuator components is 100% efficient. This means the instantaneous electrical and mechanical power should be equal as:

$$uI = \omega T \quad (5.21)$$

In the PMSM the rotational velocity of the motor axle is determined by the electrical frequency in the stator windings. The electromotive force (EMF) and thus the voltage across the motor is also dependant on this electrical frequency. In finding the transmission properties of the PMSM, some assumptions are made. First, the motor is assumed to only operate within the constant field strength region. This means the field weakening region is not considered in the servo motor operation. This assumption is valid as a servo motor should be capable of delivering high speeds and high torque at the same moment across its entire speed envelope. Next, we assume electrical losses can be well approximated with root mean square (RMS) current values. As a result,

it is possible to develop a motor constant for the PMSM based on the EMF generated by the rotating magnets in the rotor.

The EMF of the PMSM is modelled by [127, 142] as a function of the electrical frequency  $f_c$ :

$$EMF = \sqrt{2}\pi f_c \phi_{av} k_{ws} N_s [\text{V}] \quad (5.22)$$

The required electrical frequency is dependant on the number of pole pairs and the instantaneous speed of the motor:

$$f_c = \frac{p_p \omega}{2\pi} [\text{Hz}] \quad (5.23)$$

The magnetic flux per pole  $\phi_{av}$ , harmonic winding factor  $k_{ws}$  and the number of stator turns  $N_s$  are all detailed in [142] and are explained in Appendix C.1.1.

Assuming a three phase motor and using the transmission ratio (5.21), the required electric current needed to deliver the instantaneous torque is now defined as:

$$I_s = \frac{T\omega}{3EMF} [\text{A}] \quad (5.24)$$

Above relations are used to determined the working point dependant motor losses.

### 5.2.3 Electric losses

The electric losses of the PMSM comprise the copper losses in the windings, the iron losses in the stator steel, losses due to extra harmonics in the EMF of the motor and some additional losses due to the PWM modulation of the electrical controller. The electrical losses of the PMSM are modelled in [117]. The corresponding equations are shown below. The harmonic losses which occur due to the stator slot openings and the rotating rotor are ignored as they are much smaller then the copper and iron losses. The total electrical losses are defined by the summation of these individual losses. The different electrical loss components are explained below.

**Copper losses** The copper losses are the losses associated with the resistivity of the copper conductor used in the stator windings. Assuming a 3 phase machine, the copper losses can be determined according to:

$$P_{cu} = 3R_s I_s^2 [\text{W}] \quad (5.25)$$

**Iron losses** The iron losses comprise the eddy current losses and hysteresis losses associated with a rotating magnetic field. The iron losses can be divided in the stator yoke core losses and the stator tooth core losses [117]. Both loss factors are determined in [117] according to:

$$P_{Fe} = k_{Fe} P_{15} \left( \frac{B_c}{1.5} \right)^2 m_c \left( \frac{f_c}{50} \right)^{3/2} [\text{W}] \quad (5.26)$$

Here  $k_{Fe}$  is an experimental correction coefficient,  $B_c$  the magnetic flux strength correction factor and  $P_{15}$  an experimental power density factor. Values of these parameters are found in [117] and are shown in Appendix C.  $m_c$  is the mass of the yoke and stator respectively, the masses of these components are modelled in [117]. The sizing model of [117] is shown in Appendix C.1.1.

**Additional losses** The additional losses model the losses associated with the PWM modulation in the electrical controller of the PMSM. These losses are taken as a percentage of the total electrical input power in [117]:

$$P_{PWM} = 0.015 |P_{in}| [\text{W}] \quad (5.27)$$

**electrical loss trends** The total electrical losses are defined by the sum of all loss components. The total current needed to overcome these losses  $I_{motor,loss}$  used in (2.3) and (2.6) is then defined as:

$$I_{motor,loss} = \frac{P_{cu} + P_{Fe} + P_{PWM}}{U} \quad (5.28)$$

Taking into account the copper and iron losses, the working point dependant power losses are expected to scale with the torque and speed of the motor according to:

$$P_{Electrical} \propto T^2 \quad (5.29)$$

$$P_{Electrical} \propto \omega^{3/2} \quad (5.30)$$

The additional losses are linearly proportional to both the torque and speed of the motor as they are a percentage of the total power.

Figure 5.5 and 5.6 show the speed and torque dependant loss trends respectively.

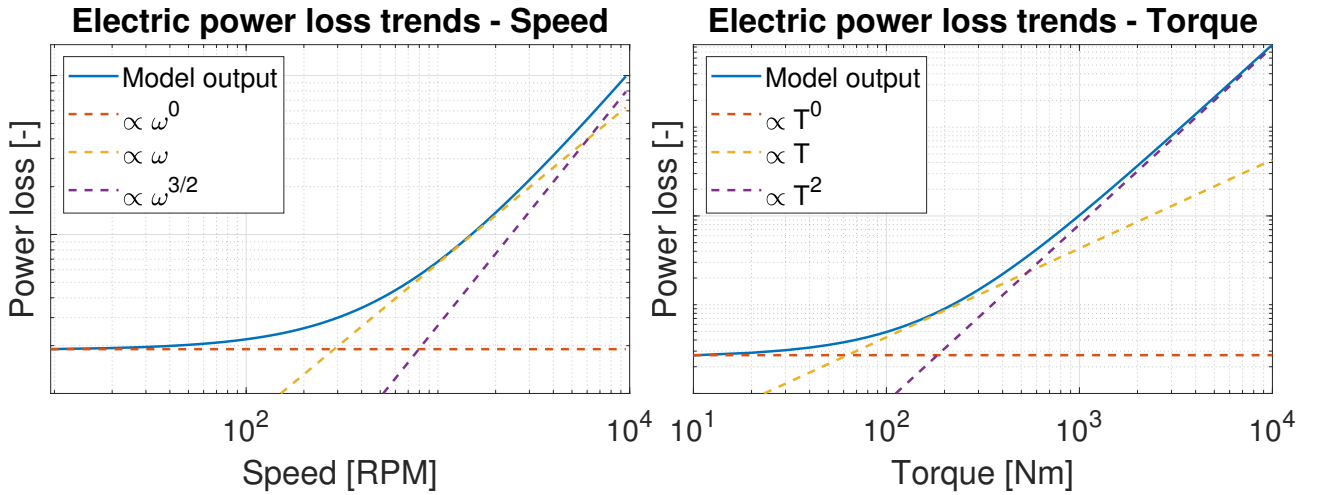


Figure 5.5: Electrical power loss trends - Speed (loglog) Figure 5.6: Electrical power loss trends - Torque (loglog)

## 5.2.4 Mechanical losses

The mechanical losses of the PMSM are mostly found in bearings supporting the motor axle. During operation, the bearings turn and induce a frictional moment. The product of this frictional moment and the speed result in a power loss. The rolling frictional moment of the bearings is expected to scale with the motor speed squared as is found in the modelling of the EMA transmission in Chapter 3.

The mechanical losses of the PMSM are modelled by [127] according to:

$$P_{mech} = k_p 2r_{rotor} (L_{rotor} + 0.6\tau_p) v_r^2 [\text{W}] \quad (5.31)$$

Here  $k_p$  is an experimental loss factor determined in [127].  $v_r$  is the surface velocity of the rotor which is defined as:

$$v_r = \omega_r r_{rotor} \quad (5.32)$$

The other parameters are geometry related. [117] describes a model for these parameters as shown in Appendix C.1.1.

The mechanical losses in the PMSM can be expressed as a friction torque  $T_{motor,loss}$  used in (2.3) and (2.6) as:

$$T_{motor,loss} = \frac{P_{mech}}{\omega_1} \quad (5.33)$$

### 5.2.5 PMSM loss trends

The losses of the PMSM are expected to be dominated by the electrical loss factors with respect to both the operating speed and torque. As such the power relations found in Subsection 5.2.3 should largely explain the PMSM losses. Figure 5.7 and 5.8 show the total PMSM loss trends with respect to the speed and torque respectively.

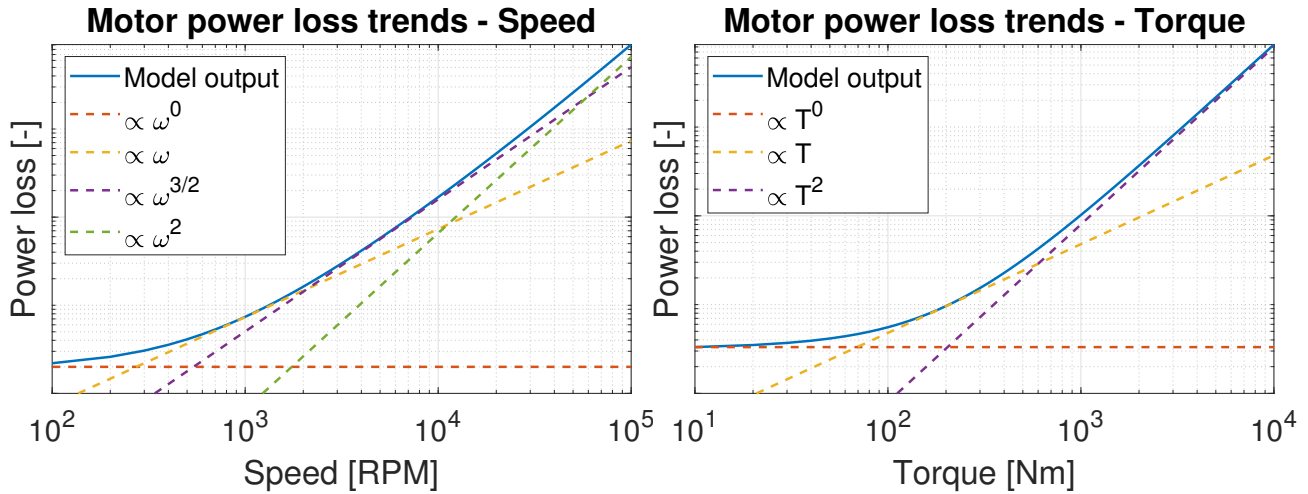


Figure 5.7: PMSM power loss trends - Speed (loglog) Figure 5.8: PMSM power loss trends - Torque (loglog)

The total PMSM loss trends largely resemble the electrical loss trends shown in Figure 5.5 and 5.6. The speed dependant losses also show the mechanical loss factor. However, the mechanical losses only start to dominate at motor speeds much above the eigenfrequency and balance limit of existing motors. The dominant speed trend in the operating region of the motor is linear:

$$P_{PMSM} \propto \omega \quad (5.34)$$

The loss trends with respect to the torque are not influenced by the mechanical losses. the trend lines correspond completely to the electrical loss factors.

## Chapter 6

# High power linear actuator properties in hexapod applications <sup>1</sup>

### Abstract

*Electro mechanical and electro hydrostatic linear actuators are often used for different actuation applications up to 45 kW maximum output power. For applications requiring higher power output, the advantages of one over the other technology become unclear. Existing research clearly shows benefits of both technologies over conventional hydraulic actuation. This chapter compares both actuator types on power losses and mass for a specific high power application. Mathematical models are used to perform preliminary actuator sizing and to simulate application dependent actuator losses. A case study is performed to evaluate both actuator technology properties on a specific application.*

### 6.1 Introduction



Figure 6.1: Ampelmann A-type crew transfer gangway (Ampelmann Operations B.V.)

Linear actuators are devices capable of converting electrical energy to linear mechanical energy. Often a rotary motor is used to drive a rotary to linear hydraulic or mechanical transmission. Current developments in various technical fields concerning actuation are focused in a large part on efficiency. Efficiency is often important with respect to environmental consid-

erations; achieving more with less environmental costly resources. Increased efficiency however also has a financial consequence by lowering operating costs. Similarly, reducing actuator mass can impact operational costs directly. Especially in mobile actuator applications, system mass footprint becomes an important factor in the total payload capacity of the carrying vessel and therefore on the productivity of the vessel trip. Next to financial consequences, mass of the actuator is often an important factor in stability of the carrying vessel.

This chapter focusses on linear actuators of hexapod steward platforms which are capable of power output with an order of magnitude of  $10^5$  Watt. An example of such a system is the Ampelmann A-type crew transfer gangway shown in Figure 6.1. These systems use six linear actuators to compensate vessel motion and create a still standing platform from which offshore crew can be transferred between the vessel and a fixed structure.

Linear actuators in high power applications are often dominated by conventional hydraulic technology. Conventional hydraulics are known for their high loss factors with maximum system efficiencies ranging around 35% [100, 180]. In the aviation industry, a development called the more electric aircraft (MEA) found that electro hydrostatic actuators (EHA) and electro mechanical actuators (EMA) both offer significant ad-

<sup>1</sup>This chapter is based on the draft paper provided in Appendix F.3

vantages on both system efficiency [22, 33, 128] and reduced actuator mass [22, 41, 128, 163].

Both EHA and EMA are driven by an electric rotary machine to convert electrical energy in rotary mechanical energy. The EHA uses a hydrostatic transmission with a pump and hydraulic cylinder to obtain a linear force and velocity. Similarly, the EMA uses an (optional) gearbox and a screw mechanism to obtain the same linear force and velocity output. Both technologies have specific properties, however comparison between both options is lacking for high power applications in literature. Figure 6.2 from a preceding literature review (Appendix G) shows various actuator studies found in literature ranked on their maximum output force and velocity. Existing literature is seen to exist on EMA and EHA for power levels up to approximately 45kW. For higher power levels, existing research is lacking and no clear benefits of one over the other technology are defined. To further the knowledge in the use of EHA and EMA linear actuators for high power applications fundamental actuator scaling properties are defined in Chapter 3 and 4 respectively.

In this chapter, the scaling and power loss models developed in these chapters are used to make a preliminary design tool to compare EMA and EHA actuator mass and efficiency properties for specific high power applications. The focus of this chapter is on actuators for use in a sea motion compensating steward platform, however actuator properties and efficiency models are applicable to a multitude of high power actuation applications. The focus on a specific actuator application is necessary as operating regimes determine the power loss behaviour of the actuator. Actuator properties are determined with a simulation type approach. To ensure the optimal actuators of both technologies are compared, an optimization algorithm is used to determine the actuator configurations. The developed preliminary design tool is included in Appendix E.4.

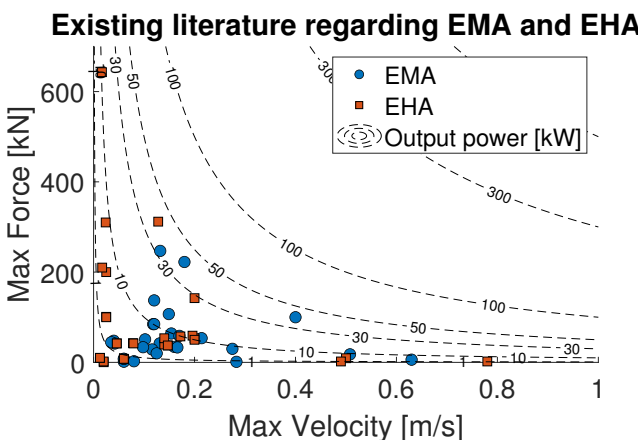


Figure 6.2: Existing actuator studies in literature ranked on maximum output force and velocity (Appendix G).

**Reading guide** To aid the reader in finding the contents of their interest in this chapter, this reading guide provides the general structure of the chapter. First the research method is discussed in Section 6.2. The general actuator properties as defined in Chapter 3 and 4 are summarised and discussed in Section 6.3. A case study using the developed preliminary design tool is performed to find the linear actuator properties for a high power linear actuator application in Section 6.4. Finally, the conclusions from this research are shown in Section 6.5.

## 6.2 Method

### 6.2.1 Actuator description

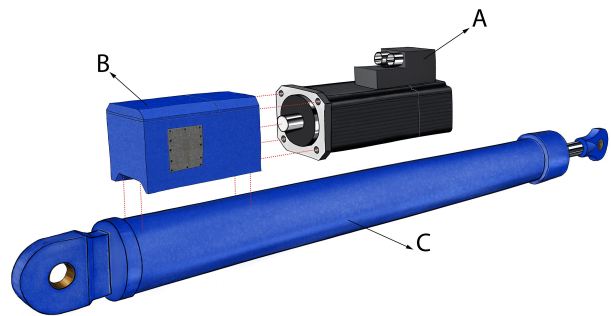


Figure 6.3: General components of the MEA

To develop a high power linear actuator preliminary design tool, the working of the linear actuator should be discussed first. For brevity the EHA and EMA can be described as a single type of linear actuator called the more electric actuator (MEA) in line with the existing naming convention in the aviation industry. The MEA has three major components which are visualized in Figure 6.3. The electric servo motor (A) is a universal component which can be considered equal in both the EHA and EMA. The motor is often implemented by a permanent magnet synchronous machine (PMSM) capable of four quadrant operation [44, 96, 174]. Connected to the motor is an intermediate stage (B). This actuator part is needed to convert the rotary mechanical power from the motor to a form which can be used by the end effector (C) of the actuator. In the EMA, this intermediate stage is found in the form of an (optional) reduction gearbox reducing the output speed and increasing the output torque of the motor towards the end effector side. The EHA uses a hydrostatic pump to convert the rotary mechanical power to fluid power. The end effector (C) is the actuator part which transfers the actuator power to the load. In the EMA the end effector is implemented as a mechanical cylinder with a screw mechanism inside. The EHA makes use of a hydraulic cylinder to drive the load. The simplified general operational principle of both actuators is explained below.

**EHA operation** In the EHA, the servo motor drives the hydrostatic pump with a defined torque and speed. The hydrostatic pump in its turn pumps fluid around in a closed loop system resulting in a volumetric flow and pressure. This closed loop system consists of the A and B chamber of the hydraulic cylinder and the hydraulic pipes connecting the pump to the hydraulic cylinder. Fluid flow in the cylinder chambers results in a linear movement of the actuator. The pressure difference between both cylinder chambers results in a net force on the piston which is transferred to the load.

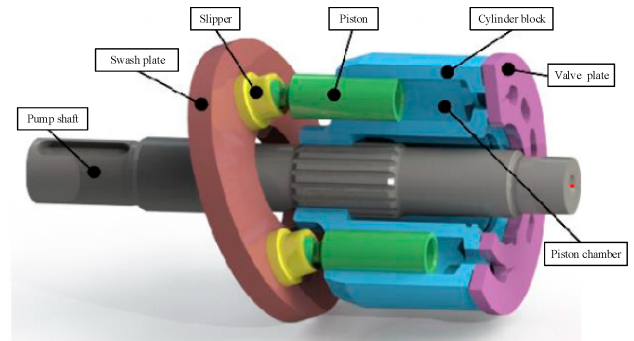


Figure 6.4: Axial piston pump main components [130].

**EMA operation** Similarly in the EMA, the servo motor drives a gearbox with a defined torque and speed. The gearbox has helical gears inside to reduce the outgoing speed by a gear ratio factor. Ideally the outgoing torque is increased by this same gear ratio. The gearbox output shaft in turn drives a mechanical cylinder screw. The screw mechanism in the mechanical cylinder transfers the delivered torque and speed to a linear force and velocity by a screw transmission ratio.

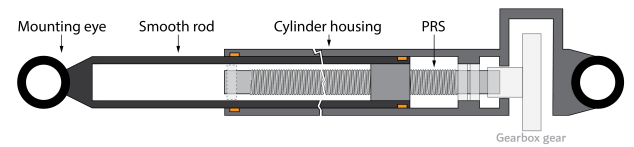


Figure 6.5: Mechanical cylinder architecture

### Actuator components

The PMSM of the MEA is a widely known and researched component [42, 44, 96, 117, 127, 135, 142]. This is also the case for the reduction gearbox of the EMA and hydraulic cylinder of the EHA. For brevity, these components will not be explained in detail. The hydrostatic pump of the EHA and mechanical cylinder of the EMA are less known and are explained below. Description of the different EMA and EHA transmission components is found in Chapter 3 and 4 respectively. The PMSM is discussed in Chapter 5.

**EMA mechanical cylinder** The EMA mechanical cylinder substitutes the hydraulic cylinder of the EHA. The cylinder is a combination of a screw mechanism and a protective housing. The general architecture of the mechanical cylinder is shown in Figure 6.5. The cylinder housing ensures the screw mechanism is protected against lateral forces and the outside environment. The actual power transmission is performed by the screw mechanism. This screw mechanism transfers rotary mechanical power to linear mechanical power.

**EHA hydrostatic pump** The EHA uses a hydrostatic or positive displacement pump to pump fluid between the cylinder chambers of the hydraulic cylinder. Various implementations of the hydrostatic pump exist in literature. The piston pump is however the most promising solution for high pressure systems such as the EHA [92, 158]. A distinction between axial and radial piston pumps is not made in this chapter. Figure 6.4[130] shows a cross section of a typical axial piston pump.

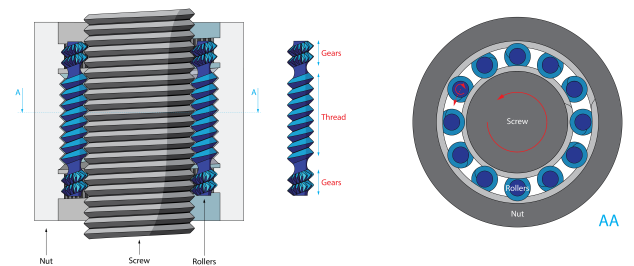


Figure 6.6: Planetary roller screw components and interaction.

The pump has a rotating cylinder block and a stationary swash plate. The slippers on the swash plate force the pistons to move in and out the cylinder block during rotation. As such, hydraulic fluid is pumped from the low to high pressure side of the pump. This chapter assumes a fixed displacement pump meaning the swash plate angle is constant and the motor speed determines the volumetric output. An alternative is a variable displacement pump in which motor speed is constant and the variable swash plate angle changes the volumetric output.

The screw mechanism in this study is implemented by a planetary roller screw (PRS). Planetary roller screws are optimally suited for high load high velocity applications [98, 162] and are known for their high efficiency [167]. Figure 6.6 shows the main parts of the PRS. The screw is driven with a speed and torque from the connected gearbox. The rotation of the screw results in rotation and translation of the contacting rollers. The rollers in turn contact the rotationally fixed nut causing a translation of the nut along the screw axis. The rollers effectively form a virtual thread between the

screw and nut. The numerous contact points between the screw, rollers and nut result in a high load rating. The virtual thread created by the rollers decreases frictional losses significantly compared to the power screw and ball screw [167]. Additional gears and a gear-ring are added on the rollers and nut respectively to eliminate slip between both components [167].

## 6.2.2 General model strategy

Comparing the EMA and EHA for a specific application requires both the mass and energy losses of each proposed actuator for the specified application. In this chapter actuator properties are determined analytically using the mathematical models developed in Chapter 3 and 4.

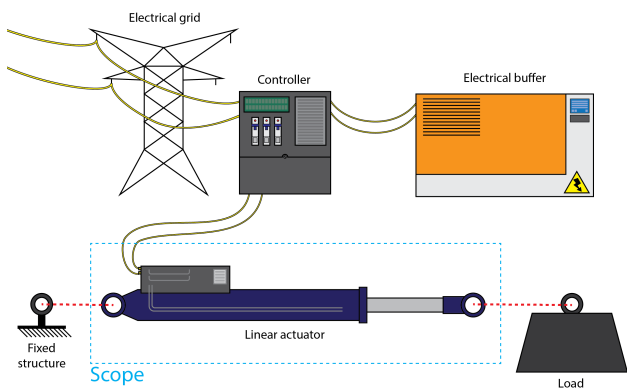


Figure 6.7: Actuator modelling scope

Actuator system properties are influenced by several peripherals. To be able to find the effect of the linear actuator technology itself, the modelling scope is limited to the actual actuator. Figure 6.7 visualises the modelling scope in the total actuator system. Power delivery to and from the actual actuator is assumed 100% efficient and masses of components outside the scope are neglected. As such, possible inertial forces on the actuator due to movement of its mounting frame are also neglected.

The EMA and EHA in this study are compared based on their mass (sizing) and power loss properties. Sizing the actuator has a large influence on the power losses, both properties are therefore inter dependent. Different sizing options of the actuator components are

possible, as such the preliminary design is an optimization problem. The MEA should be optimized for both efficiency and mass of the actuator. As these optimization objectives not necessarily result in the same actuator design, multiple optimized actuator designs for the same actuator requirements can be found. A good way to portray multiple optimization solutions for two objectives is the use of a Pareto optimal front. Such a front portrays the most optimal actuator solution for different objective weight factors. By creating these Pareto optimal fronts for both the EHA and EMA, the optimal actuator solution for both criteria can be determined. The general optimization approach is portrayed in Figure 6.8.

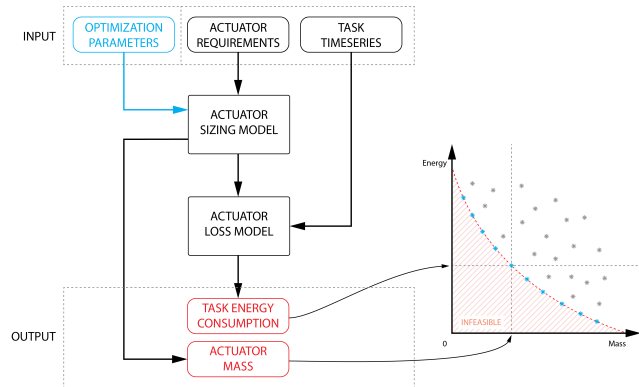


Figure 6.8: Actuator model approach.

In Figure 6.8 the optimization parameters are changed by the optimization script to find the actuators with the lowest mass and lowest task specific energy losses. A list of optimization parameters per actuator is found in table 6.1. Note that the number of pumps in the EHA optimization parameters is only added to allow redundant design comparisons. As such this parameter is not a real optimization parameter. Each run with different optimization parameters results in an actuator mass and task specific energy loss. Actuator solutions on the Pareto optimal front are shown as blue dots in Figure 6.8. These actuator solutions can no longer decrease one objective without increasing the other objective. Actuator requirements and the task specific time series remain constant in the optimization process. The models portrayed by the boxes 'Actuator sizing model' and 'Actuator loss model' are described in Subsection 6.2.3.

Table 6.1: Optimization parameters of the EMA and EHA

EMA		EHA	
Symbol	Description	Symbol	Description
$l_s$	Lead of the screw	$A_p$	Area of the cylinder piston
$r_r$	Radius of the rollers	$V_g$	Geometric volume of the pump
$N_s$	Number of screw thread starts	$N_p$	Number of pumps
$R_g$	Gear ratio of the reduction gears		

Running the actuator model of Figure 6.8 for all possible optimization parameter combinations is very inefficient. The optimization process is therefore performed by an optimization algorithm. The optimization algorithm used in this study is the multi-objective feasibility enhanced particle swarm optimization (MOFEPSO) by [147]. The use of a particle swarm optimization method ensures non-continuous models can be used. Furthermore, by first calculating constraints to evaluate feasibility, the number of function evaluations is decreased significantly. The drawback of a non gradient based optimization strategy is the optimized results are not guaranteed to portray the absolute optimum. Results on the Pareto front are expected to show some variation depending on the starting conditions of the simulation. As results of this optimization are preliminary actuator designs, this is a reasonable trade of for a robust optimization algorithm.

### 6.2.3 Actuator model

The overall actuator model discussed in the previous paragraph and shown in Figure 6.8 portrays the actuator sizing model and actuator loss model as black box input output models. Here these model parts are explained in more detail. To understand both sizing and loss calculations on the MEA, first the power relations between various actuator parts should be explained. The power relations between the three actuator parts of the MEA are visualized in Figure 6.9 and 6.10 for the EMA and EHA respectively. Actuators are sized

according to requirements posed on the actuator load side. Similarly, input power is determined as a function of load side power requirements. Therefore information on the load side can be regarded as known and  $F$ ,  $v$  and  $\dot{v}$  can be deemed the input parameters of the actuator model.

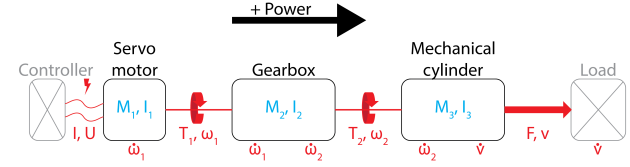


Figure 6.9: Power relations between EMA actuator parts.

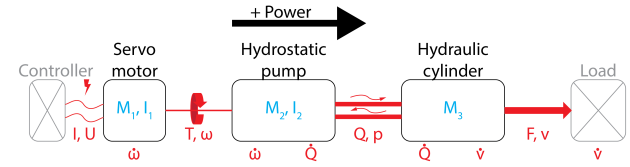


Figure 6.10: Power relations between EHA actuator parts.

Above power relations can be described in mathematical equations. As an example the linearised mathematical power relations for the EMA are given as:

$$\begin{bmatrix} \omega_2 \\ T_2 \end{bmatrix} = \begin{bmatrix} C_\omega & 0 \\ 0 & C_T \end{bmatrix} \left( \begin{bmatrix} v \\ F \end{bmatrix} + \begin{bmatrix} 0 \\ M_{3,m} \end{bmatrix} \dot{v} + \begin{bmatrix} 0 \\ F_{cyl,loss} \end{bmatrix} \right) + \begin{bmatrix} 0 \\ I_3 \end{bmatrix} \dot{\omega}_2 + \begin{bmatrix} 0 \\ T_{screw,loss} \end{bmatrix} \quad (6.1)$$

$$\begin{bmatrix} \omega_1 \\ T_1 \end{bmatrix} = \begin{bmatrix} C_{t\omega} & 0 \\ 0 & C_{tT} \end{bmatrix} \begin{bmatrix} \omega_2 \\ T_2 \end{bmatrix} + \begin{bmatrix} 0 \\ I_2 \end{bmatrix} \dot{\omega}_2 + \begin{bmatrix} 0 \\ T_{gear,loss} \end{bmatrix} \quad (6.2)$$

$$\begin{bmatrix} U \\ I \end{bmatrix} = \begin{bmatrix} C_U & 0 \\ 0 & C_I \end{bmatrix} \left( \begin{bmatrix} \omega_1 \\ T_1 \end{bmatrix} + \begin{bmatrix} 0 \\ I_1 \end{bmatrix} \dot{\omega}_1 + \begin{bmatrix} 0 \\ T_{motor,loss} \end{bmatrix} \right) + \begin{bmatrix} 0 \\ I_{motor,loss} \end{bmatrix} \quad (6.3)$$

Equations for the EHA can be described in a similar fashion but are not shown for brevity. All coefficients  $C_{xx}$  related to the actuator velocity terms represent the transmission ratio linking the velocity terms of different actuator components. All force related coefficients represent the inverse of this transmission ratio. In ideal conditions the power relations of the actuator are described only by these transmission ratio's. In practice, the power transmission is affected by inertia effects and losses in the system. Losses are represented by the different loss factors in the transmission parts. In form closed actuator parts such as the EMA transmission, losses only influence the force related terms directly. In actuator parts such as the EHA hydrostatic pump,

loss factors are also added to the velocity terms due to leakage losses. The definitions of the various transmission coefficients are defined in Chapter 3 and 4 for the EMA and EHA respectively.

**Power losses** Losses of the actuator parts are dependent on the working point of the actuator part. Hence both force and velocity related parameters influence instantaneous loss magnitude of the actuator part. As losses influence the working point of the upstream connected actuator part, losses at the end of the power path have a large influence on the total instantaneous power needed by the actuator. The power path is directed from the servo motor to the load in motoring

operation and from the load to the servo motor in generating operation.

In linear actuator applications where a load is moved around but starts and ends in the same location, no net work is delivered. In these applications, power enters the system on the motor side where it is transported through the actuator transmission to the load. At some point in the operational cycle, this power is directed again from the load to the motor side of the actuator. Power therefore travels two times through the actuator, and is affected twice by the power losses of the actuator. In applications where no net work is delivered, energy use is only defined by the losses in the system. The power losses of the EMA and EHA transmission are detailed in Chapter 3 and 4 respectively.

**Actuator sizing** Sizing of an actuator part influences losses of this actuator part but is also influenced by the losses of the connected actuator parts. Losses in the end effector and intermediate stage for example should be compensated by the servo motor, hence increasing the load requirements on that actuator component. Sizing of actuator parts is mainly determined by the maximum force requirements on the actuator. For axial loaded parts dimensions are determined by buckling and yield requirements. Rotating parts have an additional requirement on shear strength while hydraulic parts are also sized for pressure requirements. The main objective of sizing the different actuator components is finding the mass of an arbitrary actuator configuration. The mass of the MEA is simplified in this report to consist of the masses of its main components. Masses of mounting hardware and additional peripherals are ignored with this approach. A detailed description of the sizing models for both the EMA and EHA are given in Chapter 3 and 4 respectively.

## 6.3 General Actuator properties

The model described in Section 6.2 results in a Pareto optimal front of optimized actuators for a specific application. To understand the results of the actuator models, the general sizing and power loss relations found in Chapter 3, 4 and 5 are summarized and compared first. The relative influence of each actuator component is determined next.

### 6.3.1 General sizing relations

Both the EMA and EHA size with their free design variables and the actuator requirements. The sizing relations of each actuator part of the EMA and EHA are defined separately in Chapter 3, 4 and 5. In general the MEA actuator can be split in three main parts as discussed in Subsection 6.2.1: The electric servo motor, an intermediate transmission stage and the end effector. The electric servo motor is similar in both ac-

tuators, however the scaling trends of the intermediate transmission stage and the end effector can vary. The sizing relations found for these components in Chapter 3 and 4 are compared below.

**Intermediate transmission stage** The intermediate transmission stage represents the reduction gearbox in the EMA transmission and the hydrostatic pump in the EHA transmission. The gearbox scales with the maximum torque on the gearbox axles. In Chapter 3 the gearbox mass is seen to be dominated by the enclosure mass for lower torque ratings and by the gear pair mass for higher torque ratings. In the region of interest for high power linear actuators with an output force with an order of magnitude of  $10^5$  [N], the enclosure mass is still dominant and the mass scaling trend is defined as:

$$m_{gearbox} \propto T_{max}^{1/2} \quad (6.4)$$

Contrary to the gearbox mass, the mass of the hydrostatic pump is found to scale with respect to the volumetric displacement of the pump as:

$$m_{pump} \propto V_g \quad (6.5)$$

The displacement of the pump has no direct relation to the actuator load rating but is rather an optimization parameter in the design of the hydrostatic transmission. Additionally, the intermediate transmission stage mass of the EHA transmission is also determined by the mass of the hydraulic manifold. This component is expected to scale with the maximum flow rate as:

$$m_{manifold} \propto Q_{max}^{3/2} \quad (6.6)$$

As such, the mass of the EHA transmission is also dependant on the maximum design velocity of the actuator.

**End effector** The end effector of the MEA actuator is the final transmission part in the actuator which delivers a linear force and velocity to the actuator connected load. The end effector represents the mechanical cylinder in the EMA transmission and the hydraulic cylinder in the EHA transmission. The mechanical cylinder mass is expected to scale with the load bearing components. Load bearing components are loaded with tension and compression forces. The leading failure criteria within the load region of interest is yield strength of the material, resulting in a mass relation of:

$$m_{mechanical-cylinder} \propto F \quad (6.7)$$

The hydraulic cylinder mass is also determined by load sizing the load bearing parts. Next to the tension and compression forces, the cylinder is also sized to withstand the hydraulic fluid pressure. The resulting mass trends are found for low and high load ratings respectively as:

$$m_{hydraulic-cylinder} \propto F^{2/3} \quad (6.8)$$

$$m_{hydraulic-cylinder} \propto F^{6/5} \quad (6.9)$$

The transition point of both scaling trends is dependant on the stroke length and piston area of the cylinder.

### 6.3.2 Component power loss relations

Similar to the mass relations, power losses of the different MEA actuator parts are defined by different physical properties. The power losses are modelled separately for the EMA and EHA components in Chapter 3 and 4 respectively. The motor losses scale with the same physical properties in both actuator types. The power loss trends are compared for the intermediate transmission stage and the end effector below. Figures in this Subsection are shown on a loglog scale with base 10 to highlight the different trend lines found in the losses.

**Intermediate transmission stage** The intermediate transmission stage losses are found in the gearbox and hydrostatic pump of the EMA and EHA respectively. Gearbox losses are mainly caused by mechanical friction while pump losses are mainly determined by leakage losses.

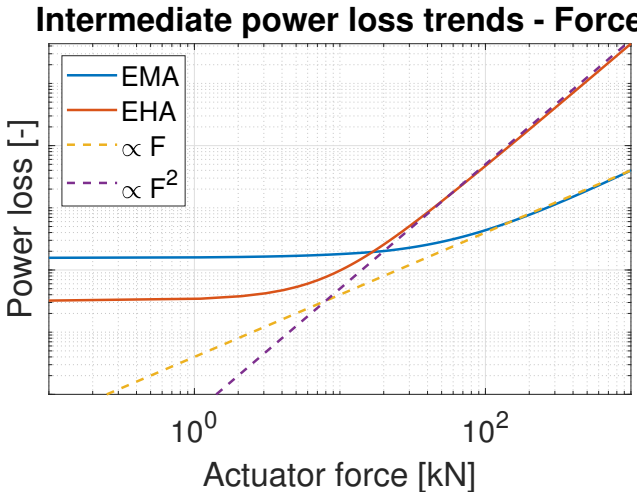


Figure 6.11: MEA intermediate losses - Force (loglog)

Figure 6.11 shows the combined intermediate loss properties of both actuator types with respect to the actuator force. At higher actuator forces the EMA power loss is almost linearly proportional to the force while

the EHA power loss has a proportionality close to  $P_{EHA,int} \propto F^2$  indicating dominant leakage losses. Losses at low forces are dominated by non-load related losses in both actuators.

Similarly, the combined intermediate loss properties with respect to the actuator velocity are shown in Figure 6.12. In general, the intermediate losses of the EMA should be lower at high velocities compared to the EHA.

### Intermediate power loss trends - Velocity

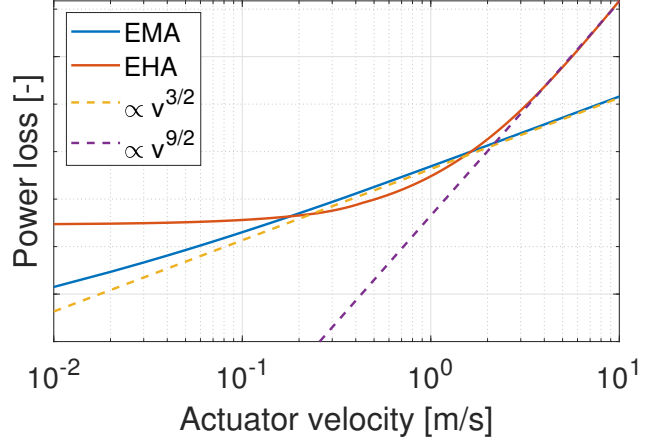


Figure 6.12: MEA intermediate losses - Velocity (loglog)

**End effector** The end effector of the MEA is a cylinder type transmission which is capable of delivering a linear force and velocity to the load. The end effector is implemented by either a mechanical or hydraulic cylinder in the EMA and EHA respectively. Losses in both end effectors are defined by friction losses.

The friction in the hydraulic cylinder is found in the linear bearings and pressure seals. The friction force in the bearings and seals is independent of the axial loading of the actuator and approximately proportional to the velocity squared due to the viscous behaviour of the lubricated contacts.

The friction forces in the mechanical cylinder are more complex. The mechanical cylinder also has linear bearings which result in frictional losses. However friction losses are also related to the PRS mechanism inside the cylinder. The rolling frictional losses in the PRS scale with:

$$P_{rolling} \propto F^{1/2} \quad (6.10)$$

$$P_{rolling} \propto v^{8/5} \quad (6.11)$$

The rolling frictional loss trend however decreases significantly at higher velocities due to a decreased lubrication film thickness as explained in Section 3.4. Figure 6.13 and 6.14 show the force and velocity related

loss trends of both end effectors. Shown losses are normalised with the input power of the end effectors.

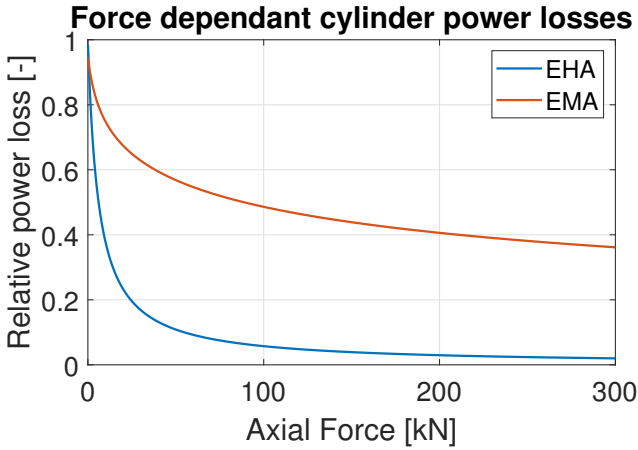


Figure 6.13: MEA cylinder losses - Force

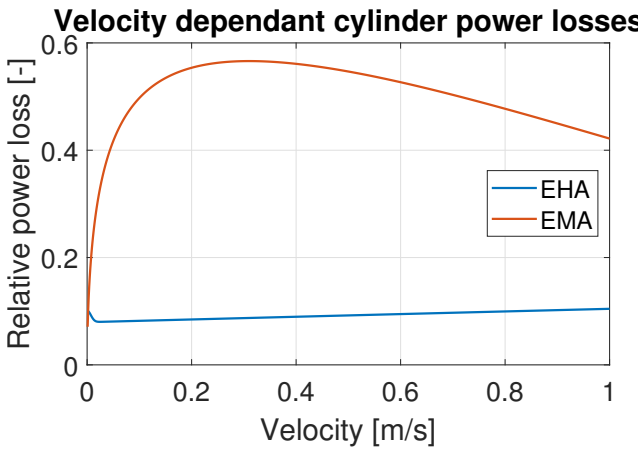


Figure 6.14: MEA cylinder losses - Velocity

The force related losses of the EHA are constant as friction forces are not dependant on the force. Their relative magnitude hence decreases fast with increasing power output. The EMA losses are much higher as is expected with the power losses from the rolling contacts of the PRS. The velocity dependant losses of the EHA are largely defined by viscous friction behaviour. As such the relative losses increase linearly with the velocity. The loss magnitude of the EMA is much higher and only decreases at high velocities due to a decreased lubricating fluid film thickness.

## 6.4 Case study

The actuator mass and loss properties are very dependant on design choices in the actuator design and to the application specific tasks. The preliminary design model described in Subsection 6.2.2 is developed to implement design choices and application specific requirements in determining the EMA and EHA actua-

tor properties. To show the results of this tool, a case study is performed on a linear actuator used in a motion compensation hexapod platform.

**Actuator requirements** The example actuator is a linear actuator for use in a hexapod motion platform. An example of such a platform is the Ampelmann A-type offshore crew transfer gangway as shown in Figure 6.1. Actuators in this platform connect a moving ship with a gangway structure. During operation, the actuators compensate the motion of the ship to create a still standing gangway with respect to bottom founded offshore structures. As the ship motion is wave induced, the compensating motion and forces are largely sinusoidal. Actuators should be capable of delivering forces in an order of magnitude around  $10^4$  [N] at a maximum velocity with order of magnitude  $10^0$  [m s<sup>-1</sup>]. To evaluate the mean power requirements of the actuator, an example task time series representing a wave motion compensating operation of a load is used. The normalized task time series is shown in Figure 6.15

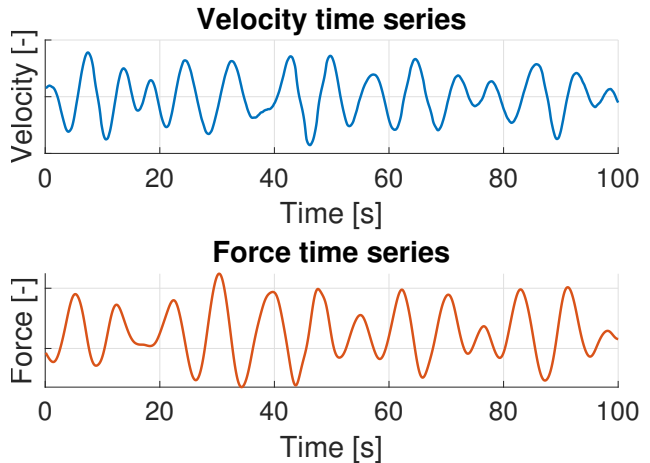


Figure 6.15: Normalized example task, velocity and force time series

The exact actuator requirements and task time series for this application are shown in Appendix E.

### 6.4.1 Actuator configurations

The preliminary design model can be run for both the EMA and EHA actuator. The result of the preliminary design model are two Pareto optimal fronts, showing the optimal actuator designs for both technologies plotted on their system mass and mean power use for the given task. The model results are shown in Figure 6.16.

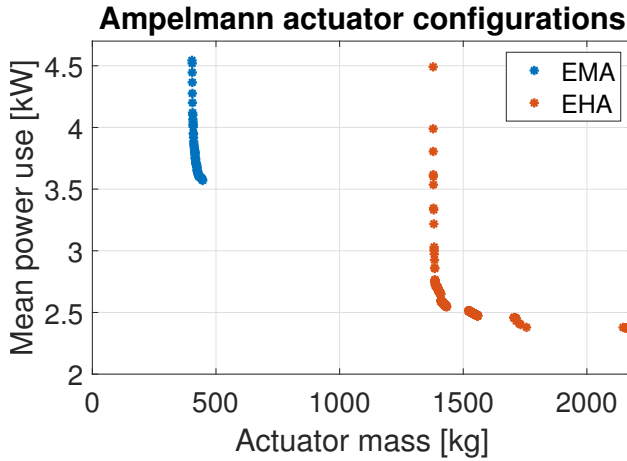


Figure 6.16: Optimized MEA configurations

When comparing the optimized configurations of the EMA and EHA, a clear difference is seen. The EMA configurations have a much lower mass compared to the EHA configurations. In contrast, the EHA configurations can reach a much lower mean power use for the same task compared to the EMA configurations. Both the EMA and EHA have more mass optimized and more efficiency optimized configurations. To better understand the configuration details, the optimized design configurations are discussed for the EMA and EHA below. The neutral design configurations for both the EMA and EHA are compared in Subsection 6.4.2.

### EMA design properties

The EMA configurations show large variability in the mean power use while showing only minor variation in the total actuator mass compared to the EHA configurations. Due to the inherent properties of the Pareto optimal front, increasing mass properties result automatically in decreasing efficiency properties. As such, the design configurations can be discussed with respect to a single objective. The EMA configurations are shown separately in Figure 6.17 for clarity.

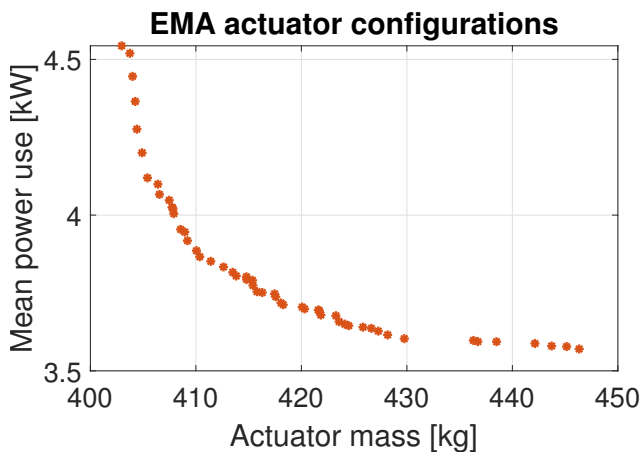


Figure 6.17: Optimized EMA configurations

The EMA configurations are optimized with respect to four design parameters. These are the lead of the PRS screw  $l_s$ , the radius of the PRS rollers  $r_r$ , the number of thread starts on the PRS screw  $N_s$  and the gear ratio of the gearbox  $G_r$ . The optimization parameters in the different optimized configurations are shown in Figures 6.18 to 6.22. To understand the limiting factors of the EMA configurations, the constraints on the actuator are shown in Figure 6.23 and 6.24.

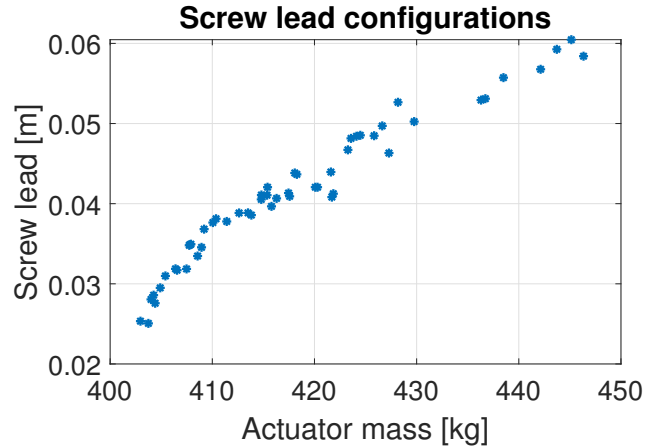


Figure 6.18: Screw lead configurations

**Screw lead** Increasing the RPS screw lead shows increasing actuator masses. The increasing screw lead means slower rotation of the screw and therefore higher torque requirements. Both the gearbox and servo motor masses increase significantly due to these high torque requirements while the mass of the mechanical cylinder is unaffected. The larger screw leads however mean the back driving efficiency of the PRS becomes higher and rolling frictional losses decrease due to the lower speeds. As such the mean power usage of the EMA decreases.

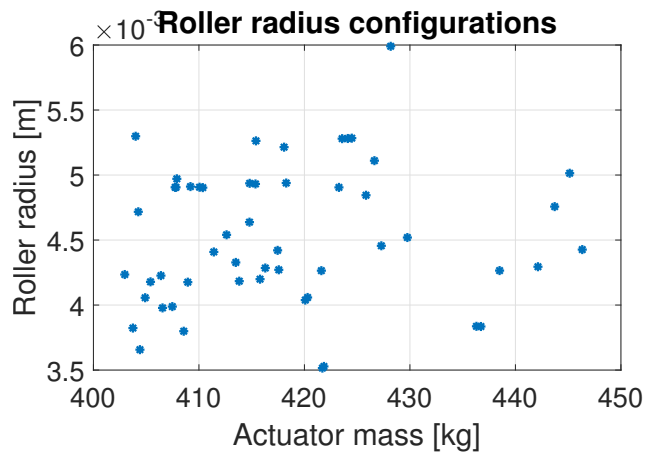


Figure 6.19: Roller radius configurations

**Roller radius** The radius of the PRS rollers has a less clear correlation to the optimization objectives.

The ratio between the screw radius and the roller radius defines the true transition ratio of the PRS mechanism with respect to the screw lead. In combination with the lead of the PRS screw, the roller radii choice becomes clear as it smooths out the transmission ratio trend as can be seen in Figure 6.20.

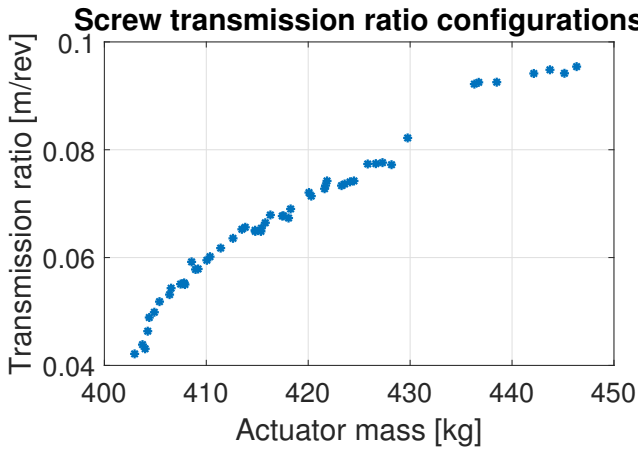


Figure 6.20: Total PRS transmission ratio configurations

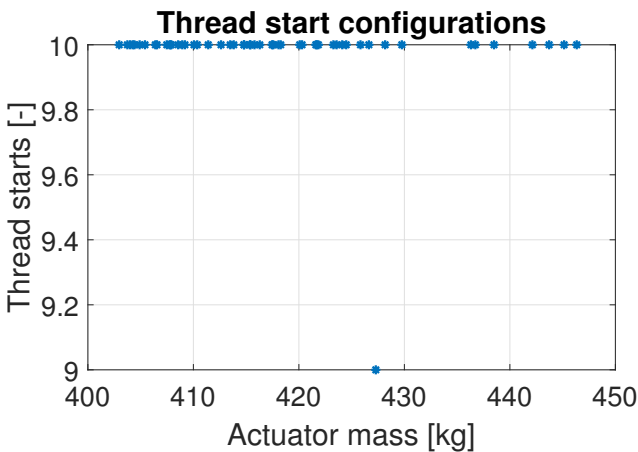


Figure 6.21: Number of thread starts configurations

**Thread starts** The number of thread starts on the PRS screw are limited by the upper bound on this optimization parameter. The number of thread starts also influences the transmission ratio of the PRS screw. More thread starts however also increase the number of contact points in the PRS decreasing the contact pressure. The number of thread starts are limited by fabrication requirements which are implemented as a fixed number in this model.

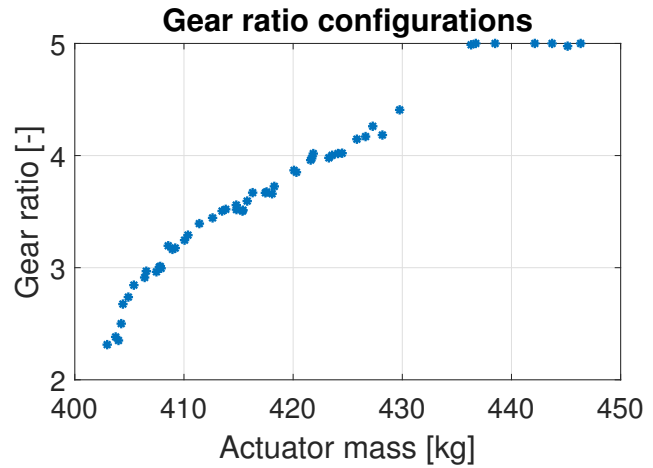


Figure 6.22: Gear ratio configurations

**Gear ratio** The gear ratio in the reduction gearbox determines the speed to torque ratio between the PRS screw and the servo motor. From the transmission ratio of the PRS screw trend above, the maximum speed of the screw is seen to increase with increasing mass and thus decrease for increasing efficiency of the actuator. Increasing the gear ratio with decreasing speed requirements on the screw means the motor speed remains approximately constant. Similarly, the required torque of the servo motor is kept low to keep the servo motor mass down. The gear ratio is limited to a maximum of 5 as only a single gear stage is used.

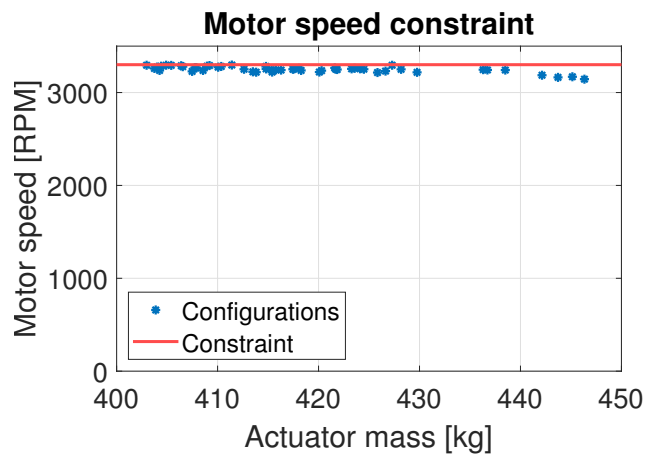


Figure 6.23: Motor speed constraint

**Motor speed constraint** The motor speed of the servo motor is limited by the eigenfrequencies of the motor components and by the balancing of the rotor. The speed constraint on the servo motor is imposed as a fixed speed value. In general the motor speed is kept close to the maximum speed limit and only starts dropping in the region where the gearbox ratio can not be increased further. Keeping the motor speed high results in lower torque requirements on the motor. Low torque requirements result in smaller motors and lower

copper losses.

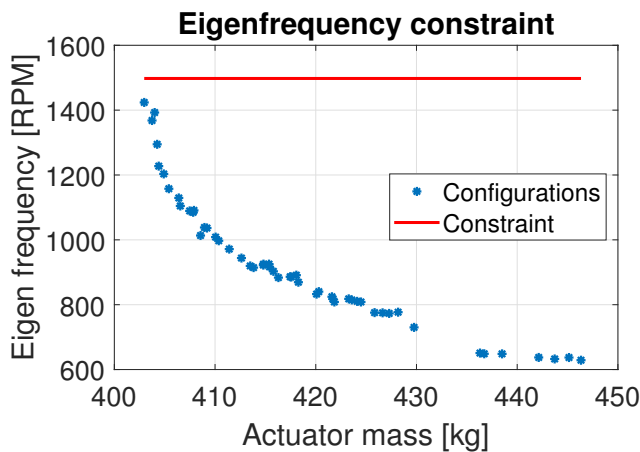


Figure 6.24: Screw eigenfrequency constraint

**Eigen frequency constraint** Just as the maximum motor speed is limited also the maximum speed of the planetary roller screw is limited by the eigenfrequency of the screw. The eigenfrequency is dependant on the length of the screw and the diameter of the screw. The maximum screw speed requirement is dependant on the actuator velocity and the mechanical cylinder transmission ratio. Decreasing the mass of the EMA is clearly limited by the eigenfrequency of the screw.

### EHA design properties

The EHA configurations show a higher actuator mass in general, however mean power of the EHA can be much lower compared to the EMA configurations. The design configurations of the EHA can be discussed with respect to a single objective again due to the properties of the Pareto front. The EHA configurations are shown separately in Figure 6.25 for clarity.

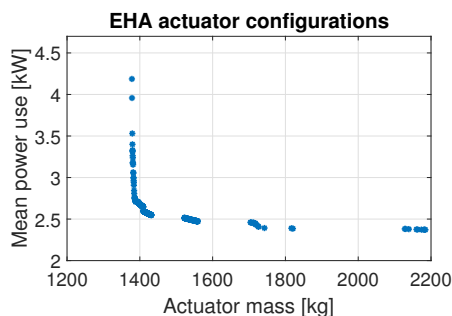


Figure 6.25: Optimized EHA configurations

The EHA configurations are optimized with respect to two design parameters. These are the hydraulic cylinder piston area  $A_p$  and the volumetric displacement of the pump  $V_g$ . The optimization parameters in the different optimized configurations are shown in Figures 6.26 and 6.27. To understand the limiting factors of

the EHA configurations, the constraints on the actuator are shown in Figure 6.28 to 6.31.

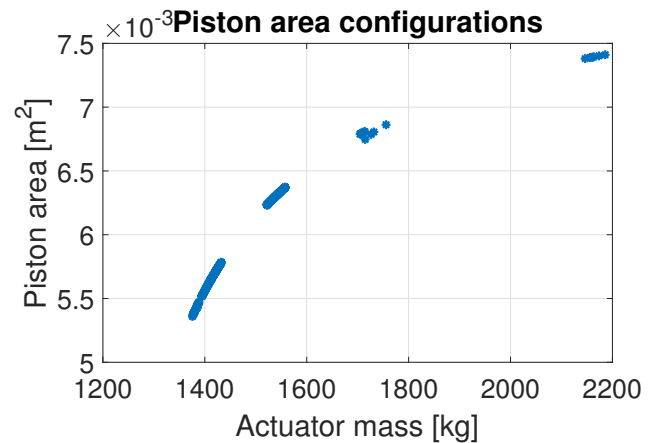


Figure 6.26: Piston area configurations

**Piston area** The mass of the EHA is seen to decrease with a decreasing piston area (see Figure 6.26). Conversely, the efficiency of the EHA increases with a larger piston area. A larger piston area means lower system pressures and a larger fluid flow. The large flow requirements however leads to a large pump and large cylinder, hence increasing the system mass. The decreased pressure also results in lower torque requirements on the motor, hence decreasing the copper losses.

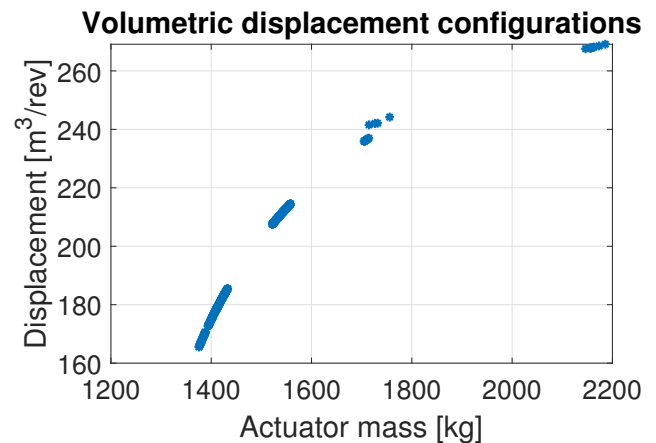


Figure 6.27: Volumetric displacement configurations

**Volumetric displacement** Increasing the piston area of the hydraulic cylinder requires a higher flow rate from the pump. As such, the volumetric displacement increases with the increase in piston area. Again, the mass is expected to increase due to the larger pump while the efficiency increases as force related losses decrease.

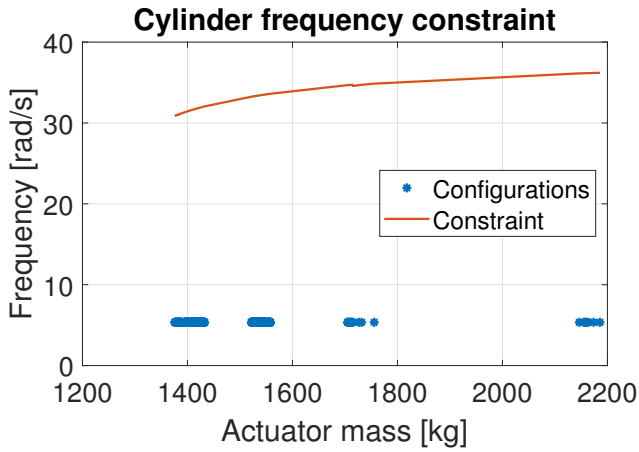


Figure 6.28: Cylinder eigenfrequency constraint

**Cylinder eigenfrequency constraint** The hydraulic cylinder has a natural frequency depending on the piston area. The eigenfrequency of the hydraulic cylinder is not reached with the acceleration profiles of the example actuator application.

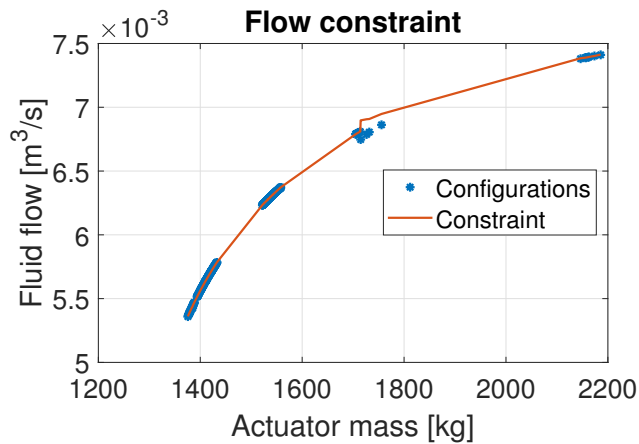


Figure 6.29: Pump flow constraint

**Pump flow constraint** The hydrostatic pump speed is limited by various factors such as lubrication and balancing limits. The speed limit of the hydrostatic piston pump is empirically determined as a function of the volumetric displacement of the pump in [118]. The maximum speed for each volumetric displacement is shown as the maximum attainable fluid flow. Maximum fluid flow is the leading limiting factor in the design of the EHA as all proposed configurations are following the constraint. A more fundamental understanding of the pump speed limitations should be developed to further optimize the EHA configuration.

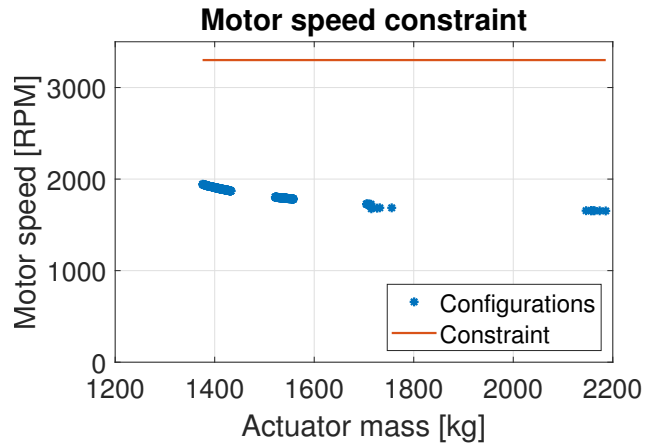


Figure 6.30: Motor speed constraint

**Motor speed constraint** Servo motor speed is constraint just as the servo motor of the EMA. Pump speed is however the leading constraint, hence critical motor speeds are not reached in the EHA configurations.

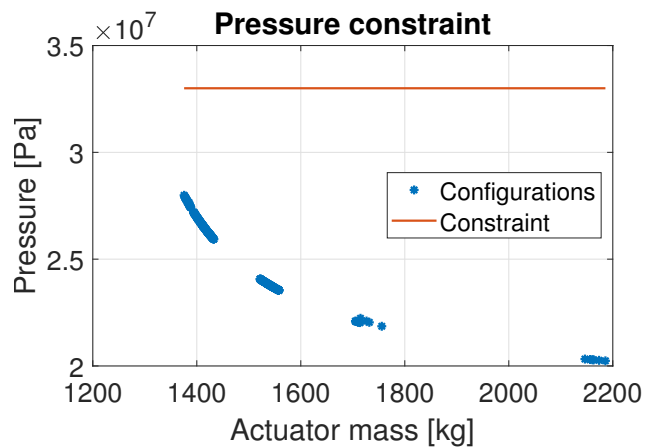


Figure 6.31: Pressure constraint

**Pressure constraint** System pressure has a direct correlation to the maximum actuator loading and the area of the hydraulic cylinder piston. System pressure can not be increased indefinitely due to safety constraints and fabrication considerations. Most hydrostatic pumps available in industry are rated to a pressure between 260 and 330[bar]. A maximum pressure of 330[bar] is imposed to limit the lower bound of the piston area. In the proposed configurations the maximum pressure constraint is never critical. The pressure constraint becomes more critical for higher load rated actuators.

## 6.4.2 Neutral configuration comparison

The neutral configuration of the EMA and EHA is the configuration in which both the mass and efficiency objective has the same weight factor in the optimization

step. The properties of the neutral configuration of both actuator types are shown in Table 6.2.

Table 6.2: Neutral configuration properties

EMA		EHA	
Property	Value	Property	Value
Mass	415[kg]	Mass	1400[kg]
Mean power	3.75[kW]	Mean power	2.5[kW]
$l_s$	4[cm]	$A_p$	56[cm <sup>2</sup> ]
$r_r$	0.42[cm]	$V_g$	175[cm <sup>3</sup> /rev]
$N_s$	10[-]		
$R_g$	3.6[-]		

The EMA has the clear mass advantage while the EHA is more efficient for the example task. Mass and power loss properties of both actuators are discussed below.

### Mass properties

The total actuator mass of the EHA is approximately 3.4 times the mass of the EMA configuration. As such the EMA configuration has the clear advantage regarding the mass objective in actuator choice. Mass of both MEA actuators is comprised of the mass of their major components. Additional masses of peripherals such as fasteners and connectors are neglected in the actuator mass models. Relative component masses of both actuators are shown in Figures 6.32 and 6.33 for the EMA and EHA respectively.

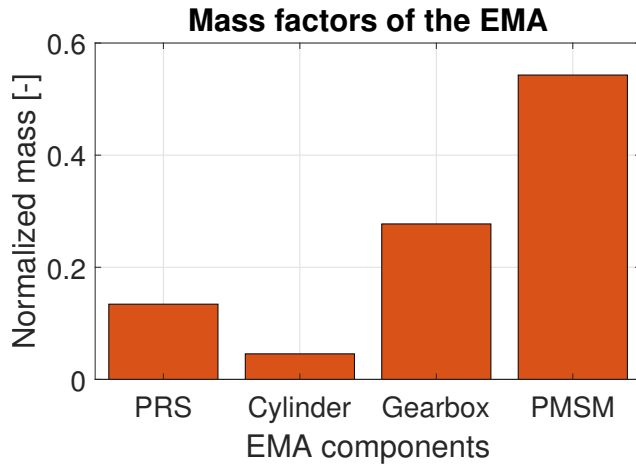


Figure 6.32: EMA mass properties

To compare both actuators, the servo motor is ideal as this component is identical in both technologies. The absolute servo motor masses are respectively 302 and 480.7[kg] for the EMA and EHA. The higher motor mass of the EHA indicates the EHA uses a lower speed higher torque motor compared to the EMA configuration. The limiting factor in the EHA is the limit on the pump rotational speed. In the EMA a reduction gearbox is used to increase the motor speed while keeping the speed of the PRS low. A possible design

iteration to decrease the EHA actuator mass could be to implement a gearbox to decrease the motor mass.

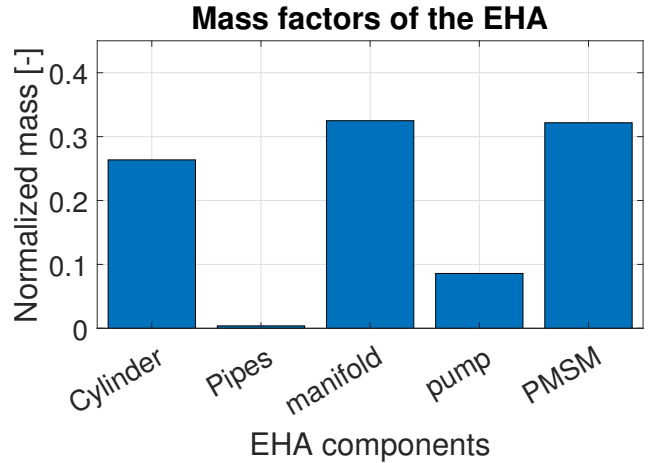


Figure 6.33: EHA mass properties

The first observation in the EHA mass is the negligible effect of the mass of hydraulic pipes. This component mass will therefore not be discussed in more detail. Mass of the EHA is determined in approximately equal parts by the hydraulic cylinder, the manifold and the servo motor. Masses of the manifold and cylinder can be decreased by decreasing the pump flow, however, this comes at a significant cost in efficiency.

The EMA mass is determined for a significant part by the mass of the servo motor followed by the mass of the gearbox. The relative high mass ratio of the motor and gearbox follow from the relative high lead of the PRS screw. The high lead results in high torque requirements and the resulting high motor mass. The high lead of the screw is necessary to increase power regeneration of the actuator. The addition of a gearbox compared to the EHA design allows to operate at the limit of the servo motor speed. The use of high speed motors in combination with higher gear ratio's therefore could decrease system mass further. As the PMSM scales with the required torque as  $m_{PMSM} \propto T^{6/7}$  and the gearbox scales initially with  $m_{gb} \propto T^{1/2}$  a mass reduction for high power applications can be expected.

### 6.4.3 Power loss properties

Power loss properties of the actuator define the mean power use for a given task. The mean power use of the EMA configuration is a factor 1.5 larger than that of the EHA configuration. The larger losses of the EMA are mainly due to more mechanical friction contacts compared to the EHA. Force and velocity related losses are discussed separately below. Power losses are defined assuming power transmission to the component is 100% efficient. Losses are normalised with respect to the output power of the actuator for ease of comparison between both actuators.

**Force related losses** Force related losses are the loss trends with respect to the working point load of the actuator. Figure 6.34 and 6.35 show the force related losses of the EMA and EHA respectively.

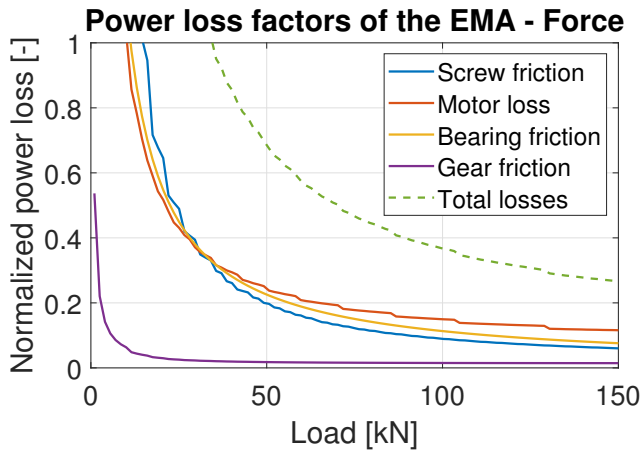


Figure 6.34: EMA power loss factors - Force

Both MEA actuators show a low load region in which the losses are much higher than the actual output power of the actuator. Back-driving the actuator in these conditions is not possible. Losses in the EMA are higher for these low load situations due to high friction terms in the PRS mechanism and the linear bearings in the mechanical cylinder. At high loading the PRS mechanism becomes more efficient making the EMA configuration better suited for applications in which loading on the actuator remains high.

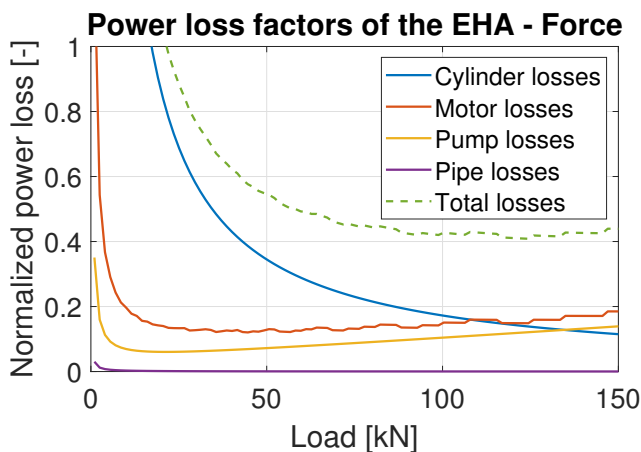


Figure 6.35: EHA power loss factors - Force

The EHA force related losses are dominated by the cylinder losses which are defined by friction forces in the linear cylinder bearings and seals. At low actuator loads the EHA is more efficient compared to the EMA, however at larger loads the volumetric losses in the pump increase. Copper losses in the motor also are higher compared to the EMA due to the high torque

low speed configuration of the EHA. The EHA is better suited for applications where loading of the actuator varies and low load conditions occur more often.

**Velocity related losses** Velocity related losses are the loss trends with respect to the working point velocity of the actuator. Figure 6.36 and 6.37 show the velocity related losses of the EMA and EHA respectively.

Velocity related losses in the EMA and EHA show largely opposite trends. As the motor speed of the EMA configuration is higher than the motor speed of the EHA, motor losses are expected to be higher in the EMA. The addition of the rolling frictional losses in the EMA screw result in decreasing efficiency with increasing speeds. The EMA is thus better suited for low velocity applications.

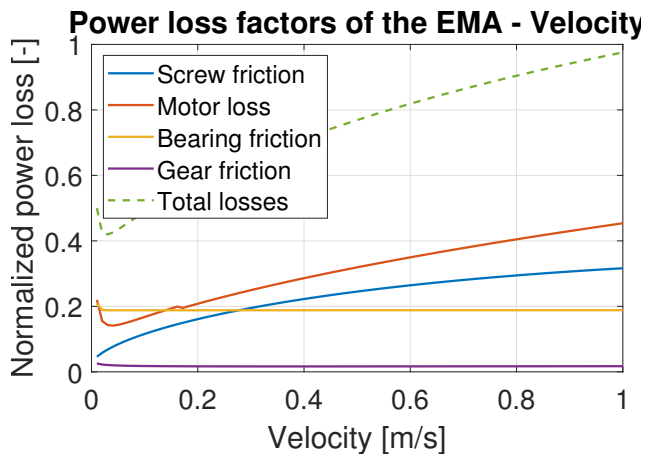


Figure 6.36: EMA power loss factors - Velocity

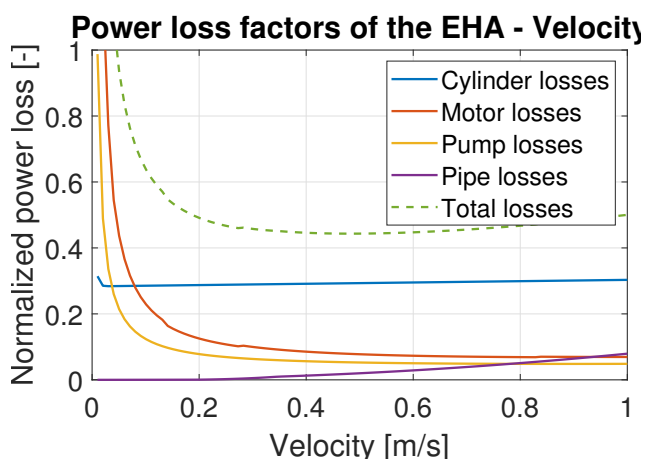


Figure 6.37: EHA power loss factors - Velocity

The EHA velocity dependant losses are shifted compared to those of the EMA due to the use of a low speed high torque configuration. Only at high velocities the flow velocity induced pressure losses become

significant making the efficiency decrease again. EHA configurations are better suited for high velocity applications compared to the EMA due to the relative constant losses at slightly higher velocities.

In both actuators, the cylinder losses (bearing friction) is linearly related to the velocity. Only at low velocities the effects of stick slip are present. This effect is much more pronounced in the EHA than in the EMA due to the larger normal forces on the linear bearings caused by the actuator weight.

#### 6.4.4 Requirement variation

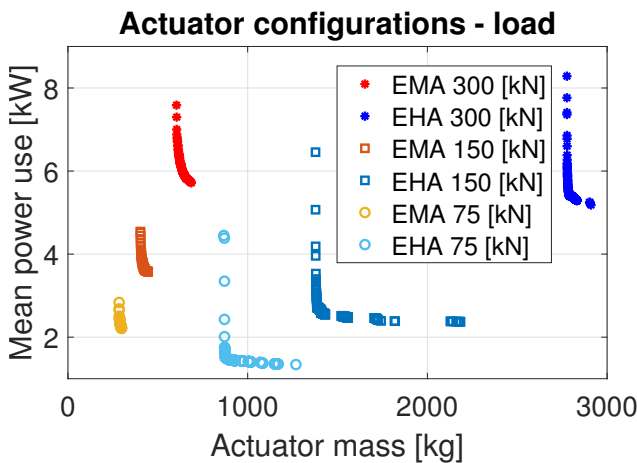


Figure 6.38: Load rating dependant actuator configurations

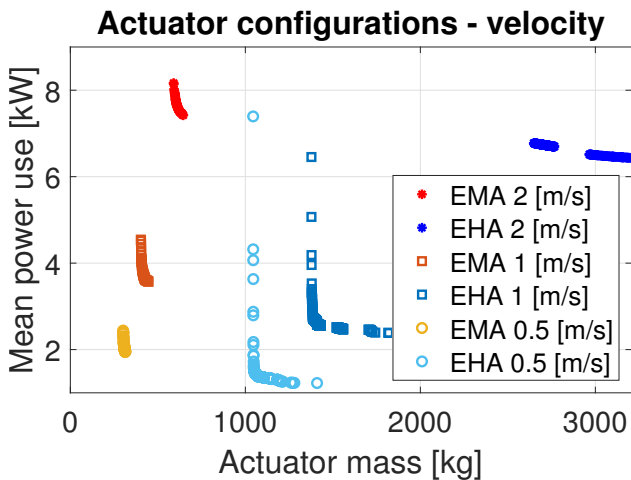


Figure 6.39: Velocity rating dependant actuator configurations

Actuator requirements determine the properties of the actuator largely. The two main actuator requirements are the load rating and the velocity rating. Figure 6.38 and 6.39 show the optimized actuator configurations for the requirements described at the start of this section and variations on the load and speed requirements

respectively. Proportionality between the actuator requirements and the task magnitudes is kept constant.

In general, the differences between the EMA and EHA properties decrease with decreasing actuator requirements. And increases with increasing actuator requirements. The EMA generally provides the more mass optimized solution while the EHA remains the more efficiency optimized solution. Upon further decreasing the actuator requirements the EMA is expected to become the optimal solution on both objectives.

## 6.5 Conclusions

This chapter uses sizing and power loss models of the electro mechanical actuator (EMA) and electro hydrostatic actuator (EHA) developed in Chapter 3 and 4 respectively to make preliminary designs of both actuator technologies for high power applications. Actuator configurations are obtained by means of an optimization process with the objective to minimize the actuator mass and maximize the actuator efficiency. A case study on an example high power linear actuator application is performed to find the optimal actuator technology for the task.

In general the EMA is seen to offer a lower actuator mass solution for high power applications while the EHA is beneficial for its higher efficiency. This statement is valid for actuators capable of delivering power in an order of magnitude of  $1e5[W]$ . The mass of the EMA is dominated by the mass of the servo motor while the mass of the EHA is defined largely by the hydraulic cylinder, manifold and servo motor mass. The lower mass of the EMA is mostly achieved by reducing the torque requirements on the drive side of the actuator. The gearbox is therefore an essential component. Further mass decrease of the EMA is limited by the maximum speed of the servo motor. In contrast, to further decrease the torque requirements of the EHA motor, the maximum speed of the hydrostatic pump should increase. A higher pump speed could increase the pump flow of the pump without increasing the volumetric displacement of the pump and therefore the pump mass.

The efficiency of the actuators is determined by the power losses in the different actuator components. The EMA is found to be better suited for applications in which the loading of the actuator is relatively constant at the high end of the load rating. For actuators where the loading varies and is often low, the EHA is found to be more efficient. On the other hand, the EMA actuator is found to be more efficient at low velocity applications, at the high end of the velocity range the losses increase significantly due to rolling friction. The EHA has less components affected by rolling friction and performs better at the higher velocity range. Stick slip behaviour at the low velocity range however results

in low EHA efficiencies at low actuator velocity.

Variation of the actuator requirements show the differences between EMA and EHA mass properties decrease with decreasing power requirements on the actuator. Upon further lowering the actuator power requirements the EMA is expected to be the optimal actuator technology on both mass and efficiency objectives. At higher power requirements the optimal actuator choice is dependant on the importance of one objective over the other.

**Future work** In running the preliminary design tool on the example actuator requirements, some critical factors in the design of the EMA and EHA are found. The general trend to decrease actuator mass is to carry the actuator power in the velocity terms. In the EMA

the rotational speed of the mechanical cylinder screw is mainly limited by the eigenfrequency of the screw. The current model optimizes the screw diameter for the load rating. Later model iterations could look at the effect of optimizing the screw diameter for the eigenfrequency requirements. In the EHA, the speed constraint is mainly imposed by the speed limitation of the hydrostatic pump. The current model implements this constraint with an empirical relation found in [118]. Future research could look into a physics based maximum operating speed model of the hydrostatic piston pump. An increase of the pump speed has the potential to reduce EHA actuator mass significantly making the EHA the optimal choice in high power applications. Alternatively, future research could look into the effects of adding a gearbox between the motor and pump to decrease torque requirements and mass of the motor.

# Chapter 7

## Conclusion

High power linear actuation is often dominated by conventional hydraulics due to widely available hydraulic parts and the well known properties of the technology. From current trends in the aviation industry, decentralised electric actuators are shown to have advantages on both actuator mass and efficiency over these common conventional hydraulic actuators. The electro mechanical actuator (EMA) and the electro hydrostatic actuator (EHA) are two electric decentralised actuator technologies which are mentioned in aviation related literature. Existing literature only exists for these actuators up to power levels of 45[kW], for higher power requirements the advantages of one over the other technology are not clear.

Ampelmann currently uses conventional hydraulic actuation on the majority of their motion compensation systems. To optimize the mass and efficiency of the platforms, possible new actuator technologies can be evaluated to replace the conventional hydraulic system. The initial focus on actuator replacements is put on the Ampelmann A type hexapod platform which is driven by 6 linear actuators each capable of delivering 150[kW]. The required power levels hence exceed existing literature on the EMA and EHA by a factor 3.

This report details a new method to generate preliminary actuator designs based on the maximum power requirements posed on the actuator and a task time series representing the working conditions of the actuator. The generated designs are optimized to minimize the actuator mass and to maximize the actuator round trip efficiency. To develop the preliminary design tool, actuator sizing and power loss models are developed in Chapters 3 and 4 for the EMA and EHA transmission respectively. The actuator models are implemented in the optimization based preliminary design tool in Chapter 6.

From the optimized actuator configurations based on the Ampelmann A-type actuator requirements, some general trends are found. In general, the EMA provides a more mass optimized actuator solution compared to the EHA. This lower mass solution however comes at the cost of a lower actuator efficiency. The EHA therefore provides the more efficiency optimized actuator configurations.

The lower mass of the EMA configurations is largely dependant on the use of a reduction gearbox between the motor and screw. The reduction gearbox ensures the motor is capable of operating at high speed and relatively low torque which is beneficial for the motor mass. In contrast, the motor speed of the EHA is limited by the speed limit of the pump. Pump speed is clearly found to be a limiting factor in decreasing the EHA mass. However, the mass of the EHA is also defined for a large part by the hydraulic cylinder mass and the manifold mass. Especially the manifold mass increases the EHA mass significantly. Mass of the manifold is modelled very crude in the current EHA model. Future research could look into the detailed physical properties which determine the manifold mass.

Mean power use of the actuators is defined by the power losses in the actuator. Power losses of the EMA configurations are generally larger than the power losses of the EHA configurations for high power applications. Based on the loss trends of both actuators, the EMA is better suited for applications where the load on the actuator is relatively constant towards the high end of the permissible actuator load and the velocity remains low. The EHA in contrast is better suited in applications where the load varies across the entire load range. Especially in the low load range, the EHA actuator becomes more efficient faster. Also at high velocities the EHA performs better compared to the EMA configurations.

The linear actuators used in the Ampelmann A-type hexapod are loaded differently due to the overhanging weight of the gangway. In general, the hexapod actuators are loaded with a constant compressive force. This is

however not true for one or two actuators placed at the opposite end of the gangway. These actuators experience forces in both tension and compression at a relatively low magnitude. An example task time series describing the time dependant loading and velocity of the linear hexapod actuator is shown in Appendix E.2. According to the power loss trends discussed above, the EMA actuator is better suited for the hexapod actuators under constant compressive loads while the EHA is better suited for the actuators with varying loading direction. Figure 7.1 shows the different optimized actuator configurations for the A-type hexapod applications. The high load configurations are optimized for the highest loaded actuator under constant compression force. The low load configurations are optimized for the lowest loaded actuator in the hexapod where the load direction changes. As the loading of the different hexapod actuators changes with the rotation of the platform, in practice, actuators can not be optimized for specific load conditions. The mean load configurations are optimized for all the load conditions combined. These configurations provide the best actuators for the general A-type hexapod actuator.

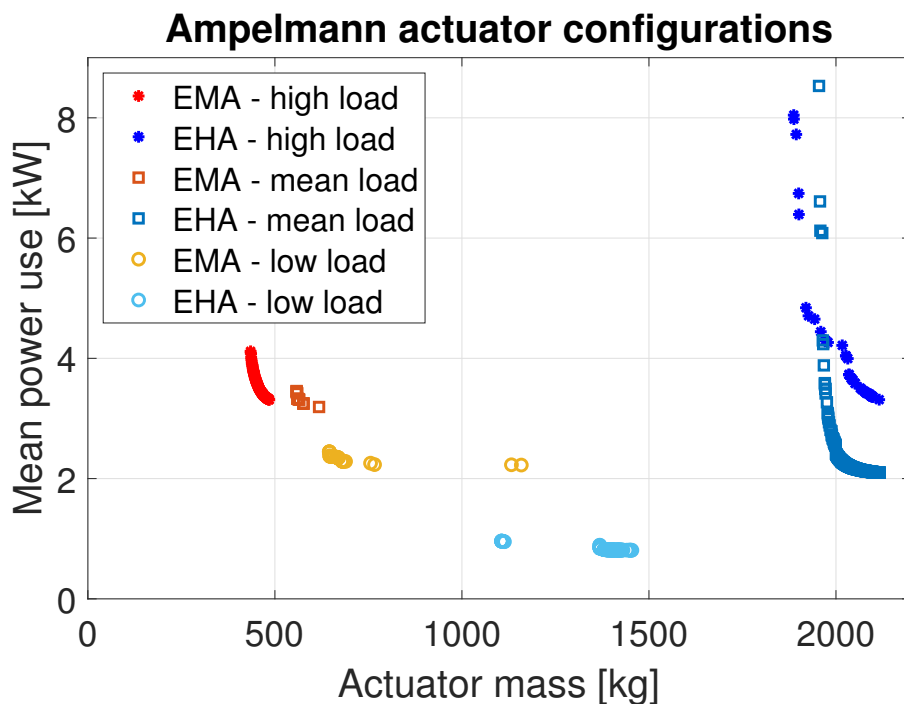


Figure 7.1: Ampelmann A-type hexapod actuator configurations.

Directly comparing the mean power use of the different actuator loading configurations is not possible as the power output of these different actuators is different. However, comparing the same loading configurations between the EMA and EHA is possible. For the low load configurations, the difference between the EMA and EHA masses decreases significantly. The relative high mass of the EMA configurations is explained by the high screw lead to enable back driving the actuator at low loads. The resulting high torque on the motor results in a high actuator mass. For the low load applications, the choice for EMA or EHA is highly dependant on the importance of actuator mass versus power use. In the high load application, the EMA and EHA mean power use becomes very similar. Due to the much lower mass of the EMA this technology is the preferred actuator type for this application.

For the general A-type actuator, the general actuator properties found before are valid. The EMA provides a more mass optimized solution while the EHA has a much higher mass but a lower mean power use for the same task. The choice between actuator technology hence depends on the importance of the mass over the efficiency properties. The weight factor of these two objectives is not fixed for every A-type hexapod application. Depending on the size of the ship, the mounting location of the platform and the function of the ship either mass or efficiency becomes the leading decision parameter. Especially on ships where the A-type is mounted on a pedestal, stability requirements make the system mass critical. On smaller ships the power availability from the ship might become a critical factor. If the ship is unable to deliver the required power additional diesel generators are needed increasing the total system mass.

## 7.1 Future work

From the development of the preliminary sizing tool and from the resulting preliminary designs, missing or incomplete knowledge can be identified. These knowledge gaps should be further researched in future work. For the interested reader and researcher, the most important knowledge gaps to be addressed in future research are summed in this section.

In modelling the preliminary design tool, the focus of actuator choice criteria is put on the actuator mass and actuator mean power losses. Except for these properties, other actuator properties are important too. In the current models, actuator stiffness in relation to control of the actuator is neglected. Actuator stiffness can be a limiting factor in which actuator technology can be used in certain applications. Future work could model control stiffness of both actuator types and implement a constraint to ensure proper controllability of the actuator. Another suggestion is the reliability of the actuator systems. Reliability of the EHA is already researched and described in aviation related literature. Reliability of the EMA however is less proven. The critical unknown part with respect to reliability is the planetary roller screw (PRS). The current EMA models design the PRS towards a desired lifetime with 99% reliability. The PRS design for reliability is however highly theoretical, and real experimental validation of the reliability of the planetary roller screw at these power levels is lacking in literature. Future research could look at a theoretical model describing the failure mechanisms of the PRS and experimental validation of PRS reliability.

In the current preliminary design tool some model simplifications prove to be of high importance in determining the total actuator mass. The three main simplifications which should be addressed in later model revisions are the critical pump speed limit, the mass modelling of the hydraulic manifold and the gearbox implementation. The critical pump speed is seen to be a limiting factor in the design of the EHA. The current pump speed is modelled by an empirical data fit described in [118]. As the pump speed proves to be a critical factor in the EHA design, a theoretical model describing the critical pump speed could be developed and implemented in the optimization step of the EHA design. Similarly, the manifold mass in the EHA is seen to account for approximately  $1/3^{th}$  of the total EHA mass. Mass of the manifold is determined based on a simple data fit as explained in Chapter 4. A proper physics based model of the hydraulic manifold would increase the accuracy of the EHA mass results significantly. The final major simplification to be addressed in future model iterations is the implementation of the gearbox. In the current model, a single stage gearbox is assumed with a fixed distance between the gear pair axis. In practice, the use of a single stage gearbox is unrealistic and limits the attainable gear ratio's significantly. Implementing a variable number of gear stages in the gearbox as an optimization parameter in the mass and power loss models of the gearbox is a valuable addition to the preliminary design tool.

Above future research suggestions all concern the developed EMA and EHA models. However, the modelled actuators only cover a single version of the EMA and EHA. Later model iterations could also look into different actuator implementations. For the EHA, especially the variable pump fixed motor (VPFM) architectures are promising to decrease losses in the motor. For the EMA, different implementations of the mechanical cylinder could be studied to compare EMA properties with ballscrews and PRS. Implementing the screw transmission with a hydrostatic screw also has the potential of reducing friction losses in the screw compared to the PRS implementation. Different implementations of the EMA and EHA actuators are discussed in detail in the literature report preceding this report: 'Linear high power actuator technology for application in the Ampelmann hexapod' (Appendix G).

# Bibliography

- [1] Amacoil - linear drives for reciprocating and indexing linear motion. <https://www.amacoil.com/products/rg-linear-drives/>. Accessed: 16-03-2020.
- [2] Ampelmann operations b.v. - motion compensated gangways. <https://www.ampelmann.nl/>. Accessed: 14-05-2020.
- [3] Exlar lineaire rollerscrew actuators. <https://atbautomation.eu/nl/exlar/>. Accessed: 16-04-2020.
- [4] understanding inertia ratio in synchronous motor control. [https://www.se.com/in/en/download/document/998-2095-07-08-12AR0\\_EN/](https://www.se.com/in/en/download/document/998-2095-07-08-12AR0_EN/), Oct 2010. Accessed: 18-11-2020.
- [5] Engineering essentials: Fundamentals of hydraulic pumps. <https://www.hydraulicspneumatics.com/fluid-power-basics/article/21884136/engineering-essentials-fundamentals-of-hydraulic-pumps>, Jan 2012. Accessed: 08-06-2020.
- [6] Roller screw, wikipedia. [https://en.wikipedia.org/wiki/Roller\\_screw](https://en.wikipedia.org/wiki/Roller_screw), Oct 2019. Accessed: 28-06-2020.
- [7] Drivelines - what's the difference between a ball screw and a lead screw? <https://drivelines.co.uk/ball-lead-screw/>, Feb 2020. Accessed: 16-04-2020.
- [8] Linear actuator, wikipedia. [https://en.wikipedia.org/wiki/Linear\\_actuator](https://en.wikipedia.org/wiki/Linear_actuator), Mar 2020. Accessed: 02-03-2020.
- [9] Mohd Arif Abu Hassan, Abdul Rahim Abdullah, Nurhazilina Bahari, and Muhammad Ihsan Mohd Sabri. Efficiency Comparison of Trapezoidal and Sinusoidal Method for Brushless DC Motor Drive. *Applied Mechanics and Materials*, 785(July):248–252, 2015.
- [10] Mohammad Abuhaiba. *Mathematical Modeling and Analysis of a Variable Displacement Hydraulic Bent Axis Pump Linked to High Pressure and Low Pressure Accumulators*. PhD thesis, University of Toledo, 2009.
- [11] Peter Achten, Robin Mommers, Kim Stelson, and Katharina Schmitz. MEASURING THE LOSSES OF HYDROSTATIC PUMPS AND MOTORS. pages 1–11, 2019.
- [12] Hamid Afshari, Warren Hare, and Solomon Tesfamariam. Constrained multi-objective optimization algorithms: Review and comparison with application in reinforced concrete structures. *Applied Soft Computing Journal*, 83(July), 2019.
- [13] AIR5713. *In-Service Reliability Data of Continuously Active Ballscrew and Geared Flight Control Actuation Systems*, jul 2006.
- [14] T. H. Akinaga, C. Pompermaier, F. J.H. Kalluf, and M. V. Ferreira Da Luz. Performance evaluation of brushless DC permanent magnet motor using Finite Element Method. *2011 IEEE International Electric Machines and Drives Conference, IEMDC 2011*, (April 2017):1165–1170, 2011.
- [15] Faisal Al-Ghathian and Muafag S. Tarawneh. Friction Forces in O-ring Sealing. *American Journal of Applied Sciences*, 2(3):626–632, 2005.
- [16] Ralph (Lockheed) Alden. C-141 AND C-130 POWER-BY-WIRE FLIGHT CONTROL SYSTEMS. *Lockheed Aeronautical Systems Company Marietta, Georgia 30063*, (Reference 1):535–539, 1991.
- [17] Gabriele Altare and Andrea Vacca. A Design Solution for Efficient and Compact Electro-hydraulic Actuators. *Procedia Engineering*, 106:8–16, 2015.

- [18] Sören Andersson, Anders Söderberg, and Stefan Björklund. Friction models for sliding dry, boundary and mixed lubricated contacts. *Tribology International*, 40(4):580–587, 2007.
- [19] Charles Bartel and Dan Foster. Life cycle motion base cost comparison: Electric vs. Hydraulic.
- [20] Abdullahi Maikanti Baru. An Investigation of Buckling Phenomenon in Steel Elements and Society An Investigation of Buckling Phenomenon in Steel Elements Abdullahi Maikanti Baru. (April), 2017.
- [21] R Bassani. The self - regulated hydrostatic screw and nut. (August):185–190, 1979.
- [22] Alireza R. Behbahani and Kenneth J. Semega. Control strategy for electro-mechanical actuators versus hydraulic actuation systems for aerospace applications. *SAE Technical Papers*, 2010.
- [23] Joseph T. Belter and Aaron M. Dollar. A passively adaptive rotary-to-linear continuously variable transmission. *IEEE Transactions on Robotics*, 30(5):1148–1160, 2014.
- [24] Naourez Ben Hadj, Rihab Abdelmoula, Mohamed Chaieb, and Rafik Neji. Permanent magnet motor efficiency map calculation and small electric vehicle consumption optimization. *Journal of Electrical Systems*, 14(2):127–147, 2018.
- [25] J. W. Bennett, B. C. Mecrow, D. J. Atkinson, and G. J. Atkinson. Safety-critical design of electromechanical actuation systems in commercial aircraft. *IET Electric Power Applications*, 5(1):37–47, 2011.
- [26] M Bildstein. A built-in testable jam release device for electromechanical actuators in flight control application. In *6th International Conference on Recent Advances in Aerospace Systems and Components, Toulouse: Service Communication*, pages 105–108, 2014.
- [27] Mohammad Mahdi Bouiabady and Aliakbar Damaki Aliabad. Switched Reluctance Motor Topologies: A Comprehensive Review. In *Intech*, volume 1, page 13. 2016.
- [28] Bert Brahmer. On Adaptive Electro Hydrostatic Actuators. *Proceedings of the 11th International Fluid Power Conference*, pages 427–435, 2018.
- [29] J. Brnic, M. Canadija, G. Turkalj, and D. Lanc. 50CrMo4 steel-determination of mechanical properties at lowered and elevated temperatures, creep behavior, and fracture toughness calculation. *Journal of Engineering Materials and Technology, Transactions of the ASME*, 132(2):0210041–0210046, 2010.
- [30] M. Budinger, J. Liscouët, F. Hospital, and J. C. Maré. Estimation models for the preliminary design of electromechanical actuators. *Proceedings of the Institution of Mechanical Engineers, Part G: Journal of Aerospace Engineering*, 226(3):243–259, 2012.
- [31] Roberto Caracciolo and Dario Richiedi. Optimal design of ball-screw driven servomechanisms through an integrated mechatronic approach. *Mechatronics*, 24(7):819–832, 2014.
- [32] Imon Chakraborty, David Jackson, David Trawick, and Dimitri N. Mavris. Development of a sizing and analysis tool for electrohydrostatic and electromechanical actuators for the more electric aircraft. *2013 Aviation Technology, Integration, and Operations Conference*, pages 1–17, 2013.
- [33] Imon Chakraborty, David Trawick, David Jackson, and Dimitri N. Mavris. Electric control surface actuator design optimization and allocation for the more electric aircraft. *2013 Aviation Technology, Integration, and Operations Conference*, pages 1–17, 2013.
- [34] Qun Chao, Junhui Zhang, Bing Xu, Yaoxing Shang, Zongxia Jiao, and Zhihui Li. Load-sensing pump design to reduce heat generation of electro-hydrostatic actuator systems. *Energies*, 11(9):1–13, 2018.
- [35] Akira Chiba, Yuichi Takano, Motoki Takeno, Takashi Imakawa, Nobukazu Hoshi, Masatsugu Takemoto, and Satoshi Ogasawara. Torque density and efficiency improvements of a switched reluctance motor without rare-earth material for hybrid vehicles. *IEEE Transactions on Industry Applications*, 47(3):1240–1246, 2011.
- [36] Mateus Cirolini, Aly Ferreira Flores Filho, Yi Chen Wu, and David G. Dorrell. Design Aspects of a Reluctance-Based Magnetic Lead Screw. *IEEE Transactions on Magnetics*, 55(7):1–6, 2019.
- [37] K. G. Cleasby and A. R. Plummer. A novel high efficiency electrohydrostatic flight simulator motion system. *ASME/BATH 2008 Symposium on Fluid Power and Motion Control*, (Fpmc 2008):437–449, 2008.

- [38] Olaf Cochoy, Susan Hanke, and Udo B. Carl. Concepts for position and load control for hybrid actuation in primary flight controls. *Aerospace Science and Technology*, 11(2-3):194–201, 2007.
- [39] Carlos A. Coello Coello, Gregorio Toscano Pulido, and Maximino Salazar Lechuga. Handling multiple objectives with particle swarm optimization. *IEEE Transactions on Evolutionary Computation*, 8(3):256–279, 2004.
- [40] Danielle Collins. L10 bearing life: What are some alternative life calculations? <https://www.linearmotiontips.com/what-are-some-alternatives-to-l10-bearing-life/>, Mar 2020. Accessed: 24-07-2020.
- [41] A.D. Core, editor. *Advances in onboard systems technology*. European Commission Aeronautics Research Series. Wiley, 1996.
- [42] Karolis Dambrauskas, Jonas Vanagas, Tomas Zimnickas, Arturas Kalvaitis, and Mindaugas Azubalis. A Method for Efficiency Determination of Permanent Magnet Synchronous Motor. *Energies*, page 15, 2020.
- [43] Buick Davison and Graham .W. Owens. *Steel Designers Manual*, volume 6. 2003.
- [44] Stijn Derammelaere, Michiel Haemers, Jasper De Viaene, Florian Verbelen, and Kurt Stockman. A quantitative comparison between BLDC, PMSM, brushed DC and stepping motor technologies. *19th International Conference on Electrical Machines and Systems, ICEMS 2016*, 2017.
- [45] Jean Claude Derrien. Electro Mechanical Actuator ( EMA )advanced technologies for flight controls. *28th Congress of the International Council of the Aeronautical Sciences 2012, ICAS 2012*, 5:3843–3852, 2012.
- [46] DNV GL AS. Class Guideline Hydraulic cylinders. (December), 2015.
- [47] Dennis Doberstein and Frank Thielecke. Model based design and experimental validation of electro-mechanic actuator systems for a nose landing gear. *28th Congress of the International Council of the Aeronautical Sciences 2012, ICAS 2012*, 5:3797–3806, 2012.
- [48] Jinhua Du Kezhi Yang, Deliang Liang, and Naming Zhang. Modeling of electromechanical actuators using multi-body dynamics. *2017 20th International Conference on Electrical Machines and Systems, ICEMS 2017*, 2017.
- [49] H. R. El-Sayed and H. A. Khataan. The running performance of externally pressurized power screws. *Wear*, 39(2):285–306, 1976.
- [50] (Exlar). Planetary Roller Screws Exlar — Your Linear Motion Experts. *Exlar*, 2011.
- [51] Meng Fanliang. *Actuation system design with electrically powered actuators*. PhD thesis, 2011.
- [52] Eric L. Faulring, J. Edward Colgate, and Michael A. Peshkin. Control and performance of the rotational-to-linear Cobotic transmission. *Proceedings - IEEE Virtual Reality*, 2006:85, 2006.
- [53] Eric L. Faulring, J. Edward Colgate, and Michael A. Peshkin. Power efficiency of the rotational-to-linear infinitely variable cobotic transmission. *Journal of Mechanical Design, Transactions of the ASME*, 129(12):1285–1293, 2007.
- [54] Eric L. Faulring, J. Edward Colgate, and Michael A. Peshkin. High performance Cobotics. *Proceedings of the 2005 IEEE 9th International Conference on Rehabilitation Robotics*, 2005:143–148, 2005.
- [55] Roy Featherstone. *The Ring Screw Mechanism Finding the Lines*. PhD thesis, Instituto Italiano di Tecnologia, 2018.
- [56] Forår. Dynamic Modelling. In *Fluid Power Systems*, pages 1–14. 2003.
- [57] Gregory L. Fronista and Graham Bradbury. Electromechanical actuator for a transport aircraft spoiler surface. *Proceedings of the Intersociety Energy Conversion Engineering Conference*, 1(September):694–698, 1997.
- [58] Jian Fu, Jean Charles Maré, and Yongling Fu. Modelling and simulation of flight control electromechanical actuators with special focus on model architecting, multidisciplinary effects and power flows. *Chinese Journal of Aeronautics*, 30(1):47–65, 2017.
- [59] Yongling Fu, Bin Yang, Haitao Qi, and Ye Zhang. Optimization of the control strategy for EHA-VPVM system. *Proceedings of 2011 International Conference on Electronic and Mechanical Engineering and Information Technology, EMEIT 2011*, 4(6):1856–1859, 2011.

- [60] Dudley D. Fuller. 2d. Coefficients of Friction. In *AMERICAN INSTITUTE OF PHYSICS HANDBOOK*, chapter 2d, pages 151–151. Columbia University, 1972.
- [61] Jihad Furqani and Agus Purwadi. Review of Switched Reluctance Motor Control for Acoustic Noise and Vibration Reduction. *International Journal of Sustainable Transportation Technology*, 1(2):59–62, 2018.
- [62] Evgeni D. Ganev and Bulent Sarioglu. *Improving peak power capability of an aircraft*. PhD thesis, 2010.
- [63] A. Garcia, J. Cusidó, J. A. Rosero, J. A. Ortega, and L. Romeral. Reliable electro-mechanical actuators in aircraft. *IEEE Aerospace and Electronic Systems Magazine*, 23(8):19–25, 2008.
- [64] Francisco M. Garcia-Guevara, Francisco J. Villalobos-Piña, Ricardo Alvarez-Salas, Eduardo Cabal-Yepez, and Mario A. Gonzalez-Garcia. Stator Fault Detection in Induction Motors by Autoregressive Modeling. *Mathematical Problems in Engineering*, 2016(April), 2016.
- [65] V Van Geffen. A study of friction models and friction Compensation. *A study of friction models and friction Compensation*, pages 1–24, 2009.
- [66] Chris Gerada, Keith Bradley, Chris Whitley, and Graham Towers. Integrated machine design for electro mechanical actuation. *IEEE International Symposium on Industrial Electronics*, pages 1305–1310, 2007.
- [67] David Gerada, Zeyuan Xu, Dmitry Golovanov, and Chris Gerada. Comparison of electrical machines for use with a high-horsepower marine engine turbocharger. *2018 25th International Workshop on Electric Drives: Optimization in Control of Electric Drives, IWED 2018 - Proceedings*, 2018-Janua:1–6, 2018.
- [68] Igor (Tolomatic) Gilkin. Leadscrew Basics. *Machine Design*, pages 57–58, 2009.
- [69] Qingbo Guo, Chengming Zhang, Liyi Li, Jiangpeng Zhang, and Mingyi Wang. Maximum Efficiency Control of Permanent-Magnet Synchronous Machines for Electric Vehicles. *Energy Procedia*, 105:2267–2272, 2017.
- [70] Yunxiao Hao, Long Quan, Hang Cheng, Lianpeng Xia, Lei Ge, and Bin Zhao. Potential energy directly conversion and utilization methods used for heavy duty lifting machinery. *Energy*, 155:242–251, 2018.
- [71] T.A. Harris and M.N. Kotzalas. *Advanced Concepts of Bearing Technology: Rolling Bearing Analysis, Fifth Edition*. Rolling Bearing Analysis, Fifth Edition. CRC Press, 2006.
- [72] Hao He, Jiao Yu Liu, Xian Xi Pan, and Li Min Kan. Design of permanent magnet synchronous motor servo system. *Advanced Materials Research*, 986-987(1):1067–1070, 2014.
- [73] Elco Heijmink. *The Ring Screw. Modelling, Development and Evaluation of a Novel Screw Transmission*. PhD thesis, Delft University of Technology, 2018.
- [74] Marius Hendriksen and Thomas Wintjes. Developments in electromechanical and electrofluid driven linear actuators. Technical report, Rexroth, 2018.
- [75] D. Howe. Magnetic actuators. *Sensors and Actuators, A: Physical*, 81(1):268–274, 2000.
- [76] Wunong Hu, Lei Zhou, Yisong Tian, Zongxia Jiao, Yaoping Shang, Zengning Song, and Liang Yan. Analysis for the power loss of electro hydrostatic actuator and hydraulic actuator. *IEEE/ASME International Conference on Advanced Intelligent Mechatronics, AIM*, 2015-Augus(2):613–616, 2015.
- [77] Surong Huang, Jian Luo, Franco Leonardi, and Thomas A. Lipo. A general approach to sizing and power density equations for comparison of electrical machines. *IEEE Transactions on Industry Applications*, 34(1):92–97, 1998.
- [78] Y. Huang, D. M. Pool, O. Stroosma, Q. P. Chu, and M. Mulder. Modeling and simulation of hydraulic hexapod flight simulator motion systems. *AIAA Modeling and Simulation Technologies Conference*, (January):1–15, 2016.
- [79] Jui Pin Hung, James Shih-Shyn Wu, and Jerry Y. Chiu. Impact failure analysis of re-circulating mechanism in ball screw. *Engineering Failure Analysis*, 11(4):561–573, 2004.
- [80] Mads Hvaldal. Friction modelling and parameter estimation for hydraulic asymmetrical cylinders. page 110, 2011.
- [81] Hyprostatik. Hydrostatic lead screws and corresponding bearing.
- [82] (SAE international). SAE ARP 4895 - Rev.B, 2019.

- [83] Aitor Isturiz, Javier Vinals, Jose Manuel Abete, and Aitzol Iturrospe. Health monitoring strategy for electromechanical actuator systems and components. Screw backlash and fatigue estimation. *Recent Advances in Aerospace Actuation Systems and Components*, 2012.
- [84] Heon Sul Jeong. A novel performance model given by the physical dimensions of hydraulic axial piston motors: Model derivation. *Journal of Mechanical Science and Technology*, 21(1):83–97, 2007.
- [85] A Jimenez, E Novilo, E Aguado, and E Morante. Electromechanical actuator with anti-jamming system for safety critical aircraft applications. In *Proceedings of the 5th International Conference on Recent Advances in Aerospace Actuation Systems and Components*, pages 77–83, 2014.
- [86] Wenjing Jin, Yan Chen, and Jay Lee. Msec2013-1252 Methodology for Ball Screw Component Health Assessment and Failure. pages 1–9, 2017.
- [87] Matthew H. Jones and Steven A. Velinsky. Kinematics of roller migration in the planetary roller screw mechanism. *Journal of Mechanical Design, Transactions of the ASME*, 134(6):1–6, 2012.
- [88] Matthew H. Jones, Steven A. Velinsky, and Ty A. Lasky. Dynamics of the planetary roller screw mechanism. *Journal of Mechanisms and Robotics*, 8(1):1–6, 2016.
- [89] Xianmin Kang, Weiping Fu, Dacheng Wang, and Jiansheng Wang. Analysis on the influence of the recirculation mechanism’s position on the friction torque fluctuation in ball screw. *Advanced Materials Research*, 472-475:2663–2669, 2012.
- [90] Velibor Karanović, Mitar Jocanović, and Vukica Jovanović. Review of development stages in the conceptual design of an electro-hydrostatic actuator for robotics. *Acta Polytechnica Hungarica*, 11(5):59–79, 2014.
- [91] A. Karaszkiwicz. Hydrodynamic lubrication of rubber seals for reciprocating motion; leakage of seals with an O-ring. *Tribology International*, 21(6):361–367, 1988.
- [92] H. Kauranne, J. Kajaste, and M. Vilenius. *Hydraulikan perusteet*. WSOY, 2006.
- [93] Medhat K. Bahr Khalil. Estimated versus Calculated Viscous Friction Coefficient in Spool Valve Modeling. In *IFPE2008*, pages 1–9, 2008.
- [94] Zoltan Korka. Efficiency Investigation on a Helical Gear Transmission. (October):55–66, 2017.
- [95] R. Krishnan. Selection Criteria for Servo. *IEEE Transaction on Industry Applications*, 23:270–275, 1987.
- [96] Ramu Krishnan. Application Characteristics of Permanent Magnet Synchronous and Brushless dc Motors for Servo Drives. *IEEE Transactions on Industry Applications*, 27(5):986–996, 1991.
- [97] Waldemar Latas and Jerzy Stojek. A new type of hydrokinetic accumulator and its simulation in hydraulic lift with energy recovery system. *Energy*, 153:836–848, 2018.
- [98] Pierre C. Lemor. Roller screw, an efficient and reliable mechanical component of electro-mechanical actuators. *Proceedings of the Intersociety Energy Conversion Engineering Conference*, 1:215–220, 1996.
- [99] GA Levit et al. Recirculating ball screw and nut units. *Machines and Tooling*, 34(4):3–8, 1963.
- [100] Jianming Li, Zhiyuan Yu, Yuping Huang, and Zhiguo Li. A review of electromechanical actuation system for more electric aircraft. *AUS 2016 - 2016 IEEE/CSAA International Conference on Aircraft Utility Systems*, pages 490–497, 2016.
- [101] M. C. Lin, B. Ravani, and S. A. Velinsky. Design of the ball screw mechanism for optimal efficiency. *Journal of Mechanical Design, Transactions of the ASME*, 116(3):856–861, 1994.
- [102] M. C. Lin, B. Ravani, and S. A. Velinsky. Kinematics of the ball screw mechanism. *Journal of Mechanical Design, Transactions of the ASME*, 116(3):849–855, 1994.
- [103] Franciscus Leendert Johannes Linden, Nikolaus Dreyer, and André Dorkel. EMA Health Monitoring: An overview. *Recent Advances in Aerospace Actuation Systems and Components*, pages 21–26, 2016.
- [104] I von Linsingen. *Fundamentos de Sistemas Hidráulicos*. Universidade Federal de Santa Catarina, 3th edition, 2008.

- [105] J. Liscouët, J. C. Maré, and S. Orioux. Automated generation, selection and evaluation of architectures for electromechanical actuators. *ICAS Secretariat - 26th Congress of International Council of the Aeronautical Sciences 2008, ICAS 2008*, 6:610–619, 2008.
- [106] Jonathan Liscouët, Marc Budinger, Jean Charles Maré, and Stéphane Orioux. Modelling approach for the simulation-based preliminary design of power transmissions. *Mechanism and Machine Theory*, 46(3):276–289, 2011.
- [107] Yanqiang Liu, Jianshen Wang, Hongxun Cheng, and Yapeng Sun. Kinematics analysis of the roller screw based on the accuracy of meshing point calculation. *Mathematical Problems in Engineering*, 2015:1–11, 2015.
- [108] D. Lovrec and S. Ulaga. Pressure control in hydraulic systems with variable or constant pumps? *Experimental Techniques*, 31(2):33–41, 2007.
- [109] G. Lundberg and A. Palmgren. *Dynamic Capacity of Roller Bearings*. Ingeniörsvetenskapakademiens handlingar. Generalstabens litografiska anstalts förlag, 1947.
- [110] J-C. Maré M. Budinger, J. Liscouët, S. Orioux. Automated Preliminary Sizing of Electromechanical Actuator Architectures. *ELECTRIMACS 2008 Conference*, page 6, 2008.
- [111] Shangjun Ma, Geng Liu, Ruiting Tong, and Xiaojun Fu. A frictional heat model of planetary roller screw mechanism considering load distribution. *Mechanics Based Design of Structures and Machines*, 43(2):164–182, 2015.
- [112] Shangjun Ma, Tao Zhang, Geng Liu, Ruiting Tong, and Xiaojun Fu. Kinematics of Planetary Roller Screw Mechanism considering Helical Directions of Screw and Roller Threads. *Mathematical Problems in Engineering*, 2015(February 2016), 2015.
- [113] Jean Charles MARÉ and Jian FU. Review on signal-by-wire and power-by-wire actuation for more electric aircraft. *Chinese Journal of Aeronautics*, 30(3):857–870, 2017.
- [114] M. Mazzoleni, Y. Maccarana, F. Previdi, G. Pispolo, M. Nardi, F. Perni, and S. Toro. Development of a reliable electro-mechanical actuator for primary control surfaces in small aircrafts. *IEEE/ASME International Conference on Advanced Intelligent Mechatronics, AIM*, pages 1142–1147, 2017.
- [115] T. J.E. Miller. Optimal design of switched reluctance motors. *IEEE Transactions on Industrial Electronics*, 49(1):15–27, 2002.
- [116] Tatiana A. Minav, Lasse I.E. Laurila, Juha J. Pyrhönen, and Victor B. Vtorov. Direct pump control effects on the energy efficiency in an electro-hydraulic lifting system. *International Review of Automatic Control*, 20(10), 2011.
- [117] Tatiana A. Minav, Juha J. Pyrhönen, and Lasse I.E. Laurila. Permanent magnet synchronous machine sizing: Effect on the energy efficiency of an electro-hydraulic forklift. *IEEE Transactions on Industrial Electronics*, 59(6):2466–2474, 2012.
- [118] Georgiana Claudia Negoită, Jean Charles Maré, Marc Budinger, and Nicolae Vasiliu. Scaling-laws based hydraulic pumps parameter estimation. *UPB Scientific Bulletin, Series D: Mechanical Engineering*, 74(2):199–208, 2012.
- [119] G. Niemann and H. Winter. *Maschinen elemente - Band 2 - Getriebe allgemein, Zahnradgetriebe-Grundlagen, Stirnradgetriebe*. Springer-Verlag, 1989.
- [120] Hermann Ohlendorf. *Verlustleistung und Erwärmung von Stirnrädern: Einfluss v. Schmierg, Zahnform, Bearbeitg, Werkstoff, Belastg u. Umfangsgeschwindigkeit auf d. Verlustgrad u. d. Erwärmg v. Stirnrädern mit Geradverzahnng*. PhD thesis, 1959.
- [121] D. Olaru, G. C. Puiu, L. C. Balan, and V. Puiu. A new model to estimate friction torque in a ball screw system. *Product Engineering: Eco-Design, Technologies and Green Energy*, pages 333–346, 2005.
- [122] Christoph Pohl, Jens Hesselbach, and Universität Kassel. Electro mechanical alternatives to increase the efficiency of industrial systems Saving energy by using electro mechanical actuators. *White Paper Exklar*, 2013.

- [123] H. Polinder, M. J. Hoeijmakers, and M. Scuotto. Eddy-current losses in the solid back-iron of PM machines for different concentrated fractional pitch windings. *Proceedings of IEEE International Electric Machines and Drives Conference, IEMDC 2007*, 1(I):652–657, 2007.
- [124] (Premium Transmission Limited). Premium helical gear units, 2013.
- [125] Fabio Previdi, Yamuna MacCarana, Mirko Mazzoleni, Matteo Scandella, Giulio Pispola, and Nicola Porzi. Development and Experimental Testing of a Health Monitoring System of Electro-Mechanical Actuators for Small Airplanes. *MED 2018 - 26th Mediterranean Conference on Control and Automation*, pages 673–678, 2018.
- [126] George C Puiu, Dumitru Olaru, and Vasile Puiu. Friction torque and efficiency in ball-screw systems. *Acta Tribologica*, 17:25–29, 2009.
- [127] Juha Pyrhönen, Tapani Jokinen, and Valéria Hrabovcová. *Design of Rotating Electrical Machines*. 2008.
- [128] Guan Qiao, Geng Liu, Shangjun Ma, Zhenghong Shi, and Teik C. Lim. Friction Torque Modelling and Efficiency Analysis of the Preloaded Inverted Planetary Roller Screw Mechanism. (August), 2017.
- [129] Guan Qiao, Geng Liu, Zhenghong Shi, Yawen Wang, Shangjun Ma, and Teik C. Lim. A review of electromechanical actuators for More/All Electric aircraft systems. *Proceedings of the Institution of Mechanical Engineers, Part C: Journal of Mechanical Engineering Science*, 232(22):4128–4151, 2017.
- [130] Lingxiao Quan, Haihai Gao, Changhong Guo, and Shichao Che. Assessment of the Dynamics Flow Field of Port Plate Pair of an Axial Piston Pump. *Processes*, 8(1):86, 2020.
- [131] Kang Rongjie, Jiao Zongxia, Wang Shaoping, and Chen Lisha. Design and Simulation of Electro-hydrostatic Actuator with a Built-in Power Regulator. *Chinese Journal of Aeronautics*, 22(6):700–706, 2009.
- [132] J. A. Rosero, J. A. Ortega, E. Aldabas, and L. Romeral. Moving towards a more electric aircraft. *IEEE Aerospace and Electronic Systems Magazine*, 22(3):3–9, 2007.
- [133] Mircea Ruba. Fault-Tolerant Electrical Machines and Drives. In *Fault Diagnosis and Detection*, page 22. 2017.
- [134] Mircea Ruba and Loránd Szabó. Fault tolerant electrical machines. State of the art and future directions. *Journal of Computer Science and Control Systems*, 1(May):202–207, 2008.
- [135] Tomasz Rudnicki, Robert Czerwinski, Dariusz Polok, and Andrzej Sikora. Performance analysis of a PMSM drive with torque and speed control. *Proceedings of the 22nd International Conference Mixed Design of Integrated Circuits and Systems, MIXDES 2015*, (April):562–566, 2015.
- [136] Karl-erik Rydberg. Energy Efficient Hydraulic Hybrid Drives. *The 11th Scandinavian International Conference on Fluid Power, SICFP'09, June 2-4, 2009, Linköping, Sweden*, pages 1–14, 2009.
- [137] Karl-erik Rydberg. Energy Efficient Hydraulics – System solutions for loss minimization. Number March 2015, pages 16–17, 2015.
- [138] Tom Sadeghi and Arthur Lyons. Fault Tolerant EHA Architectures. *IEEE Aerospace and Electronic Systems Magazine*, 7(3):32–42, 1992.
- [139] Ingolf Schäfer. Improving the reliability of EMA by using harmonic drive gears. *SAE Technical Papers*, (724), 2005.
- [140] Lasse Schmidt, Søren Ketelsen, Morten Helms Brask, and Kasper Aastrup Mortensen. A class of energy efficient self-contained electro-hydraulic drives with self-locking capability. *Energies*, 12(10):26, 2019.
- [141] R. Munnig Schmidt, G. Schitter, A. Rankers, and J. Van Eijk. *The Design of High Performance Mechatronics: High-Tech Functionality by Multidisciplinary System Integration*. IOS Press, NLD, 2nd edition, 2014.
- [142] Peter Sekerák, Valéria Hrabovcová, Juha Pyrhönen, Lukáš Kalamen, Pavol Rafajdus, and Matúš Onufer. Ferrites and different winding types in permanent magnet synchronous motor. *Journal of Electrical Engineering*, 63(3):162–170, 2012.

- [143] Yaoxing Shang, Xiaobin Li, Hao Qian, Shuai Wu, Qingxin Pan, Ligang Huang, and Zongxia Jiao. A novel electro hydrostatic actuator system with energy recovery module for more electric aircraft. *IEEE Transactions on Industrial Electronics*, 67(4):2991–2999, 2020.
- [144] Gary (Exlar Corp.) Shelton. Sizing and applying roller screws. *MSD motion system design*, (650), 2005.
- [145] Gary (Exlar Corp.) Shelton. Roller Screw Actuators: Benefits, Selection and Maintenance. *Exlar*, page 5, 2010.
- [146] Siemens. Simulation of a switched reluctance motor | mentor infolytica, Jun 2008.
- [147] Mehmet Sinan Hasanoglu and Melik Dolen. Multi-objective feasibility enhanced particle swarm optimization. *Engineering Optimization*, 50(12):2013–2037, 2018.
- [148] SKF. The skf formula for rolling bearing life. <https://evolution.skf.com/us/the-skf-formula/>, Feb 2001. Accessed: 18-09-2020.
- [149] SKF. SKF catalogue 4351/9E, 2003.
- [150] SKF. The SKF model for calculating the frictional moment . *Skf*, pages 1–15, 2017.
- [151] Alexander H. Slocum. Design and Testing of a Self Coupling Hydrostatic Leadscrew. *Progress in Precision Engineering*, pages 103–105, 1991.
- [152] Shane Strasser, Rollie Goodman, John Sheppard, and Stephyn Butcher. A new discrete Particle Swarm Optimization algorithm. *GECCO 2016 - Proceedings of the 2016 Genetic and Evolutionary Computation Conference*, pages 53–60, 2016.
- [153] Lennart Stridsberg. Low weight, highly reliable anti-jamming device for electromechanical actuators. *SAE Technical Papers*, (724), 2005.
- [154] Prabhata Swamee and Akalank Jain. Explicit eqations for pipe-flow problems. *ASCE J Hydraul Div*, 102:657–664, 05 1976.
- [155] TechConnect Team. Sizing tube to maximize hydraulic system efficiency. <http://blog.parker.com/sizing-tube-to-maximize-hydraulic-system-efficiency>, Dec 2013. Accessed: 03-12-2020.
- [156] Evžen Thöndel. Electric Motion Platform for Use in Simulation Technology - Design and Optimal Control of a Linear Electromechanical Actuator. *Lecture Notes in Engineering and Computer Science*, 2187(1):960–965, 2010.
- [157] Alin Ştirban, Ion Boldea, and Gheorghe Daniel Andreescu. Motion-sensorless control of BLDC-PM motor with offline FEM-information-assisted position and speed observer. *IEEE Transactions on Industry Applications*, 48(6):1950–1958, 2012.
- [158] G.E. Totten and V.J. De Negri. *Handbook of Hydraulic Fluid Technology, Second Edition*. Taylor & Francis, 2011.
- [159] Xuan Bo Tran, Nur Hafizah, and Hideki Yanada. Modeling of dynamic friction behaviors of hydraulic cylinders. *Mechatronics*, 22(1):65–75, 2011.
- [160] Transatlantic Connection Inc. Comparison: Hydrostatic Leadscrews, Linear Motors, and Ballscrews. 2007.
- [161] A. J. Turner and K. Ramsay. Review and development of electromechanical actuators for improved transmission control and efficiency. *SAE Technical Papers*, 113(2004):908–919, 2004.
- [162] A. van Beek and Technische Universiteit Delft. *Advanced Engineering Design: Lifetime Performance and Reliability*. TU Delft, 2019.
- [163] Dominique van de Bossche. More Electric Control Surface Actuation, A Standart for the Next Generation of Transport Aircraft. *Control 2004, University of Bath*, (September):1–7, 2004.
- [164] Dominique van den Bossche. the a380 Flight Control Electrohydrostatic Actuators ., *25Th International Congress of the Aeronautical Sciences*, pages 1–8, 2006.
- [165] Franciscus L.J. van der Linden and André Dorkel. Real-Time Model- and Harmonics Based actuator health monitoring. *6th International Workshop on Aircraft System Technologies (AST 2017)*, pages 43–50, 2017.
- [166] Franciscus L.J. van der Linden and André Dorkel. Linear EMA HM using oil detection. *Recent Advances in Aerospace Actuation Systems and Components*, pages 58–63, 2018.

- [167] Steven A. Velinsky, Baeksuk Chu, and Ty A. Lasky. Kinematics and efficiency analysis of the planetary roller screw mechanism. *Journal of Mechanical Design, Transactions of the ASME*, 131(1):0110161–0110168, 2009.
- [168] G. S. Veresnikov and A. V. Skryabin. The Electromechanical Actuator Technical Condition Monitoring System Based on Data Mining Methods. *Proceedings of 2018 11th International Conference "Management of Large-Scale System Development", MLSD 2018*, pages 1–4, 2018.
- [169] Sergei Vasilyevich Vladimirov and Scott Forde. Demonstration program to design, manufacture and test an autonomous electro-hydrostatic actuator to gimbal large booster-class engines. *Collection of Technical Papers - AIAA/ASME/SAE/ASEE 42nd Joint Propulsion Conference*, 1(July 2006):541–546, 2006.
- [170] Bo Wang, Jiabin Wang, Antonio Griffo, Zhigang Sun, and Ellis Chong. A fault tolerant machine drive based on permanent magnet assisted synchronous reluctance machine. *ECCE 2016 - IEEE Energy Conversion Congress and Exposition, Proceedings*, 2016.
- [171] Jiabin Wang, Kais Atallah, and Weiya Wang. Analysis of a magnetic screw for high force density linear electromagnetic actuators. *IEEE Transactions on Magnetics*, 47(10):4477–4480, 2011.
- [172] Yan Wang, Shengrong Guo, and Hongkang Dong. Modeling and control of a novel electro-hydrostatic actuator with adaptive pump displacement. *Chinese Journal of Aeronautics*, 33(1):365–371, 2018.
- [173] Chin Chung Wei, Wei Lun Liou, and Ruei Syuan Lai. Wear analysis of the offset type preloaded ball-screw operating at high speed. *Wear*, 292-293:111–123, 2012.
- [174] Li Wei and John P Fielding. *More Electric Landing Gear Actuation Study*. PhD thesis, 2009.
- [175] Norman Weir and (Boeing). Non-jamming ball screw linear actuator, 1973.
- [176] F.M. White and R.Y. Chul. *Fluid Mechanics*. McGraw-Hill series in mechanical engineering. McGraw-Hill Education, 2016.
- [177] T. Wildi. *Electrical Machines, Drives and Power Systems: Pearson New International Edition*. Pearson Education Limited, 2013.
- [178] Johannes Willkomm and Matthias Wahler. Potentials of Speed and Displacement Variable Pumps in Hydraulic Applications. *10th International Fluid Power Conference*, pages 379–391, 2016.
- [179] Johannes Willkomm, Matthias Wahler, and Jürgen Weber. Process-adapted control to maximize dynamics of speed- and displacement-variable pumps. In *Proceedings of the ASME/BATH 2014 Symposium on Fluid Power & Motion Control*, pages 1–10, 2014.
- [180] Shuai Wu, Chunfang Li, Xiangyu Zhao, Zongxia Jiao, and Tao Yang. Preliminary design and simulation of electro-hydrostatic actuator with modelica. *AUS 2016 - 2016 IEEE/CSAA International Conference on Aircraft Utility Systems*, pages 1138–1143, 2016.
- [181] Shuai Wu, Bo Yu, Zongxia Jiao, Yaoxing Shang, and P. C.K. Luk. Preliminary design and multi-objective optimization of electro-hydrostatic actuator. *Proceedings of the Institution of Mechanical Engineers, Part G: Journal of Aerospace Engineering*, 231(7):1258–1268, 2017.
- [182] Jitendra Yadav. Modeling and Simulation of Hydraulic Actuator With Viscous Friction. (03):540–547, 2015.
- [183] Xudong Yan, Liming Yu, Jiang'ao Zhao, Jian Fu, and Yongling Fu. *Hierarchical modelling and simulation of a novel integrated electro-mechanical hydrostatic actuator based on bond graph*, volume 529. Springer Singapore, 2019.
- [184] Chang Guang Zhou, Hu Tian Feng, and Yi Ou. A new model for predicting the mechanical efficiency of ball screws based on the empirical equations for the friction torque of rolling bearings. *Advances in Mechanical Engineering*, 10(9):1–8, 2018.
- [185] Li Zu, Zhou Zhang, and Liang Gao. Design and bearing characteristics of planetary roller screws based on aerospace high-load conditions. *Advances in Mechanical Engineering*, 10(11):1–11, 2018.

# Appendix A

## Mechanical transmission equations

### A.1 Planetary roller screw sizing

#### Buckling requirement

Buckling load of the screw is determined according to Euler critical load given in Equation A.1. The area moment of inertia of the screw used in Euler critical load is given in Equation A.2.

$$P_{cr} = \frac{\pi^2 EI_{screw}}{k^2 L_{screw}^2} [\text{N}] \quad (\text{A.1})$$

$$I_{screw} = \frac{\pi}{4} r^4 [\text{kg m}^2] \quad (\text{A.2})$$

Substituting Equation A.2 in Equation A.1 and rewriting for  $r$ , the minimum radius to satisfy the buckling requirements is found according to equation A.3. The critical load  $P_{cr}$  is given by the maximum force requirements on the actuator found in Section 2.5 and a structural safety factor as  $P_{cr} = F_{max} FoS$ .  $k$  is the column effective length factor of the screw. The column effective length factor is determined by the mounting configuration of the screw. According to [43],  $k$  should be equal to 0.85 for the screw by assuming the base of the screw is fixed in six degrees of freedom. The buckling length of the cylinder  $L_{screw}$  is taken as the stroke length of the mechanical cylinder. In reality, the length of the screw will be longer, it is however reasonable to assume this extra length will be used for mounting options such as bearings or bushings. Finally,  $E$  is the young modulus of the screw material.

$$r_{buckling} = \sqrt[4]{\frac{4P_{cr}k^2L_{screw}^2}{E\pi^3}} [\text{m}] \quad (\text{A.3})$$

#### Yield strength requirement

The stress in the screw material can be determined with Equation A.4. Rewriting Equation A.4 in terms of the screw radius and adding the fatigue requirement gives the minimum radius for the yield requirement (Equation A.5). The critical load  $P_{cr}$  is again given as  $P_{cr} = F_{max} FoS$ . The yield strength  $\sigma_y$  is a material specific property.

$$\sigma = \frac{P_{cr}}{\pi r^2} [\text{N m}^{-2}] \quad (\text{A.4})$$

$$r_{yield} = \sqrt{\frac{P_{cr}}{0.67\sigma_y\pi}} [\text{m}] \quad (\text{A.5})$$

#### Torsional strength requirement

The shear stress due to torsion is given by Equation A.6. Here the torque  $T$  is given by the maximum torque  $T_{max}$  multiplied with a structural safety factor  $FoS$ . Furthermore,  $J_{screw}$  is the polar moment of inertia given in Equation A.7 and  $r$  is the minor radius of the screw.

The maximum occurring torque on the screw is a function of the maximum force as seen in equation A.9. The total lead  $l_t$  of the screw is discussed further on in this section. The efficiency of the screw  $\eta$  is still unknown, as such, an estimate of the mean efficiency is used. An estimate of  $\eta = 0.85$  is used in subsequent calculations.

$$\tau = \frac{Tr}{J_{screw}} [\text{N m}^{-2}] \quad (\text{A.6})$$

$$J_{screw} = \frac{\pi r^4}{2} [\text{m}^4] \quad (\text{A.7})$$

$$T = \text{FoS}T_{max} \quad (\text{A.8})$$

$$T_{max} = \frac{F_{max}l_t}{2\pi\eta} \quad (\text{A.9})$$

The relation between the shear stress and the total stress in the material is given by Von Mises as  $\sigma_t = 1.73\tau$ . Substituting Equations A.7 and A.9 in Equation A.6 with the same rule to keep the maximum stress below 67% of the yield strength, the minimum radius due to shear requirements is obtained in Equation A.10.

$$r_{shear} = \sqrt[3]{\frac{2 \cdot 1.73 f_{sc} T}{0.67 \sigma_y \pi}} \quad (\text{A.10})$$

## A.2 Cylinder housing sizing

The mechanical cylinder is sized based on several load requirements as outlined below.

### Buckling requirement

To satisfy the buckling requirement on the smooth extending rod, a minimum area moment of inertia is needed. This minimum area moment of inertia is found by rewriting the Euler critical load equation in Equation A.11.

$$I_{min} = F_{max} \text{FoS} \frac{(kL_{cr})^2}{\pi^2 E_{st}} \quad (\text{A.11})$$

Here  $F_{max}$  is the maximum force requirement on the actuator discussed in Section 2.5 and  $\text{FoS}$  is a structural safety factor.  $k$  is the column effective length factor and  $E_{st}$  is the young's modulus of steel. The minimum outside radius of the smooth hollow cylinder for buckling can then be determined by rewriting the equation for the area moment of inertia of a hollow cylinder as shown in Equation A.12.

$$r_{cr,out,buckling} = \sqrt[4]{\frac{4I_{min}}{\pi + r_{cr,in}^4}} [\text{m}] \quad (\text{A.12})$$

### Yield requirement

The yield requirement ensures the stress inside the extending rod material does not exceed the yield stress of the material. The minimum smooth cylinder outside radius to satisfy the yield requirements is determined according to Equation A.13. Here the 0.67 factor ensures the maximum stress does not exceed 67% of the yield strength in accordance with the criteria stated in the SKF PRS design guide for fatigue life.

$$r_{cr,out,yield} = \sqrt{\frac{F_{max} \text{FoS}}{0.67 \pi \sigma_y} + r_{cr,in}^2} [\text{m}] \quad (\text{A.13})$$

### Fabrication requirement

As the smooth cylinder should be fabricated (metal turning), a minimal design thickness should be taken under consideration. This minimal thickness is taken as  $t_{cr,min} = 0.004[\text{m}]$ . As such, the minimal smooth cylinder outside radius due to the fabrication requirement is given as:

$$r_{cr,out,fabrication} = r_{cr,in} + t_{cr,min}[\text{m}] \quad (\text{A.14})$$

## A.3 Gear sizing

Table A.1: Gear sizing parameters

Parameter	Description	Unit	Value
$\alpha_p$	Pressure angle of the gears	[rad]	20[deg]
$\beta_b$	Helix angle of the gears	[rad]	30[deg]
$a_s$	Axial shift between the in- and output axle	[m]	0.2[m]

The first step in load sizing the helical gear pair is determining the diameters of the gears. The pitch diameters of both gears are a function of the gear ratio and the axial distance shift  $a_s$  between both gears. Both diameters are determined according to Equations A.15 and A.16. All equations found in this section, unless specifically stated otherwise, are found in [162].

$$d_{g,1} = 2 \frac{a_s}{R_{gear} + 1} [\text{m}] \quad (\text{A.15})$$

$$d_{g,2} = 2 \left( a_s - \frac{d_{g,1}}{2} \right) [\text{m}] \quad (\text{A.16})$$

Next to the pitch diameter, also the tip and base diameters of the gears should be determined. The tip and base diameters of both the pinion (1) and driven gear (2) are determined by Equation A.17 and A.18 respectively.

$$d_{ga,i} = d_{g,i} + 2m [\text{m}] \quad (\text{A.17})$$

$$d_{gb,i} = d_{g,i} \cos \alpha_p [\text{m}] \quad (\text{A.18})$$

The gear diameter and tooth module  $m$  determine the amount of teeth on each gear. As the number of teeth should always be a round number, a rounding function is used. Small discrepancies between the resulting real tooth module are assumed to be negligible. The number of teeth for both gears is found according to Equation A.19.

$$Z_{g,i} = \text{round} \left( \frac{d_{g,i}}{m} \right) \quad (\text{A.19})$$

To determine further properties of the helical gear stage, the transverse or working pressure angle should be determined. The transverse pressure angle is the effective pressure angle of the helical gears as a result of the helix angle of the gear teeth. The transverse pressure angle is determined according to Equation A.20 [119].

$$\alpha_{wt} = \tan^{-1} \left( \frac{\tan \alpha_p}{\cos \beta_b} \right) \quad (\text{A.20})$$

The head engagement distances of the pinion and driven gear are then determined according to Equation A.21 [119].

$$g_{ga,i} = \frac{1}{2}d_{gb,i} \left( \sqrt{\left(\frac{d_{ga,i}}{d_{gb,i}}\right)^2 - 1} - \tan \alpha_{wt} \right) [\text{m}] \quad (\text{A.21})$$

Also the gear pitch  $p_g$  (Equation A.22 [119]) and the intervention distance  $p_{ge}$  (distance between two adjacent flanks on the contact line, Equation A.23 [119]) can be calculated. Those are needed to calculate the addendum transverse contact ratio  $e_i$  of the pinion and the driven gear and the combined tooth contact ratio  $e_\alpha$ .

$$p_g = m\pi [\text{m}] \quad (\text{A.22})$$

$$p_{ge} = p_g \cos \alpha_p [\text{m}] \quad (\text{A.23})$$

$$e_i = \frac{g_{a,i}}{p_{ge}} \quad (\text{A.24})$$

$$e_\alpha = \frac{g_{a,1} + g_{a,2}}{p_{ge}} \quad (\text{A.25})$$

The tooth contact ratio should always be higher than 1 according to [119]. The tooth contact ratio can be used to determine the contact ratio factor of the gear pair according to Equation A.26. Together with the gear zone factor  $Z_h$  and elasticity factor  $Z_E$ , the contact ratio factor is later used to determine the necessary height of the gear.

$$Z_{cr} = \sqrt{\frac{4 - e_\alpha}{3}} \quad (\text{A.26})$$

$$Z_h = \sqrt{\frac{\cos \alpha_p}{\sin \alpha_p}} \quad (\text{A.27})$$

$$Z_E = \sqrt{\frac{E_{st}}{2\pi}} \quad (\text{A.28})$$

Before finding the necessary height of the gear, first the tangential force on the pitch line should be found. As the maximum torque on the screw side of the gearbox can be calculated, the maximum tangential force is determined according to Equation A.29. The minimal required tooth face width to support this tangential force is then determined by Equation A.30.

$$F_t = \frac{2T_{max}}{d_{g2}} [\text{N}] \quad (\text{A.29})$$

$$b = \left( \frac{Z_h Z_E Z_{cr}}{\sigma_{max}} \right)^2 \frac{F_t}{d_{g2}} \frac{u+1}{u} [\text{m}] \quad (\text{A.30})$$

In Equation A.30,  $\sigma_{max}$  is the maximum allowable stress in the gear material defined as  $\sigma_{max} = \sigma_{lim}/\text{FoS}$ .  $u$  is the absolute gear ratio given by Equation A.31.

$$\begin{aligned} \text{if } R_{gear} \geq 1 : & \quad u = R_{gear} \\ \text{if } R_{gear} < 1 : & \quad u = \frac{1}{R_{gear}} \end{aligned} \quad (\text{A.31})$$

Finally, the height of the gear can be derived from the minimal tooth face width by taking into consideration the helix angle of the gear. The height of the gear is given in Equation A.32.

$$h_g = b \cos \beta_b [\text{m}] \quad (\text{A.32})$$

## A.4 Planetary roller screw losses

### A.4.1 Geometry related losses

The PRS efficiency model is based on a model proposed by [167]. Both the rolling resistance and the z-directional slip is taken into account in this model assuming a constant rolling frictional moment and friction coefficient. These assumptions are discarded by implementing a model for the coefficient of rolling friction dependant on the working point as explained below. Lubrication and elastic hysteresis effects are not taken into account, as such the model is only valid in steady state operation. However, most PRS transmissions can be modelled with quasi-steady state behaviour [88]. Furthermore, [128] states the PRS efficiency is almost independent on nut speed. However, higher load should result in higher efficiency. The PRS efficiency model by [167] is given as:

$$\eta_s = \frac{r_s \tan \alpha_s (\cos \alpha_s \cos \rho \sin \beta - \sin \alpha_s \sin \rho - \mu_k (\sin \alpha_s \cos \rho + \cos \alpha_s \sin \rho \sin \beta))}{r_s (\cos \rho \sin \alpha_s \sin \beta + \sin \rho \cos \alpha_s) + r_{RP}(1 - \cos \rho)(\sin \rho + \cos \rho) \cos \alpha_s \cos \beta} \quad (\text{A.33})$$

Parameters of the model are defined in Subsection 3.4.1. The helix angle of the screw is determined as a function of the screw pitch radius and the screw lead:

$$\alpha_s = \tan^{-1} \left( \frac{l_s}{2\pi r_s} \right) \quad (\text{A.34})$$

The contact angle  $\beta$  is often stated as 45 deg for practical reasons. The friction angle  $\rho$  is given as:

$$\rho = \tan^{-1} \left( \frac{\mu_r}{r_{RP} \sin \beta} \right) \quad (\text{A.35})$$

Here  $\mu_r$  is the rolling coefficient of friction between the rollers and screw, this is a variable changing with velocity and load.  $\mu_k$  is the coulomb kinetic coefficient of friction. In [167], this parameter is set equal to 0.055 for lubricated steel-steel contacts.

Finally,  $r_{RP}$  is the radius of curvature of the roller side profile. The radius of curvature is given by:

$$r_{RP} = \frac{r_r^2 + \left(\frac{l_r}{2\pi}\right)^2}{r_r} [\text{m}] \quad (\text{A.36})$$

$r_r$  and  $l_r$  are the roller pitch radius and roller lead respectively.

### A.4.2 Rolling friction coefficient

Rolling friction is the force which resists motion of a body rolling on a surface. Rolling friction is mainly caused by non-elastic effects such as hysteresis and plastic deformation. Rolling friction is often determined as a function of the normal force on the rolling body according to:

$$F_r = \mu_r N [\text{N}] \quad (\text{A.37})$$

Here  $\mu_r$  is the rolling coefficient of friction. The rolling coefficient of friction is often determined experimentally due to the various factors influencing rolling friction. As such, the rolling coefficient of friction is often taken as a mean value found from experiments. However, in reality, the rolling coefficient of friction is load and velocity dependent. Equations for the rolling coefficient of friction of the planetary rolling screw are not found in literature. However, rolling coefficient of friction of ball bearings is documented in literature. As models for the PRS can be found where the contact interface is modelled using equivalent balls, rolling friction of a ball bearing should be representative for the PRS mechanism. The screw then represents the axle in the bearing, the rollers represent the ball bearings and the nut is portraying the outer bearing race of the bearing assembly. [150] developed a model to determine the rolling frictional moment for a ball bearing. The rolling frictional moment can be converted to the rolling coefficient of friction by substituting the frictional force in Equation A.37 by:

$$F_r = \frac{T_r}{r_s} [\text{N}] \quad (\text{A.38})$$

The coefficient of rolling friction is then given as:

$$\mu_r = \frac{T_r}{r_s N} \quad (\text{A.39})$$

The rolling frictional moment is determined in [150] as:

$$T_r = \phi_{ish} \phi_{rs} G_{rr} (\nu n)^{0.6} [\text{N m}] \quad (\text{A.40})$$

Here  $\nu$  and  $n$  are the operating viscosity of the oil in  $[\text{mm}^2 \text{s}^{-1}]$  and the rotational speed of the screw in  $[\text{rpm}]$  respectively. The other three parameters are explained in detail below as found in [150].

**Inlet shear heating reduction factor -  $\phi_{ish}$**  The inlet shear heating reduction factor represents the lowering of the rolling friction due to heating of the lubricating medium. Only a very thin hydrodynamic film is formed between the contact points, the excess oil close to the contact area will be repelled and produce a reverse flow. The reverse flow shears the lubricant and generates heat. The heat lowers the oil viscosity and film thickness and consequently also lowers the rolling friction. The shear heating reduction factor can be estimated using an experimental equation:

$$\phi_{ish} = \frac{1}{1 + 1.84e-9 (nd_m)^{1.28} \nu^{0.64}} \quad (\text{A.41})$$

Here  $d_m$  is the bearing mean diameter in  $[\text{mm}]$ . The bearing mean diameter is replaced by the PRS mean diameter which is given as:

$$d_m = \frac{r_s + r_r}{2} \quad (\text{A.42})$$

**Kinematic replenishment/starvation reduction factor -  $\phi_{rs}$**  During operation, oil is being displaced due to the rolling contact point. When viscosity or speed are high, the lubricant might not have enough time to replenish the raceways resulting in a kinematic starvation effect. The starvation effect reduces the hydrodynamic film thickness and consequently the rolling friction. The kinematic starvation reduction factor is again determined by an experimental equation:

$$\phi_{rs} = \frac{1}{e^{[k_{rs} \nu n (d+D) \sqrt{\frac{k_z}{2(D-d)}}]}} \quad (\text{A.43})$$

Here  $k_{rs}$  is the replenishment or starvation constant which is dependent on the type of lubrication. For a low level oil bath or jet lubrication, this constant is equal to  $k_{rs} = 30^{-8}$ . In case of grease or oil-air lubrication, the value is almost doubled to  $k_{rs} = 50^{-8}$ . For the planetary roller screw, oil jet lubrication is assumed. Next,  $k_z$  is a bearing type related geometric constant. The bearing type related constant should be approximated for the PRS. As the PRS mostly resembles an angular contact bearing due to the axial loading direction, the geometric constant is approximated by the geometric constant of a single row angular contact bearing. This constant is given in [150] as  $k_z = 4.4$ . Finally,  $d$  and  $D$  are the bearing bore and bearing outside diameter in  $[\text{mm}]$ . Those diameters are changed to the screw pitch diameter and nut pitch diameter respectively for the PRS.

**Geometric and load dependent variable for rolling friction in radial bearings -  $G_{rr}$**  This variable determines the nominal rolling friction in function of the load and geometry. The geometry dependencies is again approximated by representing the PRS as an angular contact bearing. This variable is highly experimental and is therefore difficult to validate.

$$G_{rr} = R_1 d_m^{1.97} [F_r + F_g + R_2 F_a]^{0.54} \quad (\text{A.44})$$

Here  $R_1$  and  $R_2$  are experimental factors found in Table A.2 [150].  $F_r$  and  $F_a$  is the radial and axial loading on the bearing respectively. The radial loading is set to zero for the PRS as radial loading is taken up by the linear bearings in the mechanical cylinder. The axial load is replaced by the normal force on the contact points of the rollers as:

$$F_a = \frac{N}{\sin(\beta) \cos(\alpha_s)} \frac{N_r}{n_{eq}} [\text{N}] \quad (\text{A.45})$$

Here  $N_r$  and  $n_{eq}$  are the number of rollers and number of equivalent balls in the PRS respectively. These are used as the axial force is distributed over the various contact points. The angular contact bearing has only a single row of balls while the PRS has multiple rows on top of each other. Finally,  $F_g$  is an induced force on the bearing due to the angular velocity. This force is given by:

$$F_g = R_3 d_m^A n^2 [\text{N}] \quad (\text{A.46})$$

$R_3$  is again an experimental geometric factor given in the Table A.2. All experimental factors are assumed to correspond to the values found in [150] for a single row 25 deg angular contact bearing of the SKF 72xx series.

Table A.2: Experimental factors [150]

Factor	value
$R_1$	$3.58e - 7$
$R_2$	$3.64$
$R_3$	$3.55e - 12$

## A.5 Gearbox losses

Planetary gearbox losses are a well studied subject in literature. The gearbox losses are modelled based on the models by [94] and [119]. The complete efficiency model is given below for reference.

### A.5.1 Forces and speed

First, the tangent force on the base circle of the gears is determined. The tangent force is always expected to be positive in the efficiency equation hence the absolute value is taken:

$$F_{bt} = \left| \frac{2T_{out}}{d_2 \cos(\alpha_{wt})} \right| [\text{N}] \quad (\text{A.47})$$

The gearbox output torque and the driven gear diameter are used as the output torque corresponds with the torque on the PRS screw. Next, the linear speed of the gears on the peripheral line  $v$  and the pitch line  $v_t$  are calculated. As the speed on the screw side of the gearbox is known, the speeds are calculated at the driven gear side:

$$v = \omega_{out} r_{t2} [\text{m s}^{-1}] \quad (\text{A.48})$$

$$v_t = \omega_{out} r_{p2} [\text{m s}^{-1}] \quad (\text{A.49})$$

With  $r_{t2}$  and  $r_{p2}$  the driven gear tip and pitch radius respectively. Both speeds are expressed in  $[\text{m s}^{-1}]$ . The efficiency model is valid up to pitch line speeds of  $50[\text{m s}^{-1}]$ . For higher speeds, the pitch line speed should be fixed to  $50[\text{m s}^{-1}]$  according to [94].

### A.5.2 Gear losses

The power losses in the gearbox can be split into ‘No load gear losses’ and ‘Load dependent gear losses’. Here only the gear losses due to friction between the gear flanks  $P_{Vz}$  and the no-load gear losses due to windage, oil churning and oil squeezing  $P_{Vz0}$  are taken into account. Bearing losses are added separately below.

**Load dependant losses** The load dependent gear losses can be described as  $P_{Vz} = H_v P_{in} \mu_m$  [94]. Here  $H_v$  is the power loss factor,  $P_{in}$  is the input power of the gearbox and  $\mu_m$  is the average coefficient of friction. The power loss factor  $H_v$  is described by Ohlendorf's relation [119] as:

$$H_v = \frac{1 + r_{gear}}{r_{gear}} \frac{\pi}{z_1 \cos(\beta_b)} (1 - e_\alpha + e_1^2 + e_2^2) \quad (\text{A.50})$$

Here  $r_{gear}$  is the gear ratio of the gearbox,  $z_1$  is the number of teeth on the pinion,  $\beta_b$  is the helix angle on the base circle and  $e_\alpha, e_1$  &  $e_2$  is the profile contact ratio and the addendum transverse contact ratios of the pinion and driven gear respectively. The average coefficient of friction is load and speed dependent and is described by [119]. The description of the average coefficient of friction found in [119] is widely accepted for use on helical gears [94]:

$$\mu_m = 0.048 \left( \frac{P_g}{v_{\Sigma c} \rho_{redC}} \right)^{0.2} X_{oil} X_r X_L \quad (\text{A.51})$$

Here  $P_g$  is the force per unit length on the gear teeth in  $[\text{N mm}^{-1}]$ ,  $v_{\Sigma c}$  is the sum velocity at the operating pitch circle in  $[\text{m s}^{-1}]$ ,  $\rho_{redC}$  is the reduced radius of curvature at the pitch point in  $[\text{mm}]$ .  $X_{oil}$ ,  $X_r$  &  $X_L$  is the oil viscosity correction factor, the surface roughness correction factor and the lubrication correction factor (for oil lubrication) respectively. Those parameters are further detailed below. The force per unit length on the gear teeth is defined as:  $P_g = F_{bt}/b$  with  $F_{bt}$  in  $[\text{N}]$  and  $b$  in  $[\text{mm}]$ . The minimal force per unit length on the gear teeth should be  $150[\text{N mm}^{-1}]$  for the model to be accurate [119]. The sum velocity on the operating pitch circle is calculated as:

$$v_{\Sigma c} = 2v_t \sin(\alpha_{wt}) [\text{m s}^{-1}] \quad (\text{A.52})$$

The reduced radius of curvature is expressed in  $[\text{mm}]$  and is found as:

$$\rho_{redC} = 0.5(d_1/1000) \sin(\alpha_{wt}) \frac{u}{(u+1) \cos(\beta_b)} \quad (\text{A.53})$$

**Oil viscosity correction factor** The oil viscosity correction factor is determined by the dynamic oil viscosity as:

$$X_{oil} = \eta_{oil}^{-0.05} \quad (\text{A.54})$$

With  $\eta_{oil}$  the dynamic oil viscosity in  $[\text{mPas}]$  at the operating temperature of the gearbox. The operating temperature of the gearbox is assumed constant at  $30[^\circ\text{C}]$ .

**Surface roughness correction factor** The surface roughness correction factor corrects the friction coefficient for the mean surface roughness on both gear faces. The correction factor is calculated as:

$$X_r = 3.8 \left( \frac{R_a}{d_1} \right)^0 .25 \quad (\text{A.55})$$

Here  $R_a$  is the arithmetic mean roughness expressed in  $[\mu\text{m}]$  and  $d_1$  is the pinion pitch diameter expressed in  $[\text{mm}]$ . The arithmetic mean roughness is calculated as:

$$R_a = 0.5 (R_{a,1} + R_{a,2}) \quad (\text{A.56})$$

With  $R_{a,1}$  &  $R_{a,2}$  being the roughness factor of respectively the pinion and driven gear expressed in  $[\mu\text{m}]$ .

**Lubrication correction factor** The lubrication correction factor reduces the friction between the gear teeth faces to simulate lubricated contact friction. For oil, this factor is calculated as:

$$X_L = \left( \frac{F_{bt}}{b} \right)^{-0.0651} \quad (\text{A.57})$$

Here  $F_{bt}$  is the circumferential force at the base circle in [N] and  $b$  is the gear face width in [mm].

**No load losses** The no load gear power losses include losses due to windage, oil churning and oil squeezing during meshing of the gears. In [119], the no load gear power loss is determined according to:

$$P_{Vz0} = 76.92e-6bhv^{1.5}[\text{W}] \quad (\text{A.58})$$

Here  $b$  is the gear face width in [mm],  $h$  is the oil immersion depth of the gear wheel in [mm] and  $v$  is the peripheral speed of the gear wheel in  $[\text{m s}^{-1}]$ .

Note that this equation was originally developed for gears rotating around a horizontal axis. The proposed gearbox for the EMA actuator has gears turning around the vertical axis. As such, oil churning and squeezing losses are not accurately modelled in this equation. No load gear losses should be revisited in future model iterations.

### A.5.3 Bearing losses

Bearing losses are modelled in [10] as a function of the speed of the gear axles. The gearbox is assumed to contain four bearings to support both axles of the pinion and driven gear. Bearing losses are expressed as the product of the bearing frictional moment and the rotational velocity of the bearings. The rotational velocity of the pinion and driven gear are related by:

$$\omega_1 = R_{gear}\omega_2[\text{rad s}^{-1}] \quad (\text{A.59})$$

The bearing frictional moment is described in [10] by two equations for a low velocity and high velocity region. The low velocity region frictional moment is valid for  $\nu_{oil}\omega_i\frac{60}{2\pi} < 2000$  and is defined as:

$$T_{v,low} = 160e-10f_0d_m^3[\text{N m}] \quad (\text{A.60})$$

At higher velocities, the bearing frictional moment is given as:

$$T_{v,high} = 1e-10f_0 \left( \nu_{oil}\omega_i\frac{60}{2\pi} \right)^{2/3} d_m^3[\text{N m}] \quad (\text{A.61})$$

Here  $f_0$  is an index for the bearing type and lubrication type defined as  $f_0 = 1.5$  [10].  $d_m$  is the mean bearing diameter, the diameter is assumed to be equal to 115% of the screw diameter  $d_m = 2 \cdot 1.15r_s$ .  $\omega_i$  is the rotational velocity of either the pinion or driven gear depending on the bearing location. The total bearing losses in the gearbox are then defined as:

$$P_{bearing} = \sum_{i=1}^2 (2T_v(\omega_i)\omega_i) [\text{W}] \quad (\text{A.62})$$

## A.6 Loss model properties

Validation of the mechanical transmission loss models is less straight forward compared to the sizing model. Manufacturer data on losses or efficiencies of mechanical transmission components is not or very limited available. The available efficiency data is often determined in a single working point and is therefore not representative to determine energy losses for a given operation. Loss models of both the PRS and the helical gear stage are based on existing models found in literature. As such, the actual models are already proven separately. In this section, assumptions in the loss models are investigated to determine the influence of small deviations in these assumptions. Also influence of the design parameters are shown here.

### A.6.1 Mechanical cylinder losses

The mechanical cylinder has losses associated to the sliding friction of the smooth cylinder rod and to friction in the the PRS mechanism. Sensitivities of model assumptions and the influence of the design parameters are discussed below.

#### Sensitivities

**Rolling friction** The losses of the PRS are modelled in terms of efficiency with a model developed by [167]. The major change in the model is the addition of a variable rolling coefficient of friction to model the effects of axial force and speed in the PRS. Together with the fixed coulomb kinetic coefficient of friction, the rolling coefficient of friction determines the losses in the PRS. Figure A.1 shows the sensitivity of the efficiency to both parameters.

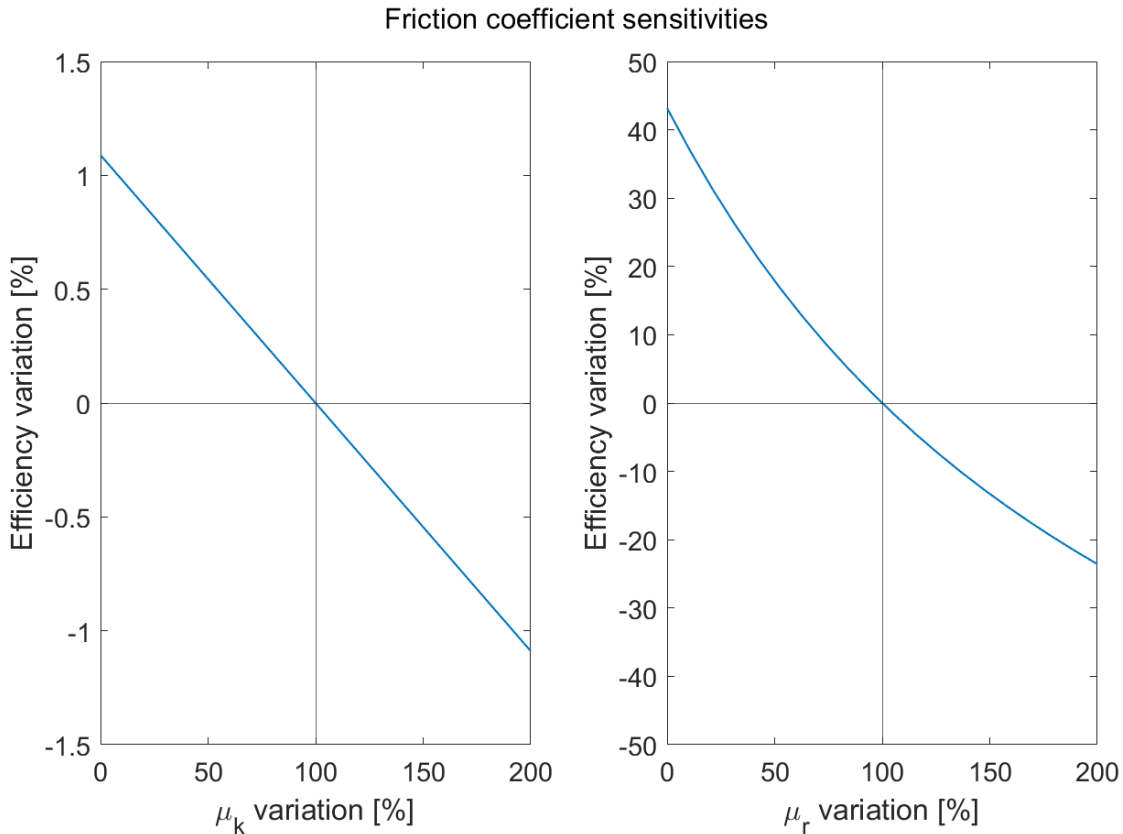


Figure A.1: PRS friction coefficient sensitivities.

The fixed coulomb kinetic coefficient of friction  $\mu_k$  has a very low and linear effect on the PRS efficiency. Doubling the coefficient only decreases the efficiency by approximately 1%. In [60] the range for the kinetic friction coefficient of lubricated hard steel-steel contacts is given from 0.029 to 0.12. With  $\mu_k = 0.055$  the efficiency variation would be  $-1.3$  to  $+0.5\%$ .

The rolling coefficient of friction has a much larger influence on the PRS efficiency. The rolling coefficient of friction directly influences the friction angle of the PRS with  $\rho_{fric} \propto \tan^{-1}(\mu_r)$ . The rolling coefficient of friction is determined using an empirical equation for roller bearings. The equations use several geometric constants which would potentially be different in a roller screw. The sensitivity of these geometric constants are determined in Figure A.2. Especially the  $R1$  and  $R2$  coefficients show large influence on the PRS efficiency. rolling friction of a PRS and ball screw should be fairly similar. However, the large sensitivity to  $R1$  and  $R2$  shows small deviations in the geometric properties can result in significant efficiency changes. Experimental validation of these coefficients with actual planetary roller screws in a later stage should be performed to increase the accuracy of the PRS loss model.

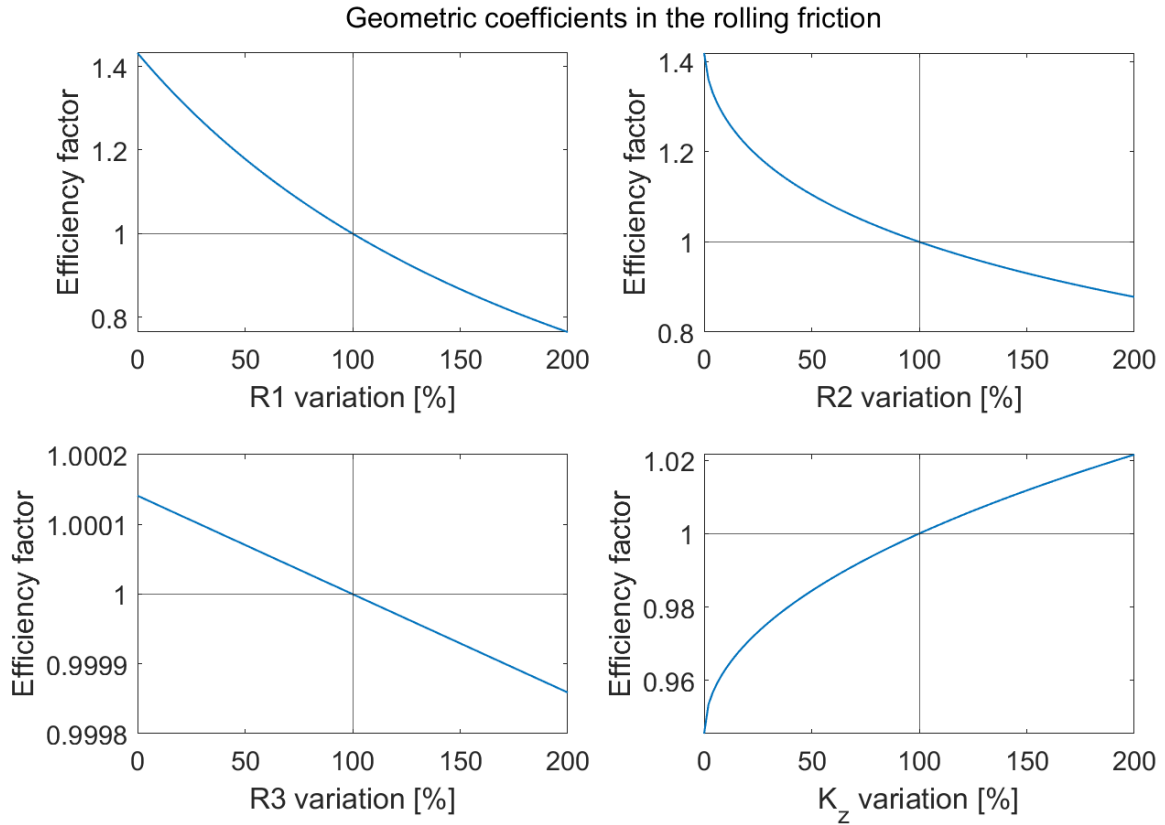


Figure A.2: Geometric coefficient sensitivities

**Linear bearing friction** The other model used to find the losses in the mechanical cylinder describes the losses due to bearing friction between the cylinder enclosure and the smooth extending rod. Bearings on the smooth rod ensure the actuator motion is constraint to a single translation axis and prevents sideways loading of the internal PRS. The bearing friction model assumes the centre of gravity of the entire actuator remains constant throughout its full range of motion. This is a reasonable assumption as the mass of the moving parts in the cylinder is minimal compared to the entire actuator mass. Two other assumptions in the model are a fixed cylinder angle and fluid film thickness between the bearings and the smooth rod. Sensitivity on the friction force in the cylinders with variations on these assumptions is shown in Figure A.3.

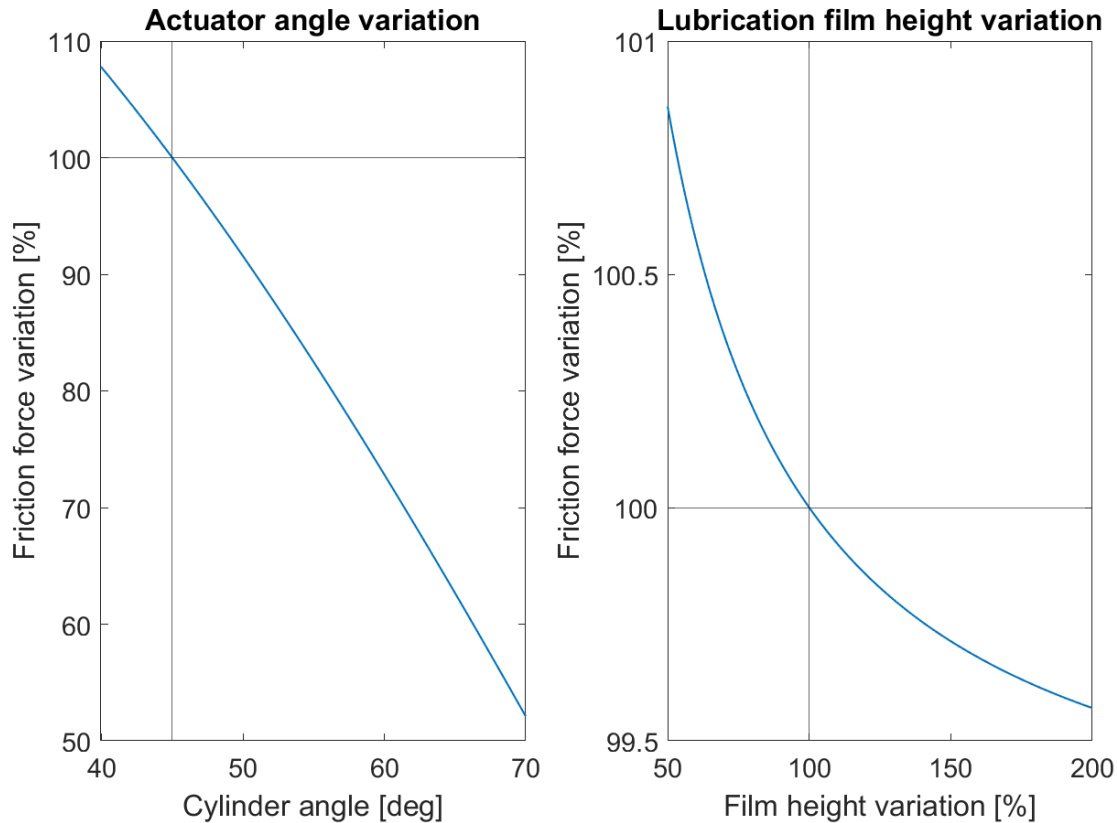


Figure A.3: Sensitivities of the bearing friction model.

Variation of the cylinder angle are seen to have a large influence on the bearing friction forces. The bending moment caused by the actuator mass is proportional to the cosine of the actuator angle. Shallower angles result in a smaller bending moment and therefore a lower bearing normal force. The current actuator angle of 45deg is rather a worst case scenario. Especially at fully extended actuator positions the actuator angle would decrease significantly. Later model iterations could include the actuator mounting geometry to increase bearing friction force model accuracy.

The film height between the cylinder housing and the smooth rod has a much smaller influence on the bearing friction force. A doubling of the film height only decreases the friction force by 0.5%. Decreasing the film height has a larger effect as this eventually results in pure mechanical friction. Halving the film height however only increases the bearing friction force by less than 1%. Assuming a constant film height is therefore a valid simplification of the bearing friction model.

### Design parameter influence

**PRS losses** The efficiency of the PRS is influenced by design parameters such as the lead of the screw, the amount of thread starts and the ratio between the screw and roller radius.

First, the influence of the screw lead is discussed. Figure A.4 shows the working point efficiency of the PRS with different screw leads. Note the overall size of the screw remains constant in this figure. The sharp transitions in the curve are caused by the rounding of contact points in the PRS. At very low lead values, the efficiency approaches 100% due to the very high rotational velocity required to reach the linear velocity of the actuator. The high velocity results in optimal fluid film characteristics with reduced friction forces. It is important to note that this optimal efficiency is not attainable due to eigenfrequency constraints. When the lead increases, the rotational velocity decreases proportionally. The viscous frictional moment is proportional to the rotational velocity by  $M_{visc} \propto \omega^2$  as can be seen in Figure A.5. The decreasing viscous friction results in higher efficiencies with increasing lead values. However, at high lead values and the corresponding large helix angle the load on the screw face becomes much larger resulting in decreased screw efficiency. This can be seen in Figure A.5 with the increasing geometric and load dependant factor.

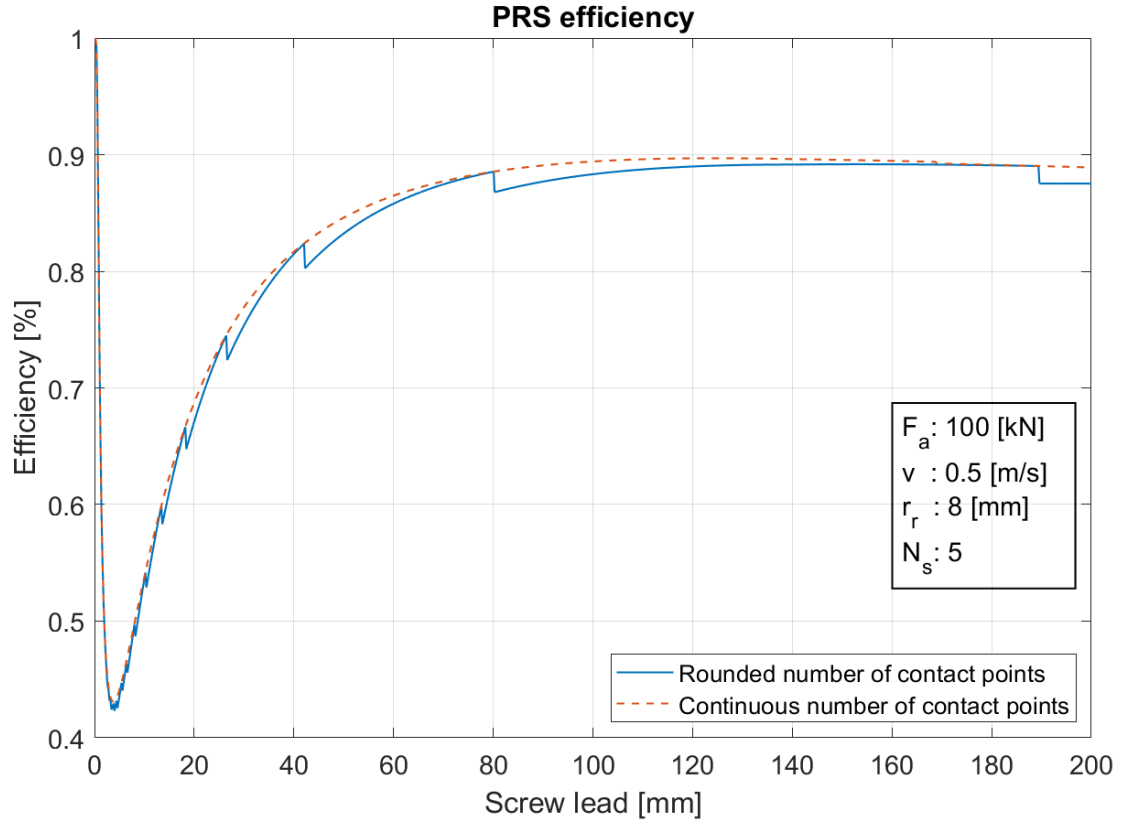


Figure A.4: PRS efficiency with different screw lead values.

Next to the lead of the screw, also the number of thread starts influence the efficiency of the PRS. The influence of the thread starts on the efficiency is shown in Figure A.6. The efficiency of the screw is seen to be highest for a single thread start and decrease with more thread starts. This has mainly to do with the reduced true lead of the screw and the resulting increase in rotational speed of the screw. The increase of rotational velocity of the screw results in much higher viscous friction.

Finally, the influence of the roller to screw radius is investigated. The radius ratio is an important factor in determining the gear ratio of the PRS. The radius ratio is defined as  $R_{r_s, r_r} = \frac{r_s}{r_r}$ , as such an increase in radius ratio with a fixed screw radius result in a decreased roller radius. The efficiency of the PRS with respect to the radius ratio is shown in Figure A.8. A smaller roller radius is seen to increase the working point efficiency of the PRS. The smaller roller radius increases the true lead of the screw and therefore decreases the rotational velocity of the screw and the corresponding viscous friction. The smaller roller radius also decreases the geometry related losses significantly as the friction arm on the contact points decreases.

## A.6.2 Helical gearbox losses

Sensitivities of model assumptions and the influence of the design parameters on the gearbox losses are discussed below.

### Sensitivities

The helical gear stage losses are discussed in Subsection 3.4.3. The gear stage losses are determined with well known loss models in literature. The major simplification in modelling the gearbox losses is the use of an empirical no load power loss model developed for vertical gearboxes on a horizontal gearbox. The total gearbox losses are a summation of the different loss components found in Subsection 3.4.3. As such, the power loss ratio of the no-load losses gives the influence of variations on the total power loss. The power loss ratio of the no-load losses is shown in Figure A.10.

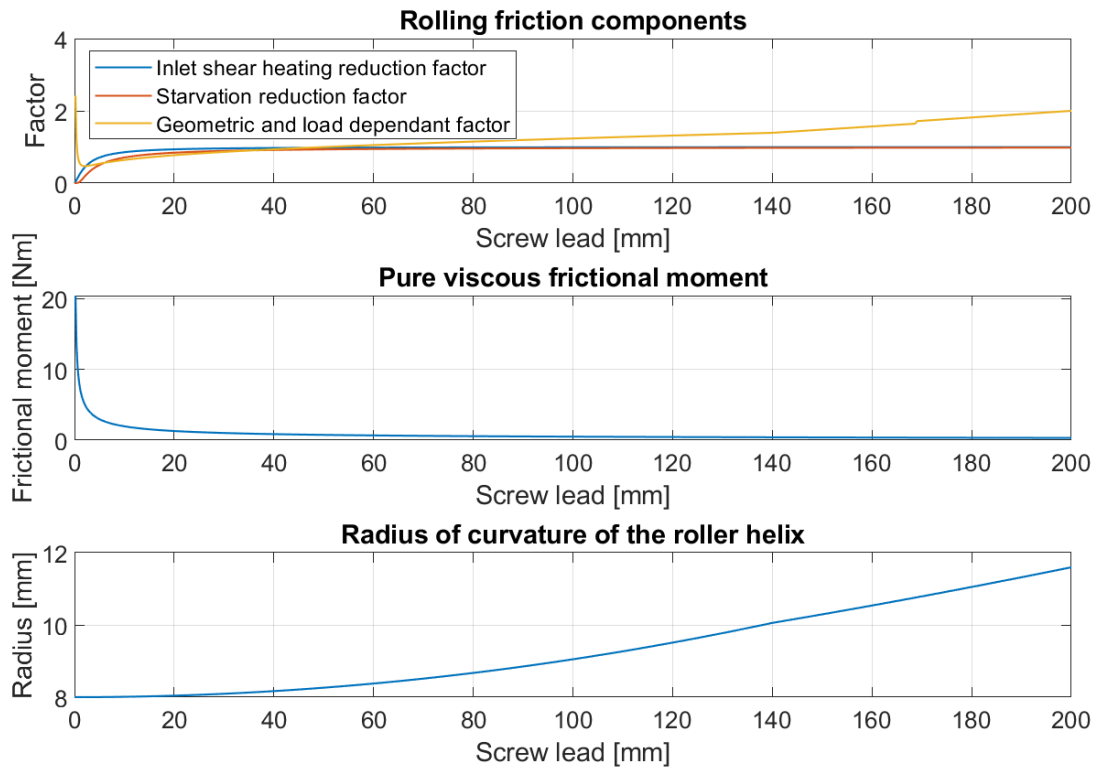


Figure A.5: Screw lead dependant  $\mu_r$ .

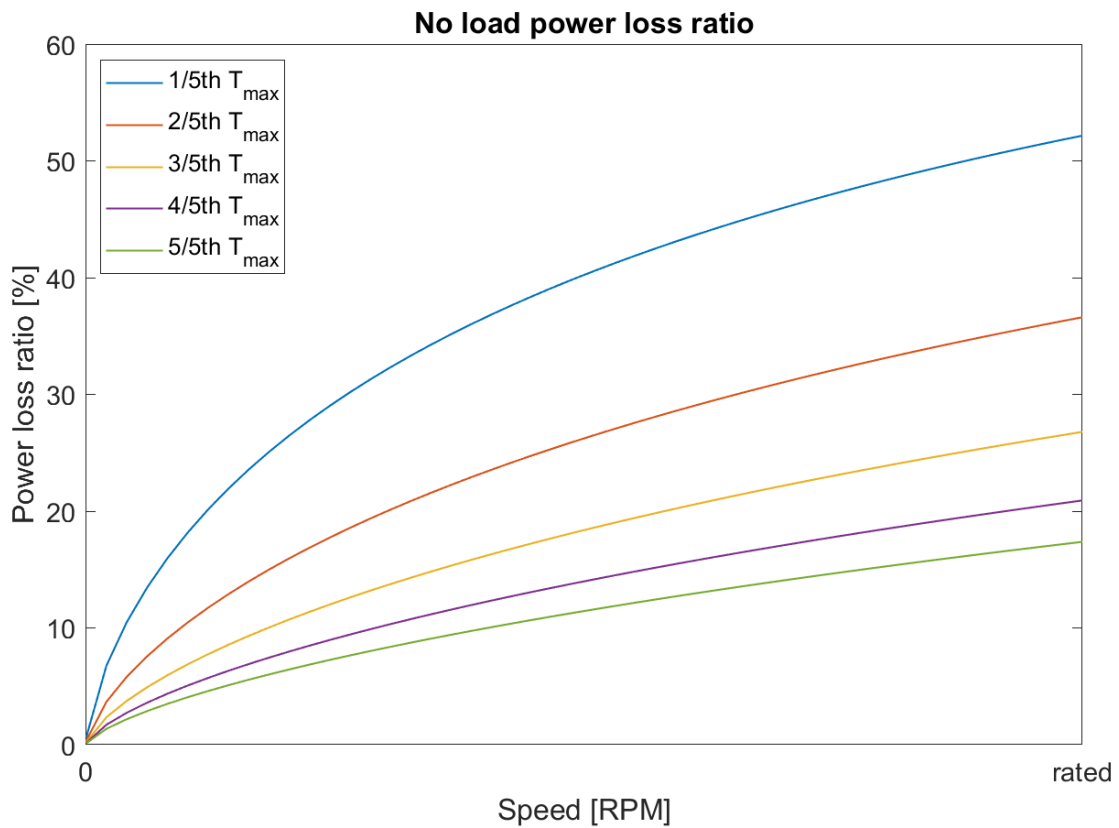


Figure A.10: No-load gear loss ratio to the total gear losses.

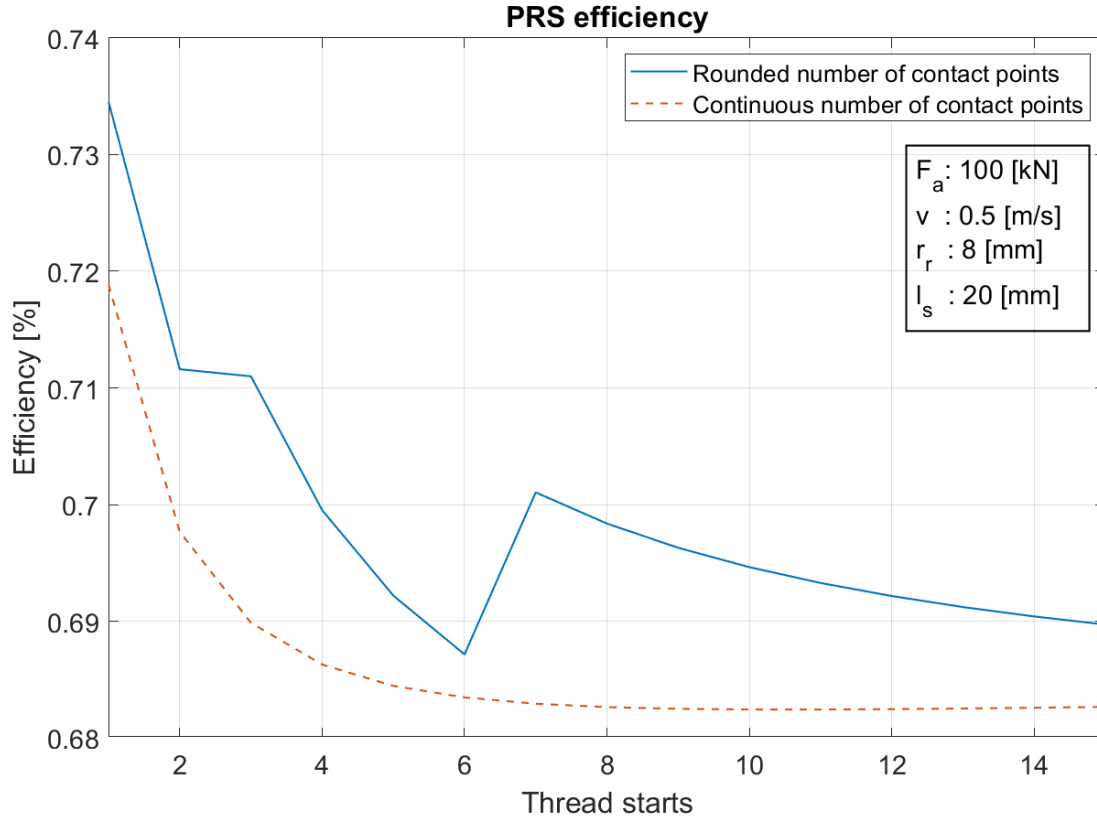


Figure A.6: PRS efficiency with different thread starts.

From Figure A.10, the no-load power is seen to make up a significant portion of the total gear power loss. Especially for lower loads and high speeds, the power loss ratio dominates the gear power loss. The power loss ratio is expected to approach 100% when the output torque approaches zero. For higher loads and lower speeds, the no-load power loss ratio decreases significantly. This makes sense as the no-load losses are independent of the load and related to the speed with  $P_{noload} \propto \omega^{1.5}$ . In contrast, the load dependant losses should behave approximately linear with the load as frictional force is linearly related to the normal force on the gears. Deviations from the linear trend are explained by the lower exponential dependencies of the coefficient of friction on the load. Dependency of the load dependant losses on the speed of the gear consequently should also be linear as the power loss is the product of friction force and sliding velocity. For applications with high output speeds and low mean torque, the effect of changing the gearbox orientation on the no-load losses should be further investigated. For higher load cases, especially with low output speeds, small variations on the no-load losses have only a small impact on the total gear power losses.

### Design parameter influence

Another input parameter of the gearbox is the gear ratio optimization parameter. The gear ratio has also an influence on the overall efficiency of the gearbox. Figure A.11 shows the power loss of an example gearbox. Especially for higher loads the power loss increases significantly for higher gear ratio's. The steps in the plotted lines are caused by the integer tooth count on the gears. The power loss with continuous tooth numbers are shown with dotted lines.

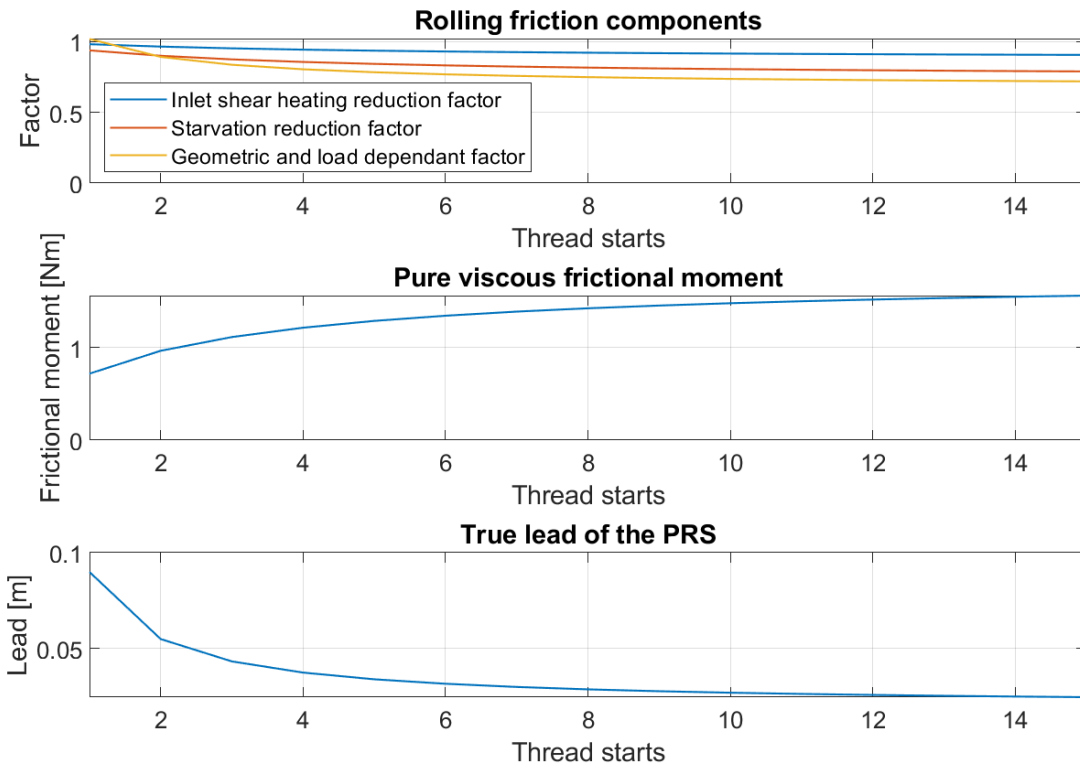


Figure A.7: Thread start dependant  $\mu_r$ .

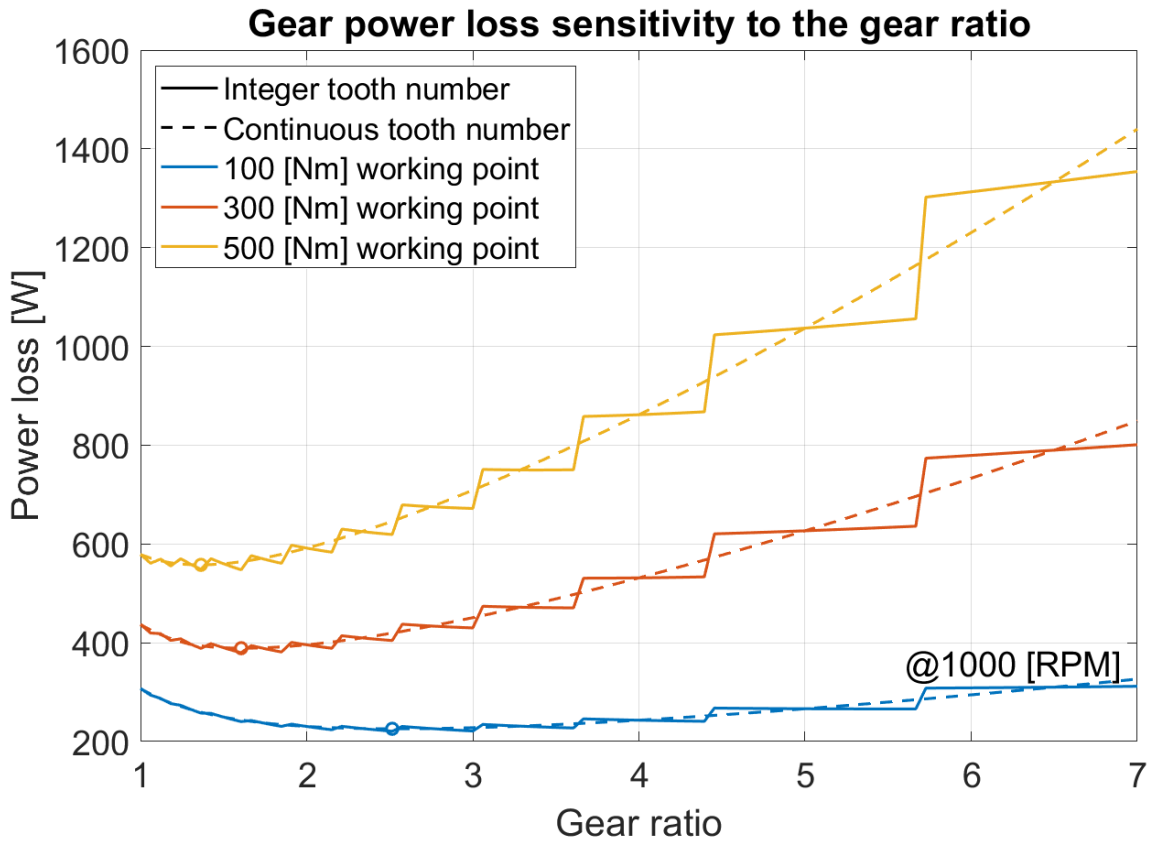


Figure A.11: Gear power loss sensitivity to the gear ratio.

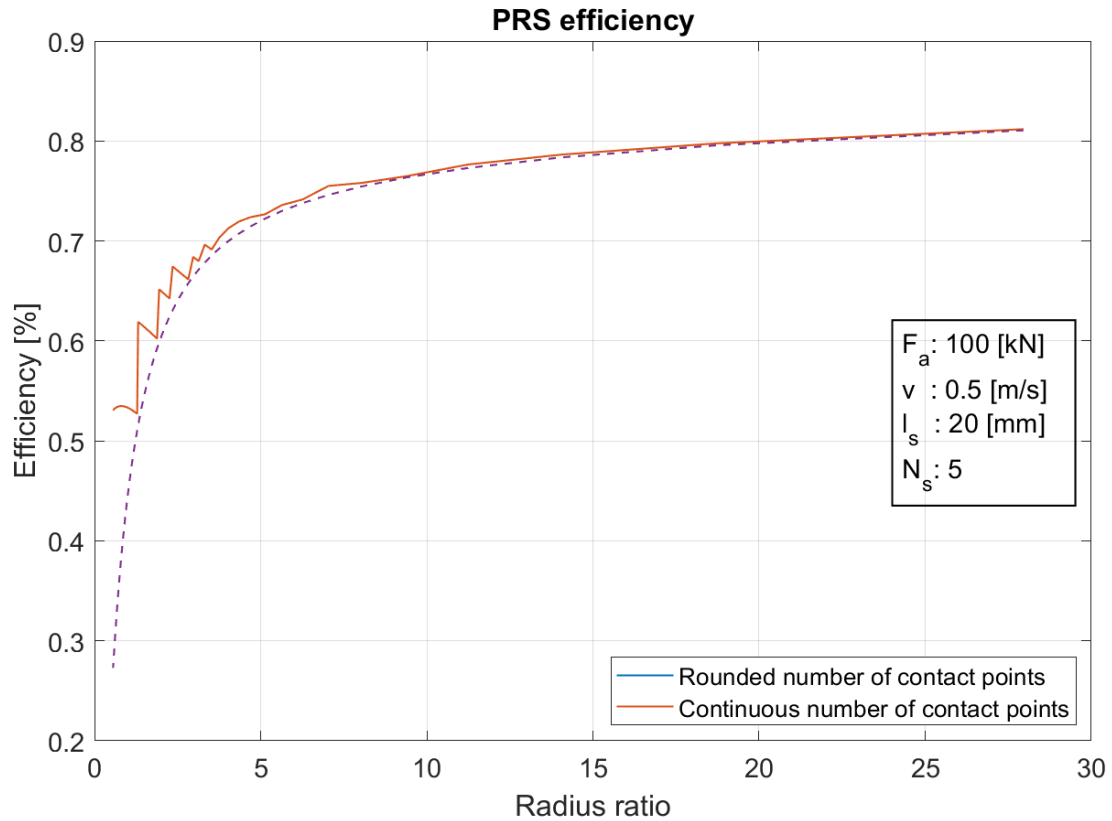


Figure A.8: PRS efficiency with different roller screw radii.

The increasing power loss for higher gear ratio's is largely explained by the larger diameter of the driven gear. A fixed output torque with an increasing driven gear radius results in a decreased maximum normal force on the gear teeth. Therefore the width of the gear teeth can be lowered. The resulting pressure on the gear teeth is, despite the lower normal force for the same torque, higher for higher gear ratio's. The higher contact pressure results in a higher mean coefficient of friction. Next to the higher mean coefficient of friction, also the geometric losses increase significantly. This has to do with the decreased number of gear teeth on the pinion gear with higher gear ratio's. A limitation of the gear model is the fixed gear teeth module. In reality the gear teeth module would decrease to increase the number of teeth on a small pinion gear. Developing a scaling law for the gear teeth module would be an interesting next step in developing the model. The combination of higher geometric losses and a higher coefficient of friction result in an increase in load dependant losses of the gearbox for higher gear ratio's. As the teeth width is lower for higher gear ratio's the no-load losses of the gearbox decrease slightly.

The optimal gear ratio is seen to shift towards a gear ratio equal to 1 with increasing output torque. This point is determined by the increasing load dependant losses and the decreasing no-load losses. Lower loads result in lower load-dependant losses and therefore have the intersection with the no-load losses further to the right of the scale.

The tooth module of the gears is mentioned above as a limitation of the model. The module is the ratio of the gear reference diameter and the number of teeth. With a constant module, the number of teeth for small gears become very low. High gear ratio's result in small pinion gears en therefore in low tooth numbers on these gears. This is not realistic as the gear module would change to accommodate for these small pinion gears. To limit the effect of this fixed gear module, the gear ratio in this optimization project will be limited to 5. Development of a scaling law for the tooth module could enable higher gear ratio's.

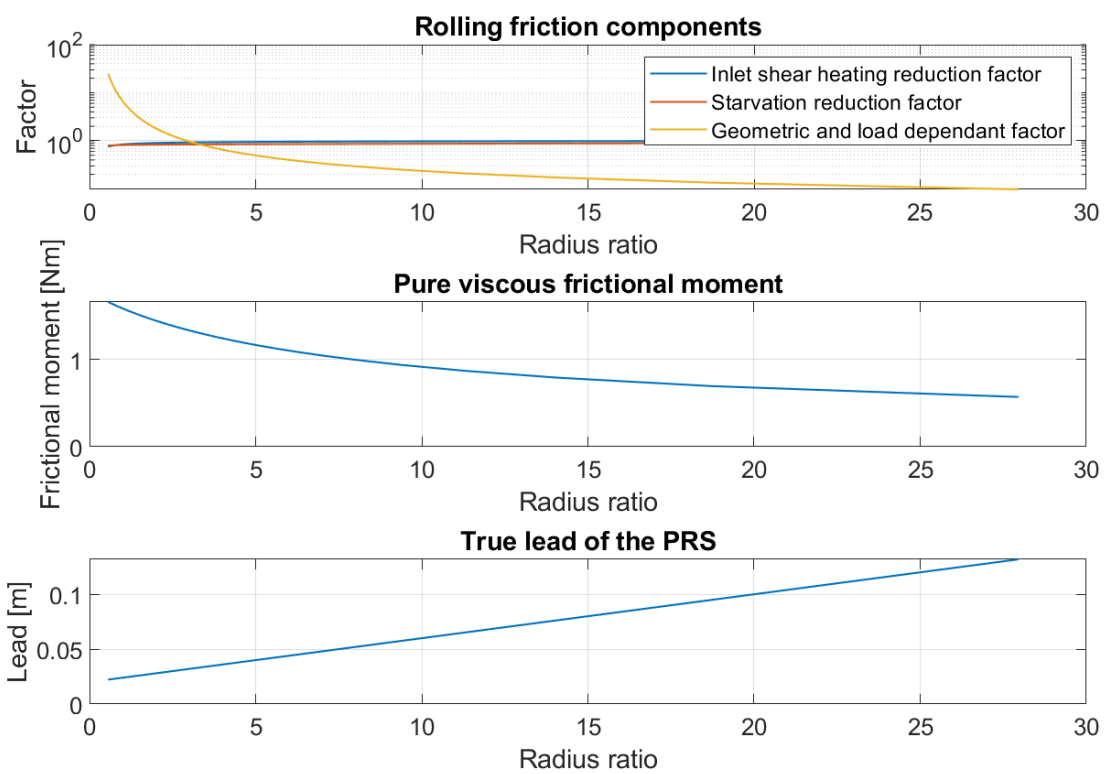


Figure A.9: Radius ratio dependant  $\mu_r$ .

# Appendix B

## Hydrostatic transmission equations

### B.1 Hydraulic cylinder sizing

#### B.1.1 Piston rod sizing

The piston rod of the hydraulic cylinder is sized based on pressure, yield strength and buckling requirements.

**Buckling requirement** The required buckling radius of the rod can be determined with the Euler critical load equation:

$$P_{cr} = \frac{\pi^2 EI}{k^2 L^2} \quad (\text{B.1})$$

By assuming a hollow cylinder with a fixed ratio between in and outside radius as described in Chapter 4, the moment of inertia of the rod can be expressed as:

$$I_r = \frac{\pi}{4} \left( r_{r,o}^4 - \left( \frac{r_{r,o}}{t_{ratio}} \right)^4 \right) \quad (\text{B.2})$$

Rewriting Equation B.2 for the outside rod radius  $r_{r,o}$  assuming the radius is a positive real number yields:

$$r_{r,o-buckling} = \frac{\sqrt{2} \sqrt[4]{I_r t_{ratio}}}{\sqrt[4]{\pi t_{ratio}^4 - \pi}} \quad (\text{B.3})$$

The required moment of inertia of the rod  $I_r$  is then given by rewriting Equation B.1 and including a structural safety factor.

$$I_r = \frac{F_{max} \text{FoS} k^2 L^2}{\pi^2 E} \quad (\text{B.4})$$

Here  $F_{max}$  is the maximum occurring compressive load on the cylinder rod. A structural safety factor FoS is added to add a margin on the maximum occurring load. The maximum occurring compressive load and the safety factor together form the critical load  $P_{cr}$ .  $k$  is the column effective length factor which can be taken as  $k = 0.85$  for the cylinder rod [20].  $L$  is the maximal unsupported length of the rod which is assumed to equal the length of the total stroke of the actuator. Finally,  $E$  is the young modulus of the piston rod material.

**Yield strength requirement** Next to buckling load, the piston rod should also be sized as to not exceed the yield strength of the material when loaded. The stress in the rod material can be determined by dividing the maximum occurring stress by the area of the rod. A structural safety factor is added to the maximum occurring force as safety margin:

$$\sigma = \frac{F_{max}FoS}{A_r} \quad (B.5)$$

The cross-sectional area of the rod is given as:

$$A_r = \pi (r_{r,o}^2 - r_{r,i}^2) \quad (B.6)$$

Substituting the thickness ratio in Equation B.6 results in the new cross-sectional area definition:

$$A_r = \pi r_{r,o}^2 \left( 1 - \frac{1}{t_{ratio}^2} \right) \quad (B.7)$$

Substituting Equation B.7 in Equation B.5 and solving for the outside radius yields:

$$r_{r,o} = \sqrt{\frac{F_{max}FoSt_{ratio}^2}{0.67\sigma_y\pi(t_{ratio}^2 - 1)}} \quad (B.8)$$

The 0.67 factor is commonly used to limit the maximum occurring stress to account for fatigue effects.

**Pressure requirement** The piston rod is loaded with the hydraulic fluid pressure on its outside surface. The required material thickness of a cylinder to withstand pressure is described by [46] as:

$$t_{pressure} = \frac{p_{max}r_{r,o}}{10\sigma_t - 0.5p_{max}} + c \quad (B.9)$$

Here  $t_{pressure}$  is given in [mm] and  $r_o$  is the outside radius of the piston rod in [mm].

$\sigma_t$  is the allowable stress in the rod material in [N mm<sup>-2</sup>] which is defined by the maximal yield strength as:

$$\sigma_t = 0.67e-6\sigma_y \quad (B.10)$$

Note the maximal yield strength should be entered in [N m<sup>-2</sup>].

The inside radius defined by the pressure requirement is then given as:

$$r_{r,i-pressure} = r_{r,o} - t_{pressure} \quad (B.11)$$

### B.1.2 Cylinder housing sizing

The thickness and radius of the cylinder housing should be sized to withstand buckling forces and the pressure of the hydraulic fluid according to [46]. Both criteria are evaluated separately.

**Buckling requirement** Buckling critical load of the entire cylinder is discussed in the DNVGL class guidelines for hydraulic cylinders [46]. The critical load is a function of a combination of the rod and housing sizing. The rod is already sized to withstand the buckling load on its own, hence the equations found in the class guidelines can be used to determine the needed housing thickness for the whole cylinder to withstand buckling. The critical load in the class guideline is given as:

$$P_E = \frac{E\pi^2}{LZ} \quad (B.12)$$

Here  $L$  is the total length of the extended cylinder in [m].  $Z$  is given as:

$$Z = \frac{L_1}{I_1} + \frac{L_2}{I_2} + \left( \frac{1}{I_2} - \frac{1}{I_1} \right) \frac{L}{2\pi} \sin \left( 2\pi \frac{L_1}{L} \right) \quad (B.13)$$

Here  $L_1$  and  $L_2$  are the lengths of the visible piston rod and cylinder housing measured from the attachment point respectively.  $I_1$  and  $I_2$  are the corresponding moment of inertia's of these parts.  $L$  is the total length of the extended cylinder and thus equal to  $L = L_1 + L_2$ .

Using the expression for the moment of inertia found in Equation B.4, the critical load equation can be solved for the outside radius of the housing (not shown).

The results from the DNVGL equation return very small thickness requirements. To backup the results, the conventional euler critical load equation is used as well assuming the load is applied at the top of the cylinder (stuck rod scenario). By rewriting the euler critical load equation in terms of the outside cylinder radius, the following equation is obtained:

$$r_{ch,o} = \sqrt[4]{\left(P_E + \frac{\pi^3 E}{4k^2 L^2} r_{ch,i}^4\right) \frac{4k^2 L^2}{\pi^3 E}} \quad (\text{B.14})$$

**Hydraulic pressure requirement** The pressure in the cylinder tends to press the sidewall of the housing outward, to ensure the cylinder walls can hold the required cylinder pressure, proper wall sizing should be performed. [46] gives an expression for the minimal wall thickness in hydraulic cylinder housings:

$$t_{cylinder} = \frac{p_{max} r_{ch,i}}{10\sigma_t - 0.5p_{max}} + c \quad (\text{B.15})$$

Here  $t_{cylinder}$  is the thickness of the housing wall in [mm].  $p_{max}$  is the design pressure in [bar],  $\sigma_t$  is the allowable stress in [ $\text{N mm}^{-2}$ ], and  $c$  is a corrosion allowance usually taken as 0.3[mm]. The allowable stress is given by 67% of the total yield strength as  $\sigma_t = 0.67\sigma_y$  to account for fatigue effects.

## B.2 Pipe loss model

Pipe losses include the pressure drop associated to pipe flow friction, friction due to resistances in the bends in the pipe and manifold and the head loss due to gravity. The pipe flow resistance losses and resistance losses are discussed below.

### B.2.1 Pipe flow resistance loss

The pressure loss in a pipe due to flow friction  $\delta p_p$  is described by the Darcy-Weisbach equation as:

$$\delta p_p = \lambda \frac{L}{d_{flow}} \rho_{hf} \frac{v_{fluid}^2}{2} \quad (\text{B.16})$$

Here  $\lambda$  is the pipe friction coefficient,  $L$  is the length of the pipe in [m],  $d_{flow}$  is the inside diameter of the pipe in [m] determined in Subsection 4.3.2,  $\rho_{hf}$  is the mass density of the hydraulic fluid in [ $\text{kg m}^{-3}$ ] and  $v_{fluid}$  is the mean fluid velocity in the pipe in [ $\text{m s}^{-1}$ ].

The mean fluid velocity in the pipe is determined by the volume flow through the pipe  $Q$  and the cross sectional area of the pipe ( $A_{pipe} = \pi \left(\frac{d_{flow}}{2}\right)^2$ ) as:

$$v_{fluid} = \frac{Q}{A_{pipe}} \quad (\text{B.17})$$

The pipe friction coefficient  $\lambda$  is different in the laminar and turbulent flow region. The laminar friction coefficient is determined in [176] as:

$$\lambda_{la} = \frac{64}{Re} \quad (\text{B.18})$$

With the Reynolds number  $Re$  defined as:  $Re = v_{fluid} \frac{\rho_{hf}}{\mu_{hf}}$ . The friction coefficient in the turbulent region can be defined with methods. Here the Swamee-Jain equation [154] is used with:

$$\lambda_{tu} = \frac{0.25}{\left(\log\left(\frac{\epsilon}{3.7d_{flow}} + \frac{5.74}{Re^{0.9}}\right)\right)^2} \quad (\text{B.19})$$

Here  $\epsilon$  is the roughness of the pipe taken as  $\epsilon = 0.05[\text{mm}]$  [176]. The different flow regions are defined based on the Reynolds number, a Reynolds number under 2300 is defined as fully laminar flow and a Reynolds number over 4000 is defined as fully turbulent flow. To account for the transition region, the friction coefficient is determined as:

$$\begin{aligned} \lambda(Re < 2300) &= \lambda_{la} \\ \lambda(Re > 2300) &= (1 - f_{turbulence})\lambda_{la} + f_{turbulence}\lambda_{tu} \\ \lambda(Re > 4000) &= \lambda_{tu} \end{aligned} \quad (\text{B.20})$$

here  $f_{turbulence}$  is the turbulence factor determined as:

$$f_{turbulence} = \frac{Re - 2300}{4000 - 2300} \quad (\text{B.21})$$

### B.2.2 Pipe restriction loss

The pressure drop in the hydraulic system of the EHA due to restrictions in the flow path is simply described by the resistance values of the bends in the pipe. Here we assume 4 90 deg corners are present in the system. The pressure drop is then defined in [176] as:

$$\delta p_r = 4K_{corner}\rho_{hf}\frac{v_{fluid}^2}{2} \quad (\text{B.22})$$

Here  $K_{corner}$  is the resistance value for a 90 deg pipe bend defined as  $K_{corner} = 0.75$  [176].

## B.3 Seal friction model

The frictional forces on the seals are expected to behave as a fluid lubricated contact. Therefore the Stribeck curve is ideally suited to model the cylinder friction. [18] describes a Stribeck function specifically for determining losses in sliding contacts. The cylinder seal friction force can therefore be defined as [18]:

$$F_{cyl,loss} = \left(F_c + (F_s - F_c)e^{(|v|/v_s)^i} \text{sign}(v)\right) + k_v v [\text{N}] \quad (\text{B.23})$$

Here  $F_c$  is the coulomb friction force which is defined as:

$$F_c = F_n \mu_f [\text{N}] \quad (\text{B.24})$$

The normal force  $F_n$  on the seals is a function of the pretension of the seal material on the sealing surface defined in [91] as:

$$F_n = \pi(2(r_s - t_s) + t_s) s_p \sigma_{av} \quad (\text{B.25})$$

Here  $r_s$  is the radius of the seal at the sliding interface and  $t_s$  is the thickness of the seal which is taken as a fixed value  $t_s = 0.008[\text{m}]$ .  $s_p$  is the contact width of the seal which is again taken as a constant value  $s_p = 0.0015[\text{m}]$ . The use of a constant contact width is warranted for high pressure step seals as they are known to behave largely independent of the working pressure. Finally  $\sigma_{av}$  is the average contact pressure of the seal which is modelled in [91] as:

$$\sigma_{av} = (2\epsilon + 0.13) \frac{\pi E_{seal}}{6} \quad (\text{B.26})$$

With  $\epsilon$  the maximum radial deformation of the seal which is often taken as  $\epsilon = 0.14[-]$  [91] and  $E_{seal}$  the young modulus of the seal material.

The stiction force  $F_s$  is assumed to be 30% larger than the coulomb friction force. Finally, the viscous coefficient of friction  $k_v$  is modelled by [93] as a function of the bearing contact area  $A_b$ , lubrication properties and the clearance between the seal and contact surface at higher speeds  $y_b$ :

$$k_v = \frac{A_b \mu_l \rho_l}{y_b} [\text{kg s}^{-1}] \quad (\text{B.27})$$

$y_b$  is assumed to be a constant value with  $y_b = 8e-6[\text{m}]$  [93].

## B.4 Loss model properties

To better understand the effect of sizing parameters on the power losses in the hydrostatic transmission, the general loss sensitivities to the piston area  $A_p$  and the volumetric displacement of the pump  $V_g$  are shown below.

**Hydraulic cylinder losses** Hydraulic cylinder losses are caused by friction of the linear bearings and seals. The piston area changes the diameter of these contact surfaces and hence influences the power loss. Figure B.1 shows the losses for the same working point of the actuator with respect to the piston area.

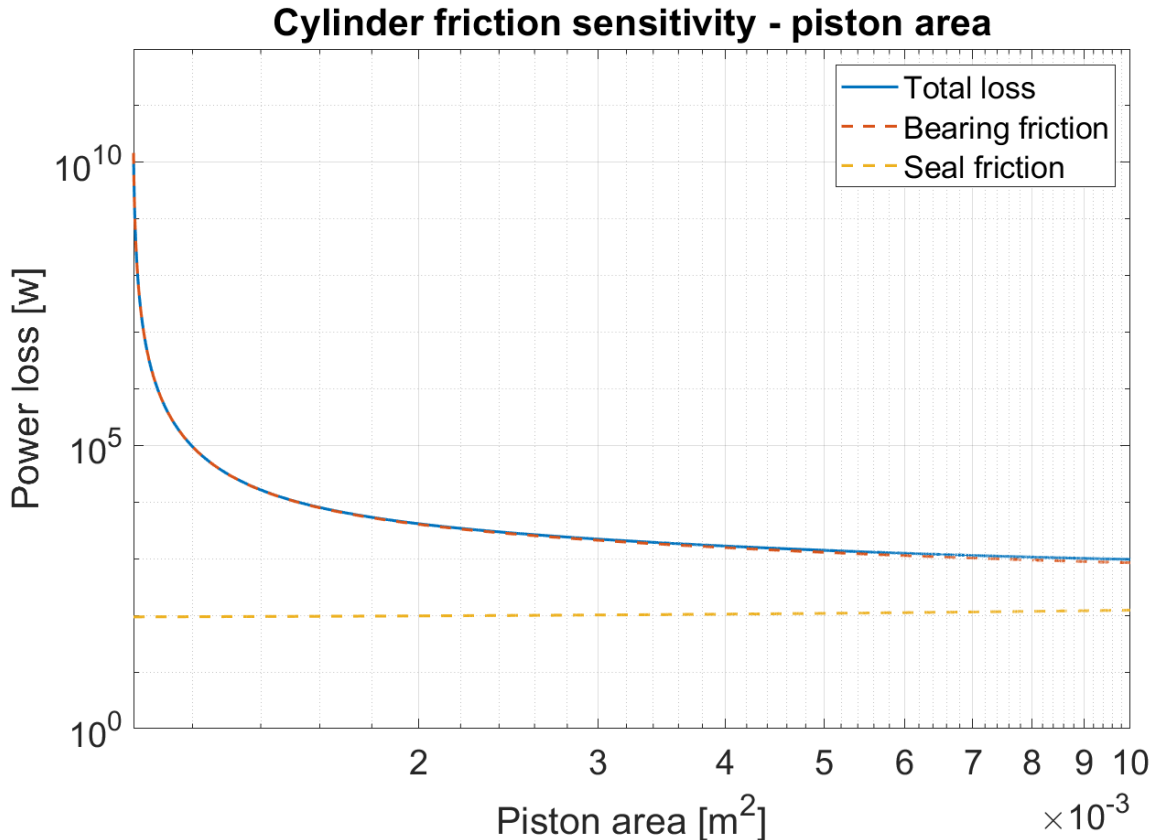


Figure B.1: cylinder friction loss sensitivity with respect to the piston area

A larger piston area results in a larger bearing contact surface and therefore decreased contact pressures resulting in a lower power loss. The reduced pressure in the cylinder as a result of the larger piston area does not influence the friction forces. The total power loss in the cylinder can be seen to be dominated by the bearing friction. Seal friction only becomes noticeable for larger pistons.

**Hydrostatic pump losses** Hydrostatic pump losses are caused by friction and leakage in the moving pump parts. Figure B.2 shows the losses for the same working point of the pump and a varying volumetric displacement. The detailed loss relations are shown in Appendix E.3.

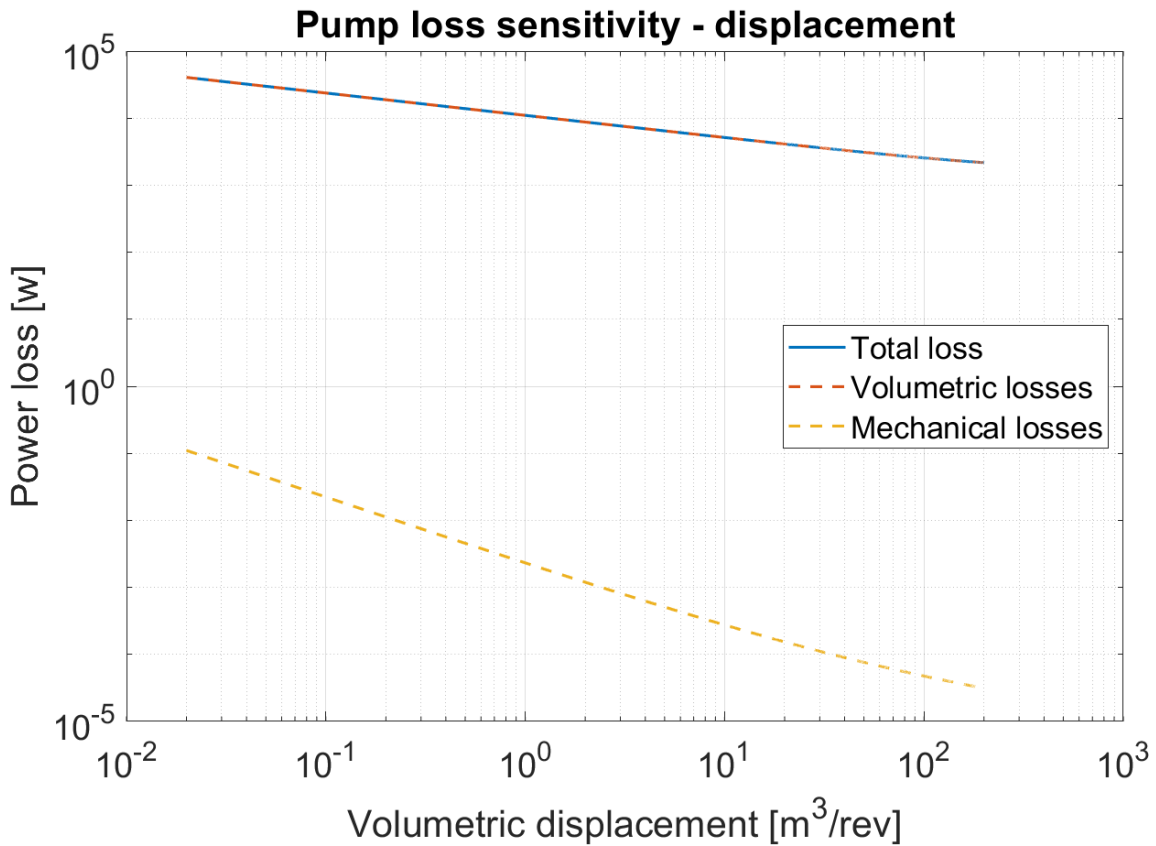


Figure B.2: Hydrostatic pump loss sensitivity with respect to the displacement

The power losses in the pump are mainly caused by the leakage in the pump. Mechanical losses are much less important which is explained by the well lubricated pump system. The overall pump power loss tends to decrease with increasing volumetric displacement. The larger pump displacement results in lower pump velocities which reduces both viscous and leakage losses significantly.

# Appendix C

## Servo motor equations

Chapter 5 discusses the model development of the PMSM. Extra information with respect to the model development is found in this appendix.

### C.1 Sizing models

#### C.1.1 Configuration sizing

**Motor pitch factors** Both a pitch factor for the poles  $\tau_p$  and slots  $\tau_u$  on the stator can be determined. Both factors are described in [72] as:

$$\tau_p = 2\pi \frac{r_a}{p} \quad (\text{C.1})$$

$$\tau_u = 2\pi \frac{r_a}{Q} \quad (\text{C.2})$$

The pole and slot pitch factors can also be used in determining the harmonic winding factor of the PMSM windings in the stator. First the pitch factor should be determined according to (Wikipedia: winding factor):

$$k_p = \cos(a/2) \quad (\text{C.3})$$

Here  $a$  is the value by which the coil is short pitched. This is calculated as  $a = \tau_p - \tau_u$ . The harmonic winding factor can then be calculated as:

$$k_{ws} = k_d k_p \quad (\text{C.4})$$

Here  $k_d$  is the distribution factor which is often taken as 1 for the permanent magnet synchronous machine.

**Tooth sizing** Next, the required tooth width on the stator can be determined. The tooth width is dependent on the magnetic properties of the motor and is described in [142] as:

$$b_d = \frac{L_m \tau_u B_{\max}}{k_{Fe} L_{rotor} B_{dper}} \quad (\text{C.5})$$

Here  $k_{Fe}$  is the stator core space factor and  $B_{dper}$  is the permitted flux density in the stator teeth in [T].

**Conductor sizing** Conductor sizing is necessary to determine the resistance in the stator windings. The resistance in the stator windings is a necessary parameter to determine the copper losses of the motor. A model to determine the stator winding resistance is found in [142]. The first step is to determine the amount of magnetic flux per pole:

$$\phi_{av} = \frac{2}{\pi} B_{\delta} (r_{\text{rotor}} + t_g) \pi \frac{L_m}{p_p} \quad (\text{C.6})$$

With the magnetic flux per pole, the number of stator turns needed for the induced EMF by the permanent magnets can be calculated. The maximum occurring EMF should be equal to the phase voltage  $U_{\text{phase}}$  of the electrical supply bus. The number of stator turns should be an integer number, as such it is determined as:

$$N_s = \text{ceil} \left( \frac{U_{\text{phase}}}{\sqrt{2} \pi f_e k_{ws} \phi_{av}} \right) \quad (\text{C.7})$$

With the number of stator turn known, the number of conductors per stator slot can be calculated according to:

$$Z_q = \text{ceil} \left( \frac{N_s}{p_p q} \right) \quad (\text{C.8})$$

Next, the conductors of the stator winding should be sized. For proper wire sizing, the maximum occurring current through the windings should be known. The maximum stator winding current is determined according to:

$$I_{\text{max}} = \frac{P_{\text{max}}}{\text{phase eff}_{es} \cdot U_{\text{phase}} P_f} \quad (\text{C.9})$$

Her  $P_{\text{max}}$  is the maximum mechanical output power of the PMSM in [W].  $\text{eff}_{es}$  is the estimated efficiency of the PMSM which is fixed to 90%.  $P_f$  is the estimated power factor of the PMSM fixed to 0.9. The maximum occurring stator winding current can then be used to determine a suitable cross-sectional area of the stator slot:

$$S_{cs} = \frac{I_{\text{max}} z_q}{I_{\text{dens}} k_{cs}} \quad (\text{C.10})$$

Here  $I_{\text{dens}}$  is the current density of the stator in [ $\text{A m}^{-2}$ ] and  $k_{cs}$  is the winding space factor which is used to account for spacing due to wire insulation. The cross-sectional area of the stator slots is then used to determine the cross-sectional area of the conductors:

$$A_{\text{con}} = \frac{S_{cs}}{z_q k_{cs}} \quad (\text{C.11})$$

Finally, the total length of copper per phase can be determined according to:

$$L_w = z_q q p (L_{\text{rotor}} + b_d) 2 \quad (\text{C.12})$$

The resistance of the windings is finally given as a function of the winding length and the cross sectional area of the winding conductors:

$$R_s = \frac{\rho_{res} L_w}{A_{con}} [\Omega] \quad (\text{C.13})$$

Here  $\rho_{res}$  is the resistivity of the winding material in [ $\Omega \text{mm}^2 \text{m}^{-1}$ ] and  $R_s$  is the total resistivity of the winding in [ $\Omega$ ].

**Stator housing sizing** Stator housing sizing is done with a model from [142]. First, the height of the permanent magnet material and the height of the stator yoke should be determined. The height of the permanent magnets is calculated as:

$$h_{PM} = \frac{U_m}{H_c - \frac{H_c}{B_r} B_{\max}} \quad (C.14)$$

Here  $U_m$  is the magnetic voltage in the air gap which is determined as:  $U_m = \frac{B_{\max} g_{eq}}{\mu_0}$  where  $g_{eq}$  is the equivalent airgap which is dependent on the chosen winding type. Here a concentrated winding type is chosen as this results in a slightly higher power density compared to distributed winding types:

$$g_{eq} = k_c t_g \quad (C.15)$$

Here  $k_c$  is carter's coefficient for a distributed winding type.  $H_c$  is the coercivity of the permanent magnet in  $[A\ m^{-1}]$  and  $B_r$  is the remanence of the permanent magnet in  $[T]$ . Next, also the height of the stator yoke is calculated:

$$h_{ys} = \frac{\phi_{av}}{2k_{Fe} L_{rotor} B_{yperm}} \quad (C.16)$$

Here  $k_{Fe}$  is the stator core space factor and  $B_{yperm}$  is the permitted magnetic flux density in the yoke in  $[T]$ . The Yoke internal radius can be determined next by adding the tooth length to the inside stator radius. The tooth height is determined by:

$$h_t = \frac{-Qb_d + 2r_a\pi - \sqrt{(Qb_d - 2r_a\pi)^2 + 4QS_{cs}\pi}}{-2\pi} \quad (C.17)$$

Here  $Q$  is the number of stator slots and  $r_a$  is the stator internal radius. Above equation is derived by rewriting the equation for the total cross sectional area between the inside stator radius and the inside yoke radius. Figure C.1 shows the main sizing parameters of the stator.

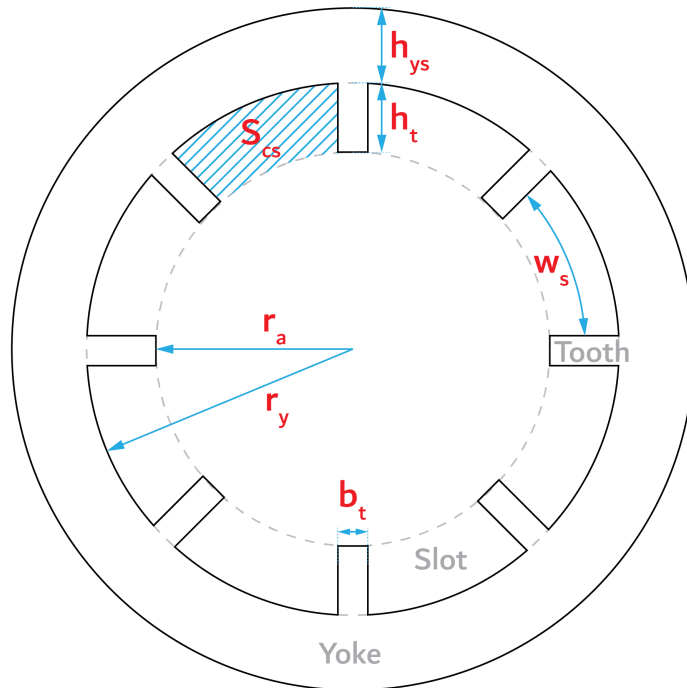


Figure C.1: PMSM stator sizing parameters.

The respective volume of the yoke and teeth can than be determined as:

$$V_y = \left( (r_y + h_{ys})^2 - r_y^2 \right) L_{\text{rotor}} \pi \quad (\text{C.18})$$

$$V_t = \left( (r_y^2 - r_a^2) \pi - QS_{cs} \right) L_{\text{rotor}} \quad (\text{C.19})$$

Masses of these components define the electrical steel mass of the PMSM. The mass of these components is an important parameter in determining the iron losses of the PMSM:

$$m_{c,y} = \rho_{es} V_y \quad (\text{C.20})$$

$$m_{c,t} = \rho_{es} V_t \quad (\text{C.21})$$

Here  $\rho_{es}$  is the density of electrical steel.

### C.1.2 Load sizing

As the axle of the PMSM should be capable of withstanding the torque induced shear forces, the minimum radius of the axle  $r_{ax}$  is determined by shear force requirements. The minimum axle radius according to this requirement si determined by:

$$r_{ax} = \sqrt[3]{\frac{1.73 f_{sc} 2T_{rated} \text{FoS}}{0.67 \pi \sigma_y}} \quad (\text{C.22})$$

Here  $f_{sc}$  is a stress concentration factor fixed to  $f_{sc} = 1.1$  and FoS is a structural safety factor. Factors 1.73 and 0.67 are respectively the von misses total stress to shear stress ratio and the fatigue correction factor.  $\sigma_y$  is the yield strength of the axle material.

### C.1.3 Static mass fit

The static mass of the PMSM is determined using a scaling law fit to mass data found in catalogue data of Rexroth (Table C.1). The scaling law is found in [30], fitting this scaling law to the catalogue data from Rexroth gives:

$$m_{PMSM} = 1.4515 T_{rated}^{6/7} \quad (\text{C.23})$$

The fitted scaling law is shown in Figure C.2.

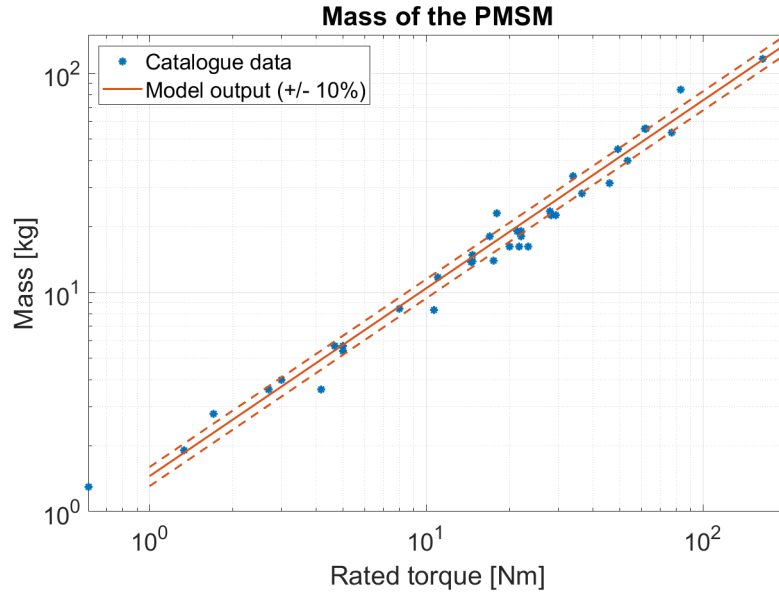


Figure C.2: Fitted scaling law of the PMSM mass.

Table C.1: Rexroth catalogue data, obtained from [www.boschrexroth.com](http://www.boschrexroth.com) MSK series synchronous servo motors

Max RPM	$T_{max}$ [N m]	$I_{max}$ [A]	$I_{rotor}$ [kg m <sup>2</sup> ]	Mass [kg]	$U_{max}$ [V]
9000	1.8	6.8	0.000013	1.3	750
9000	4	6.8	0.00003	1.9	750
6000	5.1	6	0.0001	2.8	750
7500	5.1	8	0.0001	2.8	750
6000	8.1	9.6	0.00014	3.6	750
7500	8.1	12.4	0.00014	3.6	750
7500	12.5	18.5	0.000083	3.6	750
4300	9	7.2	0.00028	4	750
6000	9	11.2	0.00028	4	750
6000	9	14.8	0.00028	4	750
4700	15	12.4	0.00033	5.4	750
6000	15	18.8	0.00033	5.4	750
6000	15	24.8	0.00033	5.4	750
4800	15	12	0.00048	5.7	750
6000	15	24.4	0.00048	5.7	750
4900	24	19.2	0.0008	8.4	750
6000	24	38	0.0008	8.4	750
4200	14	8.6	0.00044	5.7	750
3100	32	14.4	0.000752	8.3	750
4200	32	19.4	0.000752	8.3	750
6000	32	34.7	0.000752	8.3	750
2500	33	12.6	0.00291	11.7	750
5500	33	25	0.00291	11.7	750
6000	33	36.9	0.00291	11.7	750
2700	52.5	24.8	0.00375	14	750
4900	52.5	33	0.00375	14	750
6000	52.5	49.8	0.00375	14	750
2200	70	25.6	0.00458	16.2	750
5300	65	49.3	0.00458	16.2	750
6000	60	57.9	0.00458	16.2	750
3500	44	23.4	0.00173	13.9	750
5000	44	32.9	0.00173	13.9	750
5800	44	40.1	0.00173	13.9	750

3200	66	32.8	0.0023	18	750
3800	66	40.5	0.0023	18	750
6000	66	69.3	0.0023	18	750
3400	84	45.5	0.0029	23.5	750
4200	84	56.3	0.0029	23.5	750
6000	84	90.1	0.0029	23.5	750
4100	44	28.4	0.00352	14.8	750
5000	44	37.8	0.00352	14.8	750
6000	44	56.7	0.00352	14.8	750
3800	64	37.4	0.0049	19	750
4800	66	52.7	0.0049	19	750
6000	64	74.3	0.0049	19	750
3850	88	45.9	0.00613	22.5	750
5200	88	63.9	0.00613	22.5	750
6000	88	83.7	0.00613	22.5	750
4700	43.5	32.4	0.0043	13.8	750
5000	43.5	54.9	0.0043	13.8	750
4400	54	41.4	0.011	23	750
5200	54	45.9	0.011	23	750
6000	54	54	0.011	23	750
4100	102	66.2	0.0192	34	750
4500	102	78.3	0.0192	34	750
4500	102	106.7	0.0192	34	750
4500	102	110.7	0.0192	34	750
3500	148	79.7	0.0273	45.1	750
4500	148	97.2	0.0273	45.1	750
4000	148	159.3	0.0273	45.1	750
2000	187	58.5	0.035	56	750
3000	187	93.2	0.035	56	750
3000	185	135	0.035	56	750
3300	110	67.1	0.0065	28.3	750
4500	110	84.2	0.0065	28.3	750
5800	110	113	0.0065	28.3	750
3400	160	99.9	0.00932	40	750
4600	160	137.7	0.00932	40	750
6000	160	187.7	0.00932	40	750
3500	231	144.5	0.0138	53.5	750
4600	231	187.4	0.0138	53.5	750
6000	231	262.4	0.0138	53.5	750
4800	51	40	0.00442	18	750
4700	85	63	0.00594	22.5	750
4600	138	94.7	0.00894	31.6	750
3200	250	165	0.0232	84	750
3000	495	293.4	0.0382	116	750

## C.2 PMSM parameters

Table C.2: PMSM fixed parameters

Parameter	Value	Comment
$k_{Fe}$	1.5 & 2	Experimental iron loss correction factor for the yoke and teeth [117]
$B_c$	1.3 & 1.59	Magnetic flux strength correction factor for the yoke and teeth [117]
$P_{15}$	0.9[kg <sup>-1</sup> ]	Experimental power density factor [117]
$k_p$	10[Ws <sup>2</sup> /m <sup>4</sup> ]	Experimental mechanical loss factor [127]

# Appendix D

## General parameters and equations

### D.1 General parameters

Sizing and power loss models make frequent use of material properties and physical constants. These general parameters used in the various models are listed below.

Parameter	Value	Explanation
$E_{st}$	230e9 [Pa]	Young modulus of steel
$E_{hs}$	201e9 [Pa]	Young modulus of hardened steel (50CrMo4 [29])
$E_{al}$	68.9e9 [Pa]	Young modulus of aluminium (A6061 aluminium)
$E_{seal}$	4e6 [Pa]	Young modulus of rubber (70 shore A rubber [15])
$\mu_{hf}$	220e-6 [m <sup>2</sup> s <sup>-1</sup> ]	Kinematic viscosity of hydraulic fluid (mineral oil ISO 68)
$\nu_{hf}$	2e-5 [m <sup>2</sup> s <sup>-1</sup> ]	Kinematic velocity of hydraulic fluid (mineral oil ISO 68)
$\beta_{hf}$	700e6 [N m <sup>-2</sup> ]	Bulk modulus of hydraulic fluid (mineral oil ISO 68)
$\rho_{es}$	7650 [kg m <sup>-3</sup> ]	Density of electrical steel
$\rho_{st}$	7800 [kg m <sup>-3</sup> ]	Density of steel (50CrMo4 [29])
$\rho_{cst}$	7300 [kg m <sup>-3</sup> ]	Density of cast steel
$\rho_{cu}$	8960 [kg m <sup>-3</sup> ]	Density of copper
$\rho_{al}$	2710 [kg m <sup>-3</sup> ]	Density of aluminium
$\rho_{hf}$	880 [kg m <sup>-3</sup> ]	Density of hydraulic fluid (mineral oil ISO 68)
$\sigma_{y,st}$	650e6 [Pa]	Yield strength of high strength steel (50CrMo4 [149])
$\sigma_{y,al}$	310e6 [Pa]	Yield strength of die-cast aluminium
$\sigma_{gear}$	1000e6 [Pa]	Fatigue strength limit of gear material [119]
$\sigma_{c380}$	3e8 [Pa]	Compressive strength of Orkot c380 material (linear bearings)
FoS	1.5	General structural safety factor
FoS <sub>hydraulic</sub>	6	General structural safety factor
$n_{max}$	3300 [rpm]	Maximum allowable motor speed
$p_{max}$	330e5 [Pa]	Maximum allowable system pressure
$\mu_0$	4e-7 $\pi$ [H m <sup>-1</sup> ]	Permeability of free space

### D.2 Cubic Mean Load

The cubic mean load is a necessary parameter in determining the sizing of mechanical components for its design lifetime. The cubic mean load is determined based on a representative time series of the forces on the actuator during normal operation.

As the cubic mean load is influenced by preload on the mechanical transmission, the required preload is determined as well. The model determining the cubic mean load described in this section is based on equations found in the design guidelines for the planetary roller screw detailed in the datasheet of Nook industries and Rollviss swiss.

The cubic mean load or equivalent load is determined according to:

$$F_{eq} = \sqrt[3]{\frac{\sum_{i=0}^t s v_i P_i^3}{\sum_{i=0}^t s v_i}} \quad (D.1)$$

Here  $s$  is the time step of the time series and  $t$  represents the number of samples in the time series.  $v_i$  is the velocity of sample  $i$  in  $[\text{m s}^{-1}]$  and  $P_i$  is the load at sample  $i$  in  $[\text{N}]$ . The load in the actuator is given in the time series but is altered by possible preload in the transmission. According to design guidelines of Nook industries, the preload compensated actuator load is given as:

$$\begin{aligned} P(P < P_{comp}) &= 0.65 \cdot P + F_p \\ P(P \geq P_{comp}) &= P \end{aligned} \quad (D.2)$$

Here  $P$  is the load given by the time series in  $[\text{N}]$ .  $P_{comp}$  is the load compensated by the preload force in  $[\text{N}]$ .  $F_p$  is the preload force in the mechanism in  $[\text{N}]$ . The preload force is given according to Nook industries by:

$$F_p = \frac{P_{comp}}{2.83} \quad (D.3)$$

### D.3 Scaling coefficients

Mass scaling of the different EMA and EHA components is dependant on multiple parameters. As a reference for the interested reader, scaling laws with respect to the main sizing parameter for actuators resembling the Ampelmann A-type actuator are shown below. These scaling laws are derived from the models detailed in Chapter 3 and 4. Note that these scaling laws are a very crude approximation of the actual scaling and are (with exceptions) not used in the models of the developed preliminary design tool.

#### EMA

Table D.2: EMA crude scaling laws

Property	Scaling
Mechanical cylinder mass	$M_{cylinder} = 0.17 F_{max} [\text{kg}]$
Gearbox mass ( $R_{gear} = 2$ )	$M_{gearbox} = 4.3e-3 T_{max} + 4.5 T_{max}^{1/2} [\text{kg}]$
Mechanical cylinder moment of inertia	$I_{cylinder} = 2.8e-8 F_{max}^2 [\text{kg m}^2]$
Gearbox moment of inertia ( $R_{gear} = 2$ )	$I_{gearbox} = 6.9e-5 T_{max} [\text{kg m}^2]$

#### EHA

Table D.3: EHA crude scaling laws

Property	Scaling
Hydraulic cylinder mass	$M_{cylinder} = 2e-4 F_{max}^{6/5} [\text{kg}]$
Hydraulic manifold mass	$M_{manifold} = 422 + 1.53e5 Q_{max}^{3/2} [\text{kg}]$
Hydrostatic pump mass <sup>1</sup>	$M_{pump} = 0.75 V_g [\text{kg}]$
Hydrostatic pump moment of inertia <sup>1</sup>	$I_{pump} = 1.007e-1 V_g^{5/3} [\text{kg m}^2]$

<sup>1</sup> $V_g$  is defined in  $[\text{cm}^3]$

# Appendix E

## Sensitive information

This appendix has been removed to protect the commercial interests of companies providing data in this appendix. Contents of this appendix are available to members of the thesis committee mentioned on the title page and to Ampelmann B.V..

- E.1 Ampelmann actuator Requirements**
- E.2 Ampelmann actuator test timeseries**
- E.3 Hydrostatic pump losses**
- E.4 Preliminary design tool**

# Appendix F

## Papers

The paper formats of Chapter 3, 4 and 6 are added as a digital download below. Contact the author of this report should the download link not work.

### **F.1 EMA sizing and loss model development**

[https://mega.nz/file/CV4CBaxS#1m3uf2Dj\\_RApf0BeV7SGiX8a47djuZfFrdrv0fXEa41M](https://mega.nz/file/CV4CBaxS#1m3uf2Dj_RApf0BeV7SGiX8a47djuZfFrdrv0fXEa41M)

### **F.2 EHA sizing and loss model development**

<https://mega.nz/file/yUpWQIrT#HiXuCLV1Zu7QAZVUi5NYFg9n9KzvhTVucVt1E5RcE1Y>

### **F.3 High power linear actuator properties in hexapod applications**

[https://mega.nz/file/Gd4EiS7B#F0miuk-KQaZKREjXD\\_2yO\\_kHZIAAZbHDOIwoDyqwLRo](https://mega.nz/file/Gd4EiS7B#F0miuk-KQaZKREjXD_2yO_kHZIAAZbHDOIwoDyqwLRo)

# Appendix G

## Literature review

### G.1 Introduction

Motor technology is moving more and more away from fossil fuel towards electric solutions. The same trend is seen in actuator technology. Actuators are components in a machine which are capable of actively moving a mechanism. Ampelmann operations B.V. is a company specializing in offshore crew and cargo transfer. Their product line makes extensive use of high power linear actuators. Those actuators currently consist of hydraulic cylinders in combination with large hydraulic power units. To update their product line, Ampelmann is looking into electrification of the actuators with the idea of possible weight and efficiency benefits. From previous initial feasibility studies, some concerns for pure electro-mechanical actuation were expressed:

- Installation length in combination with the needed stroke could be difficult.
- Redundancy of a mechanical actuator is hard to realize.
- Active lubrication strategies are needed to prevent heat build-up.
- More power is needed due to high inertia of spindles at fast accelerations.
- Electro mechanical components are not readily available in the market.

However, no extensive study towards the different existing linear actuator technologies and their individual properties has been performed. This report details the overview of existing linear actuator technologies for use in high power applications. First the different actuator styles are discussed. Next, the most promising actuator solutions are discussed with regards to implementation in high power applications (Ampelmann requirements). Finally, a literature review is performed based on quantifiable data found in relevant papers on the subject. At the end of the report, a proposal for a new research project is given to fill a knowledge gap in high power electric linear actuation technology.

### G.2 Ampelmann specifications

Ampelmann has a goal of making offshore access as easy as crossing the street. To enable this goal, a series of motion compensated gangways are created which mount on top of a transfer vessel. Transfer between the vessel and an offshore structure is enabled by actively compensating vessel motion to create a motionless platform above the ship deck. From this platform the gangway can be positioned to create a bridge between the platform and the offshore structure. The motion compensated platform is actuated with a hexapod setup. A hexapod is a type of parallel manipulator which uses six evenly spaced linear actuators to allow six degrees of freedom motion. The hexapod setup is chosen as this eliminates any residual movements in the gangway during cargo and crew transfer over the walkway or on the cargo hook. Multiple variants of the Ampelmann system exist, each with their own set of work-ability specifications. This report will focus on the Ampelmann A type system, a people transfer system which can be used in sea states up to 3.0m Hs. The current A type with conventional hydraulic actuators is shown in figure G.1.

As the hexapod motion system actively compensates vessel motion to obtain a motionless platform, operational requirements on the actuators are largely imposed by motion of the sea and vessel response. Analysis of vessel responses to motion of the sea is an entire research project on its own. This research is already extensively



Figure G.1: Ampelmann A-type with conventional hydraulic actuators in operation.

performed by Ampelmann, as such force, velocity and acceleration requirements on the actuators are taken as a given. This chapter discusses the system requirements for the Ampelmann A type. System requirements are leading in selection of valid actuator technologies and therefore determine the range of representative literature.

## Operational requirements

As stated above, operational requirements on the hexapod actuators are taken as a given in this report and are shown in table G.1. To make the requirements more tangible, forces, velocities and accelerations of the system are obtained from an extensive time series and plotted in histograms in figure G.2. From the histograms, it is clear that the values shown in table G.1 are the absolute extremes. The velocity histogram shows a perfectly centered data distribution around standstill. Approximately 95% of the data is centered between  $\pm 0.5 \text{ m s}^{-1}$ . The maximum velocity requirement for the actuators is therefore only needed in much less than 5% of the time. The accelerations of the actuators are also centered around  $0 \text{ m s}^{-2}$ , here 95% of the data is found between  $\pm 0.5 \text{ m s}^{-2}$ . The maximum acceleration requirement is never met in this time series. The distribution of the actuator positions is a little less symmetric. The actuator position is approximately centered at 0.75 m extension and has a functional range of approximately 1.5 m. The actuator stroke requirement of 2 m thus accounts for possible uncontrolled overshoot. The mean motion amplitude is approximately 0.34 m with a mean frequency of 0.15 Hz. Finally, the force distribution shows four separate peaks. These peaks can be explained by the asymmetric loading condition of the hexapod platform. Depending on the location of the actuator in the hexapod, a different loading is expected during operation. The majority of the loads is also seen to be positive. This means actuators are mostly loaded in compression. Only in approximately 5% of the total cylinder time (all cylinders combined) is the cylinder loaded in minor tension. Furthermore we can see that the maximum needed actuator force is closer to 100 kN than the required 150 kN. Note that these results are obtained from a single time series. Other time series might yield different results. Especially the acceleration requirement is not reflected in the shown acceleration distribution. Acceleration requirements of the actuator might be interesting to reevaluate in later stages of this project.

Table G.1: Functional actuator requirements

Functional requirements	Value
Actuator stroke [m]	2
Max force [kN]	150
Max velocity [ $\text{m s}^{-1}$ ]	1
Max acceleration [ $\text{m s}^{-2}$ ]	4.8

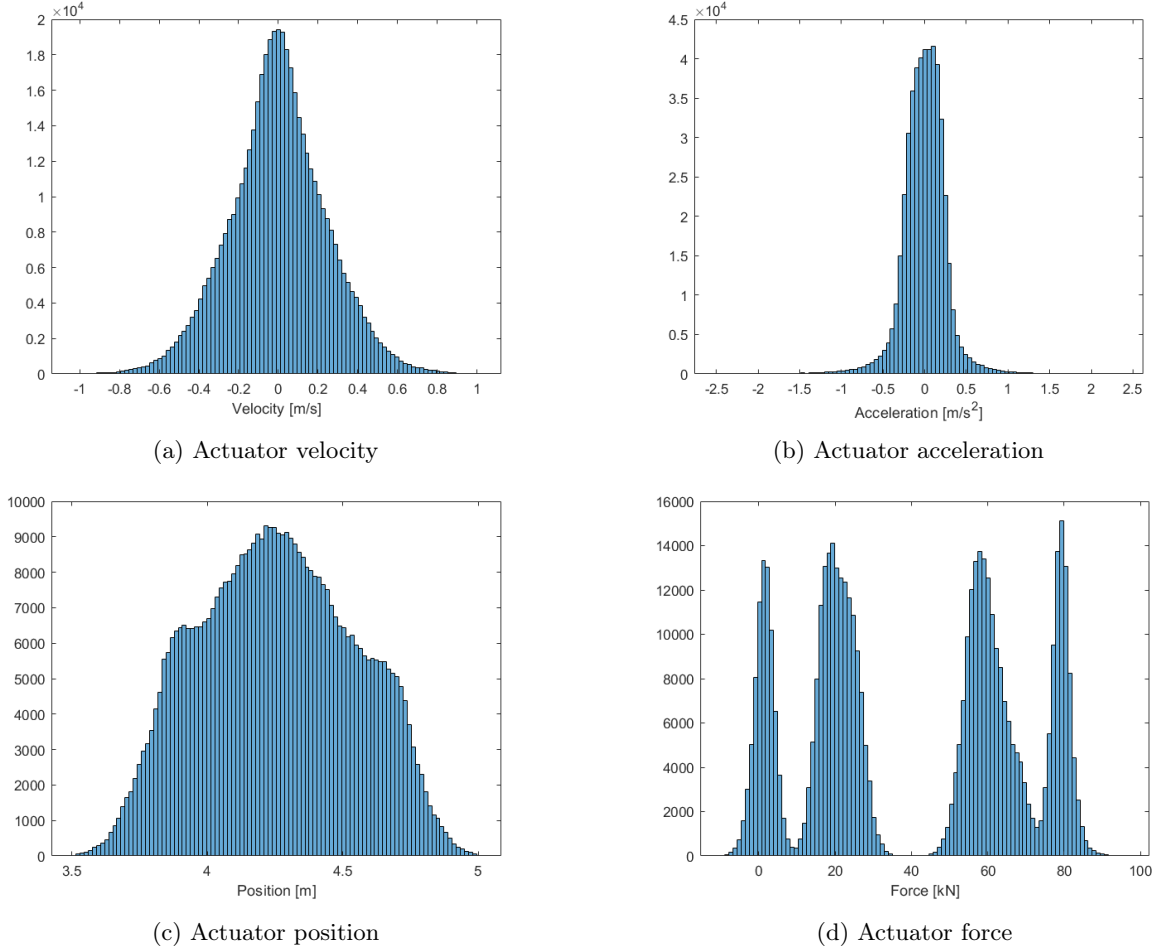


Figure G.2: Operational requirement histograms

## Functional requirements

Next to the operational requirements, some requirements based on the functionality of the actuators are given. These requirements have to do with energy efficiency, cost efficiency, mass and reliability of the system.

### Energy efficiency

An important goal of Ampelmann is the reduction of energy consumption during operation. This goal is not only driven by the environmental implications, but is also necessary due to the limited electric energy supply on board a vessel. In reality, an electric power supply of two times 16 kW is present on the vessels where Ampelmann systems are installed. As the motion of the hexapod platform is cyclic, energy regeneration is a very convenient way to reduce total energy consumption. To be able to use the principle of energy regeneration, the actuator should be backdrivable or not self-locking. A self-locking actuator would require positive power input for both actuation directions resulting in two quadrant motoring operation.

## Cost efficiency

The Ampelmann A-type is a commercial product, as such the hexapod actuators should be economically viable. Cost efficiency of an actuator has much to do with detailed design choices, however use of exotic materials and complex designs should be avoided. Gains in energy efficiency and weight reduction should always be weighted against added production costs. The order of magnitude for the build cost of a single actuator should not exceed € 100000.

## Weight reduction

Ampelmann systems are mounted on top of crew and transport vessels. Weight and footprint of the Ampelmann system severely influences the remaining capacity of the vessel for other cargo. A lighter system is therefore preferable to costumers as the vessel trip will be more profitable when more cargo can be loaded. Weight reduction puts a high emphasis on an increased power density of a system. Note that the emphasis lies on weight and not on mass or inertia as dynamic effects due to a higher mass of the actuator are less of an issue than the total weight of the system in this specific use case. Mass and inertia of the moving parts of the actuator on the other hand should be kept low for better acceleration behavior.

## Reliability

Safety is the core idea behind the Ampelmann system. As such reliability plays a major role in selection of actuator technology. Current Ampelmann hydraulic actuators are made for 10 years design life. However, cylinders are only used for 5 years at a time before maintenance is needed due to salt water corrosion. Hence average cylinder life time would be 5 years or approximately 5000 operating hours. As current Ampelmann actuators don't experience failure due to failure mechanisms, no practical failure data is available.

		SEVERITY RANKING				
		CATASTROPHIC 5	MAJOR 4	SEVERE 3	MODERATE 2	MINOR 1
CRITICALITY RANKING	FREQUENT 5	INTOLLERABLE	INTOLLERABLE	INTOLLERABLE	UNDESIRABLE	TOLERABLE
	PROBABLE 4	INTOLLERABLE	INTOLLERABLE	UNDESIRABLE	TOLERABLE	TOLERABLE
	OCCASIONAL 3	INTOLLERABLE	UNDESIRABLE	TOLERABLE	TOLERABLE	BROADLY ACCEPTABLE
	REMOTE 2	UNDESIRABLE	TOLERABLE	TOLERABLE	TOLERABLE	BROADLY ACCEPTABLE
	IMPROBABLE 1	TOLERABLE	TOLERABLE	BROADLY ACCEPTABLE	BROADLY ACCEPTABLE	BROADLY ACCEPTABLE

Figure G.3: FMECA ranking system.

From a failure mode, effects and criticality analysis (FMECA) performed by Ampelmann on the A3.0 hexapod system, loss of actuator control is classified as 'Catastrophic'. The different severity and criticality ranks which can be found from FMECA are shown in figure G.3. To get the hazard down to an 'Undesirable' acceptability level, the remote criticality ranking should be reached. As such, the probability of occurrence of events leading to loss of actuator control should be below 1%. With a total life time of 10000 operating hours, this would yield a maximum failure rate of  $1e - 6$  failures per hour for failure modes leading to loss of actuator control. This is for example valid for failure modes leading to a jammed actuator.

For lifetime assessment, the total distance traveled per operating hour per cylinder should be known. From the simulation discussed above, the maximum distance traveled per operating hour per cylinder is equal to 760 m. Over the course of the entire system lifetime, a total distance of 7600 km is traveled by a single actuator.

## Current Ampelmann actuation

Ampelmann uses conventional hydraulic actuators in combination with a large hydraulic power unit (HPU) on the majority of its systems. A large drawback of conventional hydraulics is the large power loss in velocity control due to the throttling valves [76, 47]. In the Ampelmann A-3.0, these conventional hydraulic actuators are replaced by electro-hydrostatic actuators (EHA). EHA combines the advantages of hydraulic power with the flexibility and controlability of electric solutions (see section G.3). The EHA setup in the A-3.0 is currently being tested by Ampelmann, the expected performance is discussed below as a benchmark for future actuator concepts.

The EHA setup used in de Ampelmann A-3.0 consists of two redundant permanent magnet synchronous servo motors in combination with two redundant axial piston displacement pumps. The pumps have a variable displacement architecture but are set to a fixed displacement using a setscrew. The pumps are coupled through a redundant set of cartridge valves to both ports of a symmetric double acting hydraulic cylinder. A small accumulator is used to avoid cavitation at the suction side of the pump. An additional charge pump is used to compensate leakage of all six actuators of the hexapod. The charge pump also pressures the low pressure side of the hydraulic system to a minimum pressure to obtain a better drive stiffness. The actuator is operated with power electronics controlling the motor speed and torque. The redundant setup ensures the system can still operate at approximately 70% capacity when a single motor, pump or valve fails. More information on EHA architectures is found in section G.3.

As the motion platform of the Ampelmann system moves up and down, power consumption of the actuators varies a lot during operation. Determining a single efficiency is therefore almost impossible. The energy efficiency of the actuators will vary according to the required force and velocity at a given instant. To get an idea of the system efficiency, an efficiency surface based on the required force and velocity can be made. The efficiency analysis of the electro-hydrostatic actuators will be performed based on an Ampelmann internal power balance prediction made with manufacturer data. Results will be based on the same time series as used in section G.2. In combination with the operational requirement histograms of figure G.2, the efficiency at different working points can be discussed. The power density of the EHA actuators can simply be determined by dividing the maximum power capacity by the total actuator system mass.

## Efficiency analysis

The efficiency analysis of the A-3.0 hexapod actuators poses some difficulty. Due to the four-quadrant operation of the actuators, power levels can cross zero when the actuator moves from the motoring to generating regime and vice versa. Calculating the efficiency as  $\eta = \frac{P_{out}}{P_{in}}$  will therefore result in asymptotic behavior of the efficiency over time. Furthermore, the data for both  $P_{out}$  and  $P_{in}$  switches as motoring and generating efficiencies are given by respectively equation G.1 and G.2 [11]. Here  $F$  and  $v$  are the force generated by the actuator and the linear velocity of the actuator.  $V$  and  $I$  are the voltage and current fed to the system.

$$\eta_{motoring} = \frac{F \cdot v}{V \cdot I} \quad (G.1)$$

$$\eta_{generating} = \frac{V \cdot I}{F \cdot v} \quad (G.2)$$

As a result, the efficiency over time is determined by a discontinuous function. When both input and output power are positive, efficiency is determined according to the motoring regime. When both input and output power are negative, efficiency is determined according to the generating regime. In all cases where input and output power have different signs, the efficiency equals zero. By having different signs for input and output power, calculated efficiency would be negative. In practice this means the efficiency is equal to zero in this transition region as no useful power is created. The different efficiency regions are shown in figure G.4. Note that the shown efficiencies are examples and do not represent the general efficiencies of motoring and generating regimes. The slight shift in the zero-efficiency point seen around the transition zone is due to discretization of the data.

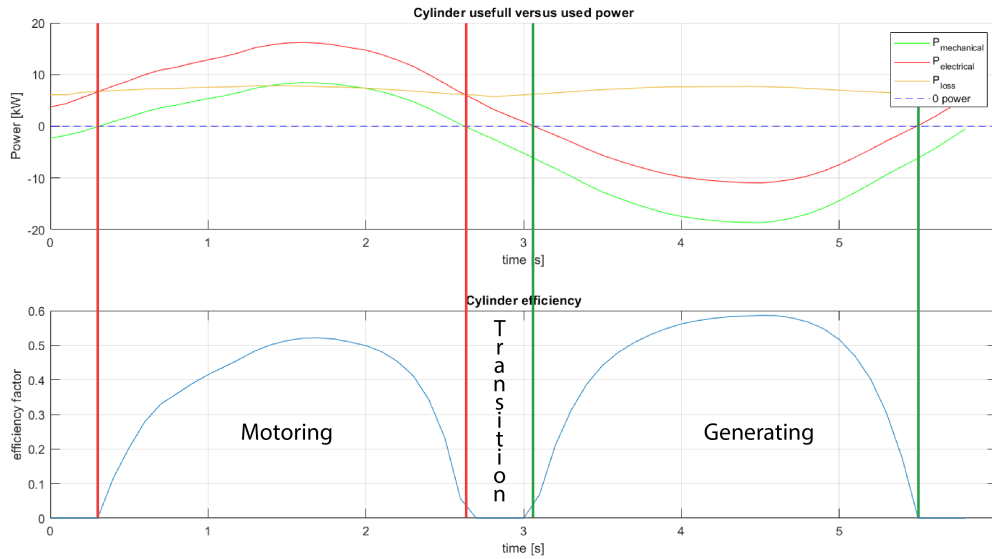


Figure G.4: Efficiency regions over time

With the information above, the efficiencies for each operating point of the actuator can be found. Operating points are defined by the combination of a force and velocity value. In figure G.5, the efficiency is determined for all motor speed and torque combinations (mechanical input power).

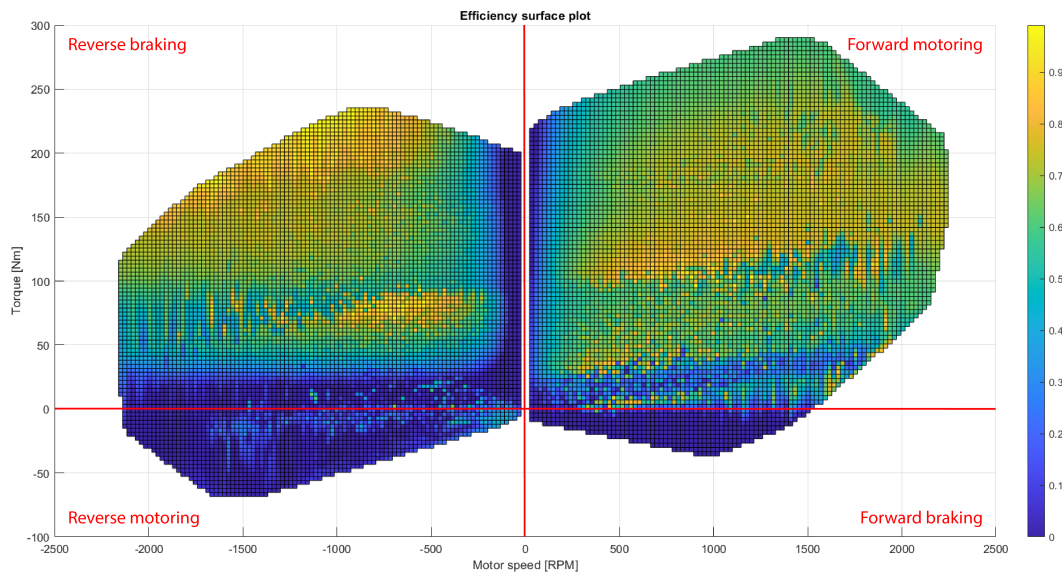


Figure G.5: Efficiency surface

The efficiency surface plot clearly shows that both the forward braking and reverse motoring quadrants are used only with very small loads at low efficiency. The majority of operating points is situated in the forward motoring and reverse braking quadrants as can be expected for a heavy system as gravity effects become more dominant. Some discontinuities in the efficiency surface are seen. This can be explained by the combination of data from different cylinders, at the edges of the operating point of a single cylinder less data points are obtained, this results in poor surface generation at locations where non of the cylinders is frequently operating.

Calculating the overall energy efficiency of the system poses another problem. Energy efficiency is fundamentally defined as the ratio of work done by the system to heat provided to the system. Mechanical work is defined as

the product of force and displacement. The Ampelmann platform starts and ends in the same location with respect to its boat fixed frame, as such no useful work is performed by the system. Using a zero value for performed work in the energy efficiency equation, we find the Ampelmann platform has a fundamental energy efficiency of 0%. As such, all energy (heat) going into the system is defined as energy loss. Required energy for a given task therefore is a better metric to compare linear actuators for a specific application compared to efficiency of the actuator at a single working point.

## Power density

Power density of the actuator is defined as the peak available output power per unit mass of the actuator system. The actuator system is the combination of all actuators and peripherals such as power electronics and energy storage needed for operation. The peak available output power of the actuator is determined from the functional requirements on force and velocity. Peak output power is thus defined as  $P_{peak} = 150$  kW per actuator and as  $P_{peak,system} = 900$  kW. The mass per actuator as defined by Ampelmann equals 1850 kg excluding power electronics and other peripherals. An approximate weight of 2000 kg per actuator including peripherals thus seems as a reasonable estimation. The power density of the electro-hydrostatic actuator system currently being tested at Ampelmann is therefore equal to approximately  $0.075$  kW kg<sup>-1</sup>.

## G.3 Linear actuator technologies

Chapter G.2 introduces the Ampelmann motion compensated gangway platform and the associated actuation requirements of the linear actuators moving the platform. Linear actuators exist in different forms and sizes. To find an optimal actuator design for the requirements given in chapter G.2, it is important to be aware of existing linear actuator technologies and their properties. This chapter will provide an overview of existing linear actuator technologies. The focus will be on actuator technologies suited for high power levels given by a combination of high forces and high velocities. First, a general description of a linear actuator is given. Next, the linear actuator is discussed in the context of the hexapod motion platform. Finally, different actuator technologies and their variants will be discussed. In chapter G.4 the most promising technologies will be discussed and compared in more detail.

### Linear actuators

A linear actuator is a device which converts a form of potential energy such as electrical potential or chemical potential energy to a linear motion and corresponding force. The linear motion can either be generated by a linear motor or by a combination of a rotary motor and a rotary to linear transmission system. Every transmission system has its own set of benefits and drawbacks. In general, linear actuators are compared on efficiency, load capacity, operation velocity, cost, lifetime, accuracy and backlash [73]. In general, the high power linear actuator consists of a few major parts shown in figure G.6. First, electrical or mechanical energy is converted to mechanical energy by a motor (part A). Next, this mechanical energy is converted for transportation (part B). Finally, a cylinder type transmission (part C) is used to convert the input power to the final linear force and velocity required from the actuator.

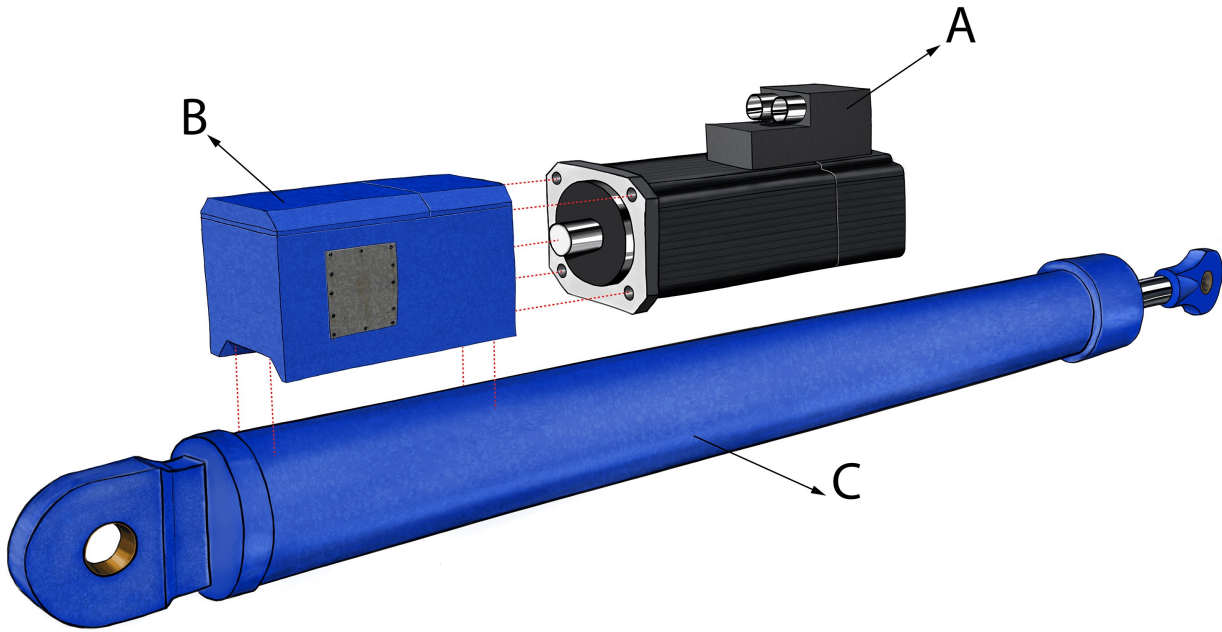


Figure G.6: High power linear actuator components

### The hexapod actuator

The hexapod is the kinematic platform used in the Ampelmann motion compensated gangways as seen in figure G.7. The hexapod is a 6-DOF parallel manipulator consisting of a moving platform and a fixed base connected by six linear actuators [78]. The non-linear platform mechanics require advanced control of the actuators to correctly control the platform dynamics [78, 156]. A lot of research has been performed towards the motion dynamics of hexapod type manipulators, often in the context of full motion flight simulators. The majority of these hexapod manipulators are actuated using conventional hydraulic actuators (see section G.3) due to their high power to size ratios (on cylinder level) and high stiffness [78].



Figure G.7: Ampelmann A-type motion compensated gangway on the hydraulic hexapod platform. [2]

As the hexapod largely determines the loading of the individual actuators, ideally actuator technologies are studied within the application of hexapod manipulators. [37] describes the use of the electro-hydrostatic actuator (EHA, see section G.3) to actuate the hexapod. With a motion frequency and amplitude of respectively 0.2 Hz and 0.1 m power consumption of the EHA is only 4.7 kW. This is almost a factor 10 lower compared to the 45 kW needed with conventional hydraulic actuators [37]. The same paper also indicates overall power saving is difficult to predict as the duty cycle and magnitude of motion will change with different flight training scenarios. The same is true on a more global scale as power consumption and efficiency is very dependent on the specific application of the actuator. In a whitepaper by Moog Inc. the conventional hydraulic actuators are compared to electro-mechanic actuators (EMA, see section G.3) based on a life cycle cost analysis. The paper assumes an actuator with a maximum load rating of 133.5 kN and a maximum stroke of 1.5 m. System losses of both actuators are found to be 39.4 kW and 10.07 kW for the conventional hydraulic actuator and electro-mechanic actuator respectively [19]. The EMA setup hence needs  $\frac{1}{4}^{th}$  the power of the conventional setup. The potential of energy regeneration in the EMA setup is however neglected, making the comparison between the EHA and EMA setup unfair. In general however, both EMA and EHA actuators seem to have an advantage on energy consumption compared to the conventional hydraulic actuators.

The amount of papers discussing linear actuator technology in context of hexapod platforms is limited. As such, the remainder of this report will look at literature concerning the actuator as an individual object.

## Hydraulic actuators

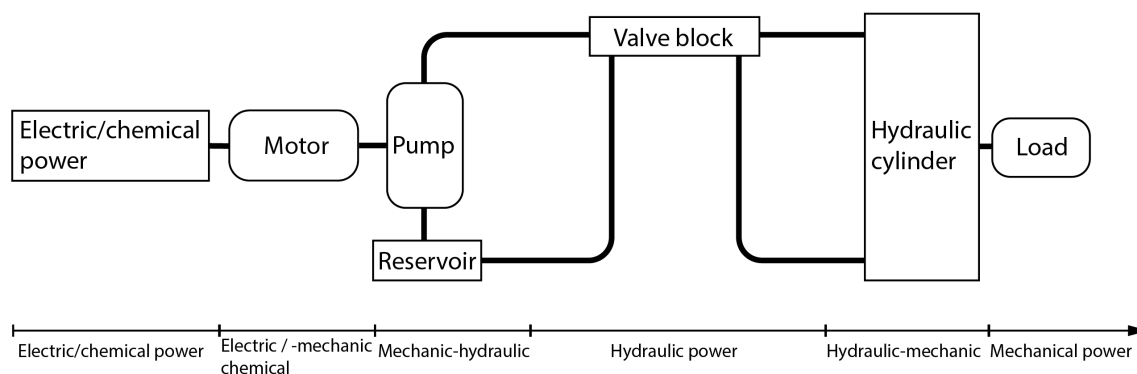


Figure G.8: Simplified representation of a conventional hydraulic actuator

Conventional hydraulic actuators are the workhorse in construction machinery. They use a combination of a hydraulic pump, valve system and a hydraulic cylinder to convert rotary mechanical energy in linear mechanical energy. A simplified representation of the hydraulic actuator is shown in figure G.8. A hydraulic pump connected to a diesel or electric motor continuously keeps a hydraulic network at a preset pressure. The double acting hydraulic cylinder has two sides called the A and B chambers as can be seen in figure G.9. To extend the actuator, a servo valve regulates the pressure to the A chamber of the hydraulic cylinder to obtain the desired force. Retraction is obtained by connecting the B chamber to the pressure reservoir while releasing the pressure on the A side to an atmospheric pressure tank. As the majority of the hydraulic actuator components can be placed a distance away from the actual hydraulic cylinder, a small and light cylinder can produce high forces [47]. Power density of the hydraulic cylinder is about five times higher compared to electric machines [136], up to  $10 \text{ kW kg}^{-1}$  [113]. When accounting for the entire actuator system, power density is significantly lower compared to the cylinder only and similarly sized electric machines.

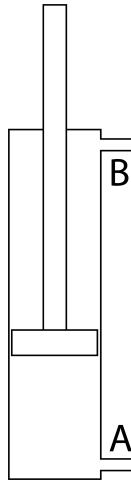


Figure G.9: Double acting hydraulic cylinder layout

Many linear actuators operate in cyclic motions, to decrease energy consumption of conventional hydraulic actuators, energy recovery principles can be used. In an electric system, energy recovery can be implemented by using the electric motor as an electric generator. As such, electrical energy can be delivered back to the power grid. Often a battery or capacitor bank is used to store regenerated electrical energy to relief the actual power grid. In conventional hydraulics, energy recovery can be implemented by means of hydraulic accumulators. An accumulator is a pressure storage reservoir where hydraulic fluid is held under pressure of either a spring or compressible gas. A schematic representation of an accumulator using a compressible gas is shown in figure G.10. The use of hydraulic energy recovery and storage is advantageous as hydraulic accumulators have one order of magnitude higher power density compared to electric batteries with respectively  $5 \text{ kW kg}^{-1}$  and  $0.5 \text{ kW kg}^{-1}$  [136]. Round trip efficiency of a hydraulic accumulator can reach 94% compared to 81% for an electric battery, especially at frequent acceleration and braking [136]. Combined with less conversion steps compared to electric hybrids, this enables more efficient recovery of kinetic energy [97]. The disadvantage of the hydraulic accumulator compared to electric batteries is the much lower energy density. Energy density of the hydraulic accumulator is approximately two orders of magnitude smaller compared to the energy density of an electric battery [97].

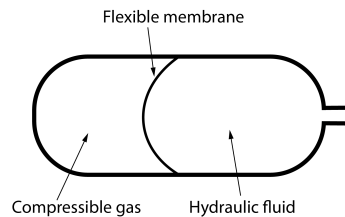


Figure G.10: Hydraulic pressure accumulator using a compressible gas.

Another option to reduce energy consumption of the conventional hydraulic actuator lies in the control of the servo valves. Under normal operation, a constant hydraulic pressure is needed for the actuator to work correctly. As such, the hydraulic pump is continuously being driven to keep the hydraulic network under pressure. When the actuator is at standstill, all input power is then converted into heat [63, 76]. By closing the servo valves, hydraulic actuators don't require additional energy to hold a constant load [22]. This enables reduction of pump operation in periods of continuous load.

Efficiency of the conventional hydraulic actuator depends on multiple factors. Power losses occur due to mechanical friction in the cylinder, hydraulic leakage in the pump and electrical losses in the motor. However, the largest losses occur as a result of velocity control in the hydraulic orifices and servo valves [76, 47]. Approximately 30% of hydraulic power is lost in these valves [180]. As a result, conventional hydraulic actuators can reach maximal efficiencies of approximately 70% [122]. This efficiency is only reached under seldom occurring perfect conditions. A system efficiency of 30 to 35% is more realistic during operation [100, 180]. Due to the risk of hydraulic fluid spills, high maintenance requirements result in high operating costs [129]. Even though

highly inefficient, the conventional technology has some beneficial characteristics such as four quadrant operation, high drive stiffness, high durability, reliable operation, low power consumption with stationary loads, and high scalability [140].

## Electro-hydrostatic actuators

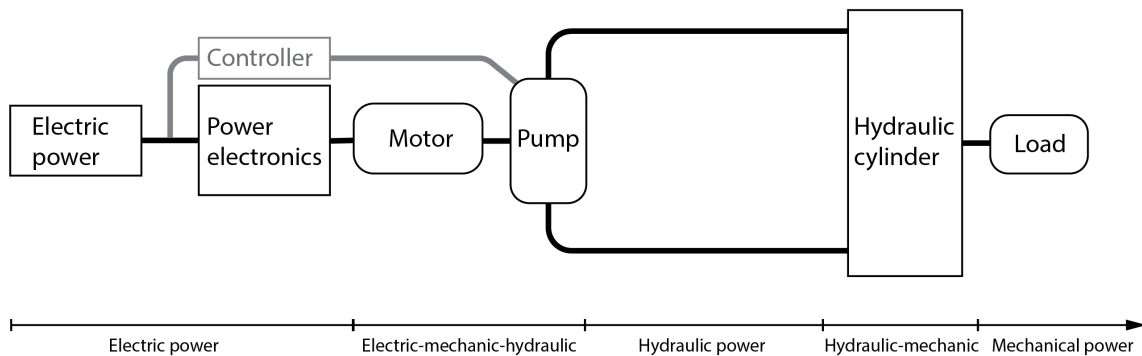


Figure G.11: Simplified representation of an electro-hydraulic actuator

Electro-hydrostatic actuators (EHA) are a class of actuators which use hydraulic technology for the transmission of rotary mechanical energy to linear mechanical energy in combination with an electric drive. As such, electro-hydrostatic actuators combine the power density of conventional hydraulics with the flexibility and controllability of electric solutions [17]. This means EHA maintains largely the same characteristics of back-driving, overload protection and damping as conventional hydraulics [58]. A simplified representation of the electro-hydrostatic actuator is shown in figure G.11. In EHA, a hydraulic cylinder is directly connected to a four quadrant positive displacement (hydrostatic) pump [5] which in turn is connected to an electric machine. Here the hydraulic cylinder and pump represent part C and B of figure G.6 respectively. The positive displacement pump can be implemented as either a fixed displacement or variable displacement pump. Figure G.12 [140] shows the architecture of actuators using both pump options and an additional open circuit variation. Both options are discussed in subsection G.3 and G.3 respectively.

An alternative EHA architecture with multiple cylinder surfaces is proposed in [28] with the potential of decreasing the necessary installed power of the motor. This is done by alternating between actuation surfaces in the cylinder to obtain the optimal transmission ratio for the operating point. For large stroke machines, this architecture becomes very bulky and impractical to use. Alternatively, decreasing necessary installed power can be achieved by compensating the static load on the hydraulic cylinders with a gas spring. As such, the electro-hydrostatic circuit only needs to control the dynamic loading [74].

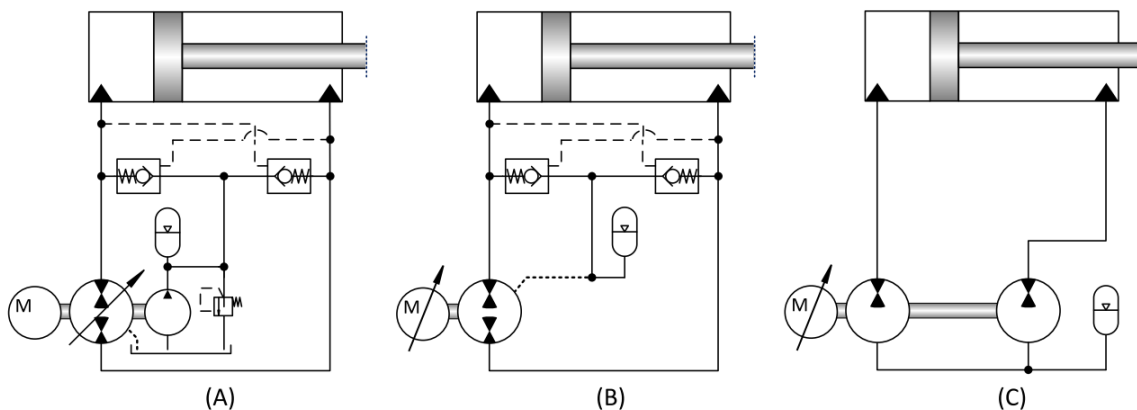


Figure G.12: Examples on EHA architectures. (A) Variable displacement, closed circuit drive (B) Variable speed (fixed displacement), closed circuit drive. (C) Variable speed, open circuit drive.[140]

The major difference between EHA and conventional hydraulics is the lack of velocity control valves. The EHA is controlled directly by either the motor or the pump. Fluid in the EHA is pumped from one cylinder side to the other resulting in a closed circuit system [140]. The closed loop means an accumulator is needed in the system to avoid cavitation in the pump due to low pressure on the suction side and to make up for any dynamic leakage [62]. Alternatively, a charge pump can be used to the same purpose [90].

According to Li et al.(2016), overall system efficiency of the EHA can be as high as 60% compared to 30 to 35% for conventional hydraulic actuators [100]. This efficiency is largely influenced by the potential of energy regeneration in the system. As any hydraulic machine can both be used as a hydraulic pump and motor [116], potential energy of the system can be recovered to electric energy. An alternative to electric energy regeneration is found in hydraulic energy regeneration as proposed by [180]. The architecture of this hydraulic energy recovery EHA as seen in figure G.13 uses two hydraulic accumulators and two servo valves. This setup reduces the needed motor currents during peak accelerations and therefore increases thermal performance of the actuator. The use of servo valves means this EHA architecture is more complex and heavier compared to traditional EHA. To lower the weight penalty of hydraulic energy recovery, [143] proposes a similar hydraulic energy recovery system where only a single accumulator and valve block is used. The other accumulator and valve block are replaced by pilot operated check valves. Complexity of the system however remains higher compared to electric regeneration alternatives.

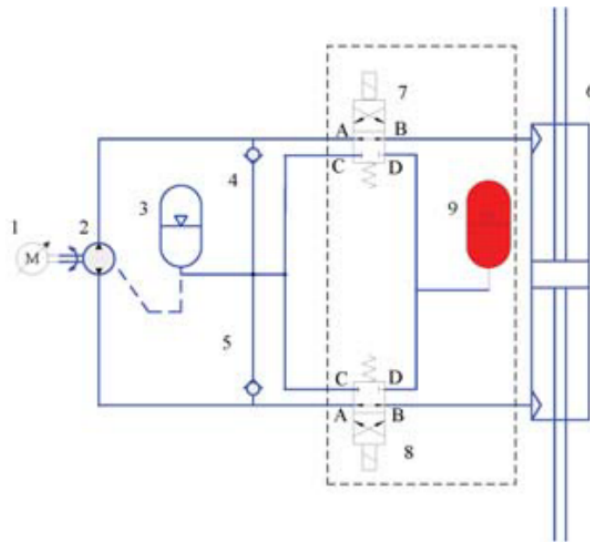


Figure G.13: Diagram of the hydraulic energy recovery EHA. Components are: 1-servo motor, 2-hydraulic pump, 3-low pressure accumulator, 4,5-check valves, 6-hydraulic cylinder, 7,8-servo valves, 9-high pressure accumulator [180].

Due to the compact design of the EHA, the system can operate at lower pressures compared to conventional hydraulics. Lower pressures result in lower internal leakage of the hydraulic machines leading to higher volumetric efficiencies [116]. Hydraulic pump efficiencies for EHA are studied by Kauranne et al.(2006) as shown in figure G.14 [92]. From the figure, piston type pumps prove to be more efficient for pressures above 90 bar compared to other pump technologies. For axial piston machines, cycle energy efficiency can be as high as 90% for lifting and 85% for lowering with non zero loads compared to 80% and 70% for internal gear pumps with pump pressures ranging from 50 to 130 bar. [116]. According to [158], both radial and axial piston machines can even reach up to 95% overall efficiency with working pressures up to 815 bar.

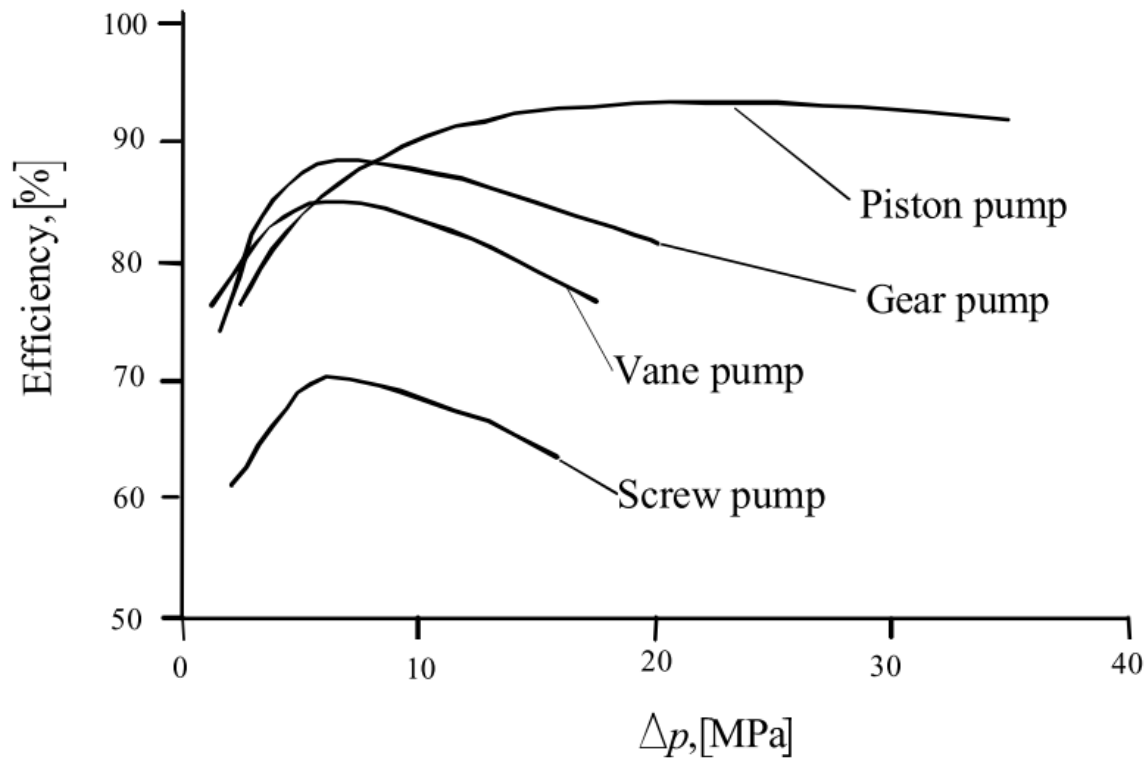


Figure G.14: Comparison curves of power efficiencies for different hydraulic pumps at constant speed [92].

Next to the efficiency of an actuator, also the weight is an important factor in choosing an actuator technology. Weight of the EHA is mainly determined by the individual weights of the hydraulic cylinder, hydraulic pump, electrical machine, integration block and power electronics [33, 181]. Hydraulic pump size and weight are proportional to the displacement [174] while electric motor size and weight are proportional to the torque [177]. Lower weight is thus achieved by decreasing pump displacement and motor torque. In turn, this would require high motor/pump speeds. According to Wei et al.(2009), existing hydraulic pumps are capable of reaching speeds up to 10000 rpm [174].

Finally, electro-hydraulic actuator reliability is already studied and sufficiently guaranteed for use in the aviation industry [63]. As EHA doesn't suffer from jamming problems and is well sealed, it is an ideal technology in harsh environments [17]. The main drawbacks are high maintenance cost of hydraulic equipment [63] and the higher risk of oil spills compared to non-hydraulic technology [129]. The individual benefits and drawbacks of the two main EHA architectures will be discussed in more detail in the following subsections.

### Fixed displacement pump

Electro-hydrostatic actuators with fixed displacements pumps (figure G.12 B) are controlled by a variable motor speed. These actuators have an advantage in structural simplicity and show a high energy efficiency [131, 59]. The simple structure is also seen in a general pump size reduction and weight savings compared to other EHA technology [34]. A hydraulic accumulator is often used to aid during acceleration and a hydraulic lock can be used to disconnect the load from the motor in stationary conditions [131]. The hydraulic lock can realize zero energy consumption in these stationary situations. However, in the presence of a small leakage the actuator is not self locking but quasi self-locking [140], reducing the effectiveness of the hydraulic lock. Fixed displacement EHA due to its simplicity can reach a failure probability of 13574.4 hours MTBF according to [41]. This number excludes the loss of hydraulic and electric power supplies and is based on a 30 kN load capacity actuator.

A typical operating curve for a fixed displacement pump is shown in figure G.15 [104]. In the 'Handbook of Hydraulic Fluid Technology', Totten and De Negri conclude that mechanical efficiency ( $\eta_m$ ) increases with decreasing volumetric efficiency  $\eta_v$  (increasing leakage flow) due to improved lubrication and resulting reduced friction torque. Overall efficiency ( $\eta_t$ ) is seen to be highest between 20 and 120 bar. The strong reduction in overall efficiency at low pressures is a consequence of poor lubrication and high friction in this operational range. As such, a minimal operating pressure is recommended for these kind of pumps [158].

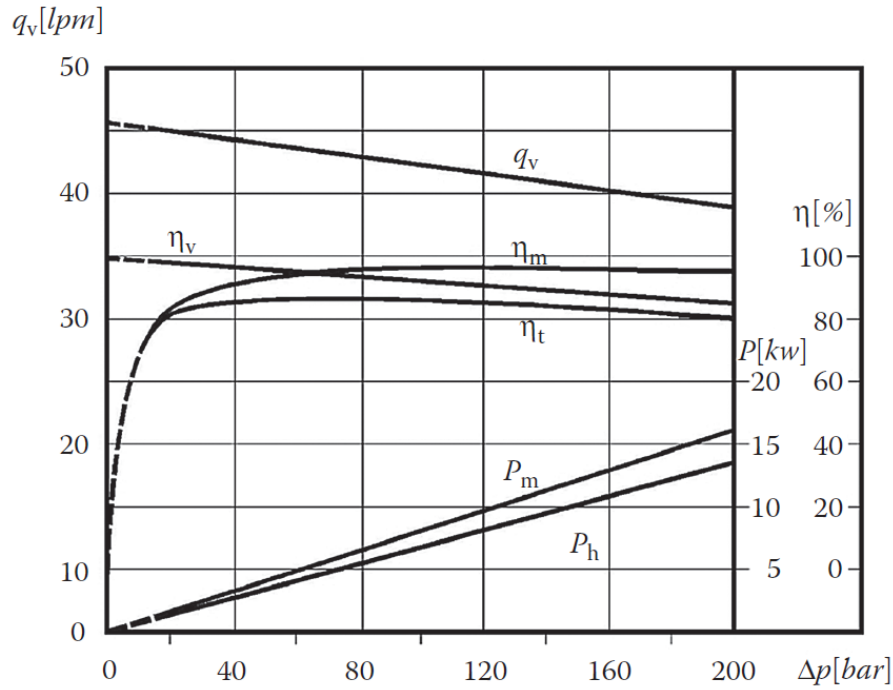


Figure G.15: Operating curves of a fixed-displacement pump. [104]

A disadvantage of the configuration shown in figure G.12 B is low drive stiffness due to low pressure in the non-load carrying cylinder chamber. This low pressure results in undissolved air in the hydraulic fluid and corresponding compliance of the fluid [140]. Also filtering and cooling of the hydraulic fluid is difficult as the majority of the fluid volume is circulated continuously through the cylinder [140].

One method of increasing the drive stiffness according to Schmidt et al.(2019) is the use of separate forward and return flow paths and two separate fixed displacement pumps (figure G.12 C)[140]. As the system is now an open circuit, cooling and filtering of the hydraulic fluid becomes much simpler. However, energy regeneration by external cylinder loads is not possible anymore. The separate return flow path prevents hydraulic fluid from passing through the pumps when pushed out of the cylinder. This can be seen more clearly in figure G.16 [140]. Next to increased drive stiffness, the open loop approach also has self locking properties, reducing power requirements at position holding operations.

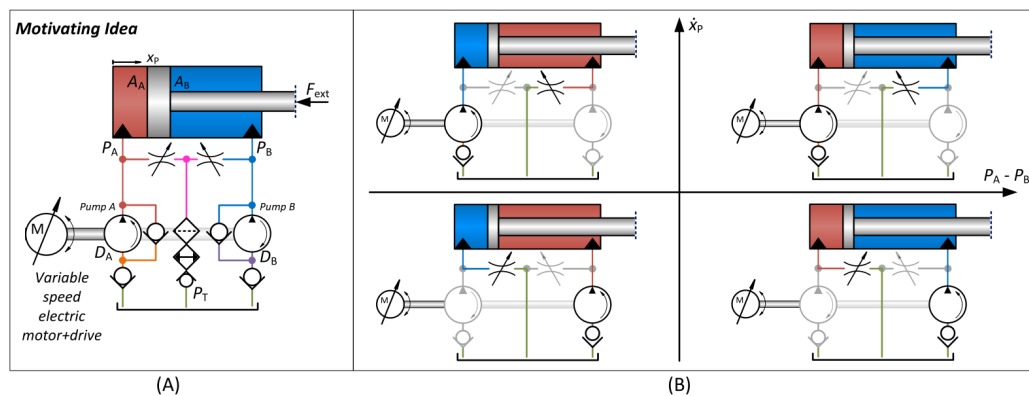


Figure G.16: (A) Self-locking open circuit pump drive concept. (B) Four quadrant illustration of the intended basic drive operation. [140]

Another solution to increasing drive stiffness requires an additional charge pump to prevent the pressure from dropping too low at the low pressure side of the fixed displacement pump. This technique is further discussed in subsection G.3.

One more inherent disadvantage of FPVM-EHA is the large amount of heat generated by the motor. As armature current is proportional to the motor torque, the motor generates a lot of heat due to copper losses when working in high pressure low speed conditions [34].

### Variable displacement pump

Electro-hydrostatic actuators with variable displacement pumps are attached to a fixed speed electric motor. The actuator is controlled by changing the displacement of the pump. According to Behbahani et al.(2010) and Schmidt et al.(2019) this approach has thermal benefits over the fixed displacement setup as fluid filtering and cooling may be realized via the associated fluid reservoir (see figure G.12 A) [22, 140]. Furthermore, due to the lower chamber pressure being held at a certain level by the charge pump, a proper drive stiffness of the actuator is maintained. The constant flow output needed for this stiffness however induces additional losses [140]. Also, the efficiency at low slew rates and duty cycles is reduced due to specific variable displacement pump characteristics [22]. Other literature claims variable displacement EHA technology also suffers from low drive stiffness [113], indicating different architectures are possible within both variable and fixed displacement EHA. Here the addition of a charge pump increases the drive stiffness of the EHA actuator. In general fixed motor variable pump EHA is known to have a lower efficiency compared to fixed displacement pump architectures according to [59]. On the other hand, the dynamic response of the variable displacement architecture should be faster as the inertia of a swash plate is much lower compared to the inertia of the motor in a variable speed architecture [108]. Response can be four to five times faster compared to similarly sized FPVM actuators [108].

An alternative to the fixed motor configuration is the variable pump variable motor (VPVM) EHA. This architecture combines the advantages of the variable motor speed with those of the variable pump displacement. The result is a linear actuator with a fast dynamic response and high efficiency in low load situations [59]. The maximum volume flow gradient can be doubled while reducing the necessary motor speed by as much as 40% using the proper control according to [179]. According to [178], energy consumption can be reduced by 20% compared to both FPVM and VPFM actuators. Also peak power requirements on the motor are reduced as the pump shaft can be used as flywheel prior to peak power demand of the actuator [178]. As more components are needed in this configuration, the VPVM-EHA is more complex and has a lower power density compared to other EHA architectures. This can be explained by the need for both heavy power electronics for the motor and a secondary motor and swash plate mechanism for the pump. Furthermore, the non-linearity of a double input single output system poses a great challenge for the control of this EHA type [172].

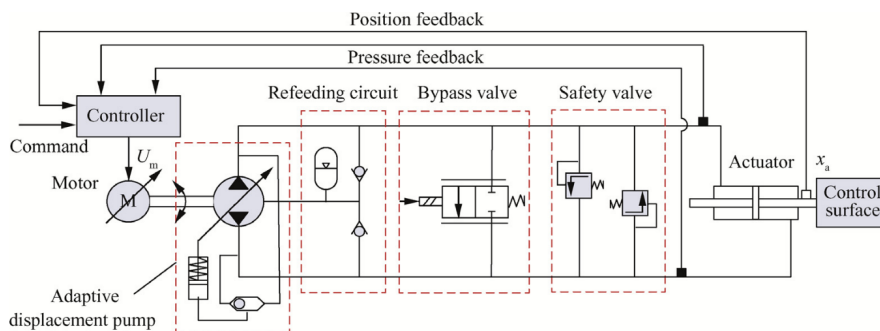


Figure G.17: EHA APVM architecture. [172]

To simplify the control, Wang, Guo and Dong (2018) propose an adaptive pump displacement and variable motor (APVM) EHA shown in figure G.17. The APVM is controlled with the motor speed while the displacement is adapted with a mechanical controller responding to the system pressure. The APVM inherits the same advantages as the VPVM but simplifies control as the system is single input single output [172]. The adaptive pump control realizes high speed under light load or low speed under heavy load. As such the maximum power requirement on the motor is lowered considerably resulting in a lower size and weight of the EHA-APVM [34, 172]. Simulations show the power requirement on the APVM-EHA can be as low as 41.67% compared to that of a FPVM-EHA depending on the operating conditions [172]. As such, heat dissipation due to copper losses of the APVM-EHA is drastically reduced compared to other EHA architectures. This is confirmed in figure G.18 from [34].

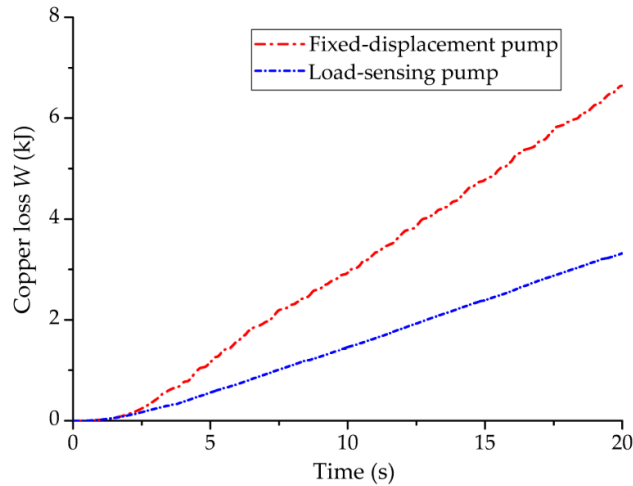


Figure G.18: Copper loss comparison for fixed displacement and load sensing pumps in equivalent test setups [34].

### EHA comparison

With the main characteristics of the different EHA architectures known, it is interesting to compare EHA variations. In [41], a comparative study is performed on both the fixed displacement and the variable displacement (fixed pump) EHA based on a nominal loading of 30 kN on an airplane actuator. Relevant results of this study are shown in tables G.2 and G.3. The mean time between failures of both architectures seems to be very close with the variable displacement setup having a slight advantage. Power needed to hold a load at standstill is less in the variable displacement architecture. Higher energy consumption than expected for the fixed displacement pump simulation are allocated to high internal leakage in the pump. Results from the sine wave loading test are difficult to compare as both simulations don't use matching parameters. The author concludes the fixed displacement architecture is better suited for small to medium power levels while the variable displacement shows higher efficiencies for higher power levels. This matches the statement by [22] about low efficiency at low slew rates for the variable displacement architecture. [22] assumes the achievable performance with the variable displacement pump should be higher than shown due to improvements in variable displacement pump technology.

Table G.2: EHA fixed displacement performance [41]

Property	Value
Failure probability	13574.4 h MTBF
Power to hold 33 kN load	742 W
Loaded sine wave (16.5 kN tensile load)	max 750 W
Temperature after 20 min at 33 kN	82 deg

Table G.3: EHA variable displacement performance [41]

Property	Value
Failure probability	13911 h MTBF
Power to hold 36 kN load	510 W
Loaded sine wave (25 kN compressive load)	max 15 + 800 W

The low drive stiffness of the fixed displacement EHA mentioned in subsection G.3 is a result of the specific architecture seen in figure G.12 B. The lack of an additional charge pump such as used in the variable displacement architecture of figure G.12 A results in a low pressure of the non driven cylinder side. Adding the charge pump to the fixed displacement architecture thus seems as a reasonable approach to increase the drive stiffness of this EHA type. As such, EHA architectures could be classified as a combination of different sub architectures as shown in figure G.19. Table G.4 summarizes the findings of the three main EHA architectures as discussed above. Properties such as drive stiffness and energy recovery can then be altered with the use of extra components such as a charge pump and hydraulic energy recovery unit.

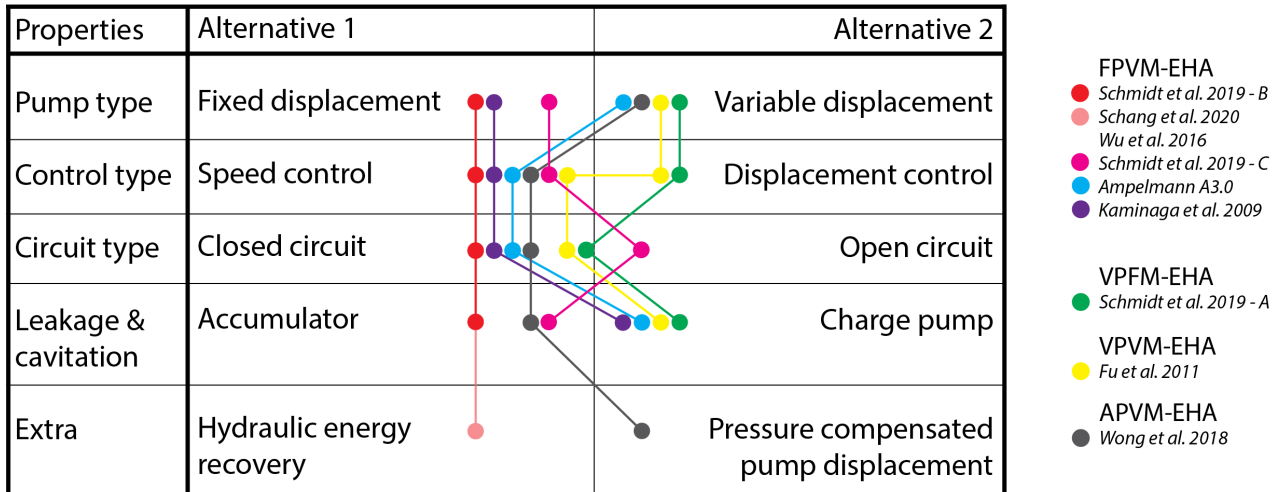


Figure G.19: EHA morphological chart.

Table G.4: Comparison of EHA architectures

Property	FPVM-EHA	VPFM-EHA	VPVM-EHA	APVM-EHA
Advantages	Simple structure Good efficiency High power density	Fast dynamic response	Fast dynamic response High efficiency (even in low load situations) Low noise level	Fast dynamic response High efficiency High power density
Disadvantages	Heat generation	Low efficiency	Complex structure Lower power density Complex control	

## Electro-mechanic actuators

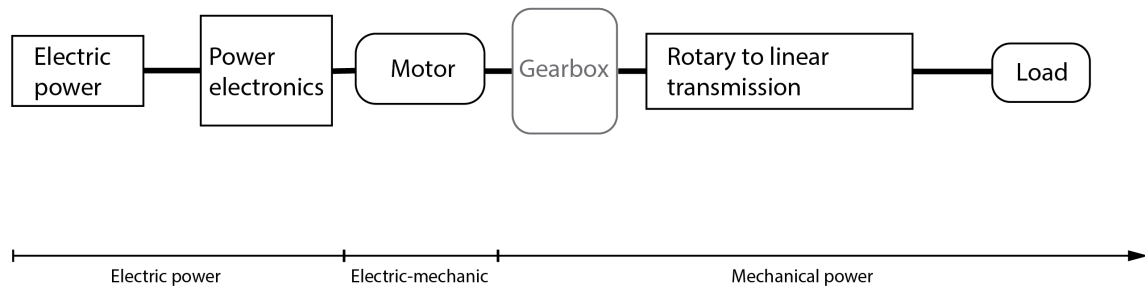


Figure G.20: Simplified representation of an electro-mechanic actuator

Electro-mechanic linear actuators (EMA's) are actuators using a mechanical rotary to linear transmission in the form of a screw coupled to a rotary electric machine with a reduction gear box. Here the reduction gearbox and the screw represent parts B and C in figure G.6 respectively. A simplified representation of the electro-mechanic actuator is seen in figure G.20. As only a single energy conversion step is needed, EMA has a natural advantage on energy efficiency and power density over hydraulic actuators according to [100]. The mechanical rotary to linear transmission used in EMA's comes in various forms. Those will be discussed in subsections G.3, G.3, G.3 and G.3 respectively. Efficiency of the EMA is largely determined by the (low) efficiency of these mechanical transmissions [17, 174], largest efficiency increases are therefore made with the transmission design.

Compared to conventional hydraulics, EMA shows increased safety and reliability and better dynamics due to absence of hydraulic fluid [128]. Also weight, volume, power requirements and overall complexity are drastically reduced [22, 33, 128]. The all electric setup furthermore increases the ease and flexibility of installation and decreases component and maintenance costs [22, 45, 128]. On the other hand, some inherent hydraulic properties such as damping and overload protection need to be integrated explicitly. This is done by for example electromagnetic dampers in the gearbox and a friction clutch or control circuit to limit motor current [41]. Nevertheless, mechanical transmissions need to be sized to the maximal expected overload force to prevent failure. In contrast, hydraulic solutions can absorb overload forces simply with a pressure relief valve [74]. The overload sizing could be reduced by implementing some mechanical force limiter with for example a pre tensioned spring. This would however result in a more complex design and no existing work on this solution is found in literature. An experimental study of Pohl et al.(2013) shows EMA needs up to 77% less energy compared to conventional hydraulics for the same lifting task [122]. Initial higher fabrication costs should be amortized in approximately 2.5 years [122] as operational costs are reduced due to absence of wearing parts such as seals [16, 174]. Note that these values are representative for aerospace applications.

While overall system weight can be lower, EMA does not reach the power density of a conventional hydraulic cylinder [17] resulting in a heavier in-situ actuator. Weight advantage of the EMA therefore only applies to configurations where the total actuator system weight is important [45]. EMA system weight is mainly dependent on component weight of the motor, gearbox, power electronics and transmission [32]. According to motor design theory, size and weight of the motor are directly proportional to the maximum torque developed [177]. This would mean the addition of a reduction gearbox between the motor and rotary to linear transmission is beneficial to reduce motor weight. In general the weight of an architecture tends to decrease when transmission ratio increases. However, at high transmission ratios, efficiency of the transmission decreases. It also implies higher speeds at the input shaft which impacts fatigue sizing. These effects tend to limit the use of high transmission ratios [110]. Gerada et al.(2007) proposes a gearbox free integrated machine design to reduce component count and jamming probability while increasing system efficiency [66]. This design could show an overall weight and volume reduction compared to gearbox designs. This direct drive architecture is also shown in [58] with the associated weight savings and high potential for geometrical integration. The use of these direct drive actuators is however limited to low power applications as rotational velocity of the spindle and inertia effects become a limiting factor with higher loads. Another method of decreasing system weight and increasing power density is the use of high pole number electrical machines [66]. The use of permanent magnet machines also increases power density and enables use of fault tolerant electric drives [25]. Fault tolerant electric machines are discussed further in section G.4.

Energy consumption of the EMA actuator can be reduced by implementing energy regeneration. EMA technology can make use of energy regeneration by backdriving the actuator with an external load. This in turn means continuous power must be applied to the electric motor to develop holding torque in stationary conditions [22]. This results in zero efficiency at standstill. EMA is therefore ideally suited for small to moderate loads and continuous motion according to [22]. For larger loads, high inertia has to be expected from the mechanical parts. This limits the achievable acceleration of the actuator [38]. In contrast to the earlier stated inertia limitations of a gearbox free design, [66] and [41] state here that elimination of an intermediate gearbox might prove useful to reduce the inertia of the system and the corresponding inertia losses.

A major drawback of EMA technology is its susceptibility to jamming which completely locks the actuator in place [17, 22, 33, 63, 87, 100, 113, 171]. Jamming probability of an active actuator is estimated to be  $1.2e-7 \text{ h}^{-1}$  according to [41]. It is not specified to which exact transmission architecture this number corresponds. Qiao et al.(2017) proposes a method to reduce friction torque in mechanical transmission to reduce this problem [128]. Stridsberg [153] proposes a redundant setup with dual actuators and explosive devices to disengage the jammed actuator. Use of a redundant setup reduces the overall dimension and weight advantages of EMA [63]. Minimizing the weight penalty can be achieved by using health and usage monitoring to reduce the risk of jamming without the need for redundant components as described in [58] and [168]. This technique is however difficult to implement due to a lack of means for early detection of faults in a real environment and due to a lack of models for predicting the evolution of faults into jamming failures [113]. Multiple other research projects try to create jam tolerant actuators [113], however research to jam free EMA is not readily found. Some examples of such research can be found in [26] and [85]. These papers implement a double mechanical path either by summing the forces (parallel) or summing the displacements (series). This same approach is taken by [105] where force summing allows force control when a single power path becomes uncontrollable. Conversely, displacement summing allows displacement control in case of a single power path experiencing jamming. In a Boeing patent of 1973, the displacement summing is implemented by using two nuts on a single spindle. One of the nuts acts as the ground fixed reference while the second nut acts as the attachment point of the load. To maintain the full range of motion upon fallout of a single nut mechanism, the spindle should be at least double the length of the desired stroke [175]. This is impractical in the hexapod design used by Ampelmann.

Next to mechanical jamming, Bennett et al.(2011) shows that failure probability of electric components is much larger than that of the mechanical components [25]. One solution for this is the use of dual-lane fault tolerant electric drives resulting in a system failure probability of  $8.68e-6$  failures per hour [25] or 115207 hours MTBF in combination with a roller screw transmission. Another method to reduce electrical failure impact is the use of multi-phase motors. The fallout of one phase does not significantly reduce the torque output of these motor types according to [128].

In general, EMA technology lacks an accumulated knowledge base compared to conventional hydraulics and EHA. According to Behbahani et al.(2010), an analysis regarding the critical failure modes and a criticality analysis should be performed for this technology [22]. [51] concurs by indicating the need for further work on reliability analysis of the technology. This is especially needed with respect to fault tolerance or resistance to jamming [58]. Also studies on backlash and nonlinear friction are needed to increase achievable control performance and dynamic bandwidth [171]. Finally, [58] states also size and weight constraints for integration and heat rejection are technical challenges still to overcome. More on EMA reliability can be found in section G.4. Specific properties and advantages of individual transmission technologies will be discussed in the following subsections.

## Ball screw transmission

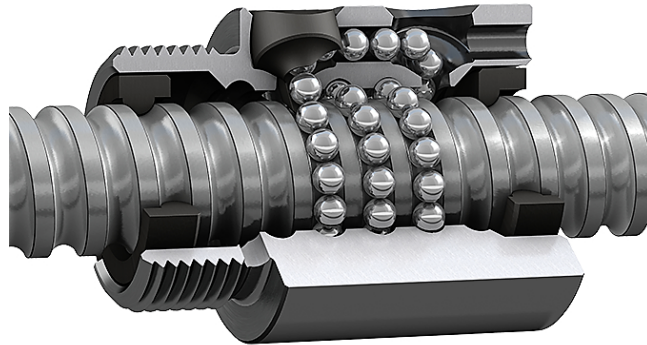


Figure G.21: Ballscrew cut out [7]

The ball screw transmission consists of a spindle with helix shaped grooves and a ball bearing carrying nut. The ball bearings transfer the load from the spindle to the nut and provide a rolling interface between both surfaces. By pre-loading the ball bearings, vibration and backlash of the mechanism can be kept to a minimum [173]. In the ideal case, the ball screw is able to operate slip free as is described in [99]. In reality, there will always be slip on the normal plane of at least one contact point as proven by Lin, Ravani and Velinsky (1994) in [102]. Next to slip on the normal plane, also slip in the tangential direction is present at the contact points [101]. As a result of this slip sliding wear occurs in the ballscrew mechanism. This wear decreases the preload of the ball-screw over time. This is the main cause of failure for a preloaded ball-screw [173]. To reduce the sliding wear in the transmission, Wei, Liou and Lai (2012) propose an increased ellipticity ratio in the ball groove design which reduces the plastic contact ratio [173]. Lubrication of the ball-screw can also reduce friction and provide cooling to prolong the life of the transmission [86]. Lin et al.(1994) uses an approximate closed-form ball-screw model which is valid for screw speeds up to 2000 rpm. With this model, it is clearly shown an optimal contact angle of the ball-screw exist for peak efficiency. This is explained by the frictional force component along the tangential direction dissipating more energy than the frictional force component on the normal plane. This becomes more important at higher contact angles [101].

Another source of frictional force as explained in [89] is the re-circulation mechanism. Upon moving from the nut groove to the recirculation tube the force acting on the bearing ball has to overcome friction in the recirculating mechanism and the weight of the ball. This friction force varies with up or down movement by the effect of gravity. The recirculating mechanism determines for a large part the maximum rotational speed of the ball-screw [68].

The model of Lin et al.(1994) shows an optimal efficiency of 86.1% for all helix angles and their corresponding contact angle of the ball screw. This optimal efficiency is valid for both driving and backdriving of the transmission. Self braking is seen to occur in designs with low contact angles in the driving case and for low helix angles combined with high contact angles in the backdriving case. Furthermore load capacity is seen to be highest with a large spindle radius, small helix angles and large contact angles [101].



Figure G.22: Ring screw render [73]

An alternative to the ball screw is the ring screw as proposed in the thesis of Heijmink [73] and paper by Featherstone [55]. The ring screw makes use of adapted circular ball bearings which make angled contact with a specially shaped screw for perfect line contact. The use of a perfect line contact is very important in maximizing the load capacity of the ring screw. Due to the shape of screw and circular ball bearings, no sliding occurs during motion of the screw relative to the nut captivated ball bearings. This makes the ring screw highly efficient with prototypes reaching 90% efficiency. The ring screw can provide the same functionality as the ball screw. The main advantage over the ball screw is the much higher operational speed limit. The first functional prototype is able to operate at speeds up to 16500 rpm. This maximal speed is mainly determined by the maximum speed of the bearings or the resonance frequency of the screw. The ball screw however is only a concept at this stage and has no full scale applications or test data yet.

### Roller screw transmission



Figure G.23: Roller screw cut out [3]

Roller screws or planetary roller screws are very similar to ball screws, except instead of ball bearings, several rollers are used to transfer the load from the spindle to the nut. Three different roller screw designs are known of which the planetary design is best suited for high accelerations and speeds in combination with very heavy load capabilities [98, 162]. The rollers of the planetary roller screw have a helical thread and have therefore numerous contact points along its length with the spindle and nut. These contact points make the roller screw capable of substantial larger load bearing compared to the ball screw [128, 145, 162, 167] with current examples going up to 350 t [145]. Load bearing capacity can be up to 69% greater than that of ball screws due to more contact points alone. Another 5% can be won in difference between geometry and the associated friction terms [167]. [98] gives some sizing examples showing roller screws have a dynamic load rating approximately three times larger compared to similarly sized ball screws. For a dynamic load rating of 189.3 kN a diameter and lead combination of only 48x10 mm is needed here. Furthermore, the roller screw has a very good resistance to shock loading [128]. According to Jones et al.(2012) and Beek (2006), roller screws also have a longer life, higher speed & acceleration ratings and finer lead possibilities [87, 162]. The longer (fatigue) life is explained in [98] as fatigue life is proportional to the cube of the dynamic load rating. As such, roller screws can outlive ball screws of comparable size by a factor of 15 [162] to 30 [98]. This is also seen in practical examples of machine tool applications and aircraft carrier catapults [98]. Finally, roller screws are seen to generate lower noise levels compared to ball screws at similar rotational velocities [98]. Due to the complexity of the mechanism, the roller screw is however an order of magnitude more expensive compared to the more conventional ball screw [6].

Efficiency of the roller screw is mainly determined by the slip in the mechanism. Roller screws only have an axial slip component while ball screws have slip mainly in the tangential direction (see subsection G.3). Due to geometry of the mechanism, tangential slip forces have more work associated with them compared to forces in the axial direction [167]. Efficiency of the roller screw is therefore higher compared to the ball screw mechanism [101]. At higher transmission ratios, efficiency of the roller screw however decreases. The associated higher operating speed at the input shaft also impacts the fatigue sizing of the part [110]. Sizing of the roller screw is directly related to the given output force with a mass and size scaling ratio equal to  $M^* = F^{*3/2}$  and  $l^* = F^{*1/2}$  according to [110]. Here  $F^*$  represents the force scaling factor to a given reference. This scaling law is plotted against manufacturer data in figure G.24 [110].

Due to the kinematics of the roller screw, slip is always occurring in the roller mechanism. Lateral motion is not influenced by this slip [167]. However, axial migration of the roller relative to the nut caused by slip is an undesirable phenomenon which can cause binding of the mechanism [87]. Due to the numerous metallic contact points of the rollers with spindle and nut, jamming probability of the roller screw is higher compared to the ball screw [128]. In contrast, Lemor (1996) states the jamming probability of a roller screw is very low due to the absence of a recirculating mechanism as is found in ball screws [98]. According to Liscouët, Maré and Orioux (2008), failure behavior of the roller screw is well-known and not subject to jamming in useful life conditions [105]. The most probable modes of failure are identified in [98] as metal fatigue failure and wear of the load transmitting surfaces. Again, surface wear under normal operating conditions is not expected before 15 to 25 years of service.

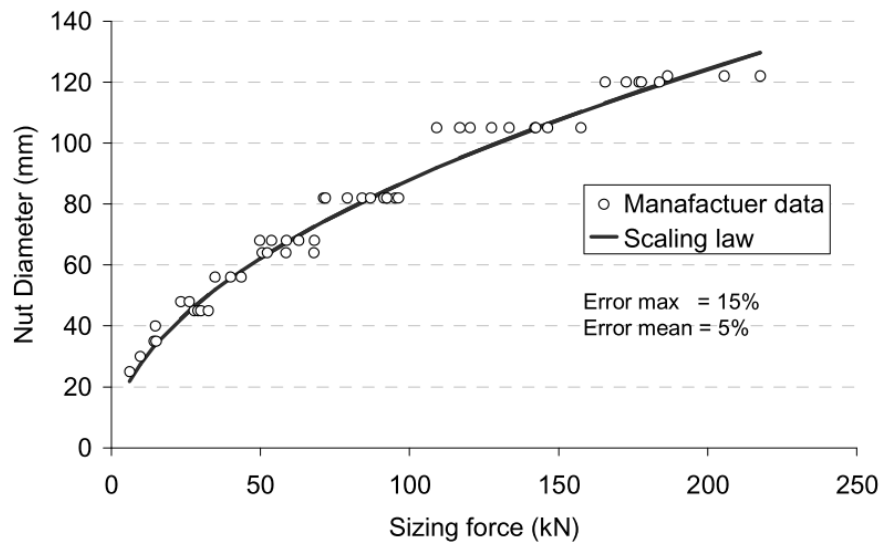


Figure G.24: Nut diameter versus roller screw load capacity [110].

### Friction screw transmission

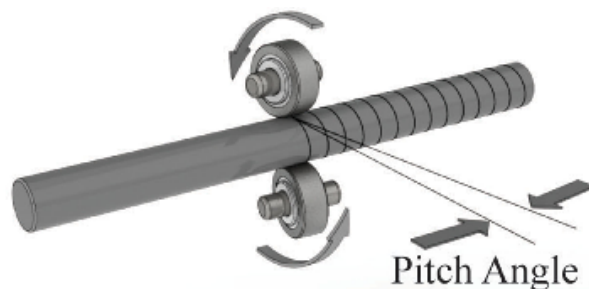


Figure G.25: Friction screw principle sketch [23]

A major obstacle of both the ball screw and roller screw transmission is the high susceptibility to jamming. A fundamental solution to this problem is the use of force closed instead of form closed mechanisms. The friction screw is a good example of such a force closed mechanism. The friction screw consists of a smooth spindle and a nut with angled ball bearings as wheels. The angle of the wheels with the spindle determines the transmission ratio of the mechanism [23]. To obtain load bearing capacity, the wheels are pre-tensioned against the spindle. This effectively deforms the spindle locally to form a helix shaped guide way [53]. Due to the force closed design the transmission is able to slip when overloaded. For this reason friction screws are being utilized in a variety of haptic devices [53]. In contrast to conventional transmissions with a narrow peak of efficiency or power region [23], the friction screw provides a variable transmission ratio for optimal efficiency over a large operating region [23, 52, 53, 54]. The variable transmission ratio is realized by controlling the angle of the wheels with respect to the spindle. Energy efficiency of the actuator system in stationary conditions is further improved by turning the wheels perpendicular to the spindle, effectively decoupling the load from the motor

[53]. Also backdrivability of the mechanism can be controlled with this method for optimal energy regeneration [54]. Control of the wheel angle can either be active or passive as proposed by Belter and Dollar [23]. Use of passive angle control eliminates the need for additional sensing and actuation in the transmission leading to a more weight efficient design.

Axial slip of the wheels limits the maximum axial load of this transmission. Maximal load capacity is given by Belter and Dollar (2014) in equation G.3 [23]. Here  $F_n$  is the normal force on each wheel,  $n_{rollers}$  is the total number of rollers used,  $\mu$  is the friction coefficient between the roller material and shaft material and  $\theta$  is the angle between the wheel and a line perpendicular to the axis of the spindle (lead angle). Using a lead angle of 10 deg, a set of 8 wheels and a friction coefficient of  $\mu = 0.6$  (steel on steel, kinetic), a preload of approximately 32 kN is needed for a 150 kN load capacity. As rolling losses are non linearly related to preload [53], this clearly shows the friction screw becomes impractical for use in high load capacity applications. Practical examples up to 2 kN are found in industry [1].

$$F \leq F_n \cdot n_{rollers} \cdot \mu \cdot \cos(\theta) \quad (\text{G.3})$$

The wheel and spindle both exhibit elastic deformation and inelastic behaviors, leading to lateral creep and rolling losses. Rolling losses include rolling friction and wheel bearing friction [53]. To reduce the lateral creep, the modulus of elasticity should be increased. On the other hand, an increase of the coefficient of friction drastically reduces the required preload and thus nearly all forms of dissipation except lateral creep [53]. The gain in weight efficiency from operating at the most efficient operating point of the motor should thus be weighted against reduced efficiency of the friction based drive [23].

### Hydrostatic transmission

The hydrostatic lead screw eliminates friction related issues of both the ball and roller screw by removing mechanical contact between the screw and nut. A hydrostatic fluid bearing is used to transfer load between the spindle and nut. As a result, the lead screw experiences no wear, backlash or mechanical friction with an axial stiffness up to  $10^9 \text{ N m}^{-1}$  [151]. To guarantee load bearing capacity even at very low spindle speeds, the hydrostatic nut is pre tensioned using a constant pressure supply [21]. Upon deactivation of this external pressure supply, hydrostatic lead screws show self locking properties [81]. A disadvantage of this type of transmission is the need for seals to reduce fluid leakage. Seals introduce mechanical slip in the system reducing the efficiency of the actuator [21]. However, a transmission efficiency up to 99% can be reached according to El-Sayed and Khataan [49].

In industry, these transmissions already exist commercially up to load capacities of 750 kN [81]. Most of these transmissions however max out at a linear velocity of  $0.5 \text{ m s}^{-1}$ . Speed of the hydrostatic lead screw is limited by fluid film effects. Above certain speeds, flow in the inner region of the thread surface will vanish, resulting in a decreased film thickness and load carrying capacity [49]. The major drawback of the hydrostatic lead screw is however the high cost compared to commercially available ball screws. [160]

### EMA comparison

EMA actuators are mainly differentiated by the motor type and the transmission type used. Furthermore, different redundancy options are available or should be designed. In this literature review the focus is set on the transmission options of EMA actuators. The choice of motor types and their properties is discussed in less detail as this dives too deep in the electrical domain. To give an overview of the discussed EMA actuators, a global comparison of the different rotary to linear transmissions is given in table G.5. Figure G.26 also shows the positioning of the rotary to linear transmission in the mechanical linear actuator. For a more global overview of linear actuator components refer to figure G.6.

The main rotary to linear transmissions found in literature are the ball-screw and the roller-screw. Ball-screws need relative high lead values to react to dynamic loads. This will increase the reduction ratio needed in the gearbox to keep the motor torque under control. With roller screws, reduction can be achieved by the planetary reducer of the screw mechanism reducing the reduction ratio of an additional gearbox or even completely eliminating this gearbox [41].

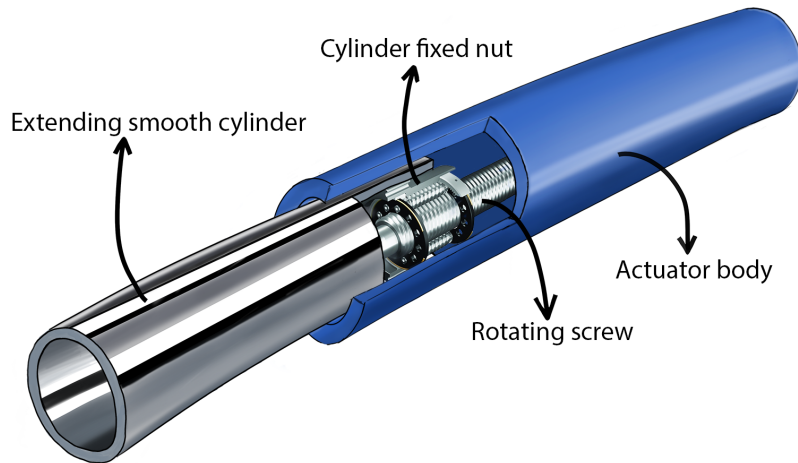


Figure G.26: Position of the rotary to linear transmission in the linear actuator. The rotary to linear transmission is here portrayed by a planetary roller screw.

Table G.5: Comparison of EMA rotary to linear transmissions

	Ball-screw	Roller-screw	Ring-screw	Friction-screw	Hydrostatic-screw
<b>Load capacity (dynamic)</b>	Up to 380 kN available.	Up to 3994 kN available, much higher compared to similarly sized ball screw.	Tested to 750 N, but theoretically higher load capacity compared to ball-screw.	Low due to slip. Practical examples up to 2 kN	Up to 750 kN available
<b>Efficiency</b>	Up to 97% in literature	Up to 97.4% in literature	Prototype up to 90%. Theoretically higher than ball-screw.	Low due to high friction forces	Up to 99%
<b>Velocity</b>	Up to $0.9 \text{ m s}^{-1}$ in literature	Up to $1 \text{ m s}^{-1}$ in literature	very high, only limited by ball-bearing rating and resonance frequency	Depending on the load with the variable lead angle.	Around $0.5 \text{ m s}^{-1}$ . Limited by fluid film properties.
<b>Weight</b>			Unknown	Variable lead angle enables use of lighter motors.	
<b>Cost</b>	Low	High	Unknown	Unknown	High
<b>Failure modes</b>	Mechanical jamming	Mechanical jamming	Unknown	Slipping when overloaded.	Self locking on loss of fluid pressure.
<b>Lifetime</b>		Examples of 15 to 20 years. Factor 15 to 30 higher compared to a similar ball-screw.	Unknown		

Comparing actuators in simple numbers is very difficult as properties are dependent on several factors. Maximum load capacity and velocity are for example only seldom met. In literature the majority of the research is focused on output power levels far below the required output power for the Ampelmann actuator. Further research is thus needed to find the properties of selected transmission technologies at higher load and velocity combinations.

## Electro-magnetic actuators

Next to the hydraulic and mechanical solutions, a third linear actuator technology can be distinguished. The electro-magnetic actuators use electric and magnetic fields to convert electrical energy in linear motion. By omitting mechanical contact, electro-magnetic actuators can operate very efficient across a wide range of operating points [171]. The lack of mechanical contact also reduces maintenance requirements and eliminates mechanical jamming found in electro-mechanic actuators altogether [171].

The majority of electro-magnetic actuation solutions are linear motors. These actuators use the exact same principles as rotary electric motors. Where a rotor spins and reuses a magnetic pole on every turn in a rotary electric motor, the magnetic poles of a linear motor are repeated along the motion direction [8] as can be seen in figure G.27. As only a fraction of the volume is active at any given time to produce thrust force, power density of the linear motor is very low [75].

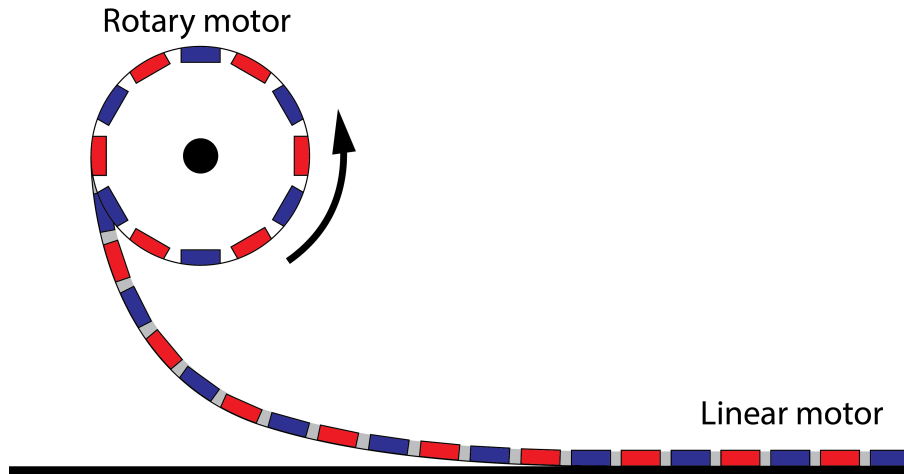


Figure G.27: Permanent magnet arrays on a rotary and linear permanent magnet machine.

To increase the power density of linear motor, Wang J., Atallah and Wang W. [171] propose a high force density linear electromagnetic actuator based on the concept of the magnetic screw-nut as seen in figure G.28. This actuator achieves the same gearing effect as a mechanical spindle but without direct mechanical contact. A trust force density of  $10 \text{ MN/m}^3$  can be achieved using this design. The magnetic lead screw uses helical disposed radially magnetized permanent magnets on both the nut and screw to replace the threads on a mechanical spindle. A magnetic force and torque is developed between the magnetic nut and screw to hold a load. The use of a magnetic field to hold the load also provides an inherent overload protection as nut and screw poles can snap upon reaching the load limit. A major disadvantage of the magnetic lead screw is the high cost and weight of the helical magnets on both the nut and spindle. This is especially relevant for large stroke machines [36].

To reduce the cost of magnetic lead screws for long stroke actuators, Cirolini, Filho, Wu and Dorrell [36] propose a new type of reluctance-based magnetic lead screw. This design only uses helical magnets on the stator (nut), therefore drastically reducing the amount of permanent magnet material in the actuator. The spindle is made of ferromagnetic steel and resembles a traditional threaded lead screw. Permanent magnets in the nut are arranged such that magnetic flux is concentrated towards the smallest airgap between the nut and the spindle. As such, the rotor (spindle) rotates to move the stator (nut) up and down. The force and torque transmission relationship of this actuator is equivalent to a mechanical leadscrew. A higher gear ratio can be obtained by using a lower pole pitch ( $\tau_p$ ) and a lower pole number of the nut. This is shown in equation G.4. Assuming a motor torque of  $500 \text{ Nm}$  can be provided to a two pole lead screw, a pole pitch of approximately  $1 \text{ cm}$  is required to reach  $150 \text{ kN}$  holding force (provided the pull-out force of the reluctance circuit is high enough). To reach a linear velocity of  $1 \text{ m s}^{-1}$ , a spindle speed of  $6000 \text{ rpm}$  is needed. At these speeds, the outside of a  $90 \text{ mm}$  spindle would experience a centrifugal acceleration of approximately  $17800 \text{ m s}^{-2}$ . These simple calculations show the need for a gearbox in the design to increase th pole pitch and decrease the rotational velocity of the spindle.

$$G = \frac{2\pi}{\tau_p \cdot n_{poles}} \quad (\text{G.4})$$

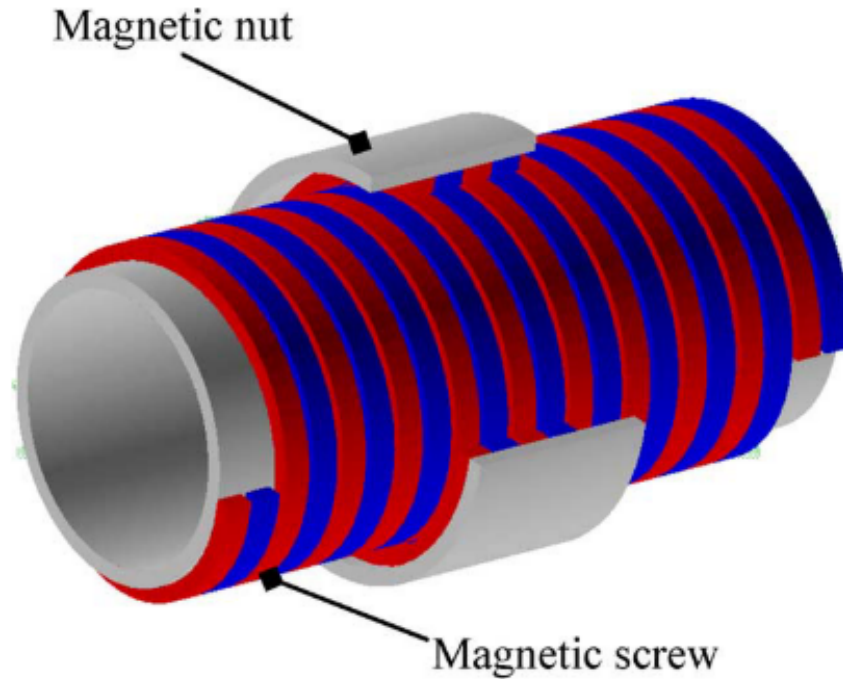


Figure G.28: Magnetic lead screw simplified representation as proposed by [171].

Another problem regarding the reluctance based lead screw is the snapping tendency of reluctance circuits. Reluctance force is inversely proportional to the air gap length squared [141]. As a result, a slight asymmetry in the nut-screw alignment will cause snapping resulting in mechanical contact of the nut and screw. This snapping problem can be reduced with bearing design. This would however diminish the contact free advantages of the reluctance-based lead screw.

As the nut still makes use of a continuous helical magnet, producing this actuator is difficult. Cirolini et al.(2019) proposes to discretize the permanent magnets to approximate a helically shaped structure as can be seen in figure G.29. Discretization has a deteriorating effect on the maximum pull out force of the actuator [36]. With four segments per turn, the pull out force is reduced to 54.3%. A 24 segment approximation yields 91.7% of the ideal pull out force.

Finally, an estimate of the sizing for 150 kN pull-out force is made. A simplified MATLAB model is used. The model calculates the attraction force between a single helical stator pole and the ferromagnetic rotor. The airgap area is assumed to be the overlapping area of the ferromagnetic thread in the stator and the tooth surface of the rotor. The model assumes zero flux leakage and no interference of other poles. To obtain force capability of a two-pole system, the force of the single pole calculation is doubled. The reluctance-based attraction force is assumed to work perpendicular to the axial direction of the lead screw. To obtain the maximum pull out force, the angle between the centroids of the ferromagnetic thread and the tooth of the lead screw is calculated. The pull-out force is then calculated as  $F_{pull} = \tan(\alpha) \cdot F_{attraction}$ . Linking the pull-out force to the perpendicular attraction force using an angle is not very accurate and is not reliable for larger magnet sizes. However, as a first indication the values in table G.6 give an idea of the sizing for a 150 kN pull-out force actuator.

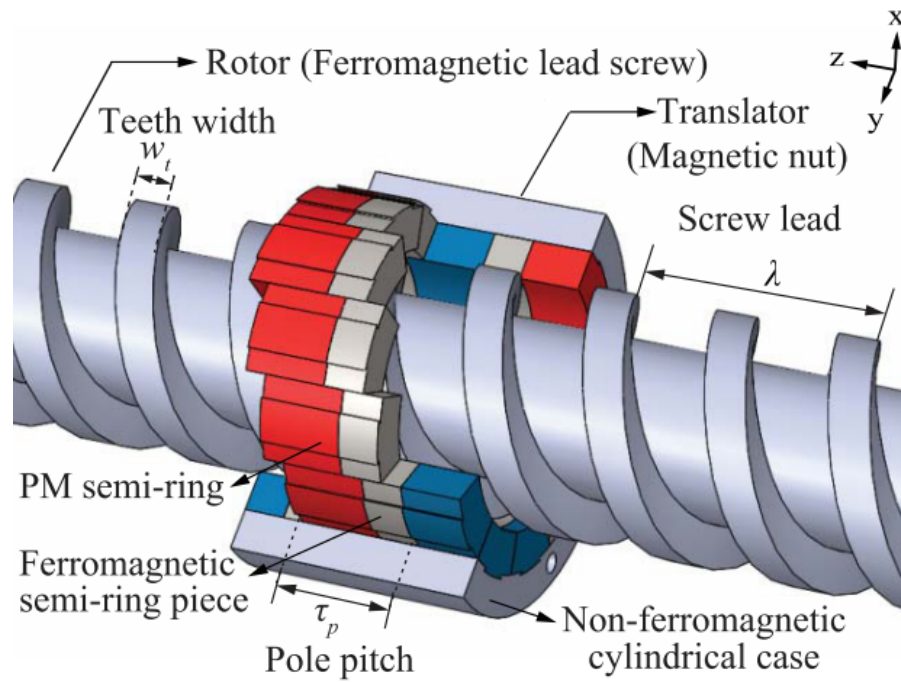


Figure G.29: Discretized permanent magnet configuration in the nut of the reluctance based lead screw [36].

Table G.6: Sizing indication for a 150 kN pull-out force reluctance based lead screw.

Property	value
Poles	2
Flux density $B_r$	1.48
Relative permeability $\mu_r$	5000
Permanent magnet to ferromagnetic ratio	0.4
Pole pitch (lead)	0.05 m
Screw diameter	0.1 m
Length of nut	0.35 m
Height PM	0.03 m
Width PM	0.1 m
Air gap	0.001

The sizing example above shows the nut becomes very large. The main problem with this design is the air gap of only 1 mm which is not practically manageable on this size actuator. For larger airgaps, the required permanent magnet size increases fast. As such, the reluctance based lead screw is ideally suited for smaller loads and becomes impractical for high load applications. [22] states this is mainly due to magnetic saturation of the magnetic materials used in the actuator design.

## Conclusion

This chapter discussed the available technologies for linear actuators. Four main classes of linear actuation technologies are distinguished: hydraulic actuation technology, electro-hydrostatic actuation technology, electro-mechanic actuation technology and electro-magnetic actuation technology. The electro-hydrostatic actuation technology could also be classified as a hybrid of hydraulic and electro-mechanic actuation technology. In discussion the general properties of each actuation technology, the electro-magnetic technology is seen to be

advantageous only in low power applications. As such, this actuator technology will not be further discussed in the context of linear actuation for Ampelmann. Both electro-hydrostatic and electro-mechanic actuation technology have shown potential in weight and efficiency benefits over conventional hydraulic actuation technology. The most promising configurations of both electro-hydrostatic and electro-mechanic linear actuators will be compared in chapter G.4.

## G.4 Actuator comparison

In chapter G.3, different linear actuation technologies are discussed with their main advantages and disadvantages. This chapter will discuss the linear actuation technologies which are suited for high power applications in more detail. The best actuation concepts will be compared to each other on requirements of load bearing capacity, maximum acceleration and velocity, energy efficiency, power density, reliability and cost efficiency.

### High power linear actuation

In chapter G.3, some actuator technologies proved less applicable to high power applications. This is the case for the electro-mechanical friction screw and the electro-magnetic solutions. As such conventional hydraulic, electro-hydrostatic and electro-mechanic ball-screw, roller-screw and hydrostatic screw are left as viable alternatives for a high power linear actuator.

In literature, the economic benefit of further refinement of traditional hydraulic devices appears to be limited due to the parasitic energy consumption from pumping and associated system losses [113, 161]. This matches other statements in literature about an overall efficiency advantage of electric solutions over conventional hydraulics [22, 33, 122, 129]. Furthermore, multiple sources state that 'more electric' technologies have advantages in system mass, volume, motion dynamics [22, 41, 129, 163], safety and maintenance [41, 45] over conventional hydraulic systems. Consequently, further research in the development of conventional hydraulics seems inefficient for the next generation high power linear actuator.

The most referred to designs for more electric actuators are electro-hydrostatic and electro-mechanic ball- and roller-screws. Together with the electro-mechanic hydrostatic screw, these linear actuator types will be discussed and compared in more detail in the following section. These actuator designs all share a decentralized architecture compared to conventional hydraulics. Decentralisation has some associated disadvantages such as less inherent heat rejection [58] and the introduction of power electronics and their specific losses. On the other hand, the lack of hydraulic piping needed to support an actuator enables more flexible placing of the actuator and less failure points in the power supply of the actuator.

### Electro-hydrostatic versus Electro-mechanic

The current trend in actuation technology for the aviation and heavy machinery industry is moving towards more electric actuation. More electric actuation had some major drawbacks regarding power to weight ratio, limited available electric power and lack of experience and demonstration of fail safe-characteristics. Technical developments in the last decade turned the cards with advances in magnetic materials, brushless DC machines and FEM calculations [41]. As such, 'more electric' solutions are becoming more and more the standard in actuation technology. Especially synchronous machines are often used as drive in these actuators because of their high efficiency and power density. Although synchronous machines require much more complicated controllers compared to induction motors and don't offer the same torque smoothness, mass and reliability advantages make this motor the current standard in actuation applications [105]. Electro-hydrostatic actuation (EHA) and electro-mechanic actuation (EMA) are both popular subjects for research in the aviation field. Both actuator types offer a more electric approach for lightweight and efficient actuators in airplanes and other mechanical machines. Fault tolerant architectures [138] and health management technology of both actuator technologies results in a reliability advantage over conventional hydraulic solutions [51]. As the main benefits of more electric actuators over conventional hydraulics are weight savings and increased efficiency [33], those are clearly important metrics in comparing different actuator technologies. Existing research especially focuses on the advantages of both technologies compared to conventional hydraulic actuators. Research regarding weight and efficiency advantages between EHA and EMA varies in outcome. Existing literature regarding comparisons on weight and efficiency advantages is discussed in the subsections below. Other factors are discussed in subsection G.4

## Weight comparison

Chakraborty, Trawick and Jackson (2013) state it is generally accepted that, when sized for the same actuation requirements, EMA enjoys a weight advantage over EHA [33]. This statement is repeated in [129]. The weight advantage has the potential of becoming larger with higher loads based on theoretical comparison for three load cases up to 51 kN and  $0.1 \text{ m s}^{-1}$ . This finding matches with the graph (figure G.30) published by Vladimirov and Forde (2006) [169]. The graph is found again in [100] to show the higher power density of EMA over EHA technology.

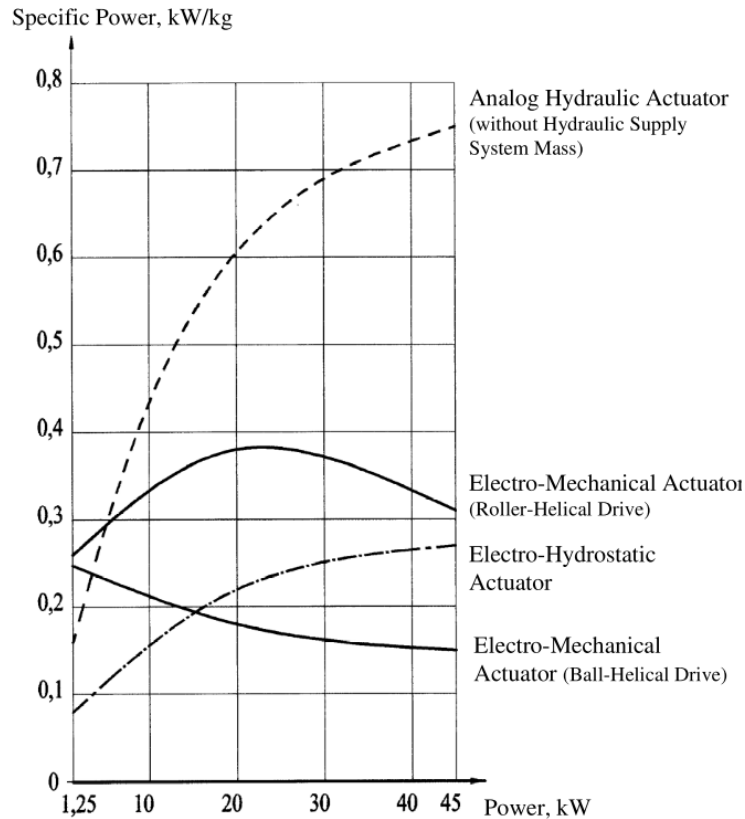


Figure G.30: Comparison of Specific Power vs. Power Output for Various Actuator Types [169]

In the figure both EMA with a roller-screw drive and EMA with a ball-screw is seen to have a higher power density at power levels of approximately 5 kW. The graph clearly shows EMA roller-nut drives have a weight advantage over EHA drives up to power levels of 45 kW. Continuation of the power density plot for values above 45 kW is lacking, and a parametric model describing the graph can not be found in literature. [137] furthermore states that for heavy operations, EHA has a lower unit weight and cost compared to EMA. This statement however is not backed up by rigorous argumentation. Similarly, [164] states EMA has a weigh advantage over EHA in low power applications. In his thesis, Fanliang describes lots of simulations and experiments show a clear weight advantage for EMA over EHA [51]. This is based on papers [163], [41] and [38] that all describe more electric actuators for large aircraft with a max load rating between 15 and 30 kN.

In general the consensus seems to be that EMA technology has a weight advantage over EHA technology for low power applications. For higher power applications, this weight advantage seems to decrease and maybe even switch. This conclusion seems to match with the statement by Behbahani and Semega (2010) that EMA is ideally suited for smaller loads and continuous motion, and to a lesser extend for larger loads and position holding [22]. Rigorous argumentation to back this up is lacking in existing literature. Furthermore, alternative transmission architectures such as hydrostatic nuts are not compared in the context of electro-mechanical actuators.

## Efficiency comparison

EMA in contrast to EHA does not use hydraulic power. [114] states this results in a more efficient and leak-free actuator solution referring to [100]. Both [100] and [41] come to this conclusion based on simulations with

regard to medium power actuators with load ratings up to 30kN often found in control surface actuators of large aircraft. On the other hand, [113] states EMA loses the natural advantages of hydraulics which results in lower overall efficiency due to use of a low efficiency mechanical transmission. This opinion is shared by [174] and [137]. it is important to note that these last three references base their results on either landing gear actuators or crane actuators with power levels ranging from 50 to 350 kW. A reference to a specific transmission is not present. Efficiencies of roller helical screws etc. can reach 90% and more, hence it is reasonable to assume these statements refer to more common transmissions such as leadscrews and or reduction gearing. Again, the consensus seems to be EMA is the more energy efficient option for low to medium power actuators while EHA becomes more efficient for higher power applications.

In a study by Montero (1996), EMA and EHA architectures are simulated to hold a load of 20 kN at standstill [41]. Required power is shown in table G.7. Here the fixed displacement EHA architecture clearly is seen to use less power for this task compared to roller-screw EMA and variable displacement EHA. As this is only at standstill, results are difficult to use in efficiency comparison during operation.

Table G.7: Actuator 20 kN load holding comparison [41]

Architecture	Required power
EMA roller-screw	125 W
EHA fixed-displacement	88 W
EHA variable-displacement	270 W

Efficiency and energy usage is very dependent on the specific application of the actuator. The majority of research towards electro-hydrostatic and electro-mechanic linear actuators is focused on the aviation industry and its corresponding load and motion cases. Control surface actuation presumably has a very different load and motion profile compared to linear actuators in the Ampelmann hexapod setup. This makes comparing efficiencies found in literature very difficult to apply to Ampelmann requirements. An application specific efficiency analysis should be performed to be able to find the most efficient actuator architecture.

### Other metrics

Next to weigh and efficiency, another often used metric to compare EHA and EMA is reliability, focused on mechanical jamming. As discussed in section G.3, EMA has a large susceptibility to mechanical jamming due to the numerous mechanical contact points in its transmission [33]. EHA doesn't suffer from this jamming problem due to its hydraulic transmission. As such, reliability of this actuator type can be much higher compared to EMA. Furthermore [17] states this makes EHA ideal for use in harsh environments. On the other hand, [164] states reliability of EMA is higher compared to reliability of EHA in low power applications. No further argumentation for this statement is found. Reliability of the EMA is further discussed in section G.4.

Possible additional advantages for EMA over EHA technology according to [164] are reduced complexity and maintenance requirements. This is also seen in a white paper by Shelton (Exlar) where roller-screw EMA is shown to have simple controls, a small footprint, low maintenance requirements and no fluid leakage risk [145].

According to [174], the biggest advantage of EMA over EHA is its lower operating cost. This is explained by experience from conventional hydraulic systems with high hydraulic operating costs. This hydraulic operating cost would transfer to any system containing hydraulics. Operating cost of a mechanical setup is expected to be less costly. Operating cost is also reduced by lower maintenance requirements on the mechanical spindles. While operating cost might be lower, the same paper states EHA has smoother dynamic behavior compared to EMA based on simulation results. Although, EMA should only be slightly inferior to EHA. [41] clarifies that EHA with a fixed displacement pump indeed has better dynamic performance while EHA with a variable displacement pump shows worst dynamic performance compared to EHA-fixed pump, EMA-ball screw and EMA-roller screw. These last actuator types all pass the dynamic criteria set for airplane actuators, making this a minor criterion. The slight discrepancy in dynamic behaviour might be explained by the higher inertia of mechanical parts such as rotor, gears and nut components compared to the single piston used in EHA technology [38]. Typically, inertia of the EMA drive is 10 to 20 times greater than the load itself in aviation related applications [58]. This ratio is expected to reduce for higher load applications.

## Reliability of EMA

Reliability of existing electro-mechanic actuators is widely named as the main disadvantage preventing EMA systems from being used as primary actuators in critical applications. This is discussed in section G.3. EMA's should be proven to achieve the same safety and reliability as hydraulic based actuators. Jam cases don't occur very often, however it is one of the least desirable failure modes of an actuator as the actuator turns into a rigid beam after jamming failure occurs [13]. As such, references [22], [38], [51], [58], [63] and [129] all state the need for further work on reliability analysis and jam free transmission technology. Jamming occurs because load is transmitted through mechanical contacts under very high hertz stresses, therefore fatiguing the material. This degrades the contact surfaces of the transmission leading to increased power consumption and finally mechanical jamming [83]. Lifetime sizing should prevent fatigue damage to occur within the lifetime of the actuator [105]. For both ball- and roller-screws the  $L_{10}$  life is often used as a lifetime scaling tool [148]. As discussed in section G.2, probability of occurrence of severe failure should be below 1%. As such, the  $L_{1m}$  equation given in eq G.5 [40] is more suitable giving a lifetime estimate with 99% reliability.

$$L_{1m} = 0.25 \cdot \left( \frac{C}{F_{eq}} \right)^p \cdot 10^5 [km] \quad (G.5)$$

$$F_{eq} = \sqrt[p]{\frac{1}{l} \cdot \sum_{i=1}^n |F_i|^p \cdot l_i} \quad (G.6)$$

In equation G.5, the  $p$  exponent is defined as 3 or 3.3 for ball- or roller-screws respectively [148]. The equivalent dynamic load  $F_{eq}$  can be determined according to equation G.6. Rewriting equation G.5 in function of the dynamic load rating  $C$  and filling in the given Ampelmann requirements results in a required dynamic load rating of 49.5 kN and 51.7 kN for the ball- and roller-screw respectively.

Reliability analysis of the EMA is often performed with failure mode and effect analysis. Previously performed reliability analysis give insight in the most critical components of the actuator with regard to reliability. From a failure mode and effect analysis performed by Linden, Dreyer and Dorkel (2016), the components leading to the highest jamming rates are identified as bearings, ballscrews and gears. Furthermore, loss of lubrication is seen as the highest indirect failure mode [103]. In [168], also the influences of large temperature fluctuations are marked as a potential degradation factor leading to indirect failure modes.

Mazzoleni, Maccarana and Previdi (2017) present a failure mode effect and criticality analysis (FMECA) performed on an EMA for primary control surface actuation in an aircraft. The FMECA results are then validated with an experimental setup in [125]. A total of 1950 failure modes are identified [114]. The relevant failure mode effects are summarized in table G.8. The same authors performed a fault tree analysis to find the risk likelihood of these failures. Results are summarized in table G.9. Note that the values found in tables G.8 and G.9 are representative for EMA actuators with a maximum force of 1.5 kN and speed of 0.08 m s<sup>-1</sup> using a ball screw transmission. Values for larger actuators or different transmissions might differ but are not readily found in existing literature.

Table G.8: Failure mode effect summary [114]

End effect	Failure per million hours [fpmh]
Actuator jam	3.647e-2
Actuator runaway	6e-6
Loss of actuator	6.152
Loss of service communication	5.748e-2

Table G.9: Fault tree analysis summary [114]

FTA event	Risk likelihood [h <sup>-1</sup> ]
Actuator loss of control/function	6.218e-6
Actuator free floating	6.0e-9
Actuator runaway	2.0709e-12
Actuator jam	3.648e-8

To lower the risk of actuator failure, health monitoring is mentioned as a promising approach in literature. Health monitoring monitors actuator properties such as noise and vibration to estimate the state of deterioration of different components. The technique is already widely used in electric motors and electronic component analysis [125]. [103] shows a health monitoring approach for EMA without need for additional sensors. This approach can be used to identify jamming, remaining life and to facilitate preventive maintenance. The lack of additional sensors reduces cost of the added monitoring functionality [83]. The shown health monitoring approach clearly shows faults in gears in different operating regimes. In 2016, this technology was rated at TRL4 which means the technology is validated in a lab. The same authors explain a method of filtering and interpreting the data from the conventional EMA sensors for health monitoring in [165]. In a more recent paper, the authors describe a health monitoring system based on oil volume estimation. As loss of lubrication is an important indirect failure mode, estimating oil volume in the actuator can reliably predict failure before actual failure occurs according to [166]. The additional benefit of a health monitoring system next to increased reliability is more efficient maintenance task scheduling [83]. Although multiple data acquisition methods for health monitoring are researched already, more work towards diagnostics [83] and fault detection models [113] is needed to use this data. On the other hand, the authors of [125] state no accurate model of the system is needed in case frequency analysis is applied based on accelerator data to predict mechanical failure.

Next to health monitoring, lowering internal friction of the transmission is a solution to lower jamming probability. Schäfer (2005) proposes the use of a harmonic reduction drive instead of conventional reduction gearboxes to improve reliability of electro-mechanical actuators. Next to very low internal friction, this transmission type has no failure modes resulting in jamming behavior. Furthermore the harmonic drive has very high efficiency and a torque density equal to conventional transmissions twice its size and three times its weight [139]. The harmonic drive is however not able to transmit power between two radially displaced axis.

## Motor technology

Despite being an intrinsic part of both electro-hydrostatic and electro-mechanical actuators, motor technology is not discussed extensively in this report. The focus is put on the mechanical aspect of these actuators and corresponding improvement areas. To fill in the gaps, this section will discuss often named motor technologies in literature on a global level. Note that the various motor technologies can all be applied on both electro-hydrostatic and electro-mechanical actuators.

The motor technologies classifying for use in linear actuators as discussed in chapter G.3 all fall within the rotary servo motor class. Servo motors enable control of angular acceleration, velocity and position by use of dedicated servo drives and transducers which operate in a closed loop. Servo drives operate in constant torque mode from 0 to rated speed and in constant power mode from rated to maximum speed [96]. The most often referred to servo motor technologies in literature are the permanent magnet synchronous machine (PMSM) and the brushless direct current machines (BLDCM). Also the switched reluctance motor (SRM) is often named due to its electrically independent winding design. An older variant of the BLDCM which is sometimes used in servo applications is the permanent magnet brushed direct current machine (BDCM). Finally, some servo applications make use of induction or asynchronous machines (IM). Krishnan (1991) uses a diagram for servo motor selection seen in figure G.31 [96]. The choice between brushed and brush-less technology is trivial in favour of brush-less according to [96] due to the higher robustness, higher maximum torque, higher speed bandwidth and lower maintenance intervals. The mechanical commutators and brushes in brushed motors also enforce a severe limitation on the maximum speed and over-current capacity compared to brush-less designs [44]. Most of the technologies shown in the figure use radial field designs. Axial field design has some advantages over conventional field design with respect to power density and torque to inertia ratios, however these motors are less frequently found on the commercial market [96]. Below, the most promising motor technologies are discussed separately. In subsection G.4, a conclusion on which motor technology is appropriate for a high power linear actuator is drawn.

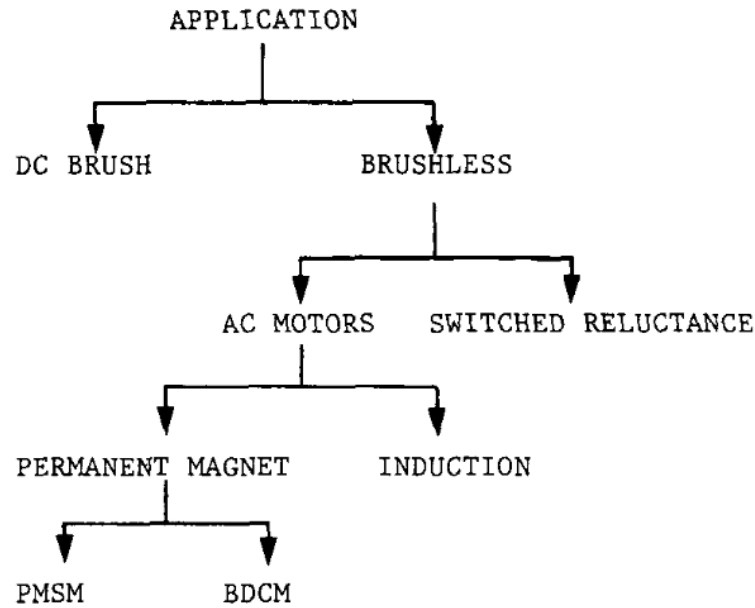


Figure G.31: Servo motor selection procedure.[96]

### Switched reluctance motor

Switched reluctance motors (SRM) are a type of electric machines which make use of reluctance force to rotate the motor. As such the construction of the SRM is much more simple compared to that of other motor technologies [115]. The rotor and stator both have salient poles where the stator poles are lined with concentrated winding's. Special drive electronics are needed to facilitate electric commutation of the independent winding's. A schematic representation of the flux path in the SRM is shown in figure G.32. The lack of permanent magnets and the simple construction in this motor type results in a lower construction price per kilowatt compared to an induction motor [67]. However, the control electronics, concentricity requirements on the construction and the need for high grade encoders outweighs these weight benefits largely [115].

Due to low excitation losses in the SRM, an efficiency up to 97% can be reached at higher speeds (4000 to 7000 rpm). However, due to the lack of permanent magnet excitation, the SRM needs a little higher current to reach the same torque compared to the PMSM [35]. In general, the majority of the SRM losses occur in the stator, making cooling much easier compared to motor technologies with winding's on the rotor [115]. Short term overload capacity of the SRM is also very high due to less heat sensitive components compared to PM machines. Overload torques of 5 to 10 times the overload torque of PM motor technologies can be reached [115]. As such, the torque to inertia ratio of these type of motors can reach up to  $6 \text{ krad s}^{-2}$  [95]. Switched reluctance

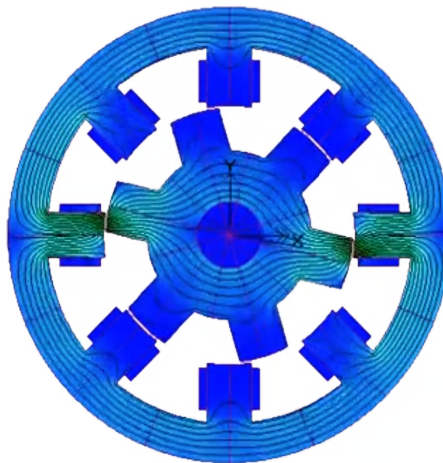


Figure G.32: Switched reluctance machine (SRM) flux path [146]

motors are often stated as fault tolerant [57, 115]. This is explained by the independence of the winding's and the absence of demagnetization risk. It is important to note that independence of the windings can be achieved to a large extent in other motor technologies as well. Similarly, the risk of demagnetization is also absent in for example induction machines.

Ruba (2017) proposes a fault tolerant SRM architecture with 8 modular isolated modules in the stator. The modular architecture and corresponding flux paths can be seen in figure G.33. By using a separate half H-bridge per module, a faulty module can be isolated and the remaining modules can be supplied with a higher current to make up for the torque loss. The machine can continue to operate even with four of the eight coils not operational at 60% of the rated torque. This however is at the expense of a larger torque ripple [133]. The larger torque ripple can be reduced to a satisfactory level with torque smoothing strategies such as direct instantaneous torque control or current profiling [133]. Alternatively, a design with more teeth can be used to assure low torque ripple in case of different faults [134]. The modular design of the proposed SRM allows quick replacement of a faulty module for fast field repair [133].

Some larger drawbacks of the SRM technology are the inherently high noise levels due to pulsed excitation combined with a salient mechanical structure and the high torque ripple [67, 96, 115]. Furthermore, very few established commercial sources who supply variable reluctance motors exist [115]. The high noise levels could potentially be reduced by active noise cancelling strategies such as direct instantaneous force control or current profiling [61]. The lack of commercial applications after more than 40 years of research also indicates the technology can not compete with more established technologies such as the PMSM.

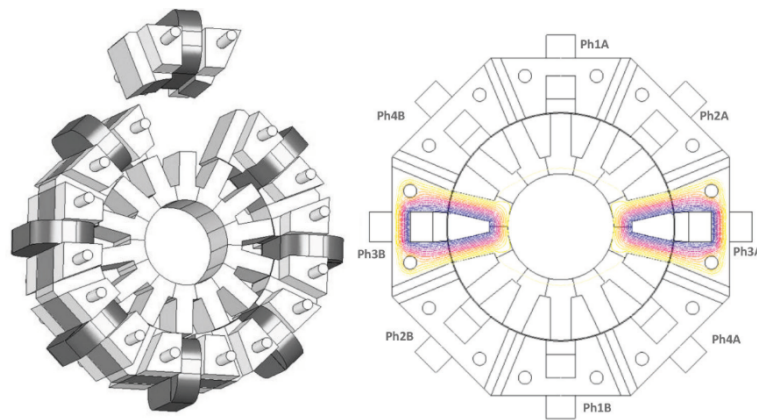


Figure G.33: Modular switched reluctance machine as proposed by Ruba (2017) and the corresponding flux paths. [133]

An alternative to the switched reluctance machine is the permanent magnet assisted synchronous reluctance machine (PMA SynRM). This machine should reduce the torque ripple compared to the conventional SRM with higher efficiency and torque density [170]. In a finite element simulation, a torque ripple of about 16.8% during normal operation is observed with a 6<sup>th</sup> and 12<sup>th</sup> harmonic, mainly due to the rotor saliency and stator slotting interaction [170]. In case of an open or short circuit fault, a 2<sup>nd</sup> harmonic is added to the ripple. The architecture and corresponding flux path of this machine are shown in figure G.34. In comparison with a PMSM, field weakening properties are more favourable with comparable performance and less permanent magnet material usage. The field weakening properties mean the machine can be driven at higher than rated speeds at reduced torque values. Furthermore, the use of reluctance torque results in lower back EMF aiding in keeping power surge to the DC bus upon inverter failure to a minimum [170]. The magnetic torque is able to overcome the reluctance torque and as such the generated cogging torque of the motor is neglect-able [27]. The fault tolerant PMA SynRM proposed by [170] has three segregated 3-phase sets of winding's for physical and thermal isolation. Electrical isolation is achieved by using three standard inverters to drive each 3-phase set separately. A faulty 3-phase winding set can be deactivated by opening all the switches of this set while the remaining two 3-phase sets can keep operating with about 1/3<sup>th</sup> reduction in output power. In case of a short circuit, the low permanent magnet flux in the machine ensures the short current is restricted below the rated value [170]. Furthermore, in the unlikely event of partial demagnetization of the permanent magnets, reduction in torque capability will be limited as magnetic torque only accounts for 30% in this machine.

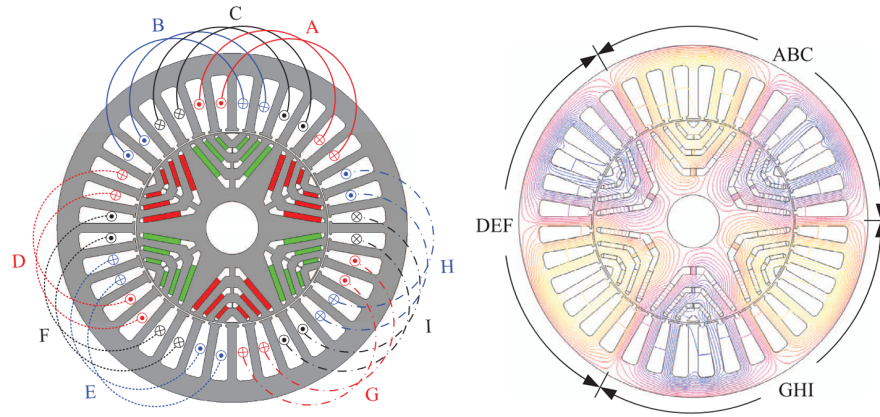


Figure G.34: Permanent magnet assisted synchronous reluctance machine (PMA SynRM) architecture and corresponding flux path. [170]

### Induction motor

Induction motors are three phase motors with either distributed or concentrated winding's on the stator and a squirrel cage embedded in a laminated core as the rotor. Alternatively a slip ring design with a wound rotor can be used. An alternating current is needed to create a rotating magnetic field on the stator poles. Torque is initially proportional to the slip of the rotor with respect to the rotating magnetic field. For larger slip values this relation becomes non-linear. As such, the rotor will always turn slower than the magnetic field when load is applied. The induction motor is often called the workhorse of the industry and therefore is also often the cheapest option compared to other motor technologies [96, 67]. Also, due to the absence of permanent magnets, much higher rotor operating temperatures are allowed [96]. The resulting axial temperature variations are well conducted due to the high copper content of the rotor [67]. Induction motors naturally have a large field weakening range and are easy to control in this region [96]. Furthermore, they suffer less from cogging torque and need less expensive transducers compared to permanent magnet machines [96]. The distributed winding scheme of the induction machine however results in faults of a single phase to propagate to other phases. The windings of the induction machine when connected in star are shown in figure G.35 [64].

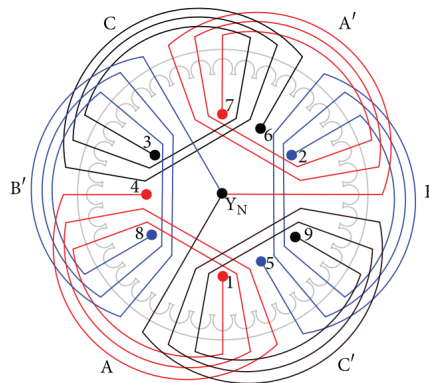


Figure G.35: Induction machine (IM) wiring in star connection. [64]

### Permanent magnet synchronous machine

The most often selected motor technology in servo applications is the permanent magnet (PM) machine. Permanent magnet machines use permanent magnet material to excite the field eliminating the need for windings on the rotor. Permanent magnet motors generally have a lower inertia, higher torque to inertia ratio and higher efficiency compared to induction motors [96]. The permanent magnet machine is also often smaller and lighter compared to similarly sized induction machines [96]. Power density of a double salient pole permanent magnet machine can be a factor two higher compared to induction machines [77]. Due to the permanent magnet excitation, PM machines need a lower rated rectifier and inverter for the same output capacity compared to both induction and SRM machines [96]. On the other hand, poor field weakening properties of the distributed wound

PM machine requires the converter to be oversized [67]. The concentrated wound PM machine has better field weakening properties, but at higher frequencies the rotor losses become too high resulting in excessive rotor temperatures [67]. Field weakening is of lesser importance in servo type motors as high torque and high speed often occur together in servo applications. The disadvantage of permanent magnet material on the rotor is the limit on thermal capacity on the motor. Higher temperatures will demagnetize the permanent magnet material and degrade the motor performance significantly [95].

Within the permanent magnet machines, two designs are often used in literature; the permanent magnet synchronous machine (PMSM) and the brushless direct current machine (BLDCM). The architectures and corresponding flux paths of both machine types can be seen in figures G.37 and G.36 respectively. Both motor technologies have almost equal architectures. The PMSM has a sinusoidal back EMF (AC supply) while the BLDCM has a trapezoidal back EMF (electrically commutated DC supply) [96]. Practical limitations on the maximum achievable speed arise when the back EMF equals the DC voltage of the bus, As a result, PMSM has a higher speed range with the same supply compared to the BLDCM. Also the torque to unit peak current of the PMSM is 1.33 times higher compared to that of the BLDCM with the same peak value back EMF [96]. The maximum speed of the PMSM is often limited by the ability of the power converter to generate the sinusoidal current profile [44]. Application of the sinusoidal current waveform to the PMSM however results in ripple free torque generation with energy efficiencies up to 97% [44]. An analytical efficiency map by [24] shows that more than 50% of the PMSM operational range has efficiencies higher than 90% resulting in efficient overall operation. Power density of the PM machine is limited by the heat dissipation capability of the machine. This is mainly determined by the stator surface area. As such, the BLDCM is capable of supplying up to 15% more power compared to the PMSM in the same frame size according to [96]. This is however nuanced by [44] which states PMSM have a higher torque density compared to BLDC motors at higher power levels. The working principle of the PMSM requires position sensing to be continuous in contrast to the discretized position sensing for the BLDC machine, as a result the construction cost of the PMSM is always higher [44]. As accurate position feedback is needed for proper torque generation, the PMSM is best suited for high-end industrial position or speed controlled applications [44].

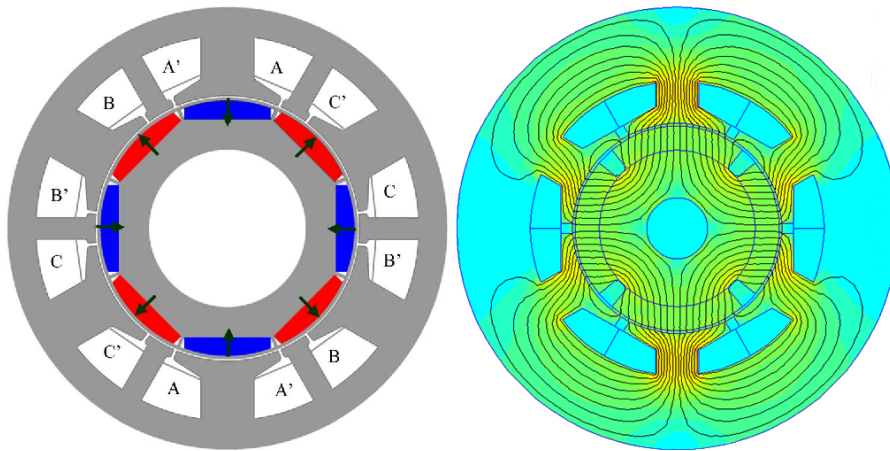


Figure G.36: Brushless direct current machine architecture [157] and the flux paths of a similar machine [14].

Ruba (2017) proposes a fault tolerant PMSM with nine magnetically separated phases as each phase is formed by a single coil surrounding one tooth. The architecture is shown in figure G.37 together with the corresponding flux paths. The inverter divides these nine phases in three groups of three phases each connected in star to form a neutral point. This neutral point is connected to an additional inverter leg which can be used in case a fault occurs in one of the three phases of a single star. Consequently, the machine is able to operate with only two of the nine phases. Without the use of the additional inverter leg, the machine is able to keep the torque constant by increasing the current with a factor  $\sqrt{3}$  in case of a single fault [133]. When increasing the current upon faults, it is important to take into account the thermal effects. Winding's should be designed on the thermal load of the fault induced current [134]. When keeping the current constant, approximately  $2/3$ th of the rated torque will be produced with one faulty phase. Fallout of a phase will create torque ripples, by engaging the fourth leg when a fault occurs the current is shifted to the correct timing and the torque ripple is kept to a minimum [133]. In general a high number of coils and phases can be applied to reduce the effects of winding damages. Fractional slot concentrated winding's with permanent magnets assure higher torque density,

negligible cogging torque and a smaller torque ripple [134].

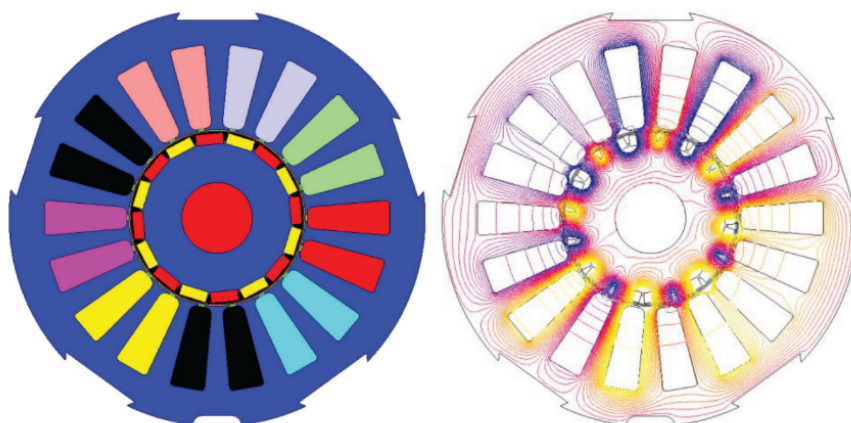


Figure G.37: Nine phase PMSM as proposed by Ruba (2017) and the corresponding flux paths. [133]

### Linear actuator motor

Two requirements on the electric machine driving the high power linear actuator are high power density and high efficiency. The permanent magnet synchronous machine seems to be the current golden standard in servo motor technology offering both this high power density and high efficiency. The ability to create a fault tolerant winding scheme means redundancy in the linear electric actuator can be applied without dual motor setups. The superiority of the PMSM can also be deduced with common sense. Brushed designs have mechanical limits on velocity and are less power dense. In general those machines are replaced by their brushless counter parts. The switched reluctance motor is not currently found in commercial applications and is inherently noisy. Induction machines suffer from losses in their rotor as they need excitation current to magnetize the rotor. As such they are inherently less efficient compared to permanent magnet designs. The difference between the PMSM and the BLDCM is mainly found in their EMF profiles and sensors. The smoother EMF and current profile of the PMSM result in less torque ripple [9]. As such, the permanent magnet synchronous machine is the preferred solution in servo drives for linear actuators.

### Conclusion

This chapter discussed various aspect of the linear actuator for high power applications. Both EHA and EMA seem promising solutions for these applications. In general, the electro mechanic actuator is expected to be lighter and more efficient for lower power applications while the electro hydrostatic actuator becomes more advantageous at higher power levels. However, multiple sources make different claims indicating the absolute advantage of one technology over the other is largely unknown. On reliability, EHA clearly is the more mature technology while reliability data of EMA is less known due to less available data from practical experience. One mean factor between both actuator technologies is the electric machine allowing the actuator to be driven and to regenerate energy. In comparing various motor technologies, the permanent magnet synchronous machine seems to offer the best properties for use as a servo drive.

In chapter G.5, the quantifiable data found in literature on the different actuator technologies will be summarized to get a better understanding of the existing knowledge base on high power linear actuators. Finally, a new research proposal will be formulated to fill in some gaps in this knowledge base.

## G.5 Project proposal

In previous chapters various linear actuator technologies are discussed and reviewed for use in high power applications. In this chapter, the quantifiable data found in literature from existing and researched linear actuator solutions is summarized to visualise the existing knowledge on high power linear actuators. At the end of this chapter, a new research proposal is detailed to fill in some existing gaps in the high power linear actuator knowledge base.

## Literature review

To summarize the literature findings of chapter G.3 and G.4, a small literature review is performed. The review is based on quantified data found in the relevant papers. As such, conclusions from the literature study can be compared with the found examples. Quantifiable data is indexed based on properties such as: actuator type, maximum force, maximum velocity, power density and efficiency.

Relevant literature was mainly obtained through digital searches on various keywords relating to linear actuation. The majority of the papers studied for this literature study were published in the 21<sup>st</sup> century as can be seen from figure G.38a. From all studied papers, papers with quantified data are summarized in this section. The papers containing quantified data are presented in red in figure G.38a. As some papers contain more than one quantified example, the spread in time of all used data points is shown in figure G.38b. The subject of EHA versus EMA actuation is a hot topic in 'more electric aircraft' research. This research kicked off around 1990 according to [132]. This explains the low amount of papers on the topic before this time.

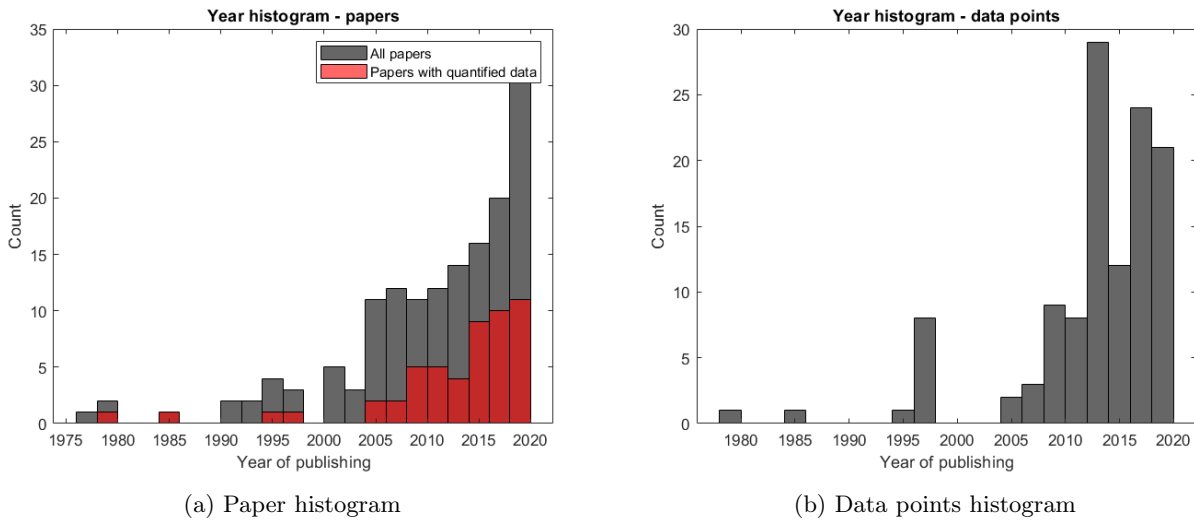


Figure G.38: Chronological distribution of analysed literature

Papers can be largely subdivided in two classes; papers about a complete actuator and papers only describing a specific rotary to linear transmission principle for use in an electro mechanical actuator. The data distribution between the different actuators and transmissions is shown in figures G.39a and G.39b. As can be seen, the majority of the data points concern EMA or EHA actuators. Only a few data points on hydraulic actuators are available. As such, hydraulic actuator data will be left out of this review.

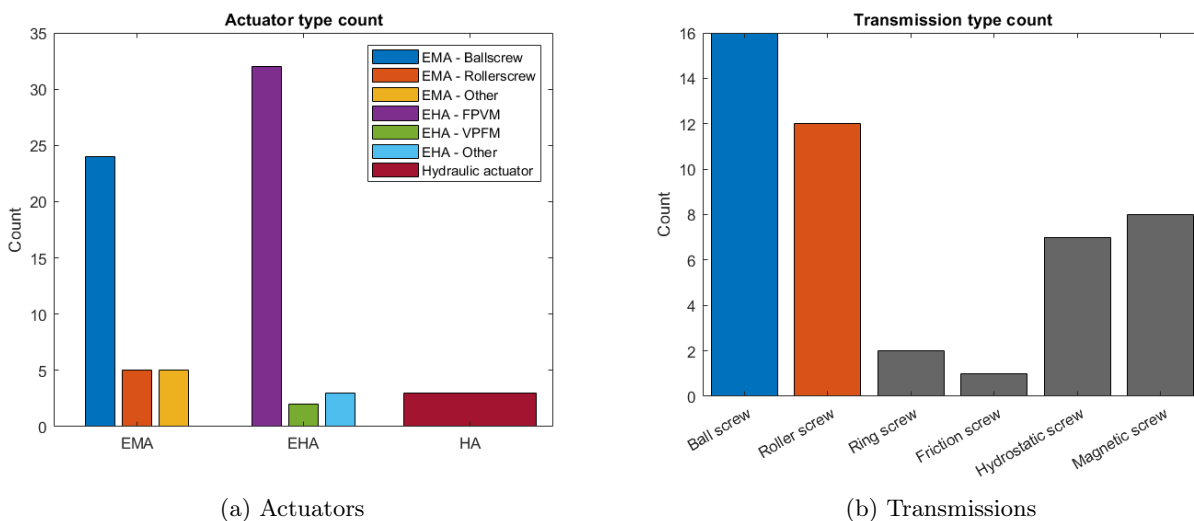


Figure G.39: Number of data points per actuator or transmission type

In figure G.40a, the actuator data is plotted on a maximum force and velocity scale with the data labelled after the respective actuator type. The majority of data points are at relatively low maximum speeds and below 100 kN maximum force. The EHA-FPVM has variants in both 'high-speed, low-force' and 'low-speed, high-force' applications while the EMA actuators seem to focus on the middle ground. Unfortunately, the data set doesn't give a clear trend towards actuator choice based on the force and speed requirements. Furthermore non of the data points come close to the requirements for the Ampelmann actuator. The lack of data points close to the posed requirements do not indicate these requirements can not be reached, only that no examples are available in the studied literature. When plotting the same data set sorted on the application type as seen in figure G.40b, the majority of data points is found in aviation related applications. This explains largely the low maximum velocities found in the majority of the data. Most aviation related linear actuators are used for control surface actuation. A small control arm is attached perpendicular to the control surface, by applying a small linear translation on the control arm an angular deflection of the control surface is induced. The length of the control arm often means a small translation induces a large angular deflection, hence low speeds induce relatively high angular deflection rates. The same conclusion can be drawn when looking at the stroke lengths of the actuators found in figure G.41. The majority of stroke lengths found in literature for both the EMA and EHA actuators are in the range of 0 to 300 mm.

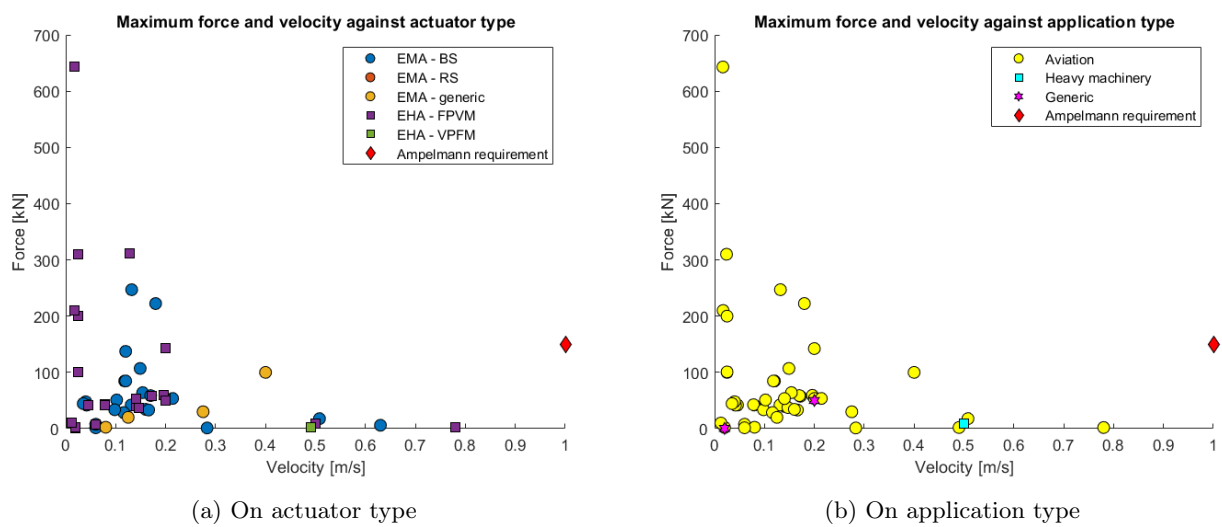


Figure G.40: Maximum force and velocity combinations in literature

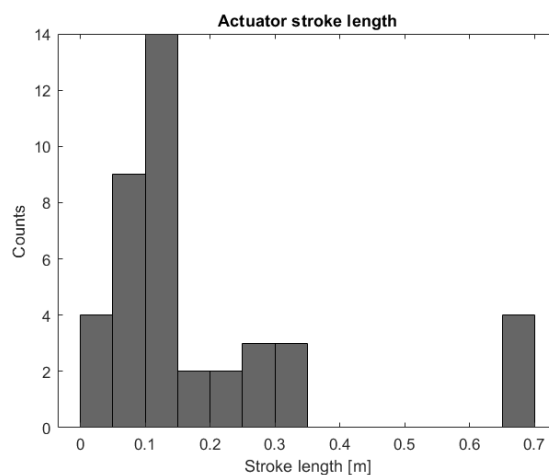


Figure G.41: EMA and EHA actuator stroke lengths found in literature

Not all data points found in literature contain information about all the indexed properties, as such a lot of data is lost in 2D plots. To confirm no actuators can be found at the required power level in the studied literature, maximum power levels per actuator type are plotted (single dimension) in figure G.42a. As can be

seen, both quantified EMA and EHA actuators found in literature go up to 45 kW of output power. When plotting the same graph for individual transmission studies in figure G.42b, the roller screw transmission is seen to be studied up to power outputs of approximately 500 kW. This indicates mechanical transmissions can be used for higher power applications. Also the hydrostatic transmission is studied at a power level with the same order of magnitude as the Amplemann requirements.

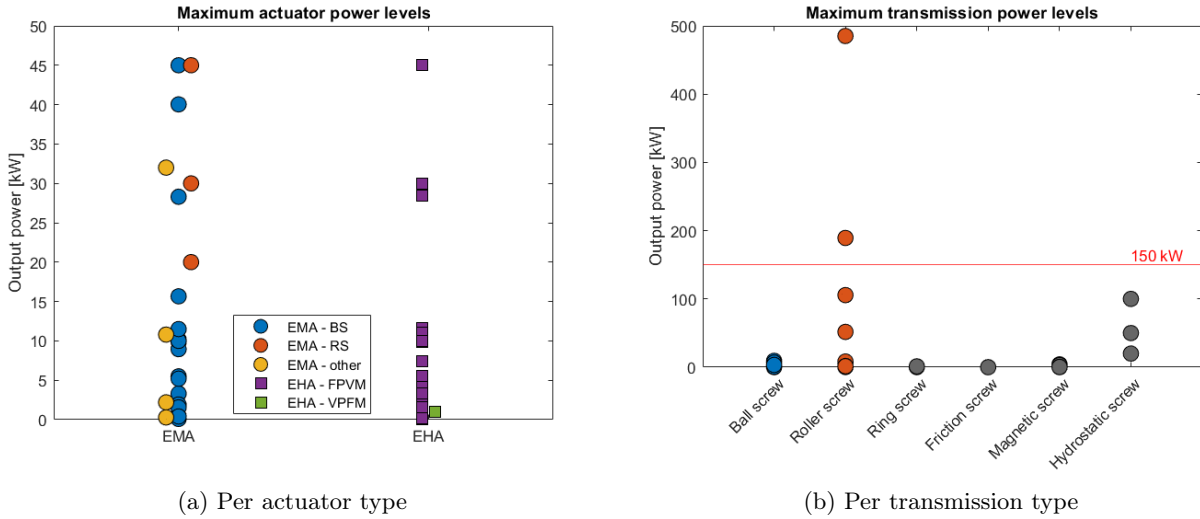


Figure G.42: Maximum power output found in literature

In figure G.43a the efficiencies stated in literature for different actuators is plotted against the maximum output power of the actuator. Note that these efficiencies indicate the mean operating efficiency and can vary substantially for different working points or conditions. The plotted efficiencies show a few outliers of both generic EMA and EHA-FPVM actuators with efficiencies below 50%. The majority of the data points however show energy efficiencies above 70% with EHA showing the highest efficiencies. However, due to the limited available data points and the large spread of these data points, no definitive conclusion can be drawn on which actuator technology is more efficient. The maximum studied power level of 45 kW means results are not necessarily applicable for stronger (larger) actuators.

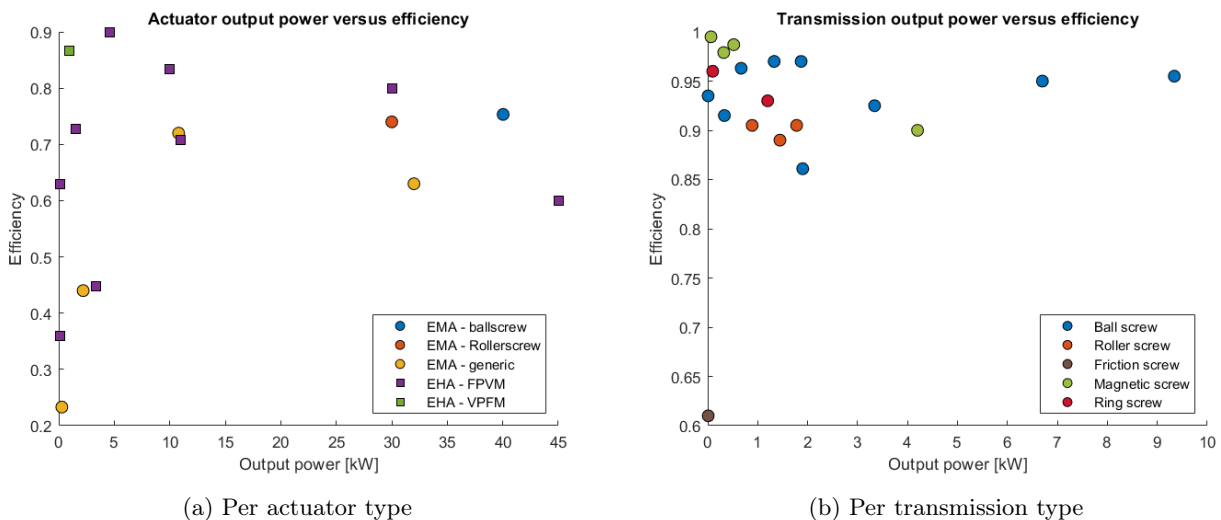


Figure G.43: Efficiencies found in literature

The same efficiency plot is repeated for papers concerning only the rotary to linear transmission principle in figure G.43b. Note that efficiencies of the transmission should be higher compared to total actuator transmission as no electric and mechanical losses in the electronics, motor and gearbox are taken into account here. For lower

power levels, magnetic screws are seen to approach 100% efficiency. Efficiency of this technology however drops for higher power levels and is not documented past 4.2 kW. Ball-screws show a relative consistent efficiency between a power level of 0 to 10 kW which is slightly higher than the efficiency of comparable roller screws. This contrasts the general notion that roller screws are more efficient compared to ball-screws in literature. However, the small data set renders it impossible to draw significant conclusions in comparing transmissions. Again, it is unclear from literature which technology is more efficient for high power applications.

Next to efficiency, also weight of the actuator is a determining factor in actuator choice. The amount of papers quantifying information about the weight of an actuator is limited, however some review papers already summarized existing weight data which is combined with some additional data points in figure G.44.

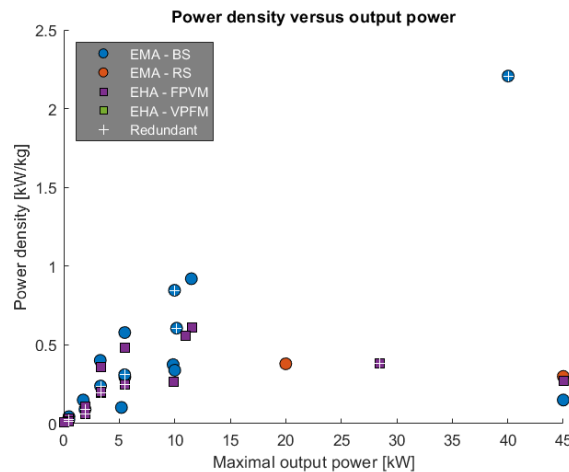


Figure G.44: Power density for different output powers.

At low output power both ball-screw EMA and FPVM EHA seem to follow a similar trend line. The low power density at very low output power can be explained by the minimal material needed to produce a working actuator. Material thickness and actuator parts can not be reduced indefinitely with reducing force and velocity requirements. Ball-screw EMA has slightly larger power densities compared to similar EHA actuators at these power levels. Also the difference between redundant design and non-redundant designs can be seen around 5 kW output power. As expected, redundant designs have generally a little lower power density compared to non-redundant designs. For higher output powers a difference is not visible in this plot due to the low amount of data points.

A single ball-screw EMA outlier is seen at a power density of 2.2 kW. This data point is found in [57] which focused specifically on the design of an electro magnetic actuator with a power density of 1 kW/lb ( 2.2 kW kg<sup>-1</sup>). The design is electrically redundant by using a switched reluctance motor and the corresponding power electronics. The switched reluctance motor is inherently fault tolerant due to the independence of its windings. Upon fallout of a single phase still 80% of the torque can be developed by the motor according to [57]. Note that the high power density is also influenced by the very short stroke of only 15 cm. Longer spindles would increase the weight of the actuator without increasing the power output, hence lowering the power density.

The final major aspect in choice of actuator technology is the reliability of the actuator. Reliability data of EMA and EHA actuators is only sparsely available in literature. The data found on mean time between failures (MTBF) is plotted in figure G.45. The first thing that comes to attention upon studying the figure is the large discrepancy between the two EMA balls-crew data points. Approximately a factor 30 difference in MTBF is not easily explained by different testing conditions. An important note is that the three lowest data points all originate from the same paper. No further explanation about how these numbers are determined is given in this paper. Both highest data points are more reliable as they are backed up by a clear fault tree and proper references. As such, the ball-screw EMA seems to be more reliable compared to the roller-screw EMA. However in comparing both values some assumptions are made which are not proven to be accurate:

- MTBF is independent of the load rating of the actuator. This might be the case if load sizing ensures the material stresses are comparable in different actuators.
- Test conditions are similar or component failure probability is obtained from the same sources. Travelled

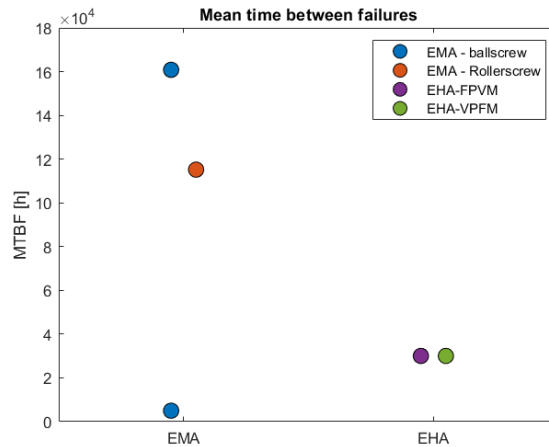


Figure G.45: Mean time between failures of different actuators.

path of the actuator between failures would be a better indicator of reliability of the actuator.

- The few data points are representative for all similar actuators.

An approximation of the second point listed above can be implemented by converting the MTBF in hours to distance with a generic airplane control surface actuator test setup found in literature. The Ampelmann actuator has a mean traveled distance per operating hour of 760 m in comparison. Actuator movement data from airplane control surfaces is not widely found in literature. An aircraft recommended practice document from the society of automotive engineering details the method to obtain actuator displacement and direction changes from data obtained in full scale test setups [82]. An example motion profile of a left stabilator (combination of stabilizer and elevator in a single actuated surface) in a formation flight is given in the same document. Assuming this motion profile is representative for the mean airplane control surface actuator, an actuator displacement per time unit can be determined. The given example has a displacement per time unit of  $14.4 \text{ cm s}^{-1}$  and has on average 6.2 direction changes per second. Converting the distance traveled to  $\text{m h}^{-1}$  gives approximately  $520 \text{ m h}^{-1}$ . Combined with a mean time between failure of approximately 120000 h for the EMA roller-screw as seen in figure G.45, a mean distance between failure of 62400 km is calculated. Next the Ampelmann displacement per hour can be used to convert the control surface actuator data to the expected lifetime in operating hours for Ampelmann. Using the above stated value of  $760 \text{ m h}^{-1}$  the mean time between failure for the Ampelmann actuator becomes approximately 82000 h. The same conversion is performed on all data points in figure G.45 and shown in figure G.46. The converted MTBF data relies heavily on the assumption that the stabilator example data is representative for the mean control surface actuator. However, the recorded formation flight could be argued to induce more control inputs and resulting actuator movement per time unit compared to straight and level cruising flight. As such, the expected MTBF for the Ampelmann actuator would most likely be lower in reality. On the other hand, mean time between failure could be argued to be lower with higher frequency movements. The Ampelmann actuator operates at much lower frequencies compared to the example stabilator data. As such, a higher mean time between failure for the Ampelmann actuator could be argued. Both arguments are needed to indicate the converted mean time between failure is an approximation and by no means gives an accurate representation of the possibly obtainable lifetime of an actuator.

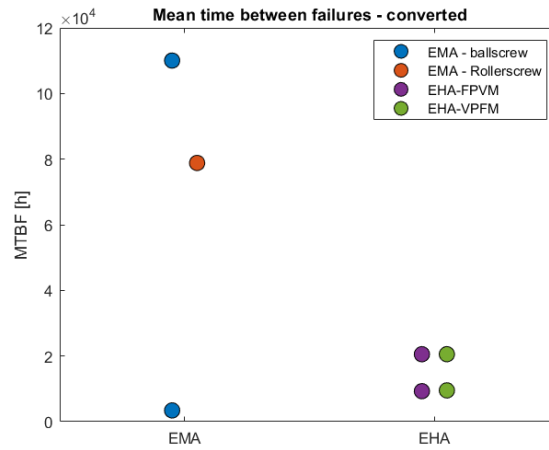


Figure G.46: Converted Ampelmann specific mean time between failures for different actuators.

Unfortunately, even the highest MTBF in figure G.46 does not satisfy the failure rate requirement stated by Ampelmann of  $1e-6$  F/h or  $1e6$  h *MTBF*. As explained in [162], the rating life is determined by the dynamic load rating and the cubic mean load. As such reliability of the transmission system can be designed for. Reliability of the complete EMA and EHA actuator however remain a large topic to be researched further in the future.

## Literature conclusion

A few things are apparent when studying literature concerning linear electric actuators. Before the 1990's, almost all high power linear actuation was facilitated by conventional hydraulic actuators. Examples of applications for these actuators are heavy machinery such as excavators, forklifts and presses or more precise applications such as aircraft control surface actuation. Around 1990, the aviation industry started looking into more electric aircraft (MEA). Electro-hydrostatic (EHA) and electro-mechanic actuation (EMA) are both identified as more electric linear actuation options. Papers on both subject are found mainly after 1990 with the majority of EMA and EHA related papers focusing on the subject of aircraft control surface actuation. Only a few papers discussing EMA and EHA are concerned with different application areas. Papers on components such as the rotary to linear transmission used in the EMA are found earlier than 1990 and are also often focused on the technique without specific applications in mind.

The focus on the aircraft industry results in a few trends found in the data. Control surface actuators generally have stroke lengths of a few centimetres and speed requirements between 0 and  $0.3 \text{ ms}^{-1}$  (see figure G.40a). The maximum load capacity changes more depending on the aircraft size and specific application. However, in combination with the slower velocity, maximum output power is limited below 50 kW. As such, research to EHA and EMA actuators at higher power levels or higher speeds is not readily available in literature. Furthermore, the available data on actuators below 50 kW is often difficult to apply to different applications. Efficiency of an actuator is very dependent on the actual use case as a backdrivable actuator for example is much more energy efficient at moving a load than at holding the load nearly stationary. This indicates the first question about EMA and EHA which is not easily found from existing literature: *"Which actuator technology has a lower energy consumption when applied in an Ampelmann hexapod platform?"*.

Another requirement for the Ampelmann actuator is the weight of the actuator. Weight of the actuator is best expressed in power density [ $\text{kW kg}^{-1}$ ] as the weight is variable with the maximum output power. This requirement is also found in aviation related applications. As such, the best actuator choice based on power density for output levels up to 45 kW can be determined from existing literature. Electro mechanical actuators with roller-helical drives seem to be favourable with respect to EHA and EMA ball-screw solutions at 45 kW output power. The data up to 45 kW is however not representative for larger actuators, data on power density of those actuators is clearly missing in existing literature. Furthermore, power density is heavily influenced by specific features such as redundancy design, fatigue sizing and embodiment design. Influences of these design choices are not researched in the papers found in this literature study. Therefore, the second and third unanswered question are formulated as: *"Which actuator technology has a higher power density when sized for the Ampelmann hexapod actuators?"* and *"What are the influences of detailed design parameters on the final actuator weight?"*.

Finally, reliability of the linear actuator is an important decision factor. Conventional linear actuators have a proven track record, hence reliability of these systems is very well known. Reliability of EHA and EMA is much less known due to its less widespread use. Reliability of EHA is often referred to as "very high" in relevant literature due to the many components inherited from conventional hydraulics. Reliability of EMA's on the other hand is much less studied and understood. EMA's suffer from single point failures leading to mechanical jamming. Relevant literature often states this as a reason to dismiss EMA options as more work is needed in reliability analysis. Health monitoring and redundant design are often named as solutions to increase the reliability. However, redundant design solutions are often limited to the electronics part of the actuator. Very few solutions on mechanical redundancy are proposed or tested. Furthermore, very few examples are available on failure rates of these type of actuators. Data on EMA actuators with different transmission principles to ball- and roller-screw is even absent in literature. Some literature however suggests failure only occurs after the useful life of the actuator, meaning proper lifetime sizing can reduce failure probability. This renders the fourth and fifth questions remaining after this literature study: *"What are failure rates of individual transmissions used in electro mechanical actuators?"* and *"How can failure rates of a transmission be reduced?"*.

## Graduation project

Literature reveals some interesting knowledge gaps regarding optimality in high power linear actuation technology. Determining exact failure rates for various actuator technologies requires extensive experimental testing of physical prototypes and goes beyond the scope of a graduation project. On the other hand, reduction of transmission failure rate or failure risk can be achieved on a fundamental level by looking at failure mechanisms and redundancy in the design. Design variations to achieve failure rate or failure risk reduction also influence both weight and efficiency of the actuator relating to questions 1, 2 and 3 stated in section G.5. The interconnected

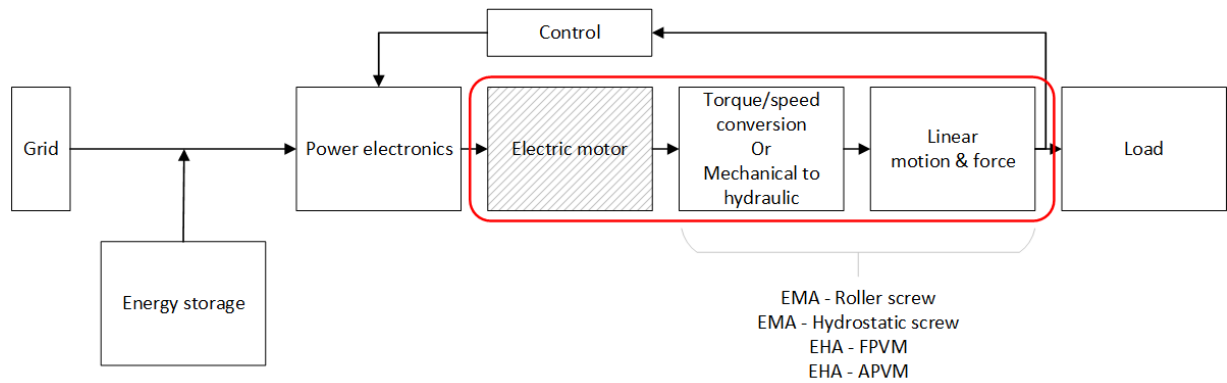


Figure G.47: Optimization scope of the proposed project.

properties of the EMA and EHA actuator make it difficult to make a proper assessment of optimality in the early concept stage of actuator design. Having an automated tool to optimize several actuator technologies on the same requirements with detailed design choice implementations would enable to make an informed deliberation of actuator technologies for a specific application. As such, the following graduation project is proposed:

*Developing an automated high power EMA and EHA sizing and efficiency estimation tool with detailed design choice effects and reliability constraints to aid in application specific optimal actuator choice.*

The tool would require inputs concerning a representative motion and load series, requirements on reliability and lifetime, and peak power capabilities. Different existing EMA and EHA architectures will be assessed and optimized based on weight and energy consumption with constraints on reliability and practical limitations. Practical limitations are for example found on maximum power supply on the vessel and maximum spindle speeds. The emphasis of the optimization should be put on the mechanical and hydrostatic principles and their specific properties. As such the scope of the actuator will be limited to the actual linear actuator itself (see figure G.47). Control effects will not be taken into account, and energy storage will be assumed to be 100% efficient. Furthermore, the electric motor in all actuator designs can be implemented by a permanent magnet synchronous machine as discussed in section G.4. As such, the extra weight and efficiency of power electronics can be left out of the equation to simplify the needed actuator models.

From the literature study, some actuator architectures are seen to have a higher potential in high power applications. As such, four different actuator architectures should be compared in the proposed tool. In electro hydrostatic actuation, both the FPVM and the APVM architectures look promising. The EHA-FPVM has a simple structure and is cheap and robust. Meanwhile, the EHA-APVM promises a superior efficiency and possible weight savings due to lower peak power rating requirements. The FPVM structure also closely resembles the hydrostatic prototype being build by Ampelmann at the time of writing this report. In electro mechanical actuation, the roller-screw transmission is clearly seen to be superior to the ball-screw transmission in high load and high velocity conditions. Furthermore, this technology is currently already used in off the shelf actuators. Also the hydrostatic-screw has potential in high load situations. The linear velocity of this technology might prove difficult, however the potential efficiency benefit makes this technology a possible contender to roller-screw transmissions.

The required number of motors and maximum motor torque can be used to estimate the weight of the motors. Furthermore, scaling laws for transmissions and pumps can be used to find the total weight of the actuator. Efficiencies can be largely found in existing analytical models and can be checked by extrapolating from manufacturer data. Several papers can be found detailing specific models regarding weight or efficiency estimates of a transmission principle. However, no literature was found on the combination of several of these models for optimization purposes or with examples in high power applications. Existing component level models can be used as a base for the automated tool. An overview of papers discussing component level models is given in table G.10.

An additional component of the model should be the discretization of the available components. Manufacturers generally produce parts in various pre determined sizes. The optimized sizing should thus be compared to existing components, follow up calculations should be performed with the closest available size to the optimum. Papers on mid level power actuators can be used for model validation purposes together with existing A3.0

actuator data within Ampelmann. Finally, reliability of actuator designs can be determined through FMECA with component level failure rates found in commercial databases.

Finally also the validity of the tool should be discussed. Validity of the proposed tool is dependent on the posed constraints, such as maximum allowable spindle speed, and on assumptions within the component models. However, validity can also be interpreted as the physical limitations on a given actuator technology. Understanding the maximum attainable forces, velocities, efficiencies and power densities of the stated actuator architectures is a large part in the scientific contribution of the proposed project.

Table G.10: Literature references containing component level analytical models.

	<b>EMA</b>	<b>EHA</b>	<b>Ballscrew</b>	<b>Rollerscrew</b>	<b>Other</b>
Efficiency	[31] (ballscrew)	[34] (VPVM) [59] (VPVM) [76] (VPFM) [76] (FPVM) [140] (open circuit) [172] (VPVM) [178] (VPVM)	[101] [121] [126] [184]	[89] [111] [112] [128] [167]	[11] (Hydrostatic pump) [24] (PMSM) [49] (hydrostatic-screw) [69] (PMSM) [70] (HA)
Weight	[129]	[181] (FPVM)			
Other	[48] (RS, Multibody) [110] (scaling laws)	[131] (FPVM, flow) [143] (FPVM, flow) [179] (VPVM, control)	[79] (Impact failure) [102] (Kinematics) [153] (lifetime) [173] (Wear analysis)	[87] (Kinematics) [98] (lifetime) [144] (sizing) [153] (lifetime)	[73] (Ringscrew design) [139] (MTBF harmonic gear) [183] (motor torque)

In the end, the tool should be able to show a pareto optimality front of actuator designs which can be compared for the given actuator technologies. Using pareto optimality instead of weighted goals enables different linear actuator technologies to be compared for a specific application with variable objective weights. As such, the sensitivities of these objectives can be discussed. Next to the optimality front with regard to energy consumption and power density, also estimates of actuator stiffness (without motor), reliability and cost should be given. These parameters are important in the commercial and control aspects of actuator decision making.

## Methods

The proposed project of section G.5 requires an extensive mathematical model of the actuator architectures and mathematical optimization techniques to find an optimum in actuator design variables. Both actions can be performed in the MATLAB environment. Assembling mathematical models of the required actuator architectures can be performed without the need for additional MATLAB toolboxes. Optimization task however can be vastly sped up by using the optimization toolbox of MathWorks. Initially, toolboxes will be used to speed up development of the proposed tool. Later on the toolboxes could be gradually replaced by simplified equivalent scripts. This later task should only be performed if time is available.

Optimization of the actuator architectures towards lowest energy consumption and highest power density poses a few requirements on the optimization algorithm which is used:

- Allow multiple objective functions
- Able to generate a pareto optimality front
- Able to handle discretized input parameters

In general, optimization algorithms are divided in two main categories; gradient based and gradient free algorithms. Gradient based algorithms are often faster, but rely on continuous objective and constraint functions. Also input parameters are expected to be continuous. With respect to the discretized availability of components, discretized input parameters should be accepted. As such, a derivative free optimization algorithm is preferred in the proposed tool. Multi objective optimizations can be handled in two ways. First, the optimization problem could be reduced to a single objective problem by implementing objective weights. The use of objective weights however enables comparison of different actuator styles only on a specific objective importance ratio. Alternatively, multiple objectives can be combined to generate a Pareto optimal front. This front shows the optimal design solutions for which an improvement in one objective requires a degradation in another. The Pareto optimal front enables comparison of different actuator architectures with variable objective importance ratios. This later solution is preferred in the proposed tool.

Pareto optimal solutions can be obtained with different gradient free algorithms. According to [12], particle swarm optimization (PSO) presents the best balance between quality of solution and number of function evaluations compared to several heuristic multi objective optimization algorithms. [39] shows multi objective particle swarm optimization (MOPSO) only needs half of the computational time compared to a micro genetic algorithm (microGA) on a benchmark problem. This is especially relevant as microGA is often referred to as a very fast optimization approach [39].

[147] proposes an improvement on the MOPSO called the multi-objective feasibility enhanced particle swarm optimization (MOFEPSO). This algorithm enhances the handling of constraint functions and enables optimization without feasible starting points. This enables the algorithm to find a feasible solution even if the feasible design space is very small [147]. [152] also shows a small change in the PSO algorithm to enable the use of discrete input variables. The MOFEPSO is therefore well suited for the optimization problem at hand. Discretized variables can be used to incorporate part availability while low computational cost will result in fast optimization results.

## G.6 Summary

Linear actuator technology is moving towards leaner design solutions using electric drives and compact high efficiency transmissions. Literature shows the majority of these new generation linear actuators are being developed for aviation related applications as the 'more electric actuator'. As such, the majority of the research found in literature is focused on linear actuation up to power levels of approximately 45 kW. In contrast, the Ampelmann hexapod actuator should be able to output a maximum of 150 kW where both the force and velocity of the actuator are often higher than those seen in aviation related actuators. The most often referred to 'more electric actuator' are the electro mechanic actuator using a ball- or roller-screw and the fixed displacement electro hydrostatic actuator. Advantages of one over the other technology are not very well documented and are largely unknown for applications requiring more than 50 kW. The main criteria to compare actuator technologies for use with the Ampelmann hexapod are actuator weight and energy losses. However, additional criteria such as reliability and manufacturing cost should also be taken into account. To obtain a clear understanding of the differences between the 'more electric actuator' technologies on these criteria, a new research project is proposed. The proposed project uses mathematical models of both electro mechanic and electro hydrostatic actuators to find the optimal sizing for efficiency and weight with regard to an Ampelmann specific force and motion case. The developed software tool will function as such that other requirements or force and motion cases can be easily inserted to optimize actuators for different applications. The overall goal of the proposed project is developing a better understanding of the physical limitations of both electro mechanical and electro hydrostatic linear actuators.

# Appendix H

## Glossary

**EMA** electro mechanical actuator

**EHA** electro hydrostatic actuator

**FPVM** fixed pump variable motor

**PRS** planetary roller screw

**MEA** more electric actuator